IEEE TRANSACTIONS ON

INSTRUMENTATION AND MEASUREMENT

SEPTEMBER 1978 VOLUME IM-27 NUMBER 3

A PUBLICATION OF THE IEEE INSTRUMENTATION AND MEASUREMENT SOCIETY

PAPER ON AUTOMATED INSTRUMENTATION

PAPERS

SHORT PAPERS

CORRESPONDENCE

IEEE INSTRUMENTATION AND MEASUREMENT SOCIETY

The Instrumentation and Measurement Society is an organization, within the framework of the IEEE, of members with principal professional interest in instrumentation and measurement. All members of the IEEE are eligible for membership in the Society and will receive this TRANSACTIONS upon payment of the annual Society membership of $5.00. For information on joining write to the IEEE at the address below.

IEEE TRANSACTIONS ON INSTRUMENTATION AND MEASUREMENT is published quarterly by The Institute of Electrical and Electronics Engineers, Inc. **Headquarters:** 345 East 47 Street, New York, N.Y. 10017. Responsibility for the contents rests upon the authors and not upon the IEEE, the Group, or its members. **IEEE Service Center** (for orders, subscriptions, address changes): 445 Hoes Lane, Piscataway, N.J. 08854. **Telephones:** Headquarters 212-644 + extension: Information -7900, General Manager -7910, Controller -7748, Educational Services -7860, Publishing Services -7560, Region/Section Services -7750, Standards -7960, Technical Services -7890. IEEE Service Center 201-981-0060. Washington Office/Professional Services 202-785-0017. Individual copies: IEEE members $5.00 (first copy only), nonmembers $10.00 per copy. Annual subscription price: IEEE members, dues plus Group fee. Price for nonmembers on request. Available in microfiche and microfilm.

Second-class postage paid at New York, NY and at additional mailing offices.

Automatic Calorimeter System for the Effective Efficiency Measurement of a Bolometer Mount in 35-GHz Band

TAKEMI INOUE, MEMBER, IEEE, KYOHEI YAMAMURA, AND TOSHIO NEMOTO, MEMBER, IEEE

Abstract—**An automated calorimetric measurement system using a microcomputer has been developed for determining the effective efficiency of a bolometer mount in the millimeter-wave region. This system consists of a calorimetric measurement part, a bolometric measurement part, and a control/data processing part.**

The system has been constructed and experimented in 35-GHz band. The accuracy of the system has been estimated within ± 0.37 percent.

I. Introduction

THERE ARE various mounts for measuring microwave and/or millimeter-wave power. If they have good characteristics enough to calibrate by any means, they are applicable to precise power meters. In such calibration, a reference mount is called a power standard mount. As the power standard mount, a bolometer mount has been widely used [1], [2]. The feature of the mount in the calibration is described by an effective efficiency. It means the ratio of the measured dc substitutional power to the net consumed millimeter-wave power in the mount. At present, a combined measurement system of the bolometer method and the calorimeter method has been considered the most accurate system for determining the effective efficiency of a bolometer mount and has been practically used [3]–[5].

Generally, the heat capacity of the thermal load used in the calorimeter is so large that the response of the system is very slow. Therefore, continual watching and controlling the system has been necessary in the measurement. For that reason, a calorimetric measurement has been much time consuming and so tedious.

Now, for the purpose of saving labor and improvement of the accuracy, we have developed an automated calorimeter system using a microcomputer for the effective efficiency measurement of a bolometer mount.

II. System Description

A. Principal System

The basic calorimeter system is shown in Fig. 1. The principle of the measurement is based on dc substitutional measurements at a thermally balancing condition [6]. The thermally balancing condition is obtained by controlling the temperature of the thermal load using thermoelectric elements and an auxiliary heater as follows. The thermoelectric cooling elements pump out thermal energy corresponding with the cooling current. The dc bias power of the bolometer mount is controlled to keep its resistance constant. The resultant temperature difference between the thermal load and the jacket flange is detected by the thermoelectric detecting elements. Then, the power proportional to it is fed back to the auxiliary heater.

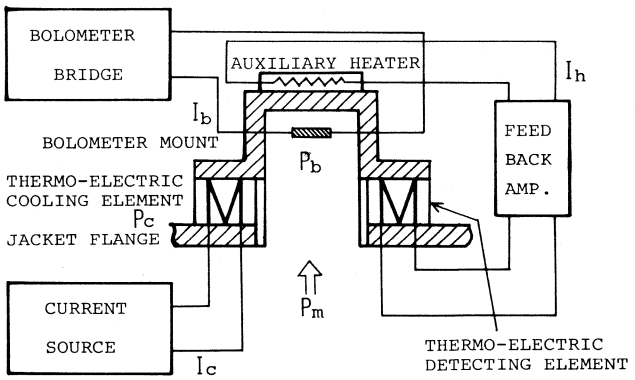

Fig. 1. Basic diagram of the thermal balancing calorimeter system.

Here, in order to have an insight into the principle of the system, suppose an ideal thermal-balancing calorimeter.

The thermal-balancing condition is described as

$$P_h + P_b + P_m = P_c \tag{1}$$

where, P_h is the auxiliary heater power, P_b is the bolometer bias power, P_m is the applied millimeter power, and P_c is the cooling power.

The dc substitutional measurement is done for the bolometer bias power and the auxiliary heater power when millimeter-wave power is applied or not. Suppose that the bolometer bias power is P_{bi} and auxiliary heater power is P_{hi} when millimeter-wave power is not applied, and they come to P_{bf} and P_{hf}, respectively, when it is applied.

For the calorimetric measurement, it is shown that

$$P_{hi} - P_{hf} = P_m. \tag{2}$$

For the bolometric measurement, we get

$$P_{bi} - P_{bf} = \eta_e P_m \tag{3}$$

where, η_e is the effective efficiency of the bolometer mount.

Manuscript received March 2, 1978.

The authors are with the Radioelectronics Section, Opto- and Radio Electronics Division, Electrotechnical Laboratory, Tanashi-shi, Tokyo, Japan.

0018-9456/78/0900-0205$00.75

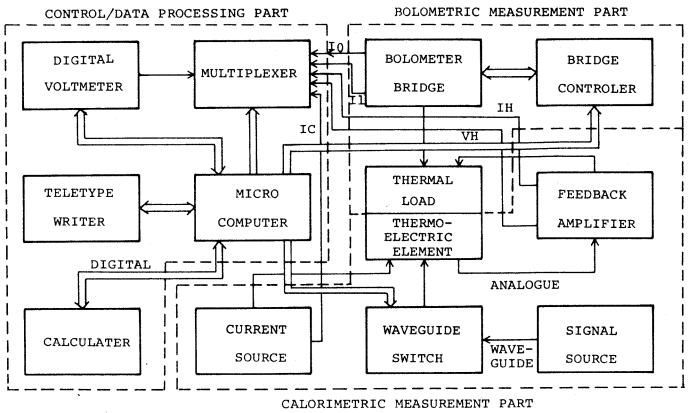

Fig. 2. Block diagram of the automated calorimeter system.

Applying (1) to the initial and final condition of bias power, and using (2) and (3), the effective efficiency of the bolometer mount is derived

$$\eta_e = \frac{1}{1+\xi} \tag{4}$$

where

$$\xi = \frac{P_{hi} - P_{hf}}{P_{bi} - P_{bf}}. \tag{5}$$

In actual calorimeter system, the thermal conductance on the thermal load must be considered. From the detailed analysis of the response of the calorimeter based on a thermal to electric equivalent circuit it is shown that (5) comes to [6]

$$\xi = \frac{P_{hf} - P_{hi}}{P_{bi} - P_{bf}} \cdot S \tag{6}$$

where

$$S = \left[\frac{dP_b}{dP_h}\right]_{P_b = P_{dc}}$$

S is the gradient of the curve of P_b and P_h at the working bias power P_{dc} of the bolometer mount under the condition of temperature balancing condition performed for constant current. Equations (4) and (6) are the measuring equation of the proposed calorimeter system.

B. Actual System

The actual system is composed of three subsystems. They are a calorimetric measurement part, a bolometric measurement part and control/data processing part as shown in Fig. 2. The outside view of the total system is shown in Fig. 3.

The calorimetric measurement part is made up of the calorimeter body and the control circuits. The calorimeter body has a thermal load which is a thin-film bolometer mount [5] with an auxiliary heater. A pair of thermoelectric cooling elements and detecting elements are set on the jacket flange as shown in Fig. 1. The former refrigerate the thermal load, and the latter detect the temperature difference between the thermal load and the jacket flange. In order to isolate the thermal load from the jacket, an adiabatic waveguide is used for introducing millimeter-wave power to the load. Millimeter-wave power is applied to the load through a waveguide switch. The calorimeter body is put in double jackets and further they are steeped in an oil bath to stabilize the inner temperature. As the supporting components of the calorimetric measurement, a constant current source is used for the thermoelectric cooling and an amplifier is used for a feedback control of the thermal load.

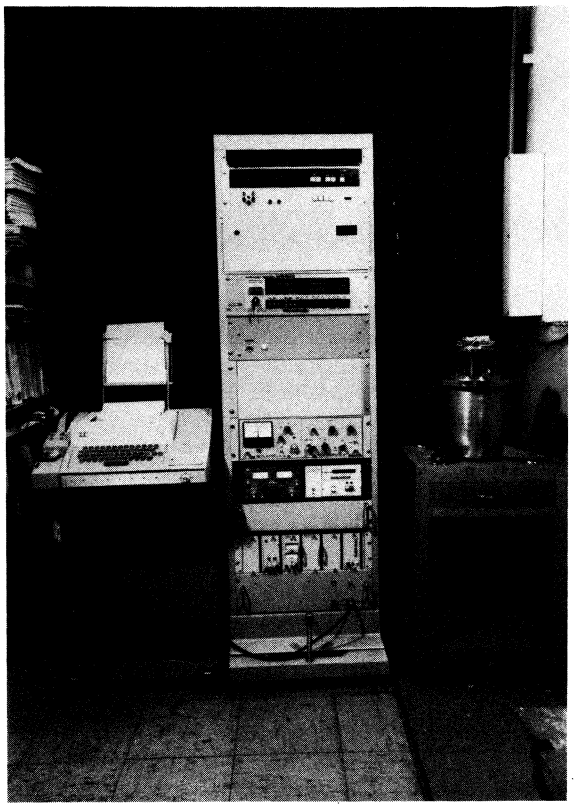

Fig. 3. Outside view of the system.

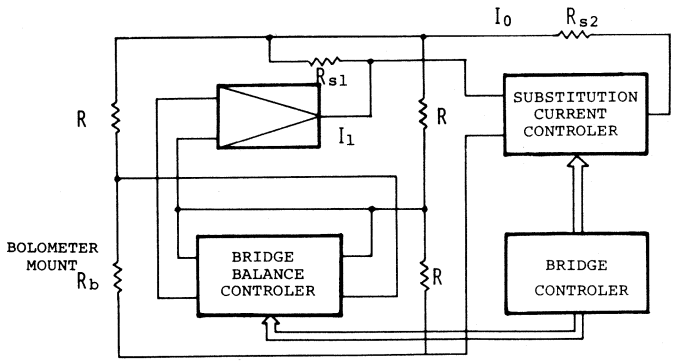

Fig. 4. Block diagram of the automatic bolometer bridge.

The bolometric measurement part consists of an automatic bolometer bridge with an adaptive control [7]. The block diagram of it is shown in Fig. 4. Conventionally, the bolometric measurement using such as an automatic bridge with simple feedback amplifier has had dominant errors due to the bolometer bias current measurement and the imperfection of the bridge control.

The bridge used in the proposed system can improve these defects by an adaptive technique which is combined of

digital and analog control. That is, the bridge current and the bridge unbalance voltage are substituted by programmable sources, and these errors are remarkably improved. In Fig. 4 the substitution current controller and the bridge balance controller are combined programmable sources made of A/D, D/A converters, and memory. The substitution current controller has a current booster in addition. The working procedure of the bridge is as follows. Initially, the bridge is balanced by the feedback amplifier as well as an ordinary autobalancing bolometer bridge. Then, the bridge balancing current I_0 through R_{s1} is roughly measured and is digitally stored in the memory. The substitutional current corresponding to I_0 is added to the top of the bridge through R_{s2} from the substitutional current controller and the current of the amplifier comes to residual one I_1. If I_0 is held constant, I_1 will be decreased to the amplifier current I_2 when millimeter-wave power is applied. Thus the millimeter-wave power P is calculated as follows:

$$P = \frac{R}{4}(2I_0 + I_1 + I_2) \cdot (I_1 - I_2) \qquad (7)$$

where, R is the working resistance of the bolometer mount. Here, $I_1 - I_2$ can be measured as accurate as I_0, therefore, the current reading error is reduced comparing to that of a method which measures total bridge current directly. The control deviation of the bridge is also measured beforehand and substituted similarly at proper timing in the power measurement. This compensation of the control deviation means that the loop gain of the bridge is improved comparing to an usual analog control one and the control error can be reduced to the resolution of the programmable source in principle.

The control/data-processing part consists of a microcomputer and its peripheral devices. The microcomputer is adopted because of its economical condition and suitability for controlling. The voltage at several terminals of the calorimetric or bolometric measurement parts are selectively measured by a digital voltmeter through a multiplexer. As the multiplexer, a mechanical scanner is used because of its superior stability and repeatability. A calculator is interfaced with the microcomputer in order to process data [8].

III. Measurement Procedure

Before starting the effective efficiency measurement, some preparations are necessary. Initially, the cooling current is manually set a little higher value than the current necessary to balance the bolometer bias power thermally. After the whole thermal system comes to a thermal balancing condition, the correction factor S in (6) is determined by measuring the bolometer bias power or heater power independently at the condition of constant cooling current.

The measurement procedure of the effective efficiency is shown in Fig. 5. With the starting the measuring program, data such as date, time and temperature, etc., are put on the TTY according to the instructions of the microcomputer. Here, the correction factor S which is measured beforehand is also input. Then the bolometer bias power measurement is

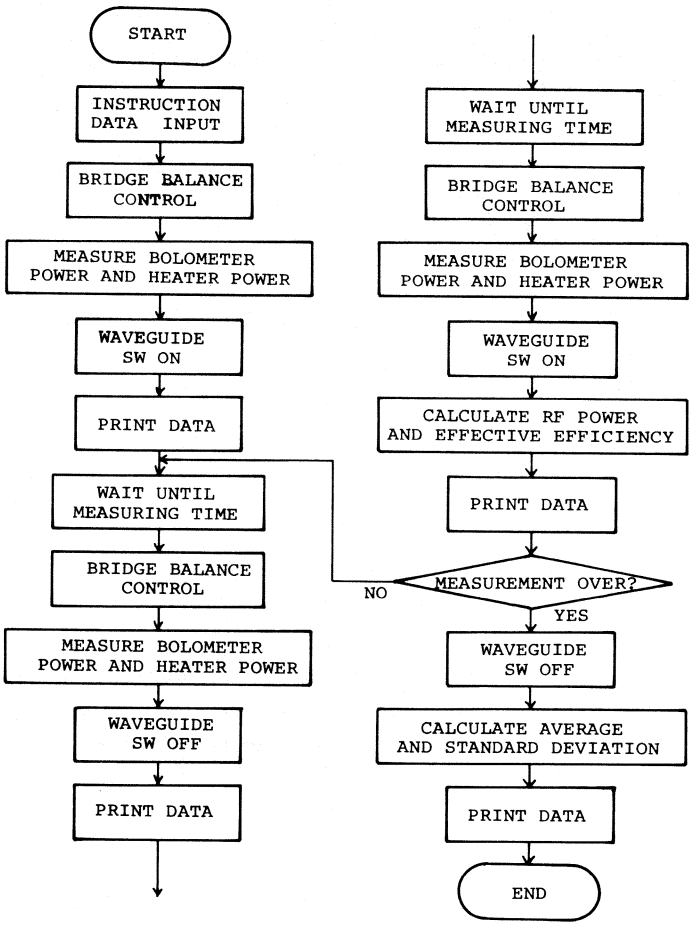

Fig. 5. Flowchart of the calorimetric measurement.

executed. This is calculated by (4) and (6). The cooling current is also measured.

The procedure of the effective efficiency measurement is repeated by five times in order to eliminate the effect of the temperature drift by averaging. The time interval of each measurement is ten minutes. The heater power is determined by voltage V_h and current I_h. In advance of the bolometer power measurement, a bridge balancing control is always done to compensate the temperature drift. The bolometer bias power and the effective efficiency of the mount are calculated and printed out per period of the measurement. Finally, the average value of them and the standard deviation of the measured effective efficiency are calculated and printed out.

An example of the measurement at the frequency of 35 GHz is shown in Fig. 6. Where, the minus sign of the measured current shows the direction of the current. In spite of the variation of millimeter-wave power the calculated effective efficiency shown in the column X agrees within ± 0.01 percent. For several measurements, the randomness of it agrees within ± 0.1 percent.

IV. Evaluation of the Measurement Error

It is important to evaluate the error factors for a precise measurement. Systematic errors are due to the uncertainty and/or instability of the system components and can be

```
BOLOMETER MOUNT EFFECTIVE EFFICIENCY MEASUREMENT
     DATE    1977/12/1
     TIME    15:40
     TEMP.   23.0
     MOUNT   NO.4
     FREQ.   35.0GHZ
     WGTYPE  REC
     S:PB/PH 0.95430
-----------------------------------------------------------------
BOLOMETER BIAS POWER MEAS.
     SUBST   I0= 26.151MA
     DIFFER  I1=-0.23540MA
     BIASPOWER= 33.580MW
COOLING CURRENT MEAS.
             199.98MA
-----------------------------------------------------------------
MEAS. START
  T       I1(MA)    I2(MA)    P(MW)     VH(MV)    IH(MA)    X(%)
15:40    -0.23440                      1022.5   -10.598
15:50              -4.6090    10.374    999.93   -10.362   95.78
16:00    -0.23900                      1023.0   -10.599
16:10              -4.6182    10.382   1000.3    -10.368   95.76
16:20    -0.24340                      1023.9   -10.608
16:30              -4.6547    10.454   1001.0    -10.372   95.76
16:40    -0.24460                      1024.2   -10.613
16:50              -4.6608    10.466   1001.1    -10.374   95.77
17:00    -0.24360                      1024.2   -10.611
17:10              -4.6302    10.400   1001.0    -10.374   95.75
17:20    -0.24530                      1024.2   -10.611
-----------------------------------------------------------------
     AVERAGE                 10.415                         95.77
     STAD. DEVIATION                                      0.009316
                        MEAS. END
```

Fig. 6. Example of the measurement.

estimated. On the contrary, a random error is caused by unexpected factors such as a personal operation or external disturbance. Therefore, it can be evaluated by a statistical processing of the data. In an automated system, the random error can be improved because of the less manual operation and making repetition of the measurement.

The error factors in this system are shown as follows:

a) dc measuring equipment error; b) auxiliary heater control error; c) measurement equation error; d) attenuation error; e) distribution equivalence error; and f) random error.

Here, an analysis and evaluation of these error factors are described.

A. DC Measuring Equipment Error ε_{dc}

This is due to the dc measuring equipment used in the system. Analyzing (4) and (6), the next error equation is obtained [6]

$$\varepsilon_{dc} = \pm 4(\varepsilon_b + \varepsilon_h) \cdot (1 - \eta_e) \tag{8}$$

where, ε_b is the accuracy of the bolometer bias power measurement and ε_h is the accuracy of the auxiliary heater power measurement. In this system, a digital voltmeter with ± 0.01-percent accuracy and standard resistors with ± 0.015-percent accuracy are used for them. Thus we obtain $\varepsilon_b = \pm 0.045$ percent and $\varepsilon_h = \pm 0.035$ percent. Therefore, ε_{dc} comes to ± 0.032 percent supposing $\eta_e = 0.9$.

B. Auxiliary Heater Control Error ε_{con}

This is due to the residual deviation of the auxiliary heater control. This fact means that the temperature difference between the thermal load and the jacket flange is not perfectly zero. This error factor is estimated as the following equation as well as (8)

$$\varepsilon_{con} = \pm 4\varepsilon_{hc}(1 - \eta_e) \tag{9}$$

where, ε_{hc} means the measurement error of the auxiliary heater power due to the control deviation. From an experiment of the thermal balancing, ε_{hc} is obtained as ± 0.2 percent. Accordingly, ε_{con} comes to ± 0.08 percent from (9) supposing $\eta_e = 0.9$.

TABLE I
MEASUREMENT ACCURACY OF THE SYSTEM

systematic error	DC measuring equipment error	ε_{dc}	±0.032%
	auxiliary heater control error	ε_{con}	±0.08 %
	measurement equation error	ε_{eq}	-0.045%
	attenuation error	ε_{att}	±0.1 %
	distribution equivalence error	ε_{dist}	±0.08 %
random error		ε_{ran}	±0.1 %
overal accuracy		+0.392 / -0.357	±0.37%

C. Measuring Equation Error ε_{eq}

When the measurement equation of the effective efficiency (4) and (6) were derived, the next term is neglected [6].

$$\varepsilon_{eq} = -\frac{k\sigma}{1 - k}. \tag{10}$$

Where, $k = r_b/(r_l + r_b)$. r_b is the thermal resistance between the bolometer element and the waveguide surface. r_l is the thermal resistance between the bolometer element and the ambient air in the mount.

For the evaluation of ε_{eq}, it is satisfactory to know the maximum value of $|\varepsilon_{eq}|$. Supposing σ is constant $|\varepsilon_{eq}|$ takes maximum value when k in (10) is maximum because of $0 < k < 1$. Analyzing the characteristics of heat transfer in the bolometer mount approximately shown in the appendix, k takes the maximum value of 0.00452. σ is nearly equal to $1 - \eta_e$. So that, ε_{eq} comes to -0.045 percent supposing $\eta_e = 0.9$.

D. Attenuation Error ε_{att}

This is due to the loss of the adiabatic waveguide. ε_{att} has already evaluated as ± 0.1 percent [5].

E. Distribution Equivalence Error ε_{dist}

This error arises because the temperature distribution on the bolometer element differs when dc power or millimeter-wave power is applied. For the 35-GHz thin-film bolometer mount, $0 < \varepsilon_{dist} < 0.08$ percent is obtained [5].

F. Random Error

Finally, the random error in the system is estimated within ± 0.1 percent from the results of several measurements such as Fig. 6.

The error factors discussed above is shown in Table I.

In consequence, the total accuracy of the automated calorimeter system is evaluated within ± 0.37 percent.

V. CONCLUSION

An automated calorimeter system for the effective efficiency measurement of a bolometer mount has been developed and experimented at the frequency of 35-GHz band. This system has proved not only useful for saving operator's labor but also highly reliable in the measurement.

The measurement accuracy of the system has been evaluated within ± 0.37 percent.

APPENDIX

The thermal to electric equivalent circuit of the bolometer element is approximately shown in Fig. 7 if the temperature of the mount is held constant. Where, P_b is the consumed power in the bolometer element. T_b is the temperature of the element. From this figure, a relation between T_b and P_b is derived.

$$T_b = \frac{r_l r_b}{r_l + r_b} \cdot P_b. \tag{A-1}$$

For a representative bolometer mount of the 35-GHz band, it was shown that $T_b = 110°C$ and $P_b = 34$ mW [5]. Hence, the next equation is obtained.

$$\frac{r_l r_b}{r_l + r_b} = 3.76 \text{ (h °C/cal)}. \tag{A-2}$$

Thus k is given as

$$k = \frac{3.76}{r_l}. \tag{A-3}$$

The evaluation of r_l is very difficult because of the complexity of thermal conduction and/or thermal convection in the bolometer mount. Here, we give an approximate analysis of it.

The thermal resistance r_l is considered, for the most part, due to the heat transfer between the bolometer element and the air around. So that r_l is given as follows:

$$r_l = \frac{1}{h \cdot S_b} \tag{A-4}$$

where h is the heat transfer coefficient at the boundary of the bolometer element and the air around and S_b is the area of the power absorbing element in the bolometer element. In the case of stationary air, the heat transfer coefficient is ordinary in the order of $3 \sim 20$ kcal/m^2 h °C [9]. The power absorbing element has the width of 0.06 mm and the length

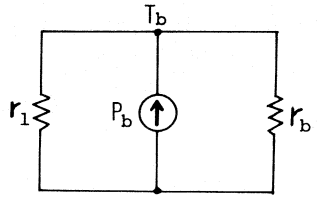

Fig. 7. Thermal to electric equivalent circuit of the bolometer element in steady state.

of 1 mm. Accordingly, substituting $h = 3 \sim 20$ (kcal/m^2 h °C) and $S_b = 0.06$ mm^2, r_l is evaluated as

$$r_l = 833 \sim 5560 \text{ (h °C/cal)}. \tag{A-5}$$

From (A-3) and (A-5), the maximum value of k is obtained as

$$k = 0.00452.$$

ACKNOWLEDGMENT

The authors wish to thank the members of the Radioelectronics Section for their continual support and also appreciate the encouragement of Dr. K. Sakurai.

REFERENCES

[1] A. C. Macpherson and D. M. Kerns, "A microwave microcalorimeter," *Rev. Sci. Instrum.*, vol. 26, pp. 27–33, Jan. 1955.
[2] M. Sucher and J. Fox, Eds., *Handbook of Microwave Measurement*. New York: Wiley, 1963.
[3] A. Y. Rumfelt and L. B. Elwell, "Radio frequency power measurement," *Proc. IEEE*, vol. 55, pp. 837–850, June 1967.
[4] K. Sakurai and T. Maruyama, "A millimeter-wave microcalorimeter," *IRE Trans. Instrum. Meas.*, vol. IM-4, p. 270, Dec. 1962.
[5] K. Sakurai, "Microwave power standard," Res. Rep., Electrotechnical Lab., no. 680, Dec. 1967.
[6] T. Inoue, K. Yamamura, and T. Nemoto, "A calorimeter for measurement of effective efficiency of 100 GHz bolometer mounts," *Trans. Soc. Instrum. Contr. Eng.*, vol. 13, no. 6, pp. 609–614, Dec. 1977.
[7] T. Inoue and K. Yamamura, "Automatic bolometer bridge using an adaptive control technique for RF power measurement," *IEEE Trans. Instrum. Meas.*, vol. IM-27, pp. 166–169, June 1978.
[8] T. Inoue and T. Nemoto, "A microcomputer for a CAM (computer assisted measurement) system," *Bull. Electrotech. Lab.*, vol. 40, no. 1, pp. 31–45, Jan. 1976.
[9] H. Gröber, S. Erk, and U. Grigull, *Fundamentals of Heat Transfer* (McGraw-Hill Series in Mechanical Engineering). New York: McGraw-Hill, 1961, p. 174.

Improvements of the Procedures Used to Study the Fluctuations of Oscillators

ETIENNE BOILEAU

Abstract—**Considering that procedures currently used to study the fluctuations in oscillators do not give directly useful results, we have tried to define a procedure more suitable for experimentalists. We have tempted to obtain a function $\sigma(T)$ which would be a kind of variance of the frequency fluctuations observed in a duration T. Taking a frequency domain point of view, we find a procedure which can yield also an estimation of the spectral density of the frequency.**

I. Introduction

In EXPERIMENTS with an oscillator, it is often important to have some statistical knowledge of the frequency fluctuations occurring in a time interval of duration T. Because of slow frequency drifts, the amplitude of these fluctuations increases with T. The variance (defined for $T \to \infty$) even seems to be infinite, however, this last point is not important here, since measurements are always performed in a finite time T. A single parameter, independent of T is currently given, supposed to describe the "short-term stability" of an oscillator, but a "finite time variance" $\sigma(T)$ could have a more precise meaning, and be very useful. Several attempts have been made to give a good definition of such a function.

Two procedures associated with two expressions of the true variance and yielding such functions have been proposed at first, and in a previous paper [1], a comparison of these two functions $\sigma_1(T)$ and $\sigma_2(T)$ has been given. This comparison was done from several points of view, but the most important one seems to be in frequency domain. In both cases, some kind of low-frequency cutoff is obtained, wrongly defined around $1/T$. This observation led us to look for a procedure which would give, at best, a cutoff at $\nu = 1/T$. In other words, assuming that the frequency F of the oscillator under study has a spectral density $\gamma_F(\nu)$, we are looking for the procedure which would give the best approximation of

$$\sigma^2(T) = 2 \int_{1/T}^{\infty} \gamma_F(\nu)\, d\nu. \tag{1}$$

Besides, such a procedure could be used to get an estimation of $\gamma_F(\nu)$ by simple derivation of the function obtained by taking the new variable $f = 1/T$ (for $\nu > f_m = 1/T_M$ if T_M is the maximum value of T used).

In a first approach, we seeked the optimal procedure using a linear filter of the frequency F [2], and later, we obtained another improvement with a quadratic procedure [3]. The aim of this paper is to present these results to the experimentalists studying oscillators.

We note that the Allan variance [4] yields another description of the fluctuations of an oscillator; $\gamma_F(\nu)$ being well approximated by a sum $\sum_i (A_i / |\nu|^{\alpha_i})$, if one of these terms is predominant in some ν interval, the Allan variance gives α_i. However, the knowledge of these α_i is clearly not as useful for the practician as that of the curve of a finite time variance.

II. Review of the First Procedures

It is assumed that sampled measurements of the frequency $F_n = F(t_0 + nT_1)$ are available, and a procedure yielding a good "finite time variance" is wanted. We have $T = pT_1$ and, except for the first case, p will be odd and we put $p = 2N + 1$. The result *a priori* will depend on both p and T_1, and also on the time constant τ of the frequency measurements; indeed the instantaneous frequency is not directly measurable, but only its average on a certain time interval τ. The dependence upon τ will disappear only if τ is choosen short enough so that fast fluctuations be not filtered off [1].

If the spectral density $\gamma_F(\nu)$ of $F(t)$ exists, the sampled process F_n has a periodic (period $1/T_1$) spectral density $\gamma(\nu)$ which is

$$\gamma(\nu) = \frac{1}{T_1} \sum_{l=-\infty}^{l=+\infty} \gamma_F\left(\nu - \frac{l}{T_1}\right). \tag{2}$$

If T_1 is small enough, $\gamma_F(\nu)$ is negligible outside the period $|\nu| < 1/2T_1$, and (2) becomes

$$\gamma(\nu) \simeq \frac{1}{T_1} \gamma_F(\nu). \tag{3}$$

Then (1) becomes

$$\sigma^2(T) \simeq 2T_1 \int_{1/T}^{1/T_1} \gamma(\nu)\, d\nu.$$

If T_1 is not small enough, $\gamma_F(\nu)$ has components for $|\nu| > 1/2T_1$ which should be estimated previously with analogic apparatus, in order to calculate their contribution to (1); the knowledge of (1) is then equivalent to that of ($f = 1/T$):

$$I(T) = J(f) = 2T_1 \int_{f}^{1/2T_1} \gamma(\nu)\, d\nu. \tag{4}$$

Manuscript received October 27, 1976.

The author is with the Laboratoire des Signaux et Systèmes, Ecole Supérieure d'Electricité, Plateau du Moulon, 91190 GIF/Yvette, France.

0018-9456/78/0900-0210$00.75

A. Two Procedures Built on the Two Expressions of the Variance [1]

For each set of p samples, the following quantities are calculated:

$$P_1 = \frac{1}{p}\sum_{n=1}^{p} F_n^2 - \left(\frac{1}{p}\sum_{n=1}^{p} F_n\right)^2 \tag{5}$$

$$P_2 = \left(F_0 - \frac{1}{2N+1}\sum_{n=-N}^{N} F_n\right)^2. \tag{6}$$

With a certain number of such sets, the following averages are estimated

$$\sigma_1^2 = E(P_1) \tag{7}$$

$$\sigma_2^2 = E(P_2). \tag{8}$$

If $\gamma_F(\nu)$ exists, we have

$$\sigma_i^2 = \int_{-\infty}^{+\infty} \gamma_F(\nu)\,|G_i(\nu)|^2\,d\nu \tag{9}$$

$$= T_1 \int_{-1/2T_1}^{1/2T_1} \gamma(\nu)\,|G_i(\nu)|^2\,d\nu$$

with

$$|G_1(\nu)|^2 = 1 - \left(\frac{\sin p\pi\nu T_1}{p \sin \pi\nu T_1}\right)^2 \tag{10}$$

$$|G_2(\nu)|^2 = \left(1 - \frac{\sin p\pi\nu T_1}{p \sin \pi\nu T_1}\right)^2. \tag{11}$$

These two functions are even and periodic (period $1/T_1$) and are plotted on Fig. 1 for $p = 31$ (i.e., $N = 15$). We see that they modulate $\gamma(\nu)$ in (9) quite differently, and are not good approximations of the periodic function $H(\nu)$ used in (4) and defined by

$$H(\nu) = \begin{cases} 0, & \text{for } |\nu| < f \\ 1, & \text{for } f < |\nu| < 1/2T_1. \end{cases} \tag{12}$$

These observations led us to look for an optimal approximation of $H(\nu)$.

B. First Optimization

We first tried to use a procedure using a filter which generalizes (6); let us put

$$P_3 = \left(\sum_{n=-N}^{N} R_n F_{-n}\right)^2 \tag{13}$$

$$\sigma_3^2 = E(P_3). \tag{14}$$

With the same assumption as before, we have (9) with $i = 3$ and

$$G_3(\nu) = \sum_{n=-N}^{N} R_n \exp(in2\pi\nu T_1). \tag{15}$$

We want that $|G_3(\nu)|^2$ be the best approximation (for a given N) of $H(\nu)$, but this condition yields nonlinear equations; to simplify, we search the R_n such that $G_3(\nu)$ be the best approximation of $\sqrt{H(\nu)} = H(\nu)$, in the mean-square sense. In other words, we minimize

$$D = \int_{-1/T_1}^{1/T_1} |H(\nu) - G_3(\nu)|^2\,d\nu. \tag{16}$$

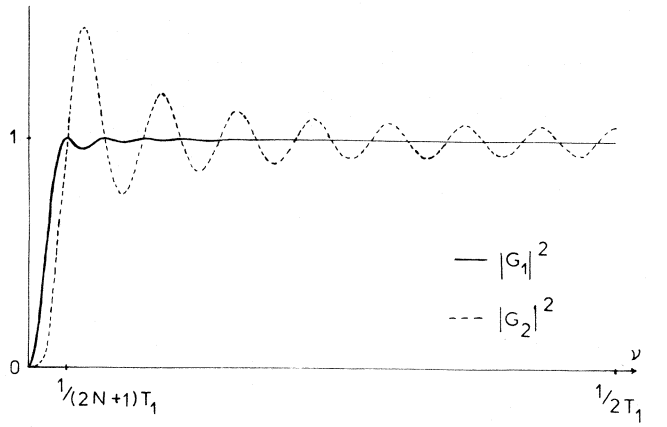

Fig. 1. Frequency ponderation obtained with the procedures P_1 and P_2.

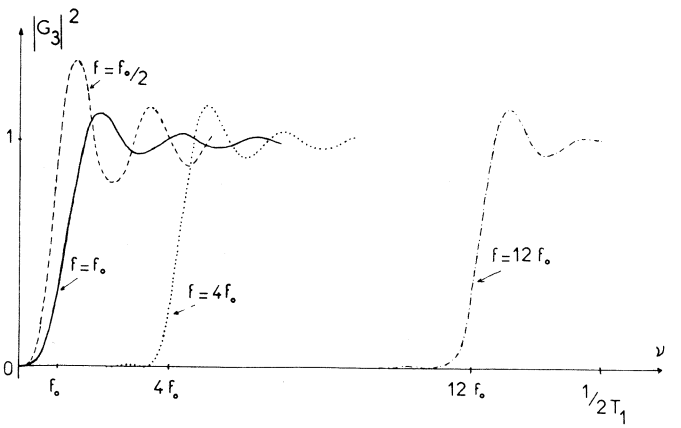

Fig. 2. Case of the procedure P_3 obtained with the discontinuous original.

As it is important to get rid of the singularity of $\gamma(\nu)$ for $\nu = 0$, we impose the supplementary condition

$$G_3(0) = 0. \tag{17}$$

It is easily shown [2], [5], that the optimal R_n are then obtained from the coefficients c_n of the complex Fourier series development of $H(\nu)$:

$$R_n = c_n - \frac{1}{2N+1}\sum_{n=-N}^{N} c_n \tag{18}$$

$$c_0 = 1 - 2fT_1 \tag{19}$$

$$c_n = -\frac{1}{n\pi}\sin 2\pi nfT_1, \qquad n \neq 0. \tag{20}$$

One will use $f = 1/T = 1/(2N+1)T_1$ to get the curve $\sigma_3(T)$. On the contrary, in order to obtain an estimation of $\gamma(f)$ we must use different values of f, but we can use the same value of T (i.e., same sets of measurements). Some curves of $|G_3(\nu)|^2$ obtained with $N = 15$ (i.e., $T = Cte$) and different values of f are given on Fig. 2. We have put

$$f_0 = \frac{1}{T} = \frac{1}{(2N+1)T_1}. \tag{21}$$

It can be observed that the overshoot increases slightly as f is increased above f_0, but increases quickly as f is decreased for $f < f_0$.

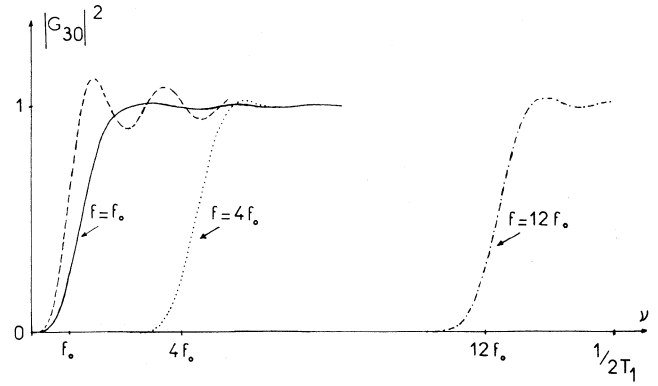

Fig. 3. Case of the procedure P_3 obtained with a continuous original, $a = f_0$.

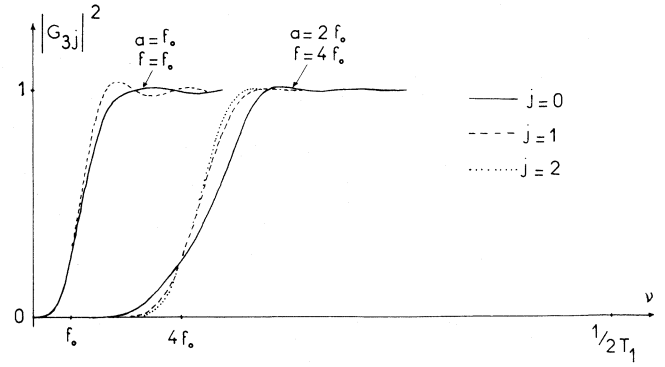

Fig. 4. Case of procedures P_3 obtained with different continuous originals.

Besides, for $f \to 0$, C_n $(n \neq 0) \to 0$, so that

$$P_3 \underset{f\to 0}{\to} \left(F_0 - \frac{1}{2N+1}\sum_{n=-N}^{N} F_n\right)^2.$$

Thus in the limit, P_3 is the process P_2, i.e., σ_2 is here optimal, if we want to get rid only of the component $v = 0$. On the other hand, P_3 can be used for a given N with f varying in $(f_0, \frac{1}{2}T_1)$. In this interval, $\sigma_3^2(f)$ gives an estimation of (4), whence, by derivation, an estimation of $\gamma(f)$ can be obtained.

III. Some Improvements

A. Use of Continuous Originals

With a finite development such as (15), discontinuous functions are not well approximated; this is known as the Gibbs phenomenon. Better results are obtained with continuous originals (functions used instead of $H(v)$ in former calculations).[1]

We have first used the function $H_0(v)$, even and periodic (period $1/T_1$) defined by $H_0(v) = 0$ for $v < (0, f - a)$, $H_0(v) = 1$ for $v \subset (f + a, 1/2T_1)$ and by the linear function which ensures continuity in $(f - a, f + a)$.

The optimal coefficients R_n are again given by (18), with c_0 given by (19), but, for $n \neq 0$, the coefficients c_n of the Fourier series of $H_0(v)$ are

$$(c_0)_n = -\frac{\sin 2\pi nfT_1}{n\pi}\,\frac{\sin 2\pi naT_1}{2\pi naT_1}. \tag{22}$$

Corresponding curves, obtained with $a = f_0$, are plotted on Fig. 3, showing a real improvement with respect to those of Fig. 2. The definition of $H_0(v)$ assumes $f > a$; we have nevertheless plotted the curve obtained with (22) and $f = f_0/2 = a/2$; the result (dotted curve) is better than with $H(v)$ but clearly worse than for $f > a$. If one wants to use $f < f_0$, one should use smaller a, but, for a given f, the overshoot increases with decreasing a (for $a \to 0$, $H_0(v) \to H(v)$). The choice $a = f_0$ seems good for $f \subset (f_0, 1/2T)$.

The improvement obtained with H_0 is associated with a steeper asymptotic decrease of the coefficients c_n, and we can go on by taking originals having as many continuous derivatives as wanted [3]. We can obtain such functions by an integration (and translation) of the functions $y_j(x)$, equal zero outside $(-a, a)$, even and such that

$$\int_{-a}^{a} y_j(x)\,dx = 1. \tag{23}$$

We use the index j to indicate the number of continuous derivatives that the corresponding original $H_j(v)$ possesses. Thus the discontinuous function $y_0(x)$:

$$y_0 = \begin{cases} 1/2a, & \text{for } |x| < a \\ 0, & \text{for } |x| > a \end{cases} \tag{24}$$

gives the original $H_0(v)$ introduced above, which has no continuous derivative.

The Fourier coefficients of $H_j(v)$ are $(n \neq 0)$

$$(c_j)_n = -\frac{\sin 2\pi nfT_1}{n\pi}\int_{-a}^{a} y_j(x)\exp(-i2\pi nxT_1)\,dx. \tag{25}$$

We choose for $y_1(x)$ the continuous triangular function (Bartlett window), which after integration gives the original $H_1(v)$ and

$$(c_1)_n = -\frac{\sin 2\pi nfT_1}{n\pi}\left(\frac{\sin n\pi aT_1}{n\pi aT_1}\right)^2. \tag{26}$$

For $y_2(x)$, we use here the following function (Hanning window)

$$y_2 = \begin{cases} (1/2a)(1 - \cos \pi x/a), & \text{for } |x| < a \\ 0, & \text{for } |x| > a. \end{cases} \tag{27}$$

It has one continuous derivative, is associated with the original $H_2(v)$ and gives

$$(c_2)_n = -\frac{\sin 2\pi nfT_1}{n\pi}\,\frac{\sin 2\pi naT_1}{2\pi naT_1}\,\frac{1}{1 - 4a^2T_1^2n^2}. \tag{28}$$

We call $G_{3j}(v)$ the best approximation of $H_j(v)$, obtained by the preceeding method. Some curves of $|G_{3j}(v)|^2$ are given on Fig. 4. With $f = 4f_0$ we have taken $a = 2f_0$, which gives improvements easy to see from $j = 0$ to $j = 2$. With $a = f_0$, we observe that the advantage of large j is less

[1] In fact we worked above on $\sqrt{H(v)} = H(v)$; in the following, originals differ from their root-squares and we shall use functions $H_j(v)$ which in this 1° play the role of root squares of the originals.

obvious; indeed, the overshoot increases more rapidly (as a decreases) with larger j.

We can then say that the original $H_0(\nu)$ is sufficient with $f = f_0$ and $a = f_0$. Nevertheless $H_1(\nu)$ and $H_2(\nu)$ can be useful for $f \gg f_0$ and large N. Besides, they will be used thereafter.

Larger values of j are easily obtained [3] but seem to have little practical interest.

B. Use of a Quadratic Process

Noting that P_1 defined by (5), does not belong to the set of processes defined by (13), among which we have looked for an optimum, we have tried to improve our results using quadratic processes of the form

$$P_4 = \sum_{i,j=-N}^{N} A_{ij} F_i F_j. \tag{29}$$

Assuming again that F has a spectral density, we have

$$E(F_i F_j) = T_1 \int_{-1/2T_1}^{1/2T_1} \gamma(\nu) \exp\left[i2\pi(i-j)T_1\right] d\nu \tag{30}$$

and we obtain

$$E(P_4) = T_1 \int_{-1/2T_1}^{1/2T_1} \gamma(\nu) Q(\nu)\, d\nu \tag{31}$$

with

$$Q(\nu) = \sum_{i,j=-N}^{N} A_{ij} \exp\left[i2\pi(i-j)\nu T_1\right] = \sum_{k=-2N}^{2N} B_k \exp\left(i2\pi k \nu T_1\right) \tag{32}$$

$$B_k = \sum_{i-j=k} A_{ij}. \tag{33}$$

The sum (32) is of the same form as the one which gives $G_3(\nu)$ in (15), but it is made of $(4N+1)$ terms whereas (15) has only $(2N+1)$ terms. This observation makes us hope for better results with an adequate choice of the B_k. However, in the interval where the original is zero, the fact that $G_i(\nu)$ is squared in (9) will be an advantage for processes of the form (13).

Let us notice that it is not necessary to keep $(2N+1)^2$ terms in (29); indeed, P_4 is determined by the sums $A_{ij} + A_{ji}$ (coefficients of the $F_i F_j$) and the value of P_4 is not changed if we take for instance

$$A_{ij} = 0, \qquad \text{for } i > j \tag{34}$$

after replacing the A_{ij} for $i < j$ by the former value of $(A_{ij} + A_{ji})$.

We want to choose the B_k so that $Q(\nu)$ be the best approximation of $H(\nu)$ defined by (12); however, as before, we get better results with smoothed originals. We use the $H_j(\nu)$ considered above; noting $Q_j(\nu)$ the corresponding optimal $Q(\nu)$, it minimizes

$$D_j = \int_{-1/2T_1}^{1/2T_1} |H_j(\nu) - Q_j(\nu)|^2\, d\nu \tag{35}$$

and satisfies

$$Q_j(0) = 0. \tag{36}$$

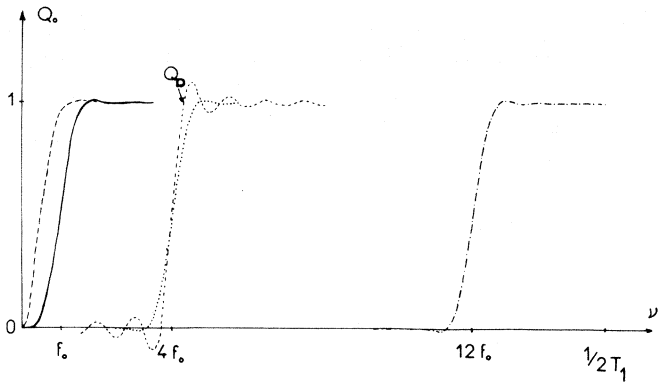

Fig. 5. Case of procedure P_4 obtained with a continuous original (Q_D is obtained with the discontinuous original), $a = \frac{1}{2}f_0$.

The same calculations as above give the coefficients of the development of $Q_j(\nu)$ with those from $H_j(\nu)$:

$$(B_j)_k = (c_j)_k - \frac{1}{4N+1} \sum_{k=-2N}^{2N} (c_j)_k. \tag{37}$$

As the originals $H_j(\nu)$ are even we have $(c_j)_{-k} = (c_j)_k$ and from (37), $(B_j)_{-k} = (B_j)_k$. This is clearly incompatible with (34) which gives $B_k = 0$ for $k > 0$. However, if we use (34), we must notice that in (31), the odd part of $Q(\nu)$ does not bring any contribution; it is the even part of $Q(\nu)$ which must be the best approximation of the original and put in (35). From (32) we see that the even part of $Q(\nu)$ is also its real part, and with (34) we obtain

$$\begin{aligned} (B_j)_k &= 2\left[(c_j)_k - \frac{1}{4N+1} \sum_{k=-2N}^{2N} (c_j)_k\right], \qquad k < 0 \\ (B_j)_0 &= (c_j)_0 - \frac{1}{4N+1} \sum_{k=-2N}^{2N} (c_j)_k \\ (B_j)_k &= 0, \qquad k > 0. \end{aligned} \tag{38}$$

It is easily verified that (37) and (38) give functions $Q_j(\nu)$ which have the same even part.

The curves[2] of the Fig. 5, compared with those of Fig. 3 show the improvement obtained with P_4; the number of samples is the same ($p = 31$) as well as the selected values of f ($f = f_0/2$, f_0, $4f_0$, and $12f_0$). With a smaller value of a ($a = f_0/2$), we have a smaller overshoot in a broader frequency interval.

For $f = 4f_0$ the curve $Q_D(\nu)$ has been added, obtained with the discontinuous original $H(\nu)$. It can then be compared with those of Fig. 2; the overshoot is smaller, but we see oscillations for $f < f_0$ which are much higher. The advantage of P_4 would then be doubtful with the discontinuous original.

We have shown on Fig. 6 the improvement obtained with originals having one and two continuous derivatives ($j = 1$ and $j = 2$). The effect is best seen with $a = 2f_0$ (used with $f = 4f_0$) but exists also with $a = f_0$, with still a very small

[2] As well as for Fig. 6, we have plotted the even parts of the functions $Q_j(\nu)$.

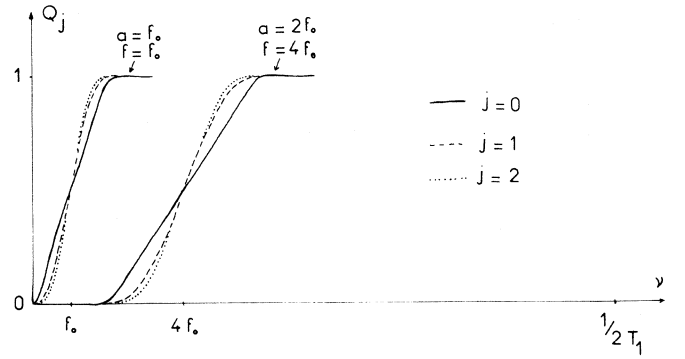

Fig. 6. Case of procedure P_4 obtained with different continuous originals.

overshoot (unlike when the process P_3 is used; see Fig. 4). Even with $a = \frac{2}{3}f_0$ we have an overshoot very small and decreasing with j (respectively, about 0.7 percent for Q_0 and 0.5 percent for Q_1 and Q_2). For $a = f_0/2$, the reverse is true (about 1 percent for Q_0, 1.8 percent for Q_1 and 2.8 percent for Q_2).

A reasonable choice of the ratio a/f_0 consists in taking it as small as possible compatible with an accepted value of the overshoot; we see then that this ratio can be taken smaller when j is smaller. This fact moderates the interest of large j values. With Q_0 and an accepted value of 1 percent for the overshoot, we then choose $a = f_0/2$ and the procedure can be used to get an estimation of $\gamma(\nu)$ for $\nu \subset (1/2T, 1/2T_1)$ as seen on Fig. 5.

For $\nu \to 0$, $Q_j(\nu)$ is of first order in ν, whereas $|G_{3j}(\nu)|^2$ is of second order and $|G_2(\nu)|^2$ of fourth order; this could be considered as a drawback of our procedure [1]. This drawback can be easily removed by adding supplementary conditions: $dQ_j(0)/d\nu = 0$, $d^2Q_j(0)/d^2\nu = 0, \cdots$, to (36) (as well as for $G_3(\nu)$ we can add $dG_3(0)/d\nu = 0, \cdots$). The solution of the problem is well known [5], and gives similar curves as far as $f > a > f_0$ [6]. However, these supplementary calculations are necessary only if $\gamma(\nu)$ has a severe singularity for $\nu = 0$.

We have seen how to choose the coefficients B_k, but (33) evidently does not determine the A_{ij} from the B_k. One can take advantage of this indetermination to minimize the variance of P_4 [3], but it implies a preliminary determination of the $\Gamma_k = E(F_n F_{n-k})$ which is not very feasible here (because of the slow drifts). In practice the following choices are sufficient:

1) If one wishes to simplify as much as possible the calculation of P_4, one takes a single $A_{ij} \neq 0$ for each $i - j < 0$, and, in order to have a factorization, we can take

$$P_4 = F_{-N}(B_0 F_{-N} + B_1 F_{-N+1} + \cdots + B_{2N} F_N). \quad (39)$$

2) In order to get an estimation of $E(P_4)$ we must calculate a certain number of samples and take their average. If we can dispose of a number of F_n which allows a strong integration on P_4, we thus obtain a good precision on $E(P_4)$. On the contrary, if, for instance, we have a given total number of F_n which does not allow strong integration, it is desirable to reduce the variance of P_4 as much as possible; we can then make another simple choice of the A_{ij} by taking them all equal for each value of $i - j$:

$$A_{ij} = \frac{B_{i-j}}{2N + 1 - |i - j|}. \quad (40)$$

The calculation of the samples of P_4 will then cost more time, but each P_4 sample will already be a combination of averages on the terms $F_n F_{n+i-j}$. The variance of P_4 will then be smaller. (The choice (40) minimizes the variance of P_4 if $F(t)$ has a correlation time short compared with T_1 [3].)

IV. Conclusion

By introducing a quadratic processing of the measurements, we have defined a procedure which gives a more accurate description of the short-term fluctuations of an oscillor than the previous ones. Moreover our procedure can be used to obtain a good estimation of the spectral density of the frequency fluctuations in the accessible interval.

References

[1] E. Boileau and B. Picinbono, "Statistical study of phase fluctuations and oscillator stability," *IEEE Trans. Instrum. Meas.*, vol. IM-25, pp. 66–75, 1976.

[2] E. Boileau, "Elimination optimale des dérives lentes dans les mesures de fluctuations," *Ann. Télécommun.*, vol. 30, pp. 163–166, May–June 1975.

[3] E. Boileau and H. Clergeot, "Optimisation de certains traitements numériques avec une forme quadratique," *Ann. Télécommun.*, vol. 31, pp. 179–189, May–June 1976.

[4] J. A. Barnes *et al.*, "Characterisation of frequency stability," *IEEE Trans. Instrum. Meas.*, vol. IM-20, pp. 105–120, May 1971.

[5] J. C. Radix, *Introduction au Filtrage Numérique.* Paris, France, Eyrolles, 1970.

[6] E. Boileau and Y. Lecourtier, "Quelques problèmes posés par l'analyse spectrale basse fréquence," in *Proc. Cinquième Colloque National sur le Traitement du Signal et ses Applications*, Nice, France, pp. 141–149, June 1975.

An Analog Parallel Fourier Transform (PFT) Equipment and Its Application to the Moving Vehicle Size Detection in a Spatial Frequency Domain

TASUKU TAKAGI, MEMBER, IEEE

Abstract—**A new type of Fourier transform system proposed by the author was realized in hardware and applied to the moving vehicle size detection. CdS photo-sensor array (9 cell units) was used to pick up the moving vehicle image which was transformed into spatial frequency domain. The experimental results showed the peak value of the fundamental component corresponded to the vehicle size.**

I. Introduction

IN A ROAD-TRAFFIC data-aquisition system, various sensors have been used, such as an inductive loop buried in a road surface, ultrasonic sensors, microwave radars, etc. A new optical sensing method of moving vehicles using photocell has been developed by the author along with real-time size-discrimination techniques of the vehicles (1). A problem in this new system was that of a background level change of the natural illumination intensity due to a position of sun, cloud, or other weather conditions. However, such a background level change can be compensated electrically at the photocell's output since it is possible to obtain the moving vehicle signals by discriminating the vehicle image response (signal) from the background level (zero level) by means of threshold devices. The computation needed to set the zero level deviation, however, is rather difficult since the natural illumination intensity varies widely compared with the intensity of the vehicle image signal on the photocell.

One of the most efficient means in eliminating the effect of background illumination intensity variation when treating a natural visible pattern is by converting the image into a spatial frequency domain. This way, since the background illumination intensity appears in a dc component in the spatial frequency domain, we can easily disregard the dc component, provided that an appropriate Fourier pattern analyzer can be obtained. An optical Fourier transform using lens system is difficult to apply on this matter because the natural reflection light is incoherent. A digital fast Fourier transform algorithm (2) may be applied, however the system will become complicated since the object is moving.

The author proposed a new analog and fully parallel Fourier transform (PFT) system (3) which can be easily applied for the above purpose. In this paper, the hardware implementation of the simple PFT (9 inputs, 9 outputs) is described in Section II, the moving vehicle detection system in Section III, and the experimental results of moving-vehicle-size detection in Section IV.

Manuscript received November 15, 1977. This work was supported in part by the Kurata Research Grant.

The author is with the Department of Electrical Communications, Tohoku University, Sendai, Japan.

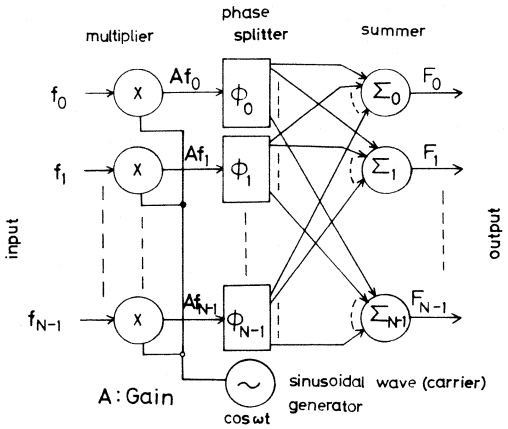

Fig. 1. Structure of the PFT equipment.

II. Hardware Implementation of Analog PFT

The proposed analog PFT (3) can be seen as a hardware substitution of an optical Fourier transform system using lens and laser, especially in the two-dimensional case, although it has been used for the optical one-dimensional Fourier transformation as well (4). The speed of the analog PFT, therefore, can be limited only by the signal transmission time because no memory device is involved. For the present purpose of detecting moving vehicle size, it is not necessary to construct two-dimensional PFT, because the vehicle size can be determined by measuring its length.

A. Construction of the One-Dimensional Analog PFT

The general schematic diagram of the one-dimensional analog PFT is shown in Fig. 1. How this construction works as the Fourier transform system has been explained in the literature (3). The number of channels N corresponds to the number of samples simultaneously applied to the PFT equipment. We take $N = 9$ for the present purpose; we shall see the reason for this in Section III.

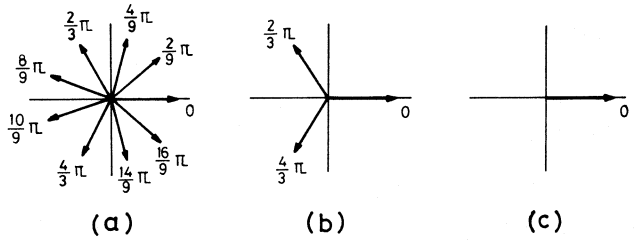

Fig. 2. Vector diagrams of the phase splitters. (a) for ϕ_1, ϕ_2, ϕ_4, ϕ_5, ϕ_7, and ϕ_8. (b) for ϕ_3 and ϕ_6. (c) for ϕ_0.

The input signals $(f_0, f_1, \cdots, f_{N-1})$ are linearly multiplied by a sinusoidal wave as shown in Fig. 1. The amplitudes of the sinusoidal waves are fed to the phase splitters $(\phi_0, \phi_1, \cdots, \phi_{N-1})$, each has N output terminals. The output phase angles of ϕ_n $(n = 0, 1, \cdots, N-1)$ can be expressed as

$$\phi_n: [0, 2\pi n/N, 2\pi 2n/N, \cdots, 2\pi(N-1)n/N]. \quad (1)$$

Fig. 2 shows the vector diagrams of each phase splitter when $N = 9$, and Table I shows the relationship between frequency components $(F_0, F_1, \cdots, F_8)$ and phase angles to be summed up by the sum $(\sum_n)$ in Fig. 1. For example, F_0 and F_1 can be obtained, respectively, as follows:

$$F_0 = A \sum_{i=0}^{8} f_i \cos \omega t = B_0 \cos \omega t \quad (2)$$

and

$$\begin{aligned} F_1 = A \Big[& f_0 \cos \omega t + f_1 \cos\left(\omega t + \frac{2\pi}{9}\right) + f_2 \cos\left(\omega t + \frac{4\pi}{9}\right) \\ & + f_3 \cos\left(\omega t + \frac{2\pi}{3}\right) + f_4 \cos\left(\omega t + \frac{8\pi}{9}\right) \\ & + f_5 \cos\left(\omega t + \frac{10\pi}{9}\right) + f_6 \cos\left(\omega t + \frac{4\pi}{3}\right) \\ & + f_7 \cos\left(\omega t + \frac{14\pi}{9}\right) + f_8 \cos\left(\omega t + \frac{16\pi}{9}\right) \Big] \\ = & B_1 \cos(\omega t + \theta_1) \end{aligned} \quad (3)$$

where A denotes the gain of the multiplier, B_0 and B_1 denote the summed up amplitude of dc (F_0) and fundamental (F_1) component, respectively. The ith frequency component (F_i) can be expressed generally like

$$F_i = B_i \cos(\omega t + \theta_i) \quad (4)$$

where B_i and θ_i denote the amplitude and phase angle, respectively. As has been described in the literature (3), we have the following relations for B_i and θ_i:

$$B_i = \theta_i = B_{N-i} - \theta_{N-i}, \qquad i \neq 0. \quad (5)$$

For $N = 9$, $B_1 = B_8$, $B_2 = B_7$, $B_3 = B_6$, $B_4 = B_5$, and $\theta_1 = -\theta_8$, $\theta_2 = -\theta_7$, $\theta_3 = -\theta_6$, $\theta_4 = -\theta_5$, respectively. Then, the highest frequency in this case, is component F_4.

The multipliers in Fig. 1 can be eliminated when an ac biased CdS photo-sensor array is used, since the outputs of the ac biased CdS photo-sensor array become the form of $Af_i \cos \omega t$ $(i = 0, 1, 2, \cdots, 8)$ as we shall see in Section III.

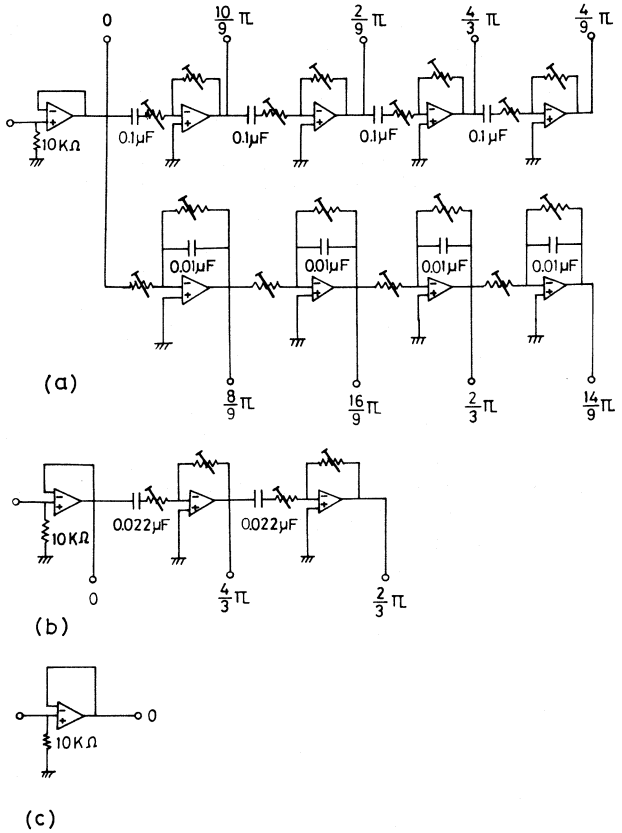

Fig. 3. Circuits for the phase splitters. (a) for ϕ_1, ϕ_2, ϕ_4, ϕ_5, ϕ_7, and ϕ_8. (b) for ϕ_3 and ϕ_6. (c) for ϕ_0.

The PFT in this case becomes simple and can be made of the phase splitters $(\phi_0, \phi_1, \cdots, \phi_8)$ and the sums $(\sum_0, \sum_1, \cdots, \sum_8)$.

B. Phase Splitters and Sums

We need 3 types of phase splitter to obtain the vectors shown in Fig. 2; a) 9-phase for $\phi_1, \phi_2, \phi_4, \phi_5, \phi_7$, and ϕ_8, b) 3-phase for ϕ_3 and ϕ_6, and c) single phase for ϕ_0.

We have many methods of obtaining the phase splitters. One of the most advanced methods is supposed to use a new semiconductor device such as a BBD or a CCD. However, since the BBD and CCD are still in advancing stage and rather expensive, and the number of phases in this case is rather small $(N = 9)$, we can make do with R, C discrete components along with operational amplifiers.

The sinusoidal wave (carrier) frequency can be chosen nearly arbitrarily in this case. The carrier frequency limits the transformation speed. However, since the PFT outputs are parallel and all frequency components are simultaneously obtained as the forms shown in (4), not so high-frequency carrier is necessary, and since (4) can be deterministic after $t = 2\pi/\omega$ $(= 1/f, f$ is carrier frequency), the transformation can be made after 1 ms when f is 1 kHz. The 1-ms transformation time is sufficient for the present purpose. Hence, we choose the carrier frequency 1 kHz.

Fig. 3 shows the circuits of the phase splitters, in which a) shows the 9-phase splitters for $\phi_1, \phi_2, \phi_4, \phi_5, \phi_7$, and ϕ_8, b) for ϕ_3 and ϕ_6, and c) for ϕ_0, which correspond to Fig. 2, respectively.

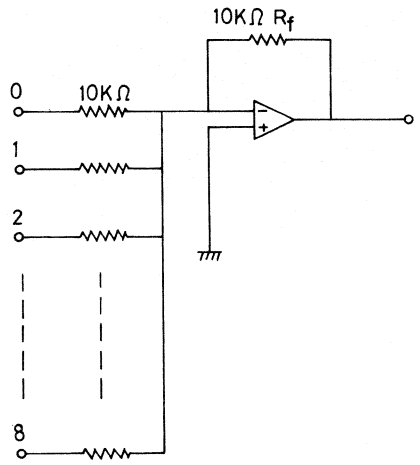

Fig. 4. Circuit of the sum.

TABLE I
RELATIONSHIP BETWEEN THE SPATIAL COMPONENTS AND THE PHASE ANGLES OF SINUSOIDAL WAVES TO BE SUMMED UP

phase splitter / summer	ϕ_0	ϕ_1	ϕ_2	ϕ_3	ϕ_4	ϕ_5	ϕ_6	ϕ_7	ϕ_8	output
$\sum_0$	0	0	0	0	0	0	0	0	0	F_0
$\sum_1$	0	$\frac{2}{9}\pi$	$\frac{4}{9}\pi$	$\frac{2}{3}\pi$	$\frac{8}{9}\pi$	$\frac{10}{9}\pi$	$\frac{4}{3}\pi$	$\frac{14}{9}\pi$	$\frac{16}{9}\pi$	F_1
$\sum_2$	0	$\frac{4}{9}\pi$	$\frac{8}{9}\pi$	$\frac{4}{3}\pi$	$\frac{16}{9}\pi$	$\frac{2}{9}\pi$	$\frac{2}{3}\pi$	$\frac{10}{9}\pi$	$\frac{14}{9}\pi$	F_2
$\sum_3$	0	$\frac{2}{3}\pi$	$\frac{4}{3}\pi$	0	$\frac{2}{3}\pi$	$\frac{4}{3}\pi$	0	$\frac{2}{3}\pi$	$\frac{4}{3}\pi$	F_3
$\sum_4$	0	$\frac{8}{9}\pi$	$\frac{16}{9}\pi$	$\frac{2}{3}\pi$	$\frac{14}{9}\pi$	$\frac{4}{9}\pi$	$\frac{4}{3}\pi$	$\frac{2}{9}\pi$	$\frac{10}{9}\pi$	F_4
$\sum_5$	0	$\frac{10}{9}\pi$	$\frac{2}{9}\pi$	$\frac{4}{3}\pi$	$\frac{4}{9}\pi$	$\frac{14}{9}\pi$	$\frac{2}{3}\pi$	$\frac{16}{9}\pi$	$\frac{8}{9}\pi$	F_5
$\sum_6$	0	$\frac{4}{3}\pi$	$\frac{2}{3}\pi$	0	$\frac{4}{3}\pi$	$\frac{2}{3}\pi$	0	$\frac{4}{3}\pi$	$\frac{2}{3}\pi$	F_6
$\sum_7$	0	$\frac{14}{9}\pi$	$\frac{10}{9}\pi$	$\frac{2}{3}\pi$	$\frac{2}{9}\pi$	$\frac{16}{9}\pi$	$\frac{4}{3}\pi$	$\frac{8}{9}\pi$	$\frac{4}{9}\pi$	F_7
$\sum_8$	0	$\frac{16}{9}\pi$	$\frac{14}{9}\pi$	$\frac{4}{3}\pi$	$\frac{10}{9}\pi$	$\frac{8}{9}\pi$	$\frac{2}{3}\pi$	$\frac{4}{9}\pi$	$\frac{2}{9}\pi$	F_8

The sum is shown in Fig. 4, which is an ordinary circuit. 9 sums are prepared, which are denoted as $\sum_0, \sum_1, \cdots$, and $\sum_8$ in Fig. 1 and Table I.

Each output of the phase splitters is summed to obtain the frequency components ($F_0, F_1, \cdots, F_8$) in such a way shown in Table I. The summation to obtain F_1, for example, is shown in (3).

Fig. 5 shows the actual view of the 9-channel PFT equipment made up by the procedure mentioned above.

C. Performance of the PFT

The analog PFT is inevitably less accurate compared to the DFT using a digital computer. The accuracy of the PFT can be tested by measuring the unwanted components when a flat input (dc) is analyzed. The flat input is realized in this case by applying the equal amplitude sinusoidal wave (1 kHz) to all input terminals.

Fig. 6 shows the experimental results when the flat input is applied. In an ideal operation of the equipment, all outputs except F_0 should be zero. However, as shown in Fig. 6, the unwanted components ($F_1, F_2, \cdots, F_8$) appear. From this result, we can estimate its accuracy as 1 percent in this case.

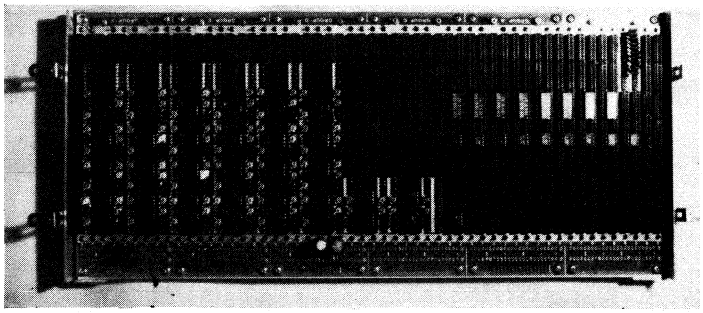

Fig. 5. Photograph of the PFT equipment.

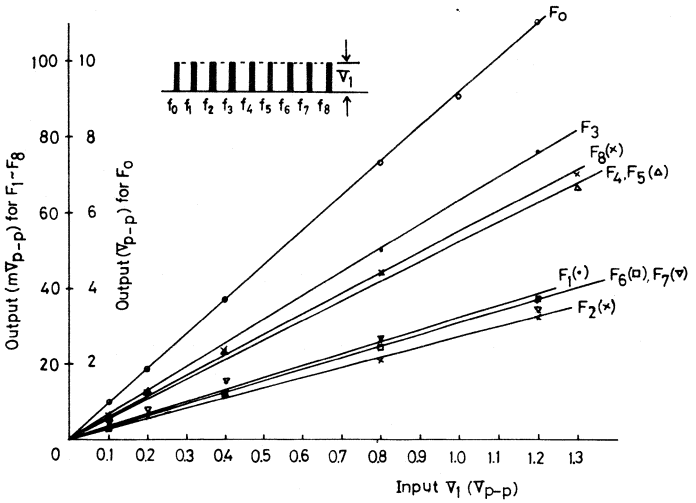

Fig. 6. Experimental result showing the accuracy of the PFT, when flat input (dc) is applied.

Fig. 7 shows the measured results of F_1 when the waveforms (spatial waveforms like those shown also in Fig. 7) were applied to the PFT input, in which each sample value shows the amplitude of 1-kHz sinusoidal wave. As we know from the nature of Fourier transformation, the magnitude of frequency components are independent of the position of V_2 wave. If the PFT equipment is errorless, the spatial frequency component for the corresponding input waveform for the given value of V_2 must be independent of the position of V_2 wave. However, the data shown in Fig. 7 have some deviation, which shows the effect of position of V_2 wave, and it comes from the error of the PFT. From this results, we can estimate the accuracy as 5 percent when $V_2 = 0.2$ V.

The experimental results shown in Fig. 7 can be seen as a simulation of a vehicle size detection, if we make V_1 and V_2 wave correspond to a background illumination level and a vehicle image level, respectively. We can see from Fig. 7 that it may be possible to discriminate the vehicle size by detecting the magnitude of F_1 component, if the vehicle image contrast is high ($V_1 < V_2$ or $V_1 > V_2$).

III. VEHICLE-SIZE DETECTION SYSTEM

A block diagram of the moving vehicle detection system is shown in Fig. 8. An optical lens (camera) views a road along which vehicles run. A CdS array sensor is installed at a focal

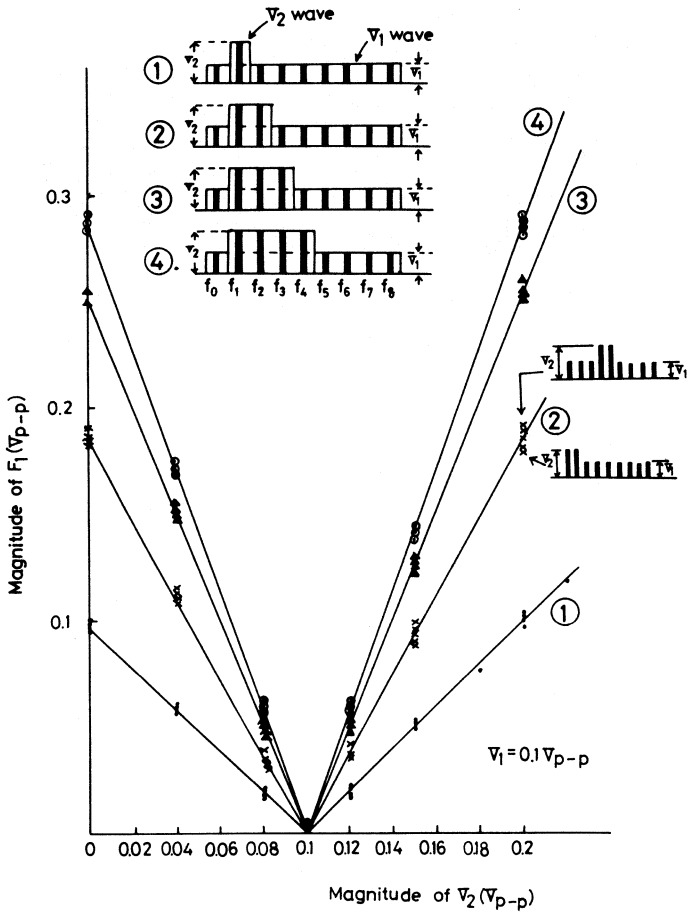

Fig. 7. Experimental result of the fundamental spatial frequency component output when the spatial waveform made of two rectangular waveforms (V_1 wave and V_2 wave) are applied.

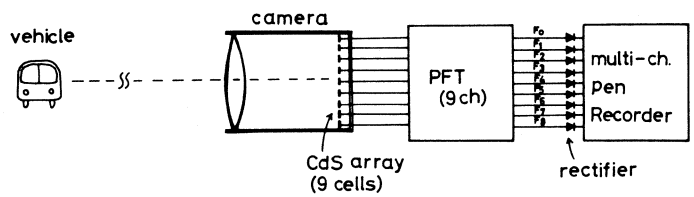

Fig. 8. A block diagram of the moving vehicle detection system.

plane of the lens. The vehicle image can be focused on the CdS array. The electric signals from each CdS cell unit can be obtained in parallel, which are applied to the PFT. The outputs of PFT are recorded on the multichannel pen recorder. Since the outputs of PFT are sinusoidal, rectifiers are necessary between the PFT and the recorder.

The PFT (9 channel) has been described in Section II. In the present detection system, an ac biased CdS array sensor (9 cells) was used as shown in Fig. 9. As a light-illumination intensity increases, the resistance of CdS cell (Rd) decreases, then the output voltage (1 kHz) of each output terminal increases. The relationship between the output voltage and the light intensity was obtained like that shown in Fig. 10. Each semifixed resistor R in Fig. 9 can be adjusted so that each output voltage has the same characteristic like that shown in Fig. 10. The characteristic shown in Fig. 10 means

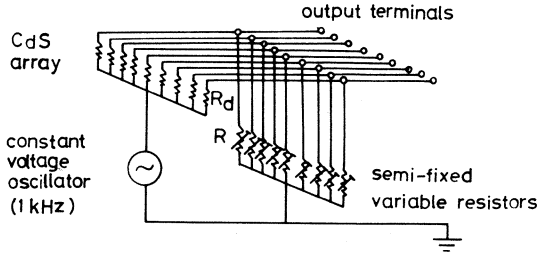

Fig. 9. Circuit of the ac biased CdS array sensor.

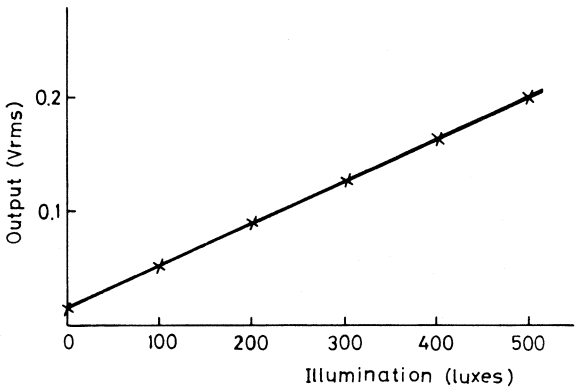

Fig. 10. Relationship between the illumination intensity and the output (rms) of the circuit shown in Fig. 9.

that the amplitude of sinusoidal wave can be modulated by the light intensity. That is to say, the ac biased CdS circuit shown in Fig. 9 can act as the multiplier between the sinusoidal wave and the light intensity. Hence the multipliers in PFT shown in Fig. 1 are not necessary in the PFT used in the vehicle size detection system shown in Fig. 8.

IV. Experimental Result

The vehicle-size detection system was set in the building room. The distance from the camera to the road was about 80 m. The vehicle image size on the CdS array was so adjusted that a city bus image (the largest) covered 4 of 9 CdS cells and a motorcycle image (the smallest) covered 1 cell. The other vehicle images fall between them. The model of these relations has been shown in Fig. 7 as the spatial waveforms in which V_2 waves correspond to the vehicle images.

Fig. 11 shows a part of recorded result, in which the spatial frequency components from dc to fourth harmonics are shown. The fourth harmonic component is the maximum spatial frequency component in this case ($N = 9$) from the relation shown in (5).

The dc component shows the mean value of light intensity on the CdS array, which, of course, changes widely due to an outdoor sunshine illumination. The vehicle image signals appear in the dc component, which can be seen the total light intensity change due to the vehicle images. The vehicle image signal detection from the dc component may be difficult because the drift of dc component is too large compared to the signal level. On the contrary, the other frequency components can drift very little as we see in Fig.

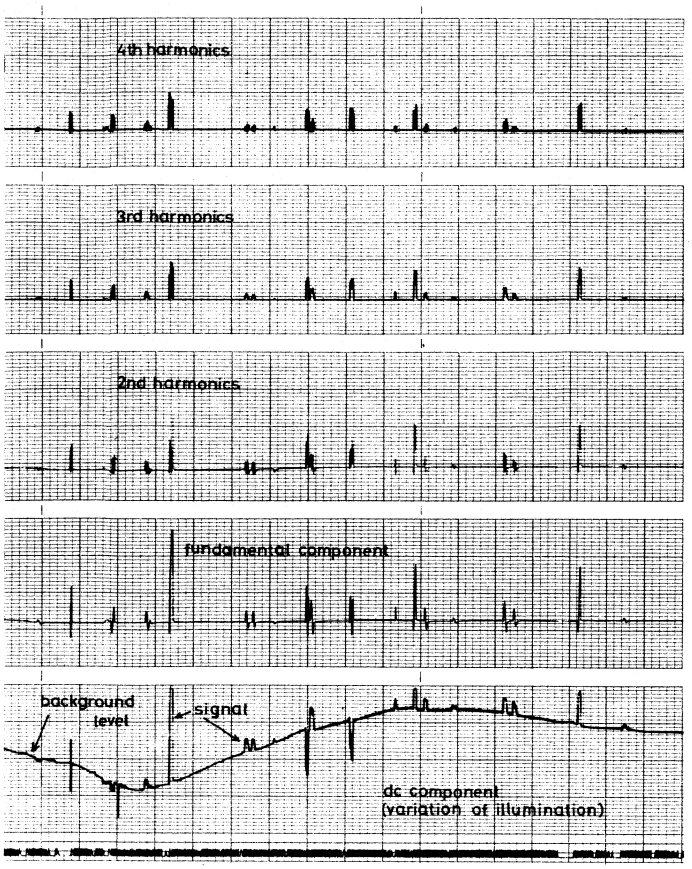

Fig. 11. An example of the recorded result of the spatial frequency components of the vehicles, 250 mV/div.

11. The vehicle signal superposed on the dc component appears either in a plus side or minus side depending on color, shadow or some complex light reflection pattern of a vehicle. However, all the other spatial frequency components can appear in a plus side only. This has been proofed in the experiment for the fundamental component as we can see from Fig. 7; the output appears in a plus side in either case of $V_2 > V_1$ or $V_2 < V_1$.

Since the high spatial components (from second to fourth component) can be considered to show a detail pattern of vehicle image, their magnitude may be almost independent of a vehicle size. The magnitude of fundamental component has depended clearly on the vehicle size as we can see from

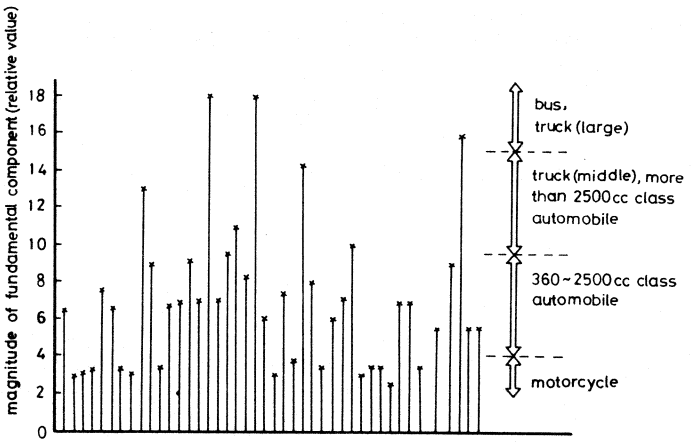

Fig. 12. Relationship between the magnitude of fundamental component and the vehicle size (class of automobile).

Fig. 12. Fig. 12 shows the relation between the magnitude of the fundamental components and vehicles detected by the method mentioned above.

V. Conclusion

A new type of one-dimensional fully PFT equipment was developed and applied to a moving vehicle detection system. The system mentioned in this article has special merits compared to the former method [1]. Firstly, the present system is rather insensitive to the outdoor-light-illumination intensity which can widely change due to a position of the sun and other weather conditions. Secondly, the spatial components can appear always in a plus side in either case where a light intensity from vehicle is above or below a background light intensity.

References

[1] T. Takagi, "Optical sensing and size discrimination of moving vehicles using photocell array and threshold devices," *IEEE Trans. Instrum. Meas.*, vol. IM-25, pp. 52–55, Mar. 1976.
[2] J. W. Cooley and J. W. Tukey, "An algorithm for the machine calculation of complex Fourier series," *Math. Comput.*, vol. 19, pp. 297–301, Apr. 1965.
[3] T. Takagi, "Structural consideration of a new type of one- and two-dimensional discrete Fourier transform system," *IEEE Trans. Systems, Man, Cybern.*, vol. SMC-6, pp. 360–366, May 1976.
[4] L. U. Almi and J. Shamir, "Pattern recognition using one-dimensional Fourier transformation," *Optic Commun.*, vol. 18, no. 3, pp. 304–306, Aug. 1976.

A Fast-Response Logarithmic Electrometer for Pulse-Reactor Experiments

TOSHIYUKI IIDA, KENJI SUMITA, NAOAKI WAKAYAMA, AND HIDESHI YAMAGISHI

Abstract—**The response time of a logarithmic electrometer was improved for pulse reactor experiments requiring long detector cables. A new phase-compensation technique was used in the circuit and it is based on the idea that a current variable resistance inserted between a detector cable and the input terminal of the logarithmic electrometer recovers the phase lag caused by the input capacitance. This stable and fast-response logarithmic electrometer was successfully applied to transient power measurements of the one-shot pulse-reactor "YAYOI."**

I. Introduction

MANY EXPERIMENTS have been carried out for the investigation of reactor safety at the pulse reactors of the "NSRR" [1], [2], the "YAYOI" [3], and others. The logarithmic electrometer, which covers a very wide current range, is useful for those pulse-reactor experiments. Its response time generally has been limited on account of instability caused by the input capacitance of a detector and a cable. It requires a large feedback capacitance to obtain the stability at high current levels. Therefore, its response time is severely degraded at low current levels. For the case when a small feedback capacitance is selected to obtain a fast response, the response of the logarithmic electrometer is often accompanied by overshoot and ringing phenomena at high current levels. Such contradictions between the response time and the stability of a logarithmic electrometer are caused by the marked change of the current-dependent resistance of a logarithmic element. This has made it difficult to design a fast response logarithmic electrometer for pulse reactor experiments.

In order to solve this problem, we proposed a phase-compensation technique which was realized by inserting a resistor between a detector cable and the input terminal of the circuit [4]. This technique made it possible to improve the response time at low current levels. However, at high current levels, the logarithmic electrometer with this technique has poor response time which is determined by the product of the inserted resistor and an input capacitance.

A new phase-compensation technique was developed to overcome this problem and the marked improvement of the response time of the logarithmic electrometer was obtained. At first, the relation between the stability and the response time of a logarithmic electrometer shall be discussed generally and then the new phase-compensation technique and experimental results of a fast-response logarithmic electrometer shall be introduced.

Manuscript received November 8, 1977.

T. Iida and K. Sumita are with the Department of Nuclear Engineering, Faculty of Engineering, Osaka University, Yamada-Kami, Suita, Osaka, Japan.

N. Wakayama and H. Yamagishi are with Japan Atomic Energy Research Institute, Tokai-Mura, Naka-Gun, Ibaraki, Japan.

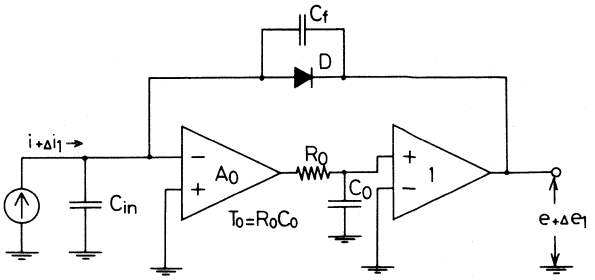

Fig. 1. Equivalent circuit diagram of a conventional logarithmic electrometer.

II. Stability and Response Time

Fig. 1 shows the equivalent circuit diagram of a conventional logarithmic electrometer. Here C_{in} represents the total input capacitance of a detector and a cable. An operational amplifier has smooth 6 dB/octave rolloff providing stable operation at all values of gain. Semiconductor diodes or silicon planar transistors have been recently employed for the logarithmic element D [5], [6]. The relation between a current i_d, flowing through the p-n junction and a voltage v_d across it is given by

$$i_d = i_s \cdot \{\exp(qv_d/nkT) - 1\} \tag{1}$$

where

- i_s the saturation current and is temperature dependent,
- q the electronic charge,
- n a factor which depends on the density of the recombination centers in the junction region,
- k Boltzmann's constant,
- T the absolute temperature, respectively.

When $i_d \gg i_s$, equation (1) is approximated by

$$v_d = \frac{nkT}{q} \ln \frac{i_d}{i_s} \tag{2}$$

which shows good logarithmic characteristics.

Fig. 2 shows the measured $i_d - v_d$ characteristics of a diode-connected model 2N3058, which was used for a newly designed logarithmic electrometer. The result gives the following values:

$$n = 1.0 \qquad i_s = 6.0 \times 10^{-14} \text{ A } (T = 300 \text{ K}).$$

0018-9456/78/0900-0220$00.75

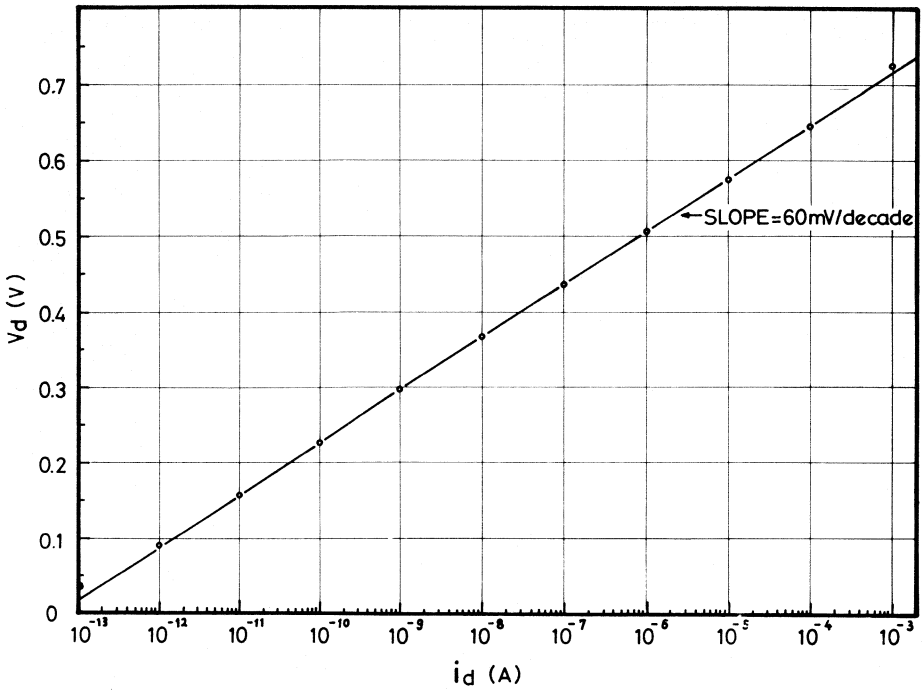

Fig. 2. Logarithmic characteristics of a diode-connected 2N 3058 for $T = 300$ K.

The transient response of a logarithmic electrometer can generally be expressed by a nonlinear differential equation with respect to time [7]. It is troublesome to solve the differential equation, so that it is difficult to obtain the simplified relation between the response time and the stability of a logarithmic electrometer. For the present purpose, a small signal-response analysis was adapted and this makes it easier to evaluate the relation between the response time and the stability of a logarithmic electrometer. It is evident from experimental results which shall be shown in Section 4 that this analysis is applicable to our purpose.

The transfer function of the logarithmic electrometer circuit shown in Fig. 1 can be described as follows:

$$G_1(S) = \frac{\Delta E_1(s)}{\Delta I_1(s)} = \frac{-r_D}{1 + (r_D C_{in}/A_0 + r_D C_f + \tau_0)s + r_D(C_{in} + C_f)\tau_0 s^2} \quad (3)$$

where

$$\tau_0 = \frac{T_0}{A_0} = \frac{1}{2\pi f_0} \quad (4)$$

$$r_D = \frac{nkT}{q} \cdot \frac{1}{i} \quad (5)$$

and

- A_0 the open-loop gain of the operational amplifier,
- T_0 open-loop time constant of the operational amplifier,
- f_0 the unity-gain crossover frequency of the operational amplifier,
- r_D the linear resistance of the logarithmic element for the small signal and it increases proportionately with decreasing bias current,
- C_f a feedback capacitance and
- s the Laplace transform variable, respectively.

Then, the stability condition of this circuit, in other words, the condition that the poles of (3) are all negative and can be expressed by

$$C_f \geq \frac{\tau_0}{r_D} - \frac{C_{in}}{A_0} + 2\sqrt{\frac{\tau_0 C_{in}}{r_D}} = C_{f_0}. \quad (6)$$

For $C_f < C_{f_0}$ the logarithmic electrometer is underdamped and a pulsed input, having high-frequency components, must cause overshoot and ringing phenomena. Such underdamped condition should be avoided in measurements of transient phenomena. The critical damping condition is realized when C_f is equal to C_{f_0}. This relation gives the fastest response of the logarithmic electrometer within the stable condition. If we substitute the relation $C_f = C_{f_0}$ into (3), the time constant T_1 at critical damping becomes

$$T_1 = \tau_0 + \sqrt{\tau_0 r_D C_{in}} \fallingdotseq \sqrt{\tau_0 r_D C_{in}} \quad (7)$$

which shows the limit of the obtainable response time of the logarithmic electrometer is determined not by C_f but τ_0, r_D and C_{in}. For $C_f > C_{f_0}$ the logarithmic electrometer is overdamped, not to mention of stable. A logarithmic electrometer should be overdamped for pulse-reactor experiments.

As shown by (5), the resistance r_D of the logarithmic element varies according to a bias current flowing through it. Consequently the damping coefficient of the logarithmic electrometer depends on the level of an input current. Hence, it is necessary in the design of a logarithmic electrometer to

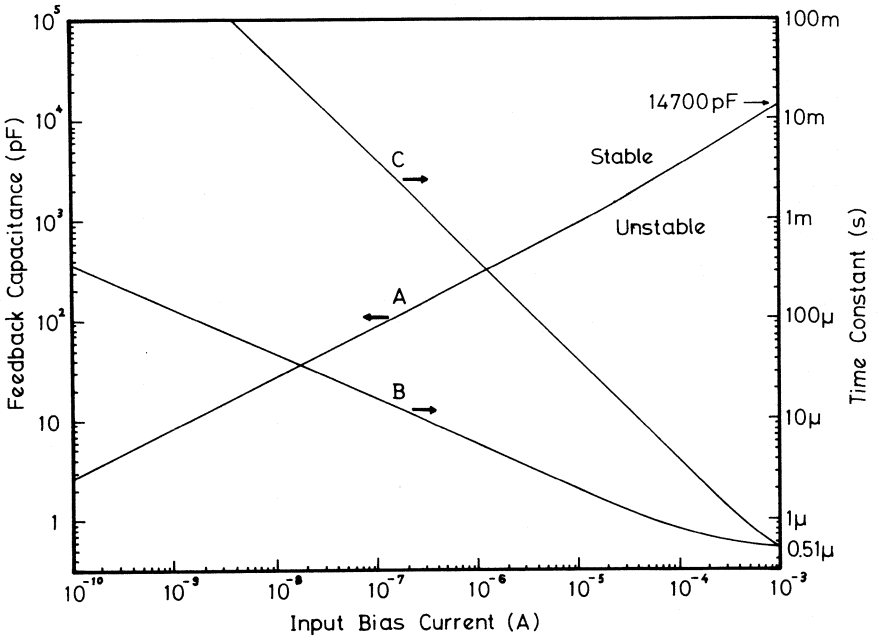

Fig. 3. The critical damping condition of the logarithmic electrometer shown in Fig. 1. Curve *A* shows the feedback capacitance for critical damping, curve *B* the time constant at critical damping and curve *C* the time constant of a conventional logarithmic electrometer. $f_0 = 1$ MHz; $A_0 = 100$ dB; $C_{in} = 3000$ pF; $nkT/q = 26$ mV.

ensure the stability all over the measuring current range.

The critical damping condition of the logarithmic electrometer shown in Fig. 1 was calculated varying an input bias current. Here input capacitance C_{in} was estimated at 3000 pF, which is nearly equivalent to the total capacitance of a detector and a cable of about 40 m. A MOSFET operational amplifier which is easily available also has the following features: $A_0 = 100$ dB, $f_0 = 1$ MHz. The feedback capacitance and the time constant at critical damping were calculated from (5), (6), and (7) using the above values. The results are shown in Fig. 3. In the design of a linear electrometer, it is possible to select an adequate feedback capacitance for each current range, but in the case of the logarithmic electrometer such a selection is impossible. When measurements of the maximum current of 10^{-3} A are assigned to the logarithmic electrometer shown in Fig. 1, it needs a feedback capacitance of 14 700 pF ($= C_{f_1}$) for the stability, which is shown in Fig. 3 (curve *A*). The response time of the logarithmic electrometer with that feedback capacitance C_{f_1} is nearly determined by the product of r_D and C_{f_1}, so that it is inversely proportional to the input bias current. This is shown in Fig. 3 (curve *C*). Consequently that logarithmic electrometer comes to suffer from the severe degradation of the response time at low current levels. For example, the response time becomes about 3.8 s at 10^{-10}-A level ($= 0.026\ \text{V} \div 10^{-10}\ \text{A} \times 14\,700$ pF). Thus the conventional logarithmic electrometer such as shown in Fig. 1 cannot be applicable to the wide range instrumentation of pulse reactors of which power widely change with very short reactor period. It is important in design of the logarithmic electrometer for pulse-reactor experiments to improve the response time especially at low current levels without any instability.

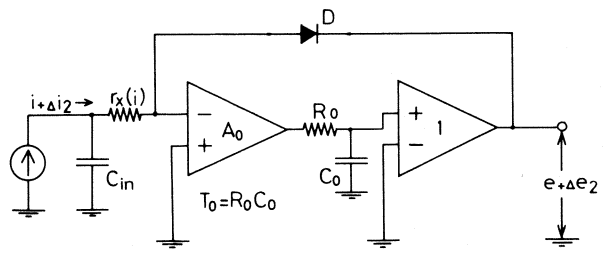

Fig. 4. Equivalent circuit diagram of a logarithmic electrometer with a new phase compensation technique.

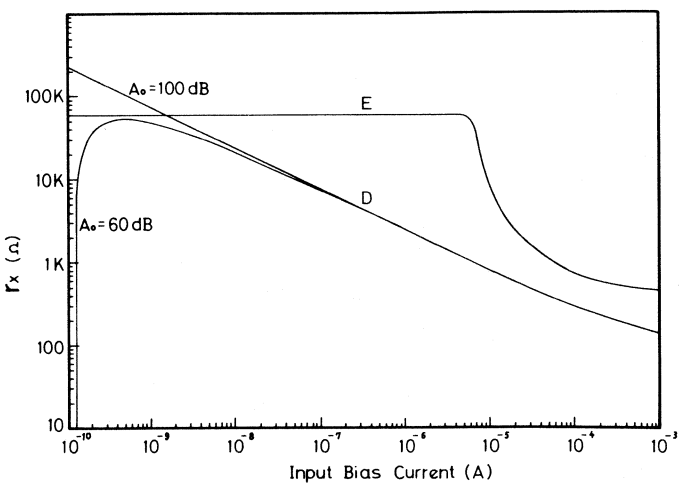

Fig. 5. The critical damping condition of the logarithmic electrometer shown in Fig. 4. Curves *D* show the inserted resistance for critical damping and curve *E* that of the logarithmic electrometer shown in Fig. 6.

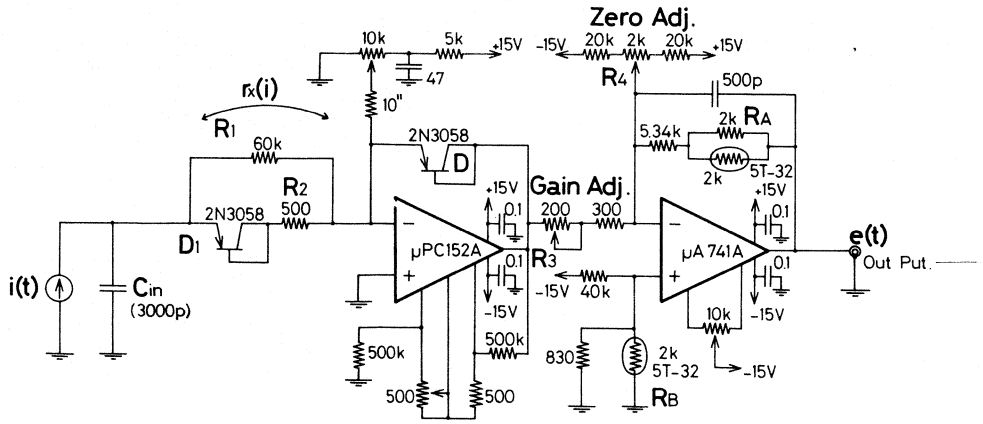

Fig. 6. A newly designed logarithmic electrometer circuit.

III. Improvement of the Response Time

If the feedback capacitance of a logarithmic electrometer can be regulated along the curve A in Fig. 3, the response time will be markedly improved without any instability. Such improvement is shown as the change from curves C to B in the same Fig. 3. The curve B shows the time constant of the logarithmic electrometer at critical damping. Such conception, using a variable impedance element for the phase compensation should be valuable in the improvement of the response time of a logarithmic electrometer. It is difficult to obtain a suitable feedback capacitor corresponding to the voltage across the logarithmic element. Thereupon, a new phase compensation technique was developed in place of the conventional method, which was using the feedback capacitance in parallel with the logarithmic element. The equivalent circuit of a logarithmic electrometer with the new technique is shown in Fig. 4. This technique is based on that a resistance r_x inserted between a detector cable and the input terminal of the logarithmic electrometer recovers the phase lag caused by the input capacitance [4], [8]. Moreover such inserted variable resistance r_x can be regulated according to the level of input current and is easily available to adapt this phase compensation technique.

The transfer function of the logarithmic electrometer circuit shown in Fig. 4 is expressed by

$$G_2(s) = \frac{\Delta E_2(s)}{\Delta I_2(s)} = \frac{-r_D}{1 + (r_D C_{in}/A_0 + r_x C_{in} + \tau_0)s + \tau_0(r_D + r_x)C_{in}s^2}. \quad (8)$$

The stability condition of this circuit can be given by

$$r_x \geq \frac{\tau_0}{C_{in}} - \frac{r_D}{A_0} + 2\sqrt{\frac{\tau_0 r_D}{C_{in}}} = r_0. \quad (9)$$

For $r_x > r_0$ the logarithmic electrometer is overdamped and for $r_x < r_0$ it is underdamped. Substituting the relation $r_x = r_0$ into (8), we obtain the time constant T_2 at critical damping as follows:

$$T_2 = \tau_0 + \sqrt{\tau_0 r_D C_{in}} \fallingdotseq \sqrt{\tau_0 r_D C_{in}} \quad (10)$$

which is the same as (7). It is evident from this that the new phase-compensation technique is effective in obtaining stable response as well as the conventional method.

The values of r_x depending on input bias current to obtain the critical damping condition of the logarithmic electrometer with this technique is shown in Fig. 5 (curves D). If the inserted resistance r_x can be regulated along the curves D in Fig. 5, the response time of the logarithmic electrometer will be ideally improved. Although it is impossible to obtain such an ideal resistor, a current variable resistor suitable for this technique can be easily obtained by the use of some resistors and a semiconductor diode, and hence the response time of the logarithmic electrometer with this technique can be markedly improved.

IV. A Practical Circuit and Experimental Results

A newly designed logarithmic electrometer circuit is shown in Fig. 6. A model μpc 152 A MOSFET operational amplifier with a unity-gain crossover frequency of 1 MHz and a bias current of 10^{-13} A is used for the input stage (Amp. 1). The open-loop gain of the operational amplifier is fixed at 60 dB by a source-feedback technique [9]. This is effective to suppress the maximum value of the inserted resistance as shown in Fig. 5 (curves D). But it will cause a steady-state off set positional error to fix the gain too low. A model 2N 3058, having a saturation current of 6×10^{-14} A, is used for the logarithmic element. The inserted current variable resistor is composed of a current variable element D_1 and two resistors R_1, R_2. The same diode mode 2N 3058 is used for D_1. The calculated resistance of the inserted resistor for small signal is shown in Fig. 5 (curve E). A logarithmic output is amplified by next amplifier (Amp. 2) built up with a model μA 741A operational amplifier. The gain of 16.7 magnifications (= 1 V ÷ 60 mV) was adjusted by a variable resistor R_3 and hence the gain per decade for this logarithmic electrometer was chosen as 1 V/decade of input current. In order to fix an output voltage to 0 V at an

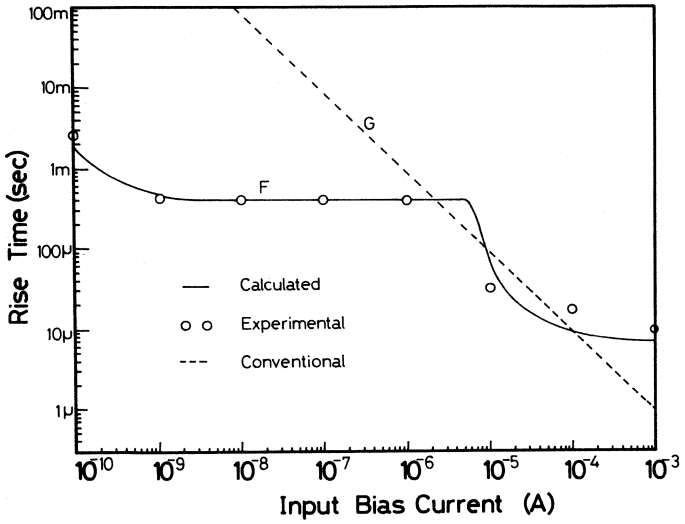

Fig. 7. Risetimes of the logarithmic electrometer shown in Fig. 6 and the conventional one.

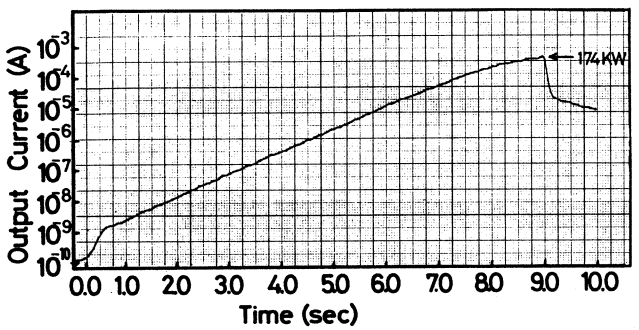

Fig. 8. An example of the observed power shapes of the "YAYOI" in the pulse operation below prompt critical state.

input current of 10^{-10} A, a bias voltage of 220 mV was applied to the Amp. 2. The zero adjustment was made by a variable resistor R_4. The temperature influence for the logarithmic element is also compensated by two thermistors R_A, R_B used in this amplifier stage. The fundamental principles are shown in [10].

The input current signal for testing was prepared from a bias current i_b and a square pulse current with an amplitude of about $0.05i_b$. As expected from the stability condition shown in Fig. 5, the observed output waveforms were accompanied by no overshoot and ringing phenomena in whole current range from 10^{-10} to 10^{-3} A. The measured results of the risetime of this logarithmic electrometer are shown in Fig. 7. The measured data agree nearly with curve F calculated from (8) using the curve E in Fig. 5. A curve G in Fig. 7 shows the risetime of the conventional logarithmic electrometer. It is evident from these results that at low current levels the response time of the logarithmic electrometer with this new phase compensation technique has been improved two decades compared with the conventional one.

Power shapes of the one-shot pulse-reactor "YAYOI" were measured by the use of this logarithmic electrometer, an ionization chamber Westinghouse type 6377 and a transient memory Iwatsu type DM 701. Figs. 8 and 9 show

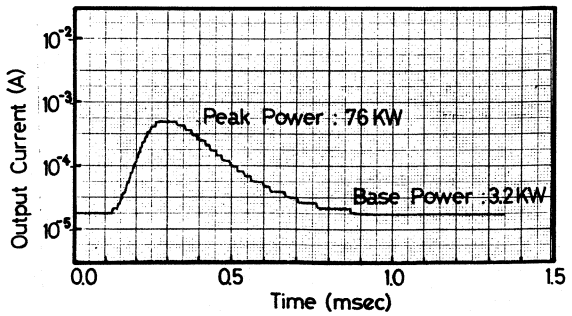

Fig. 9. An example of the observed power shapes of the "YAYOI" in the pulse operation above prompt critical state.

examples of the observed power shapes of the "YAYOI" in the pulse operation below and above prompt critical state, respectively.

V. Conclusion

It has been difficult to obtain a stable and fast response logarithmic electrometer with large input capacitance of a detector and a cable. At high current levels the stability of the logarithmic electrometer requires a large feedback capacitance, by which its response time is severely degraded at low current levels. This is due to the marked change of the current dependent resistance of the logarithmic element. In order to cope with this problem, a new phase-compensation technique was developed and a stable and fast response logarithmic electrometer was made. For example, the response time of this logarithmic electrometer with input capacitance of 3000 pF was improved about two decade compared with the conventional one at low current levels. This logarithmic electrometer circuit is based on clear transient analysis and requires no skilful adjustment. A feasibility test of this logarithmic electrometer system was also carried out by the one-shot pulse-reactor "YAYOI" and satisfactory results were obtained in transient measurements of the reactor.

Acknowledgment

Acknowledgment is due to Dr. Hiroaki Wakabayashi (the University of Tokyo) for his helpful suggestion in carrying out the logarithmic electrometer performance tests at the "YAYOI." We also wish to thank the University of Tokyo for permitting us to refer to the observed results.

References

[1] N. Wakayama, H. Yamagishi, T. Iida, N. Ohnishi, and S. Ohtomo, JAERI-M-6710, pp. 115–118, 1976.
[2] S. Saito, T. Inabe, T. Fujishiro, N. Ohnishi, and T. Hoshi, *J. Nucl. Sci. Technol.*, vol. 14, no. 3, p. 226, 1977.
[3] H. Wakabayashi, A. Furuhashi, S. An, and T. Tamura, in *Proc. U.S./Japan Seminar on Fast Reactors*, paper I-2, 1976.
[4] N. Wakayama, T. Iida, and K. Sumita, in *Preprint 1974 Fall Meeting Atomic Energy Soc. Japan* (in Japanese), paper C21, 1974.
[5] M. Y. El-Ibiary, *IEEE Trans. Nucl. Sci.*, vol. NS-10, pp. 21–31, 1963.
[6] W. L. Patterson, *Rev. Sci. Instrum.*, vol. 34, pp. 1311–1316, 1963.
[7] L. S. Horn and B. I. Khasanov, *Nucl. Instrum. Meth.*, vol. 40, pp. 267–271, 1966.
[8] K. Sumita, T. Iida, and N. Wakayama, in *Proc. U.S./Japan Seminar on Fast Pulse Reactors*, paper III-1, 1976.
[9] *NEC Electron Device Data Book* '72, p. 818, 1972.
[10] T. Furukawa and N. Wakayama, *Nuclear Electronics IAEA*, pp. 141–155, 1965.

Link Compensation in the Kelvin Bridge

GREGORY J. JOHNSON, SENIOR MEMBER, IEEE

Abstract—**Compensation for the effects of large link resistance in bridge measurement of four-terminal resistors usually requires high precision in the adjustment of the compensating ratio arms. This paper describes an alternative method which requires no change in the normal balance procedures and is inexpensive to implement using readily available operational amplifiers. A description of a particular measurement at the part-per-million level of a 10-Ω resistor with a link of 200 Ω is given. Practical circuit details are included.**

Introduction

BRIDGE MEASUREMENT of four-terminal resistors raises problems, not only because current flows in the potential leads but also because of the resistance of the link joining the potential point of the unknown to that of the standard. The difficulty of current flow in the potential leads may be surmounted by an auxiliary bridge balance whilst the technique, devised by Kelvin, of using an additional set of ratio arms across the link is usually sufficient to compensate for the link resistance. However, for a given permissible error, the precision with which this compensating ratio must be adjusted increases as the link resistance increases.

Rameley [1] has shown how to avoid the effects of large link resistance by inserting an adjustable voltage source in series in the link so that both ends of the link are brought to the same potential. This paper examines the Kelvin bridge balance procedures and describes some alternative methods of compensating for the link resistance. These were devised to facilitate the calibration of a precision potentiometer where the link resistance reached some 200 Ω; the methods are nevertheless not restricted to this application.

Balance Procedure for a Kelvin Bridge

The bridge of Fig. 1 is balanced [2] when

$$X = \frac{A + r_1}{B + r_4} S + \frac{(Q + r_3)L}{(P + Q + r_2 + r_3 + L)} \left[\frac{A + r_1}{B + r_4} - \frac{P + r_2}{Q + r_3}\right]. \quad (1)$$

In practice the resistors r_1, r_2, r_3, r_4, although adjustable, are not accurately known since they include leads and contact resistances. The uncertainty contributed by r_1 and r_4 may be eliminated by balancing a new bridge formed when SW1 of Fig. 1 is closed. Then

$$X = \frac{r_1}{r_4} S + \frac{(Q + r_3)L}{(P + Q + r_2 + r_3 + L)} \left[\frac{r_1}{r_4} - \frac{P + r_2}{Q + r_3}\right]. \quad (2)$$

Manuscript received February 3, 1978.

The author is with the Sydney County Council Measurements Laboratory, University of New South Wales, Kensington, Australia.

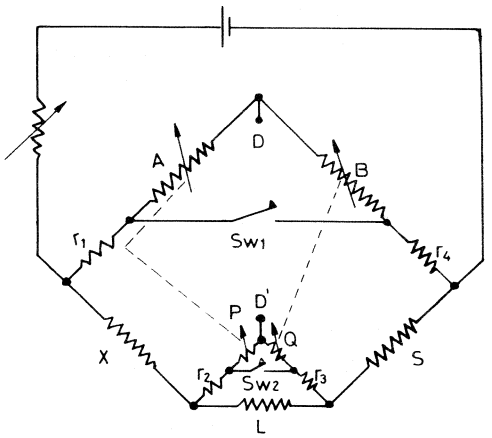

Fig. 1. Kelvin bridge showing switches SW1, SW2 used in eliminating leads and link effects.

If the balances (1) and (2) are simultaneously satisfied

$$\frac{A}{B} = \frac{r_1}{r_4} \quad (3)$$

so that

$$X = \frac{A}{B} S + \frac{(Q + r_3)L}{(P + Q + r_2 + r_3 + L)} \left[\frac{A}{B} - \frac{P + r_2}{Q + r_3}\right]. \quad (4)$$

The second term is usually small and vanishes for zero link resistance; it may be made negligible if $A/B \doteq (P + r_2)/(Q + r_3)$. This last condition may be established by balancing a third bridge formed by opening the link L and, with SW1 open, adjusting r_2 (or r_3) so that

$$X = \frac{A}{B} S + (Q + r_3) \left[\frac{A}{B} - \frac{P + r_2}{Q + r_3}\right]. \quad (5)$$

Equations (4) and (5) together establish that

$$\frac{A}{B} = \frac{P + r_2}{Q + r_3} \quad (6)$$

so that

$$X = \frac{A}{B} S. \quad (7)$$

It is not always convenient to open the link and some commercial bridges [3] use a different method of adjusting the compensating ratio. If SW2 in Fig. 1 is closed and (with SW1 open) r_2 is adjusted for a balance then the link resistance introduces no error provided $A/B = P/Q$. When A/B is not exactly equal to P/Q it may be shown that this sequence of balances leads to

$$X \doteq kS \left[1 - \frac{\alpha ML}{S}\right] \quad (8)$$

0018-9456/78/0900-0225$00.75

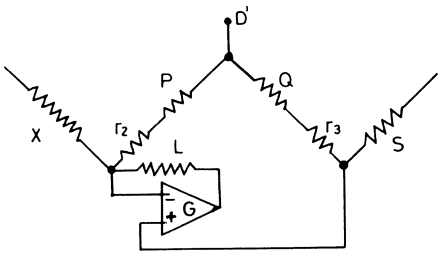

Fig. 2. Use of a high-gain amplifier to reduce the effects of link resistance.

where

$$M = [Q + r_3 + L/(k+1)]/[P + Q + r_2 + r_3 + L]$$

and

$$P/Q = (A/B)(1+\alpha) = k(1+\alpha). \tag{9}$$

P and Q are constants of the bridge and since they do not involve uncertain lead resistances may normally be preadjusted so that α is small. When L is also small the contribution of the error term in (8) will then be negligible.

Precision Required in Link Balance

If the balances leading to (1) and (2) are made exactly, equation (4) shows that the link will contribute a fractional error

$$\theta = \frac{L[Q + r_3 - (P + r_2)/k]}{S(P + Q + r_2 + r_3 + L)} \tag{10}$$

where $k = A/B$. For a particular precision in establishing the balance for (5), θ increases directly with L. In a specific case with $A = B = P = Q = 1000\ \Omega$, $X \doteq S = 10\ \Omega$, $L = 200\ \Omega$ and r_2, r_3 each about 0.1 Ω. r_2 must be adjusted with a discrimination of 110 $\mu\Omega$ for $\theta = 10^{-6}$. Since it is not necessary to know the value of $P + r_2$ accurately, it can be more convenient to use a shunt box across either P or Q or both. If the alternative technique leading to (8) is followed then the same precision in adjustment of r_2 is needed and α must also be less than 10^{-5} for the same error θ.

Automatic Link Compensation

The effects of high link resistance may be greatly reduced by connecting a high-gain amplifier as in Fig. 2.

This may be viewed as effecting automatically Rameley's insertion of an opposing voltage source in series with the link or alternatively, as a substitution of the input resistance of the feedback amplifier for the link resistance L. Since most of the current flowing in X flows through L and into the amplifier output, the amplifier must be capable of supplying (or sinking) this current.

Although Fig. 2 shows the amplifier input connected to the potential terminals on X and S it is not possible to make these connections exactly. Normally the current terminal of S will be accessible but the connection to X must be made either along the link as in Fig. 3(a) or alternatively along the potential lead to the P arm as in Fig. 3(b). In the former case the effective link resistance becomes $r_5 + r_6 + L/(G+1)$. The latter case requires somewhat more analysis for an exact solution though the final result does not differ significantly; to a sufficiently good approximation the effective link resistance is $r_6 + L/(G+1)$.

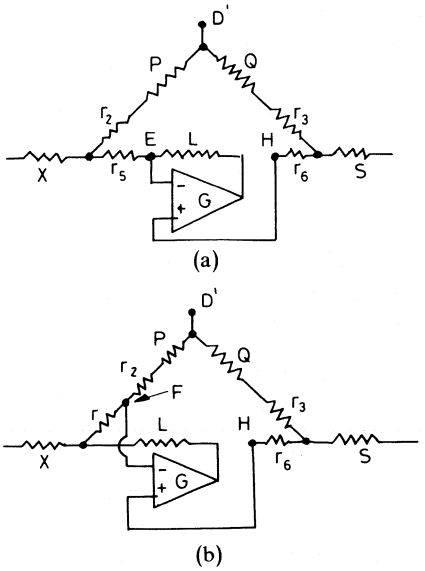

Fig. 3. Detail of the amplifier connection of Fig. 2. Connection to X is made as near as possible to the potential terminal. (a) Along the link. (b) Along the P arm.

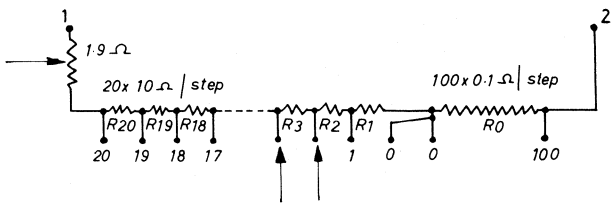

Fig. 4. Basic circuit of the two top dials of the potentiometer to be calibrated. The 1.9-Ω resistor is part of the standardizing circuit.

Offset Voltages and Currents in the Amplifier

The amplifier of Figs. 2 and 3 will introduce spurious voltages in the bridge network. These spurious voltages do not differ from the usually present thermal EMF and the same techniques for the elimination of their effects are suitable. The bridge network attenuates any detector voltage due to the amplifier offsets but it is nevertheless desirable to adjust any trim controls on the amplifier for a minimum detector voltage due to this source alone.

An Illustration

The methods described here were used to calibrate a precision potentiometer. The essentials of the two top dials are shown in Fig. 4; potential terminal-pairs appropriate to each resistor in the string are available from a double wiper which is part of the usual adjustment dial.

If the terminals 1, 2 are used as the current connections with 2 connected to S then the link resistance will vary from a few milliohms when R_0 is being measured to about 200 Ω when R_{20} is the unknown. It is of course, possible to interchange terminals 1 and 2 for half of the resistors in the series string thus reducing the maximum link resistance to

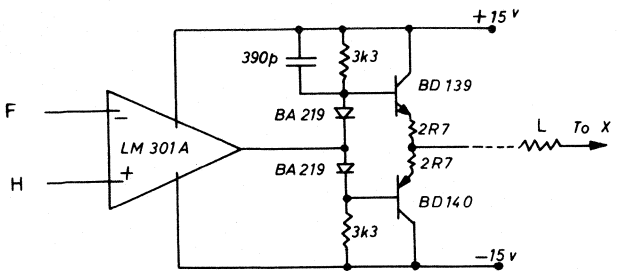

Fig. 5. Circuit of the amplifier used for link compensation. The letters *F*, *H* refer to Fig. 3(b).

about 100 Ω; with the active link compensation it is not necessary.

The amplifier of Figs. 2 and 3 was made using an LM301A to which a simple class *B* power stage was added to increase the permissible operating currents; the circuit is shown in Fig. 5. The measured gain *G* of the amplifier was 160 000 so that the $L/(G+1)$ term in the effective link resistance was negligible even for a link of 200 Ω. With a current in the unknown of 20 mA and a supply voltage of ±15 V to the amplifier of Fig. 5 a maximum link resistance of about 700 Ω is permissible. Once the active network is connected bridge balance procedure is unchanged from that required in a bridge using conventional compensation arms except that the precision needed in adjustment of these arms is that corresponding to a small link resistance.

The twenty resistors of Fig. 4 were measured against a 10 Ω standard with a discrimination of 1 ppm. The time required for a complete run was less than 1 h and the reproducibility was within 1 ppm.

Conclusion

The problems of using the Kelvin bridge with large link resistance have been considered. A method of compensating for the effects of this large link resistance using an operational amplifier has been described and its practical implementation demonstrated.

References

[1] D. Rameley, "A method of controlling the effect of resistance in the link circuit of the Thomson or Kelvin double bridge," *J. Res. Nat. Bur. Stand.*, vol. 64C, pp. 267–270, Oct.-Dec. 1960; also in "Precision measurement calibration, electricity-low frequency," *Spec. Publ. 300*, vol. 3, U.S. Dep. Commerce, NBS, Dec. 1968.

[2] F. K. Harris, *Electrical Measurements*. New York: Wiley, 1952, pp. 282–287.

[3] J. L. Williams, Melbourne, Australia, Kelvin Bridge Type KBLC6.

Manometer for Measurement of Differential Pressure of the Order of 2 Millibars

JURAJ POLIAK

Abstract—**Examining the functioning of sensors for measuring pressure shows that most of them make use of a displacement. The linearity and the sensitivity of this type of sensor are closely dependent on the value of this displacement. For the sake of linearity and repeatability of large signals, the displacement has to be small. Consequently the output signals obtained are weak.**

Introduction

A SCHEMATIC diagram of the proposed solution is depicted in Fig. 1. It has a "pressure-displacement" transducer of a classic type with a metal diaphragm, but the conversion "displacement-electric signal" is performed by means of interference and a photosensitive device. The principle of operation can be described as follows.

Manuscript received February 17, 1978.

The author is with the Ecole Polytechnique Fédérale Lausanne, Chaire d'Electrométrie, 16 Chemin de Bellerive, CH-1007 Lausanne, Switzerland.

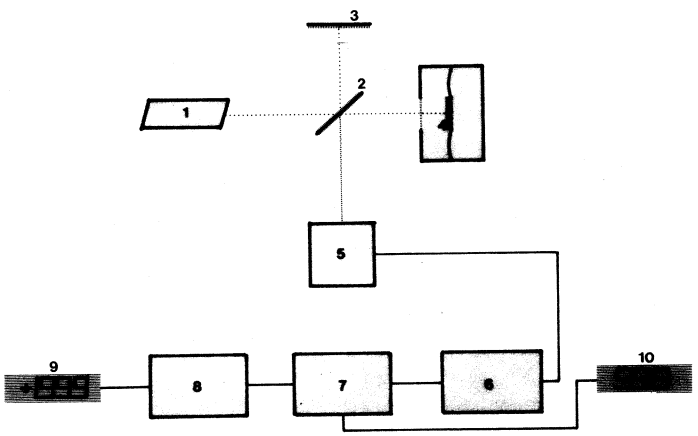

Fig. 1. 1. Monochromatic source. 2. Beam splitter. 3. Fixed mirror. 4. Diaphragm with mirror. 5. Detector. 6. Up/down counter. 7. Multiplication constant introduction. 8. Multiplier. 9. Display of the differential pressure. 10. Display of the number of interferences.

0018-9456/78/0900-0227$00.75 © 1978 IEEE

Fig. 2. Diaphragm with mirror.

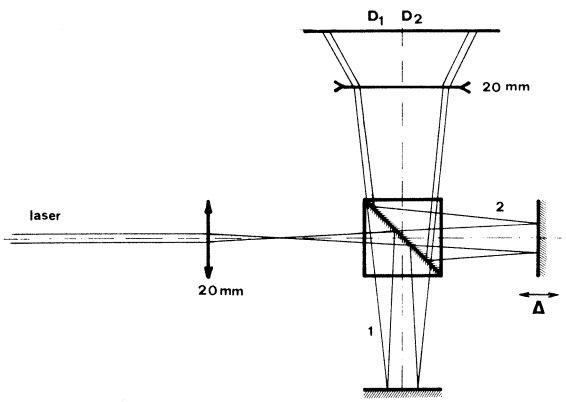

Fig. 3. Optical system.

Principle of Operation

A monochromatic light beam of known wavelength is divided by a beam splitter (Fig. 1), semitransparent mirror, into two parts—one being reflected and the remainder transmitted. The reflected beam is again reflected at mirror (3), so that it travels back towards the detector (5). Similarly, the transmitted beam is reflected from a mirror (4) on the diaphragm (Fig. 2). Both beams will recombine at the detector level, producing interference fringes. The displacement of the fringes is a function of the movement of the diaphragm, therefore of the pressure.

In order to obtain interferences, the difference in the two beam-lengths has to be smaller than the length l of coherence. This coherence length is defined as the ratio of the speed of light c to the spectral width of the source

$$l = \frac{c}{\Delta\nu} = \frac{\lambda^2}{\Delta\lambda}.$$

If the light source is a helium–neon laser, the variation in the beam length due to the movement of the diaphragm is much smaller than the length of coherence, which is some tenth of a centimeter. The interference patterns at the level of the detectors are defined by the optical system shown in Fig. 3.

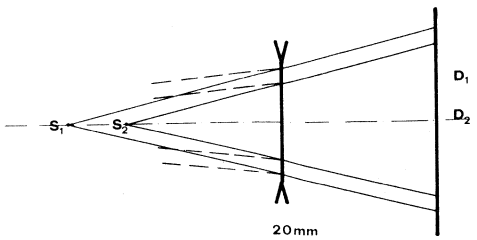

Fig. 4. Light beams as seen by the detectors.

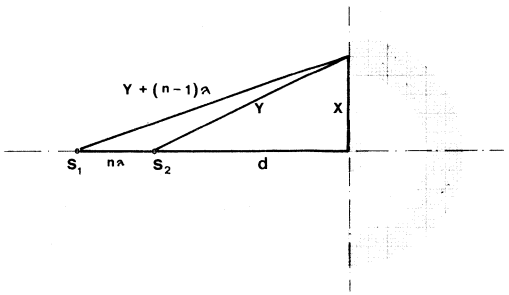

Fig. 5. Estimation of the diameter of the first interference fringe if there is a maximum in the middle.

Fig. 4 represents the light beams as seen from the screen.

The surface of constant phase difference of the two coherent point sources S_1 and S_2 are revolution hyperboloids. Their intersections with a plane perpendicular to the line connecting the two foci are concentric circles. In order to place the two photodetectors correctly, it is necessary to estimate the radius of the first circle, which corresponds to a maximum of the light intensity assumed that there is a maximum in the center (Fig. 5). If the distance $S_1 S_2$ is an integral multiple of the wavelength, there is a maximum in the center of the circles. The equations are as follows:

$$Y^2 = X^2 + d^2$$

$$(Y + (n-1)\lambda)^2 = X^2 + (n\lambda + d)^2.$$

From these equations one obtains

$$X = \sqrt{\left(\frac{2nd + \lambda(2n-1)}{2(n-1)}\right)^2 - d^2}.$$

The term in λ can be neglected; and the wavelength is involved only in the determination of the number of interferences n:

$n = \Delta/\lambda$, where Δ is a difference in the beam lengths.

Fig. 6 gives the radius X of the circle as a function of n and Δ. This curve shows that the maximum variation of x occurs when n and Δ are small. To assure a correct functioning at the level of the detectors, it is therefore necessary to provide sufficient offset in the distance between the mirror and the diaphragm, in order to avoid the critical part of the curve.

Two photodetectors are arranged in such a way that their mutual distance is equal to $\frac{1}{4}$ or $\frac{3}{4}$ of the distance between the adjacent maxima of the interference and give two out of phase signals corresponding to the movement of the diaphragm in either direction (see Fig. 7). The direction of the movement of the interferences depends upon the sense of variation in the pressure.

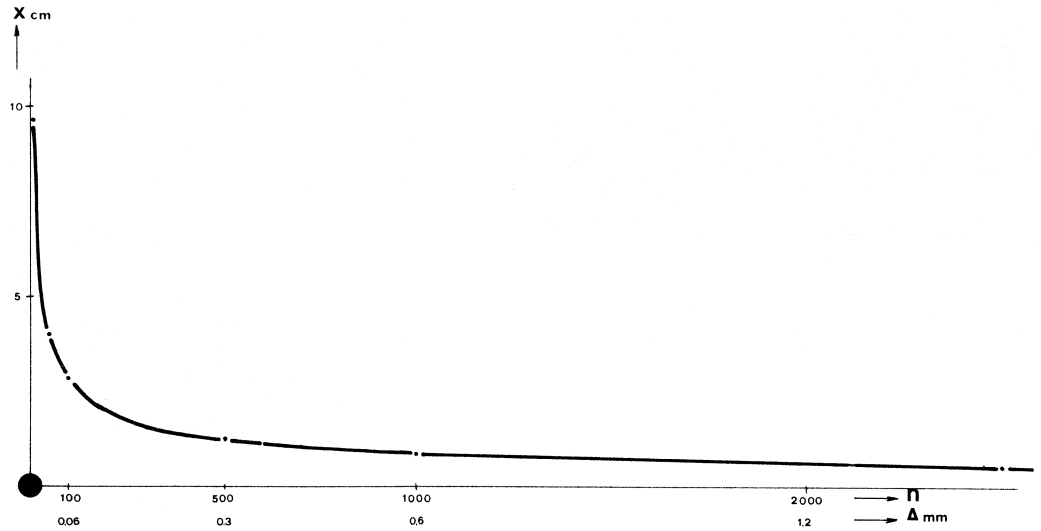

Fig. 6. Diameter of the first circle as a function of n and Δ.

Fig. 7. Arrangement of the two detectors.

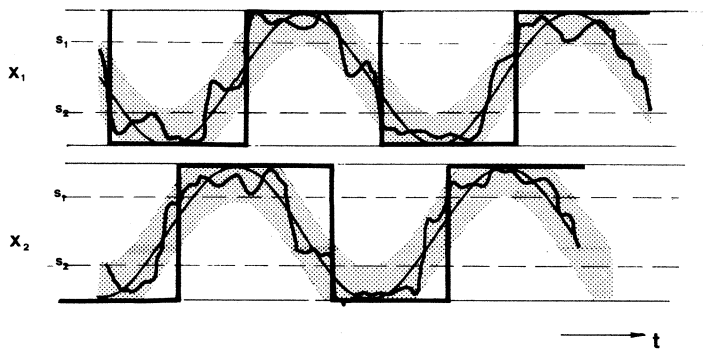

Fig. 8. Random disturbances superimposed upon the two sinusoidal signals.

If the signals from the detectors are applied to the X and Y inputs of an oscilloscope, the resulting curve is an ellipse which rotates clockwise. One of the signals is counted by a reversible counter and gives the number of interference fringes: the other signal is used for the estimation of the counting modes—counting-up or counting-down. Theoretically the two signals form two sine curves which are out of phase. In reality, random disturbances, mainly of mechanical nature, are superimposed on the two sinusoidal signals. After a minor shock or variation in pressure, the diaphragm starts to vibrate on its natural frequency and its harmonics. The disturbances can be classified into three groups depending upon the detectors output amplitude as follows:

1) disturbances with amplitudes smaller than half the maximum of the sine-wave signal;
2) disturbances between half that amplitude and the full amplitude;
3) disturbances higher than the total amplitude of the sine-wave signal.

In the first two cases, one can eliminate their effect by using a detector with hysteresis and properly adjusted threshold levels (Fig. 8).

If the disturbances are too severe, the signal is of no value. Electrical filtering cannot be used, because it would affect the counting of faster or slower pressure variations and this would limit the performance of the system. Excluding a very complicated signal processing, some elimination of the disturbances or noise can be done by proper selection of the diaphragm. Several types of capsules and diaphragms with different possibilities of fittings were tested. The diaphragm was excited by a loudspeaker till a maxima amplitude was obtained. The diaphragm giving maximum amplitude smaller than one half of the amplitude corresponding to the interference fringe was chosen.

From the detectors with hysteresis two logic signals (Fig. 8) pass through the direction discriminator and the up/down counter. The binary coded decimal (BCD) signal, corresponding to the number of the interference fringes per unit of pressure, is collected at the output of the up/down counter. The ratio between the state of the up/down counter and the pressure is defined by the wavelength of the laser and the mechanical parameters of the diaphragm.

The calibration factor of the instrument can be set according to the required display unit chosen in advance by the user.

One could adapt the characteristics of the manometer by changing the diaphragm or the wavelength of the laser; these methods would be complicated and expensive. The problem was solved as follows: The number of interference fringes corresponding to the pressure is multiplied by a constant function of the selected unit of pressure chosen for the display. The multiplication is performed automatically, in this particular case in 2.3 s: the introduction of the constant

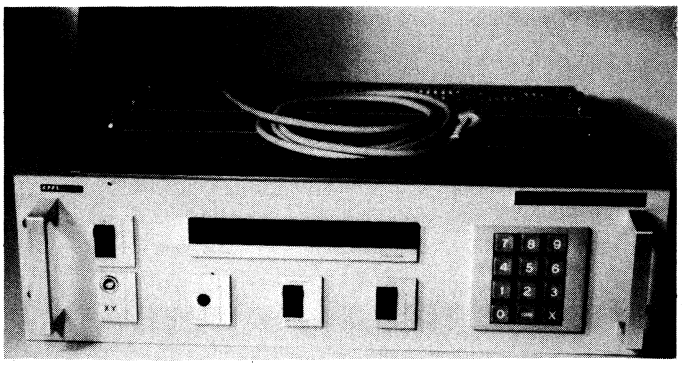

Fig. 9. Manometer mounted in a 19-in box, front view.

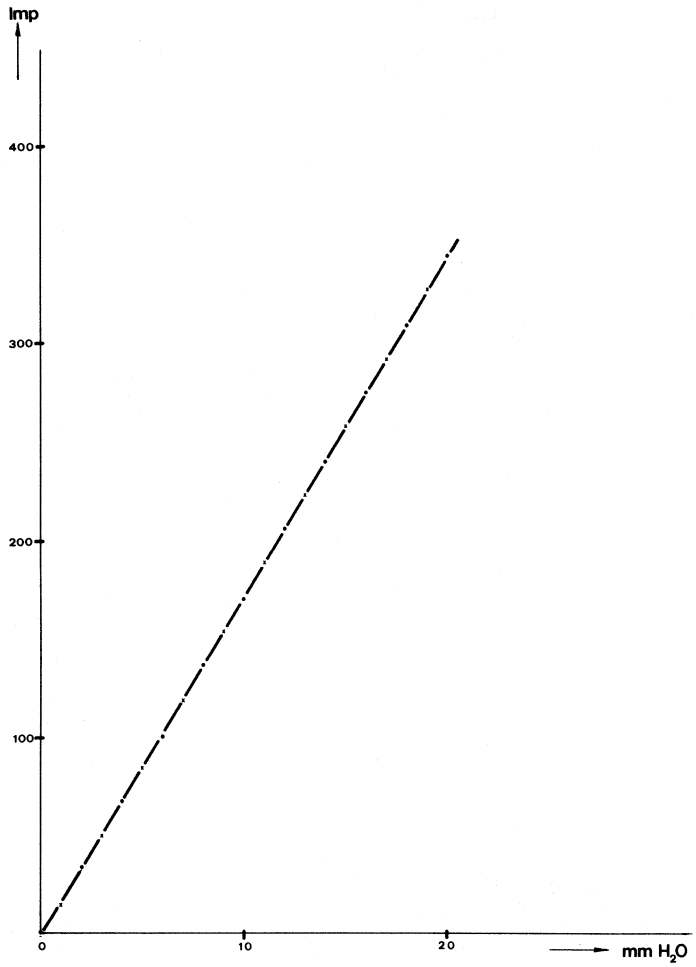

Fig. 10. Calibration curve.

is performed by means of a keyboard before the measurement starts.

Realization

Because the complete apparatus (monochromatic source of light, optical system, detectors and diaphragm) is sensitive to disturbances and noise, it has to be assembled as solidly as possible. For this reason a compact monochromatic source, the helium–neon laser model 136 of Spectra Physics was chosen. The complete system—laser, optics, diaphragm—was built into a 19-in rack tray (Fig. 9), in such a way that there is a possibility of adjusting the position of the fixed mirror by three micrometric screws.

UNITES DE MESURE	CONSTANTE	FACTEUR
mbar	56850	10^{-3}
mm H_2O	57971	10^{-2}
Torr	42640	10^{-3}
Pa N/m^2	56850	10^{-1}

Fig. 11. Multiplication constants.

Estimation of the multiplication constants was based on the calibration performed by the "Bureau Fédéral des Poids et Mesures" (Federal Bureau of Standards of Switzerland). The calibration has been made both for increasing and decreasing pressure. The results of this calibration are given in Fig. 10; Fig. 11 gives the values of some multiplication constants. The principal characteristics of the equipment are as follows.

Available ranges
2 mbar
20 mm H_2O
2 Torr
200 Pa (200 N/m^2)

Resolution
$6 \cdot 10^{-3}$ mbar
or $6 \cdot 10^{-2}$ mm H_2O
or $4 \cdot 10^{-3}$ Torr
or $6 \cdot 10^{-1}$ Pa (N/m^2)

Precision
0.5 percent of full scale

Linearity
± 0.3 percent

Hysteresis
1 digit.

Conclusions

The differential manometer presented in this paper is able to function in a large range of pressure, independent of the nature of the gas. The maximum differential pressure and the sensitivity, depend on the diaphragm chosen. The displacement of the diaphragm changes with the exponent 1.2 through 1.6 of its thickness and with the exponent four of its diameter [1]; this gives the possibility to adjust the required sensitivity of the apparatus and its range of measurement.

References

[1] H. H. Norton, *Handbook of Transducers for Electronic Measuring Systems*. Englewood Cliffs, NJ: Prentice-Hall, 1969.
[2] D. Mange, "Analyse et synthèse des systèmes logiques," Cahier de la C.S.L., no. 4 EPFL.
[3] A. Finn, *Physique Générale*. Reading, MA: Addison-Wesley, 1967.
[4] J. L. Dion, "Ondes et vibrations," Centre Éducatif et Culturel, Inc., Montreal, P.Q., Canada, 1974.

A Technique for Measuring the Efficiency of Waveguide-to-Coaxial-Line Adaptors

PETER J. SKILTON

Abstract—**This paper describes a technique for measuring the efficiency of a waveguide to coaxial line adaptor fitted with a sexless connector. Three such adaptors of the same type are required to implement the technique but there are no constraints on the characteristics of the individual adaptors; neither low dissipative attenuation nor low VSWR are necessary and identical performance of adaptors within the set of three is not assumed. Any error in the adaptor evaluation due to modes other than the principal mode propagating between "back-to-back" adaptors can be detected and eliminated.**

A method is described for quantifying the uncertainty in adaptor efficiency in terms of component uncertainties in the evaluation and the results obtained with three WG16 (WR90) to GR900 adaptors at 8.2 GHz are used to illustrate the technique. Although dependent on the reflection coefficient terminating the adaptor, typical 95-percent confidence limits for an adaptor efficiency of 99 percent vary from ± 0.08 to ± 0.12 percent.

The technique is also applicable to adaptors between waveguides of different cross-sections, e.g., circular to rectangular or taper sections, and also to sexless coaxial to coaxial adaptors.

Introduction

IN THE EVALUATION and transfer of standards of microwave attenuation, noise, and power, there is a recurring requirement for a knowledge of the loss in waveguide to coaxial line adaptors. Occasionally a comparison of waveguide and coaxial line devices is required within narrowly overlapping frequency bands where the VSWR's of the devices and adaptor approach the manufacturers specified value. Hence one requirement of any universal technique for adaptor evaluation is that no assumptions should be made of low dissipative loss or VSWR. Results of automatic network analyser (ANA) measurements of voltage reflection coefficient of three adaptors constructed for use in a narrow overlap of frequency bands showed also that no assumptions could be made about the equality of a pair of adaptors. Finally, if the coaxial line, or the connectors, approach their upper frequency limit a means is required of ensuring no propagation between adaptors in a mode other than the principal TEM if, for the purposes of evaluation, they are connected "back-to-back" at their coaxial parts.

One consequence of avoiding simplifying assumptions about the properties of an adaptor, or of not restricting the voltage reflection coefficient of its terminations to a low value, is an increase in the number of measurements required to quantify the adaptor; thus increasing the uncertainty in the final result. The uncertainty in four sequences of measurements using a set of three adaptors is analyzed in terms of the uncertainty in each stage of the evaluation and the magnitude of the cumulative uncertainty derived. Firstly, however, the theoretical basis of the method is described.

Manuscript received March 13, 1978.

The author is with the microwave standards division of the Royal Signals and Radar Establishment, Malvern, Worcestershire, England.

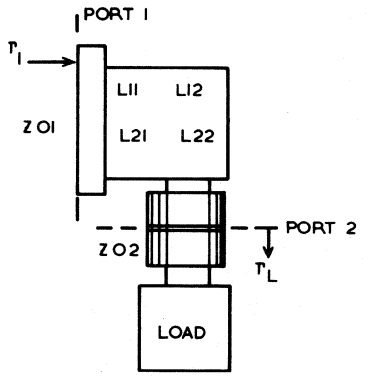

Fig. 1. Port numbering of a single adaptor.

Adaptor Efficiency

Since three adaptors of the same type are required to implement this technique the letters L, M, and N will be used to represent their scattering matrices and S to represent the scattering matrix of an assembly comprising two adaptors.

The adaptor shown in Fig. 1, terminated in a load of voltage reflection coefficient Γ_L, will have an efficiency, defined as:

$$\eta_1 = \frac{\text{Power absorbed in load}}{\text{Incident power} - \text{Reflected power}} \tag{1}$$

given by [1]:

$$\eta_1 = \frac{Z_{01}}{Z_{02}} \frac{|L_{21}|^2(1 - |\Gamma_L|^2)}{(1 - |\Gamma_1|^2)|1 - L_{22}\Gamma_L|^2}. \tag{2}$$

The quantities Γ_L and L_{22} can be determined from one-port ANA measurements and $|\Gamma_1|$ from either waveguide reflectometer or ANA measurements. The following section describes the method for determining the remaining term, $(Z_{01}/Z_{02})|L_{21}|^2$.

Measurement of an Adaptor and Air-Line Assembly

A technique for evaluating $(Z_{01}/Z_{02})|L_{21}|^2$ for a low-loss waveguide to coaxial adaptor and assigning limits to the adaptor efficiency has been described by Clark [2]. The technique requires voltage transmission coefficient measurements of each possible combination of two adaptors

0018-9456/78/0900-0231$00.75

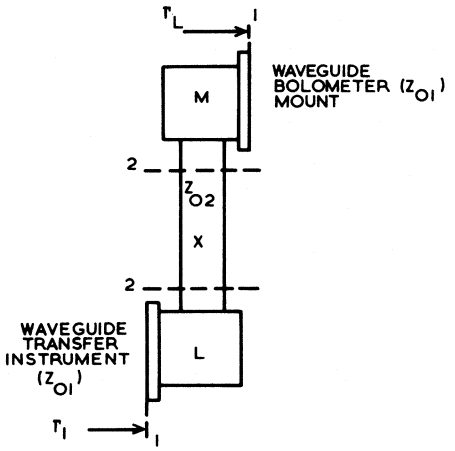

Fig. 2. Adaptor and air-line assembly.

connected "back-to-back" at their coaxial ports. To minimize the risk of propagation between adaptors of a mode other than the principal (TEM) mode this technique was modified to include a length of air-line separating the coaxial ports of the adaptor pairs. Fig. 2 illustrates two adaptors separated by an air-line of scattering matrix X. The voltage transmission coefficient $|S_{21}|$ of this assembly must be determined. One way of achieving this in a laboratory equipped for waveguide power measurement is to use a waveguide transfer instrument [3] to measure the efficiency of the assembly (η) and calculate $|S_{21}|$ from

$$|S_{21}|^2 = \eta\left(\frac{1-|\Gamma_1|^2}{1-|\Gamma_L|^2}\right)|1-S_{22}\Gamma_L|^2. \tag{3}$$

Analysis of an Adaptor and Air-Line Assembly

The scattering parameters of the assembly of adaptors and an air-line can be related to the individual scattering parameters of the three cascaded devices [1]. Assuming the scattering matrix of the air-line can be represented by

$$X = \begin{vmatrix} 0 & X_{21} \\ X_{21} & 0 \end{vmatrix} \tag{4}$$

(the error in assuming $X_{11} = X_{22} = 0$ is quantified in a later illustration of the technique) then, for the assembly in Fig. 2, putting $L_{12} = (Z_{01}/Z_{02})L_2$, etc., gives

$$S_{11} = L_{11} + \frac{(Z_{01}/Z_{02})L_{21}^2 X_{21}^2 M_{22}}{1 - L_{22}M_{22}X_{21}^2} \tag{5}$$

$$S_{12} = \frac{Z_{01}}{Z_{02}}\frac{L_{21}X_{21}M_{21}}{1 - L_{22}M_{22}X_{21}^2} = S_{21} \tag{6}$$

$$S_{22} = M_{11} + \frac{(Z_{01}/Z_{02})M_{21}^2 X_{21}^2 L_{22}}{1 - L_{22}M_{22}X_{21}^2}. \tag{7}$$

Writing (6) for the three possible combinations of the three transformers with one air-line gives

$$|S_{21}|_{LM} = \left(\frac{Z_{01}}{Z_{02}}\right)\left|\frac{L_{21}X_{21}M_{21}}{1 - L_{22}M_{22}X_{21}^2}\right| \tag{8}$$

$$|S_{21}|_{LN} = \left(\frac{Z_{01}}{Z_{02}}\right)\left|\frac{L_{21}X_{21}N_{21}}{1 - L_{22}N_{22}X_{21}^2}\right| \tag{9}$$

$$|S_{21}|_{MN} = \left(\frac{Z_{01}}{Z_{02}}\right)\left|\frac{M_{21}X_{21}N_{21}}{1 - M_{22}N_{22}X_{21}^2}\right| \tag{10}$$

from (8), (9), and (10) the following expression can be derived:

$$\frac{Z_{01}}{Z_{02}}|L_{21}|^2 = \left\{\frac{|S_{21}|_{LM}|S_{21}|_{LN}}{|S_{21}|_{MN}}\right\} \frac{|1 - L_{22}N_{22}X_{21}^2||1 - L_{22}M_{22}X_{21}^2|}{|X_{21}||1 - M_{22}N_{22}X_{21}^2|}. \tag{11}$$

The left-hand side of (11) is the quantity required in (2); the terms $|S_{21}|_{LM}$, etc., could be determined either from attenuation measurements or from (3) using efficiency and reflection coefficient data and the complex reflection coefficient at port 2 of each adaptor found from ANA measurements. The terms $(Z_{01}/Z_{02})|M_{21}|^2$ and $(Z_{01}/Z_{02})|N_{21}|^2$ can also be determined from (8), (9), and (10).

Air-Line Transmission Coefficient

The only term in (11) not yet derived is X_{21}, the air-line voltage transmission coefficient. This was estimated in the following manner. If the dissipative component of attenuation of two adaptors and an air-line, x cm in length, is denoted by α_X, then

$$\alpha_X = 10\log_{10}\frac{(1-|S_{11}|^2)}{|S_{21}|^2}. \tag{12}$$

Similarly if no air-line is used the dissipative attenuation of the pair of adaptors (α_0) can be found. Making the assumption that the total attenuation of the air-line ($10\log_{10} 1/|X_{21}|^2$) is given by $\alpha_X - \alpha_0$, the error in this assumption (δ) can be derived from the limits of

$$(\alpha_X - \alpha_0) - 10\log_{10}\frac{1}{|X_{21}|^2}. \tag{13}$$

Substitution from (5) and (6) in (12) yields α_X and setting $|X_{21}|^2 = 1$ in the result yields α_0. For the assembly in Fig. 2, δ has the limits of

$$\delta = \pm 10\log_{10}\left\{\frac{[1 + |L_{22}M_{22}X_{21}^2|]^2 - [|L_{11}|(1 - |L_{22}M_{22}X_{21}^2|) - (Z_{01}/Z_{02})|L_{21}^2X_{21}^2M_{22}|]^2}{[1 - |L_{22}M_{22}|]^2 - [|L_{11}|(1 + |L_{22}M_{22}|) + (Z_{01}/Z_{02})|L_{21}^2M_{22}|]^2}\right\}. \tag{14}$$

(Since the magnitude of the error depends on the magnitude of the adaptor reflection coefficients, the former is min-

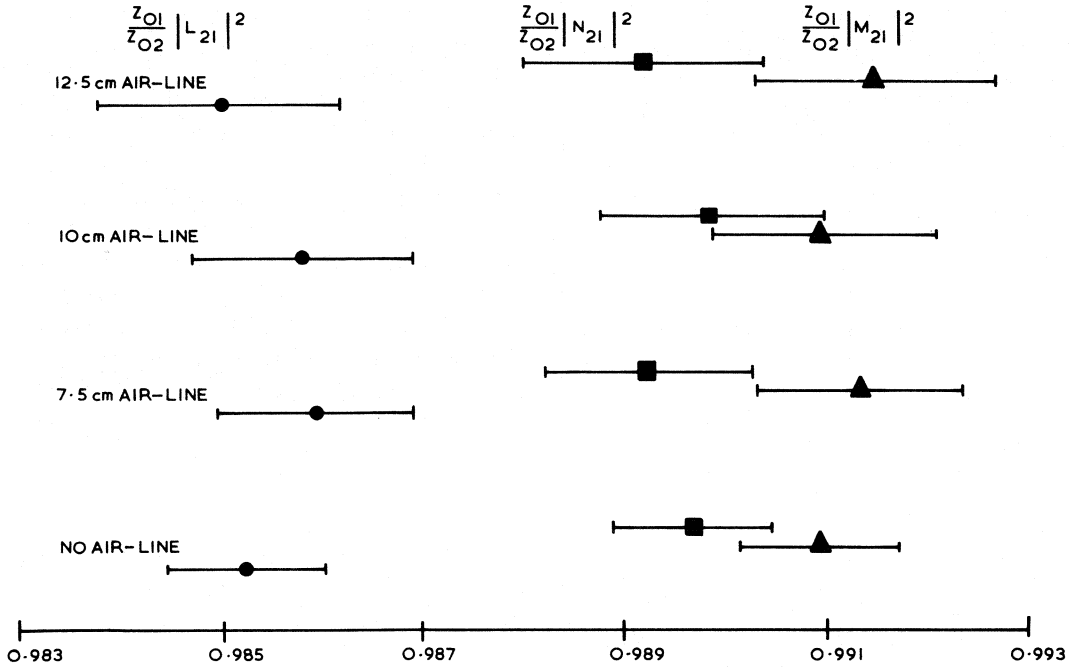

Fig. 3. Results of adaptor evaluation.

imized by using the two lowest VSWR adaptors to evaluate an air-line).

Illustration of the Technique

Evaluation of the loss in three waveguide to coaxial line adaptors was necessary to enable a comparison between the WG16 (WR90) bolometric power standards employed in the national microwave standards division of the Royal Signals and Radar Establishment and the 50-Ω coaxial line power standards employed at the National Physical Laboratory (NPL). The frequency chosen for the comparison was 8.2 GHz [4]. This was the lowest WG16 frequency at which calibrated bolometer mounts were available and the upper frequency at which the efficiency of the NPL, GR900 equipped calorimeter, had been determined. A method of adaptor evaluation which would detect the presence of moding problems in the GR900 connectors appeared desirable in view of the comparison frequency.

The adaptor evaluation was performed using the technique described with three different air-lines (7.5 cm, 10 cm, 12.5 cm) and again with no air-line. The efficiency and voltage reflection coefficient of assemblies of adaptors and air-lines were measured using a WG16 transfer instrument and values of $|S_{21}|$ calculated from the efficiencies and additional ANA results. $|X_{21}|$ was calculated for each air-line from results with the two lowest VSWR adaptors and the values of $(Z_{01}/Z_{02})|L_{21}|^2$, etc., obtained from the four sequences of measurements are shown in Fig. 3.

Uncertainty in Adaptor Evaluation

The individual random and systematic uncertainties in the measurement of six of the parameters required to evaluate (3) and (11) were quantified; both in magnitude and shape of their probability distribution.

i) ANA magnitude and phase uncertainty in S_{22} of ± 0.002 and $\pm 4°$ respectively (95 percent limits of a Gaussian distribution [5].

ii) Transfer instrument uncertainty in $|\Gamma_1|$. Dependent upon:

1) accuracy of tuning of the transfer instrument,
2) stability of power level from the source,
3) noise and drift in power meters,
4) voltage measurement,
5) equal to ± 0.001 (rectangular limits).

iii) Transfer instrument uncertainty in η_1. Dependent on the four factors in (ii) and the repeatability of the GR900 connectors. Equal to ± 0.1 percent (rectangular).

iv) Transfer instrument uncertainty in $|\Gamma_L|$ of ± 0.001 (rectangular) and ANA uncertainty in the phase of Γ_L of $\pm 4°$ (95-percent Gaussian).

v) ANA magnitude and phase uncertainty in L_{22} M_{22} and N_{22} of ± 0.002 and $\pm 4°$ (95-percent Gaussian).

vi) Uncertainty in air-line attenuation constant. Using the pair of adaptors having lowest VSWR, the limits from (14) are ± 0.004 dB; these never exceed ± 20 percent (rectangular) of the air-line attenuation constant.

The contribution of each of these six sources to the uncertainty in $(Z_{01}/Z_{02})|L_{21}|^2$ etc., was found by evaluating equations (3) and (11) 200 times with each source of uncertainty varied in turn about the mean measured value of the parameter by random selection from an appropriate Gaussian or rectangular distribution. The mean and 95-percent confidence limits of the 200 results were evaluated and the uncertainties attributable to i) to vi), above, are given in Table I, for the 12.5 cm air-line, together with the total uncertainty which, including the systematic error involved in assuming $X_{11} = X_{22} = 0$, is estimated never to exceed ± 0.12 percent (95-percent confidence limits). The

TABLE I
UNCERTAINTY IN ADAPTOR EVALUATION USING 12.5 CM AIR-LINE

Due to Uncertainty in:- \ Uncertainty in:-	$\frac{Z_{01}}{Z_{02}}\|L_{21}\|^2$	$\frac{Z_{01}}{Z_{02}}\|M_{21}\|^2$	$\frac{Z_{01}}{Z_{02}}\|N_{21}\|^2$
i) S_{11} and S_{22}	0.23×10^{-4}	0.27×10^{-4}	0.26×10^{-4}
ii) $\|\Gamma_1\|$ and $\|\Gamma_2\|$	0.68×10^{-4}	0.68×10^{-4}	0.66×10^{-4}
iii) η_1 and η_2	7.21×10^{-4}	7.13×10^{-4}	7.02×10^{-4}
iv) Γ_L	0.07×10^{-4}	0.25×10^{-4}	0.19×10^{-4}
v) L_{22}, M_{22} and N_{22}	2.16×10^{-4}	2.71×10^{-4}	2.15×10^{-4}
vi) air-line attenuation	8.53×10^{-4}	8.50×10^{-4}	8.57×10^{-4}
Total	1.14×10^{-3}	1.14×10^{-3}	1.13×10^{-3}

All limits are for 95-percent confidence.

corresponding total uncertainties for the 7.5 cm, 10 cm and no air-line results are ± 0.11, ± 0.10, and ± 0.08 percent, respectively. The agreement shown in Fig. 3 between results for $(Z_{01}/Z_{02})|L_{21}|^2$, etc., from measurements with air-lines and those with no air-line indicates for this illustration, that moding problems are not significant and the most precise determination of $(Z_{01}/Z_{02})|L_{21}|^2$, etc., has an uncertainty of ± 0.08 percent.

Fig. 3 and the preceding analysis give the uncertainty in the only term of the adaptor efficiency which is independent of the adaptor termination. The uncertainty in adaptor efficiency when used with any termination was estimated using random number selection from an appropriate distribution, similar to that already described. The uncertainty in $(Z_{01}/Z_{02})|L_{21}|^2$ etc. (taken as ± 0.08 percent) was combined with that arising from measurement of $|\Gamma_1|, \Gamma_L$, and L_{22} etc. (equation (2)). For terminating VSWR's up to 1.13 the uncertainty in adaptor efficiency varied from ± 0.08 percent for the lowest VSWR termination, to ± 0.12 percent.

CONCLUSIONS

Fig. 3 illustrates the agreement between the four, largely independent, evaluations of the three WG16 to GR900 adaptors. (The only interdependence of the four results in Fig. 3 arose from the method of evaluation of the three air-lines. Each evaluation relied on the dissipative attenuation of one pair of adaptors. Any error in the latter would influence all values of air-line attenuation, although by much less than the ± 20 percent uncertainty in this term; typically ± 2 percent). The results in Fig. 3 also show that, for this application of the technique, no significant moding problem exists. Thus the method of evaluation appears to be valid for determining

$$\frac{Z_{01}}{Z_{02}}|L_{21}|^2 \qquad \frac{Z_{01}}{Z_{02}}|M_{21}|^2 \qquad \frac{Z_{01}}{Z_{02}}|N_{21}|^2$$

and a quantitative estimate of uncertainty gives 95-percent confidence limits associated with these quantities of ± 0.08 percent (when no air-line was used).

ACKNOWLEDGMENT

The author wishes to thank R. M. Embleton and G. W. Parkes of RSRE for their assistance in providing the transfer instrument and ANA data used to illustrate the technique.

REFERENCES

[1] D. M. Kerns and R. W. Beatty, *Basic Theory of Waveguide Junctions and Introductory Microwave Network Analysis.* London, England: Pergamon Press.
[2] R. F. Clark, "Maximum limits of efficiency for low-loss reciprocal adopters," *IEEE Trans. Instrum. Meas.*, vol. IM-25, pp. 312–314, Dec. 1976.
[3] G. F. Engen, "A transfer instrument for the intercomparison of microwave power meters," *IRE Trans. Instrum.*, pp. 202–208, Sept. 1960.
[4] P. J. Skilton and A. E. Fantom, "A comparison of the United Kingdom National Standards of microwave power in waveguide and coaxial line," this issue, pp. 297–298.
[5] B. P. Hand, "Developing accuracy specifications for automatic network analyzer systems," *Hewlett Packard J.*, pp. 16–19, Feb. 1970.

The Electromagnetic Basis for Nondestructive Testing of Cylindrical Conductors

JAMES R. WAIT, FELLOW, IEEE

Abstract—**Using an idealized model, we deduce the impedance per unit length of long solenoid of many turns that contains a cylindrical sample. The sample with a specified conductivity and magnetic permeability need not be centrally located within the solenoid provided all transverse dimensions are small compared with the free-space wavelength. The derivation is relatively straightforward and it provides a justification for earlier use of the impedance formula. The dual problem, where the solenoid is replaced by a toroidal coil is also considered. It is shown that both excitation methods have merit in nondestructive testing procedures.**

Introduction

A COMMON METHOD [1] of nondestructive testing (NDT) of metal rods and tubes is to induce eddy currents by means of an encircling solenoid carrying an alternating current. The impedance of the solenoid is related to the cross-sectional area and the electrical properties of the sample. A formula for this impedance was obtained by Förster and Stambke [2] on the assumption that end effects could be ignored. Also, they assumed that the cylindrical sample was centrally located within the solenoid. The same derivation was essentially repeated by Hochschild [3] and Libby [1].

A feature of the Förster–Stambke derivation is that the effect of the air gap is introduced in a somewhat heuristic fashion wherein the field in this concentric region is assumed to be the same as the one for the empty solenoid. We feel it is worthwhile to provide a more general derivation of the impedance formula. We also show it applies to the case of a nonconcentric air gap. Finally, we mention the relevance of the current analysis to the dual problem where the cylindrical sample is excited by a toroidal coil.

Formulation

To simplify the discussion, we consider first the concentric air gap model with a homogeneous cylindrical sample of radius a with conductivity σ and magnetic permeability μ. The situation is indicated in Fig. 1 where the solenoid of radius b encloses the sample, both of which are assumed to be infinite in length. Our objective is to find an expression for the impedance of the solenoid per unit length since this is the basis of the NDT eddy current methods that are commonly used.

In terms of cylindrical coordinates (ρ, ϕ, z), the only component of the magnetic field is H_z since the exciting current in the solenoid is uniform in both the axial and in the azimuthal direction. Within the sample, H_z satisfies the Helmholtz equation

$$(\nabla^2 - \gamma^2)H_z = 0 \tag{1}$$

where $\gamma^2 = i\sigma\mu\omega$ and where we have adopted a time factor $\exp(i\omega t)$. Here ω is the angular frequency that is sufficiently low that displacement currents in the sample can be neglected. If not, we merely replace σ by $\sigma + i\varepsilon\omega$ where ε is the permittivity. Also, it goes without saying that the field amplitude is sufficiently small that nonlinear effects can be ignored.

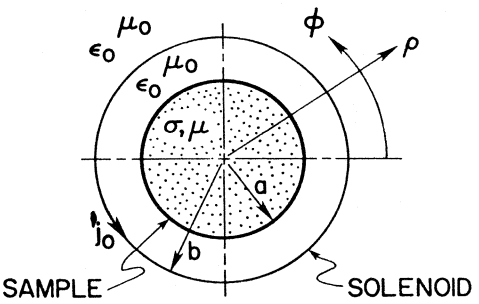

Fig. 1. Cross-sectional view of cylindrical sample located centrally within a solenoid of many turns.

Solution for Concentric Sample

For the highly idealized situation described, we can immediately write [4]

$$H_z = AI_0(\gamma\rho) \tag{2}$$

for $\rho < a$ where I_0 is a modified Bessel function of argument $\gamma\rho$ and where A is a constant. From Maxwell's equations the azimuthal component of the electric field is

$$E_\phi = -(1/\sigma)\,\partial H_z/\partial\rho = -A(\gamma/\sigma)I_1(\gamma\rho) \tag{3}$$

also for $\rho < a$. Now we can immediately form an expression for the "impedance" Z_c of the cylinder:

$$Z_c = [-E_\phi/H_z]_{\rho=a} = \eta I_1(\gamma a)/I_0(\gamma a) \tag{4}$$

where $\eta = \gamma/\sigma = (i\mu\omega/\sigma)^{1/2}$ is the intrinsic or wave impedance of the sample material.

Now, for the air gap region $a < \rho < b$, we write corresponding field expressions

$$H_{0z} = BI_0(\gamma_0\rho) + CK_0(\gamma_0\rho) \tag{5}$$

Manuscript received March 6, 1978.

The author is with the Cooperative Institute for Research in Environmental Sciences, University of Colorado/NOAA, Boulder, CO 80309.

and

$$E_{0\phi} = -B\eta_0 I_1(\gamma_0\rho) + C\eta_0 K_1(\gamma_0\rho) \tag{6}$$

where B and C are constants and where $\eta_0 = \gamma_0/(i\varepsilon_0\omega) = (\mu_0/\varepsilon_0)^{1/2} \cong 120\pi$ in terms of the permittivity ε_0 and permeability μ_0 of the air region. Here and in the above, the Bessel function identities $\partial I_0(x)/\partial x = I_1(x)$ and $\partial K_0(x)/\partial x = -K_1(x)$ have been employed.

Compatible with the requirement that tangential fields must be continuous at $\rho = a$ we can write

$$[E_{0\phi} + Z_c H_{0z}]_{\rho=a} = 0. \tag{7}$$

This immediately tells us that

$$\frac{C}{B} = \frac{\eta_0 I_1(\gamma_0 a) - Z_c I_0(\gamma_0 a)}{\eta_0 K_1(\gamma_0 a) + Z_c K_0(\gamma_0 a)}. \tag{8}$$

In the external region $\rho > b$, the field expressions must clearly have the form

$$H_{0z} = DK_0(\gamma_0\rho) \tag{9}$$

$$E_{0\phi} = D\eta_0 K_1(\gamma_0\rho) \tag{10}$$

where D is another constant.

Now the solenoid current is idealized as a continuous current distribution j_0 A/m in the azimuthal direction defined such that

$$\lim_{\Delta\to 0} \begin{cases} H_{0z}(\rho = b + \Delta) - H_{0z}(\rho = b - \Delta) = -j_0 & (11) \\ E_{0\phi}(\rho = b + \Delta) - E_{0\phi}(\rho = b - \Delta) = 0 & (12) \end{cases}$$

Application of these conditions immediately leads to

$$D = C - I_1(\gamma_0 b)B/K_1(\gamma_0 b) \tag{13}$$

and

$$B = j_0\gamma_0 b K_1(\gamma_0 b). \tag{14}$$

Among other things, this tells us that the magnetic field external to the solenoid (i.e., $\rho > b$) has the form

$$H_{0z} = \{-B[I_1(\gamma_0 b)/K_1(\gamma_0 b)] + C\}K_0(\gamma_0\rho). \tag{15}$$

The quantity of immediate interest is the impedance Z of the solenoid itself. Clearly, within the limits of our basic assumptions,

$$Z = \text{constant} \times E_{0\phi}(\rho = b)/j_0. \tag{16}$$

The corresponding impedance of the empty solenoid is denoted Z_0. Thus it follows that

$$\frac{Z}{Z_0} = 1 - \frac{C}{B}\frac{K_1(\gamma_0 b)}{I_1(\gamma_0 b)} \tag{17}$$

which is explicit since C/B is given by (8).

Quasi-Static Form

We now can simplify the impedance ratio formula if we invoke the small argument approximations for Bessel functions of order $\gamma_0 a$ and $\gamma_0 b$. That is, we use $I_0(x) \simeq 1$, $I_1(x) \simeq x/2$, $K_0(x) \simeq -\log x$ and $K_1(x) \simeq 1/x$. This exercise leads to

$$\frac{Z}{Z_0} \cong \left[1 - \frac{a^2}{b^2} + \frac{\mu}{\mu_0}\frac{a^2}{b^2}\frac{2}{\gamma a}\frac{I_1(\gamma a)}{I_0(\gamma a)}\right] = \frac{R + iX}{Z_0} \tag{18}$$

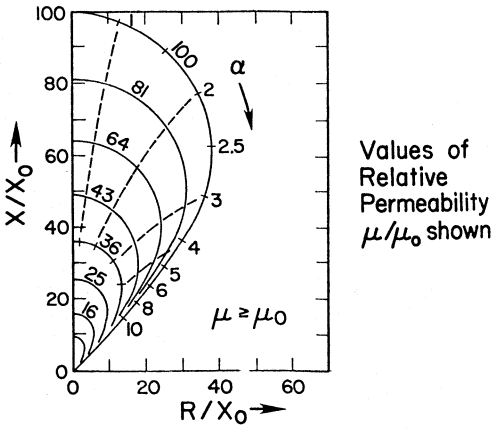

Fig. 2. Argand plot of the impedance $Z = R + iX$ normalized to the reactance X_0 of the empty solenoid, for $a = b$.

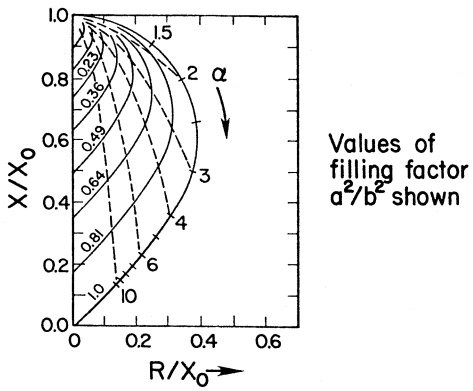

Fig. 3. Argand plot of the impedance $Z = R + iX$ normalized to the reactance X_0 of the empty solenoid, for $\mu = \mu_0$.

where no restriction has been placed on the magnitude of γa. Here R and X denote the resistance and reactance, respectively.

The formula for Z/Z_0 given by (18) is in agreement with Förster and Stambke [2] (if one remembers they used the old German designations J_0 and J_1 for modified Bessel functions). Förster and Stambke [2], Hochschild [3] and Libby [1] present extensive numerical data for this quasi-static approximation to Z/Z_0 in Argand diagrams in the complex plane for various values of $|\gamma a|$ and μ/μ_0. Two examples, using dimensionless parameters, are shown in Figs. 2 and 3 when the ordinates and abscissas are normalized by X_0 which is the reactance of the empty solenoid. That is, we assume $Z_0 \simeq iX_0$ corresponding to negligible ohmic losses in the solenoid itself. The real parameter α is defined by $\alpha = \gamma a \exp(-i\pi/4) = (\sigma\mu\omega)^{1/2}a$. In Fig. 2 the sample radius b is assumed to be the same as the sample radius a (i.e., no air gap). Different values of the magnetic permeability are shown. Not surprisingly, when α is small, R vanishes, and X/X_0 tends to μ/μ_0. However, in general, the eddy currents have the effect of reducing X/X_0, which is the effective flux, and to introduce a resistive portion R/X_0. In Fig. 3, the relative permeability of the sample $\mu/\mu_0 = 1$ but the filling factor a^2/b^2 assumes different values. The results indicate that the presence of the air gap reduces the sensitivity of the

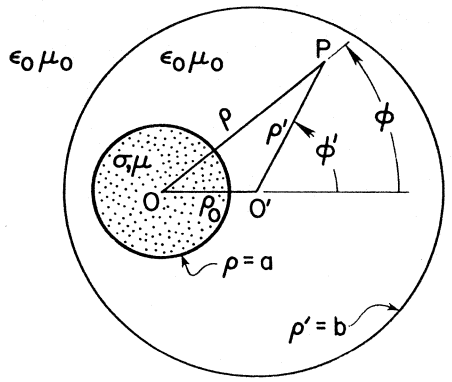

Fig. 4. Cross-section view of the noncentrally located sample.

device for probing the conductivity but the effect is predictable.

Actually, if α is sufficiently small (i.e., $|\gamma a| \ll 1$), (18) reduces to

$$Z/Z_0 \simeq X/X_0 \simeq 1 + (a^2/b^2)[\mu/\mu_0 - 1] \qquad (18')$$

which is consistent with the curves in Figs. 2 and 3. In this dc limit the results only depend on the magnetic permeability of the sample.

Analysis for Nonconcentric Sample

We now consider the formal extension of the theory to the case where the exciting solenoid is no longer concentric with the cylindrical sample. The situation is indicated in Fig. 4. As before, cylindrical coordinates (ρ, ϕ, z) are chosen coaxial with the sample. But now, the shifted coordinates (ρ', ϕ', z) are chosen to be coaxial with the exciting solenoid. The shift is ρ_0 as indicated in Fig. 4 where we do impose the rather obvious physical restriction that $b > \rho_0 + a$.

The field scattered from the solenoid now is no longer azimuthally symmetric. But, in analogy to (15), we can write

$$H_{0z} = BI_0(\gamma_0\rho') + \sum_{m=-\infty}^{+\infty} C_m K_m(\gamma_0\rho)e^{-im\phi} \qquad (19)$$

for the region $\rho > a$ and $\rho' < b$, while

$$H_{0z} = -B[I_1(\gamma_0 b)/K_1(\gamma_0 b)]K_0(\gamma_0\rho') + \sum_{m=-\infty}^{+\infty} C_m K_m(\gamma_0\rho)e^{-im\phi} \qquad (20)$$

for the region $\rho' > b$. As before, B is given by (14) in terms of the source current j_0 in the solenoid. Here C_m is to be determined.

To proceed further, we now note that the field inside the sample (i.e., $\rho < a$) must have the form

$$H_z = \sum_{m=-\infty}^{+\infty} H_{mz} \qquad (21)$$

where

$$H_{mz} = A_m I_m(\gamma\rho)e^{-im\phi}. \qquad (22)$$

Similarly, for the same region,

$$E_\phi = \sum_{m=-\infty}^{+\infty} E_{m\phi} \qquad (23)$$

where

$$E_{m\phi} = -(\gamma/\sigma)A_m I'_m(\gamma\rho)e^{-im\phi} \qquad (24)$$

where the prime indicates differentiation with respect to $\gamma\rho$. Now we define the cylinder impedance parameter Z_{mc} for harmonic waves of order m by

$$Z_{mc} = [-E_{m\phi}/H_{mz}]_{\rho=a} = \eta I'_m(\gamma a)/I_m(\gamma a) \qquad (25)$$

in analogy to (4). In fact, $Z_{0c} \equiv Z_c$.

A known addition theorem [5] for modified Bessel functions $I_0(\gamma_0\rho')$ allows us to write (19) in the form

$$H_{0z} = \sum_{m=-\infty}^{+\infty} H_{0mz} \qquad (26)$$

where

$$H_{0mz} = \{B(-1)^m I_m(\gamma_0\rho_0)I_m(\gamma_0\rho) + C_m K_m(\gamma_0\rho)\}e^{-im\phi}. \qquad (27)$$

Similarly, for the same region,

$$E_{0\phi} = \sum_{m=-\infty}^{+\infty} E_{0mz} \qquad (28)$$

where

$$E_{0mz} = -\eta_0\,\partial H_{0mz}/\partial(\gamma_0\rho). \qquad (29)$$

Application of the condition

$$[E_{0m\phi} + Z_{mc}H_{0mz}]_{\rho=a} = 0 \qquad (30)$$

now leads to the relation

$$\frac{C_m}{B} = \frac{(-1)^m I_m(\gamma_0\rho_0)[\eta_0 I'_m(\gamma_0 a) - Z_{mc}I_m(\gamma_0 a)]}{-\eta_0 K'_m(\gamma_0 a) + Z_{mc}K_m(\gamma_0 a)}. \qquad (31)$$

Inserting this result into (19) or (20) yields explicit expressions for the fields external to the sample. However, in order to deduce the resultant impedance of the solenoid, it is desirable to reexpress H_{0z} in terms of the (ρ', ϕ', z) coordinates. Here we use a known addition theorem [6] for $K_m(\gamma_0\rho)\exp(-im\phi)$. The rather horrendous result is

$$H_{0z} = BI_0(\gamma_0\rho') + \sum_{m=-\infty}^{+\infty} C_m \sum_{n=-\infty}^{+\infty} K_{m+n}(\gamma_0\rho')I_n(\gamma_0\rho_0)(-1)^n e^{-i(n+m)\phi'}. \qquad (32)$$

This is valid in the nonconcentric air gap region (i.e., $\rho > a$ and $\rho_0 < \rho' < b$). The needed azimuthal component is obtained from

$$E_{0\phi'} = -\eta_0\,\partial H_{0z}/\partial(\gamma_0\rho'). \qquad (33)$$

The relevant quantity for the impedance calculation is the "average" field $\bar{E}_{0\phi'}$ at the solenoid. Clearly, this is given by

$$\bar{E}_{0\phi'} = \frac{1}{2\pi}\int_0^{2\pi} [E_{0\phi'}]_{\rho'=b}\,d\phi' = -\eta_0 BI_1(\gamma_0 b) - \eta_0 \sum_{m=-\infty}^{+\infty} C_m K'_0(\gamma_0 b)I_m(\gamma_0\rho_0)(-1)^m. \qquad (34)$$

Thus it follows that the impedance Z per unit length of the solenoid with the sample divided by the impedance Z_0 of the empty solenoid is given by

$$\frac{Z}{Z_0} = 1 - \frac{K_1(\gamma_0 b)}{I_1(\gamma_0 b)} \sum_{m=0}^{\infty} \varepsilon_m \frac{C_m}{B} I_m(\gamma_0 \rho_0)(-1)^m \quad (35)$$

where $\varepsilon_0 = 1$ and $\varepsilon_m = 2$ for $m \neq 0$ and where C_m/B is given explicitly by (31). Not surprisingly, (35) reduces to (17) for the centrally located sample, i.e., $I_m(\gamma_0 \rho_0) = 0$ for $\rho_0 \to 0$ when $m \neq 0$.

We again may invoke the small argument approximations for Bessel functions of order $\gamma_0 a$, $\gamma_0 b$, and $\gamma_0 \rho_0$. That is, for $m = 1, 2, 3, \cdots$, we use

$$I_m(x) \simeq x^m/(m!\, 2^m),\ I'_m(x) \simeq x^{m-1}/[(m-1)!\, 2^m]$$

$$K_m(x) \simeq (m-1)!\, 2^{m-1}/x^m \text{ and } K'_m(x) \simeq -m!\, 2^{m-1}/x^{m+1}.$$

Lo and behold, these show that Z/Z_0 reduces again to the formula given by (18). This confirms the conjecture of Förster and Stambke who seemed to be gifted with keen physical insight into such problems. Of course, we do not expect the result to hold in any sense when the dimensions of the solenoid become comparable with the free-space wavelength. In that case, many other complications arise such as the assumed uniformity of the solenoid current.

The Dual Problem and Concluding Remarks

There is an extremely interesting duality to the problem we have discussed. That is, rather than exciting the cylindrical sample with an *azimuthal electric current*, we employ an *azimuthal magnetic current*. This is an idealized representation for a thin toroidal coil but, again, it effectively is of infinite length in the z or axial direction. The assumed source discontinuity is now in the electric field at $\rho = b$ which has only a z component. The much more complicated case of the toroidal coil of finite axial extent was analyzed recently [7].

Under the present assumption of axial uniformity, the admittance Y per unit length of the toroid is the dual of the impedance Z of the solenoid discussed above. Thus all the earlier equations apply if we make the following transformations: $i\mu\omega \to \sigma$, $\mu_0 \to \varepsilon_0$, $\eta \to \eta^{-1}$, $\eta_0 \to \eta_0^{-1}$, $H_z \to E_z$, $E_\phi \to -H_\phi$, $H_{0z} \to E_{0z}$, and $E_{0\phi} \to -H_{0\phi}$. Then the dual of (18) is the ratio of the admittance Y of the toroidal coil with the sample to the admittance Y_0 without the sample. It is written explicitly

$$\frac{Y}{Y_0} = \left[1 - \frac{a^2}{b^2} + \frac{\sigma}{i\varepsilon_0 \omega} \frac{a^2}{b^2} \frac{2}{\gamma a} \frac{I_1(\gamma a)}{I_0(\gamma a)}\right]$$

for the case where $|\gamma_0 b| \ll 1$. That is, the radius of the toroidal coil should be much smaller than the free-space wavelength. Also, in full analogy to the earlier discussion, the quasi-static result holds for any location of the cylindrical sample within the toroid. Furthermore, in the low frequency limit where $|\gamma a| = \alpha \ll 1$, we see that

$$Y \simeq Y_0[1 + (a^2/b^2)[(\sigma/i\varepsilon_0 \omega) - 1]]$$

which depends only on the conductivity of the sample. Thus this type of excitation should be preferred with probing the effective conductivity in the axial direction in the sample.

References

[1] H. L. Libby, *Introduction to Electromagnetic Nondestructive Test Methods*. New York: Wiley, 1971, Sect. 5.2, pp. 135–150.

[2] F. Förster and K. Stambke, "Theoretische und experimentelle Grundlagen der zerstörungfreien Werkstoffprüfung mit Wirbelstromverfahren, Pt. III," *Zeits. Metallkde.*, Bd. 45, Heft 4, pp. 166–179, 1954.

[3] H. Hochschild, "Electromagnetic methods of testing metals," in *Progress in Non-Destructive Testing*, E. G. Stanford and J. H. Fearon, Eds. New York: Macmillan, 1959, pp. 58–109.

[4] J. R. Wait, *Electromagnetic Radiation from Cylindrical Structures*. Oxford and New York: Pergamon Press, 1959.

[5] A. Erdélyi, Ed., *Higher Transcendental Functions*. New York: McGraw-Hill, 1953, vol. 2, p. 102 (no. 36 for $\nu = 0$).

[6] —— (*loc cit.*, p. 102, no. 35 with the substitutions $Z \to \gamma_0 \rho'$, $z \to -\gamma_0 \rho_0$, $\psi + \phi \to -\phi$, $\phi \to -\phi'$).

[7] D. A. Hill and J. R. Wait, "Analysis of alternating current excitation of a wire rope by a toroidal coil," *J. Appl. Phys.*, vol. 48, no. 12, pp. 4893–4897, 1977.

Noise Spectra for Monolithic Detector Arrays

MITCHELL W. FINKEL, LESLIE L. THOMPSON, AND ROBERT J. SULLIVAN

Abstract—**A brief review of nonstationary processes is extended so as to include mixed stationary processes as they apply to the determination of the power density spectrum for monolithic detector arrays. An analog method for determining noise spectra is developed. Both theoretical and experimental results are presented.**

Introduction

With the rapid maturation of large-scale integration (LSI), hundreds, even thousands, of detectors are now contained within a single monolithic device. Evaluating the performance of these devices requires that we review some of the measurement procedures. Certainly the noise power density spectrum is one such fundamental measurement. The usual noise model is something of a compromise between simplicity and fidelity. A more realistic model would not only consider the contributions made by each noise generator, but also because of the distributed nature of these sources, the model would consider the associated transformations. For example, the transformation associated with correlated sampling which effectively suppresses low-frequency (LF) noise is graphically illustrated by the power density spectrum.

Thus the power spectrum affords us a more informed view of a noise process than is revealed by merely considering the moments of some presumed distribution (e.g., the mean and variance). Indeed, if we begin with the presumption that we are dealing with a normal process, then the entire statistical structure is revealed by the spectrum. In addition, there is the bonus that even a cursory reading of the spectrum should help distinguish between intraneous and extraneous noise.

Perhaps we should say something about the nature of the output of monolithic detector arrays. Typically, signals are processed in the analog domain, and after passing through a sample-and-hold (SH) circuit, the final video output is provided for display or digital conversion. Since a great many detectors are sequentially read out through a single video channel, what one observes is a contiguous stream of nearly rectangular pulses of constant width but varying amplitudes (similar to pulse amplitude modulation). It is these varying amplitudes that abound with information about both the response by each detector to the incident irradiance and the associated noise. Our primary concern will be the extraction of this information, particularly as it relates to the noise content.

We will begin with an abbreviated discussion of spectra for nonstationary processes, since in general we should anticipate a nonstationary noise process. Initially, we will essentially follow the Bendat–Piersol [1] exposition. Subsequently, we will develop a rather direct method for realizing the noise power spectrum. Although the measurements contained in the following sections pertain to a 96-element Westinghouse photodiode linear array, the method outlined should be applicable to any monolithic device.

Manuscript received March 6, 1978.
The authors are with NASA/Goddard Space Flight Center, Greenbelt, MD 20771.

Nonstationary Processes

The spectra of special interest, the time-averaged power spectrum, can be expressed as

$$G(f, T) = \frac{1}{T}\int_T \frac{1}{\Delta f N}\sum_{i=1}^{N} x_i^2(t, f, \Delta f)\, dt \tag{1}$$

where the x_i's are sample functions forming a random noise process, f is the center frequency, Δf is the bandwidth of definition about the center frequency, and T is the time interval over which the spectrum is averaged. Suppose we follow the steps implicit in this expression: 1) filtering, 2) squaring, 3) ensemble averaging, and 4) time averaging. We can begin with a sample function, $x_i(t)$, which is a member of the ensemble and consider the input–output relationship of a filter as given by the convolution integral,

$$x_i(t, f, \Delta f) = \int_{-\infty}^{\infty} h(\xi) x_i(t - \xi)\, d\xi. \tag{2}$$

For an ideal bandpass filter whose frequency response $H(v)$ is unity within the bandpass and zero elsewhere, a transform exists such that,

$$h(\xi) = \int_{-\infty}^{\infty} H(v) \exp(2\pi j \xi v)\, dv = \frac{\sin(\pi \Delta f \xi)}{\pi \xi} \cos 2\pi f \xi. \tag{3}$$

Now squaring,

$$x_i^2(t, f, \Delta f) = \iint_{-\infty}^{\infty} h(\xi) h(\eta) x_i(t - \xi) x_i(t - \eta)\, d\xi\, d\eta. \tag{4}$$

Ensemble averaging and dividing by the bandpass leads to time-varying power spectrum,

$$G(t, f) = \frac{1}{\Delta f}\iint_{-\infty}^{\infty} h(\xi) h(\eta) \phi(t - \xi, t - \eta)\, d\xi\, d\eta \tag{5}$$

where $\phi(t-\xi,\ t-\eta)=\phi(t_1,\ t_2)$ is the autocorrelation function of $x(t)$. We can remove the time dependence by averaging the autocorrelation function. But first let us introduce a new set of variables

$$t'=t-\xi$$
$$\tau=\xi-\eta$$

so that the time-averaged autocorrelation function can now be written as

$$\frac{1}{T}\int_0^{T-\tau}\phi(t',\ t'+\tau)\,dt'=\langle\phi(\tau,\ T)\rangle. \tag{6}$$

Inserting (3) and (6) into (5), we have

$$G(f,\ T)=\frac{1}{\Delta f}\int_{\infty}^{\infty}\langle\phi(\tau,\ T)\rangle\exp\,(-2\pi jf\tau)\cdot\frac{\sin\,\pi\Delta f\eta\,\sin\,\pi\Delta f(\tau+\eta)}{\pi^2\eta(\tau+\eta)}\,d\tau\,d\eta. \tag{7}$$

Integrating with respect to η yields [2]

$$\frac{1}{\Delta f}\int_{-\infty}^{\infty}\frac{\sin\,\pi\Delta f\eta\,\sin\,\pi\Delta f(\tau+\eta)}{\pi^2\eta(\tau+\eta)}\,d\eta=\text{sinc}\,\pi\Delta f\tau. \tag{8}$$

So we can now say,

$$G(f,\ T)=\int_{-\infty}^{\infty}\langle\phi(\tau,\ T)\rangle(\text{sinc}\,\pi\Delta f\tau)[\exp\,(-2\pi jf\tau)]\,d\tau. \tag{9}$$

The time-averaged power spectrum (9) submits to several possible interpretations. Turning to the convolution theorem, for example, we interpret (9) as a running mean. That is, multiplying the autocorrelation function by the sinc function in the transform domain corresponds to the convolution of $G(f)$ with the rectangle function $\Pi(f)$ in the frequency domain. Or to put it another way, the weighting function, sinc $\pi\Delta f\tau$ can be viewed as a kind of sliding scale factor which continuously renormalizes the instantaneous power spectrum so that, effectively, it becomes locally stationary. We also note that in the limit as $T\to\infty$ and consequently $\Delta f\to 0$, equation (9) reduces to the more familiar representation

$$G(f)=2\int_{-\infty}^{\infty}\phi(\tau)\exp\,(-2\pi jf\tau)\,d\tau. \tag{10}$$

We conclude that once the appropriate weighting function is introduced, determining the noise power spectrum reduces to the familiar Weiner relationship.

Noise Spectra

Our treatment thus far has been quite general. Again, we consider the typical output of a linear array. (Note: The following can be easily interpreted to apply to frame imaging devices as well.) Fig. 1 is meant to be a representation of such a video output. As the figure suggests, each detector element is read out sequentially. At the end of the line time T, the

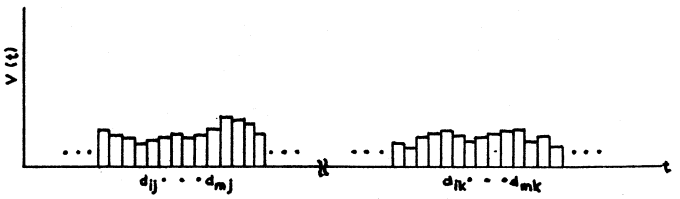

Fig. 1. An idealized representation of an output of a linear array showing two consecutive sequences of rectangular pulses with constant widths ζ and random heights. Each detector element is tagged with a double subscript. The first subscript identifies the element number and the second refers to the sequential order.

sequence is once again initiated and another video line is read out. The process repeats until the end of the data collection/imaging frame. In the figure, each detector element is tagged with a double subscript. The first subscript identifies the element number and the second refers to the sequential order. Now suppose we select some detector, ignoring for the moment all others, and sequentially display its output signal line after line. What one would see is a series of rectangular pulses of identical widths but varying amplitudes depending upon the instantaneous signal and noise level. We can represent this series by [3],

$$f(t)=\sum_N X(t)\Pi\left(\frac{t-b_N}{\zeta}\right) \tag{11}$$

where $X(t)$ refers to the random heights and $\Pi(t)$ represents the rectangular function with displacement b_N and widths ζ. Since $f(t)$ is a random function, the spectrum must be determined according to the Weiner theorem by transforming the autocorrelation function. Autocorrelating $f(t)$, we find that

$$\phi(t_1,\ t_2)=\phi_x(t_1,\ t_2)\sum_N\Pi\left(\frac{t_1-b_N}{\zeta}\right)\cdot\sum_M\Pi\left(\frac{t_2-b_M}{\zeta}\right) \tag{12}$$

where $\phi_x(t_1,\ t_2)$ is the autocorrelation function for the random part of $f(t)$. We note that the series multiplication is prescribed according to $t_2=t_1+\tau$ and that the rectangle functions are centered on b_N and b_M at t_1 and t_2, respectively. In other words, the correlation must reflect the allowed displacements. But the autocorrelation of a rectangle function can also be expressed in terms of the triangle function. Hence,

$$\sum_N\Pi\left(\frac{t-b_N}{\zeta}\right)\cdot\sum_M\left(\frac{t+\tau-b_M}{\zeta}\right)=\sum_N\Lambda\left(\frac{\tau-b_N}{\zeta}\right) \tag{13}$$

where $\Lambda(\tau)$ is the triangle function. Introducing the replicating function $\text{Ш}(\tau)$, equation (13) can also be written as,

$$\phi_\Pi(\tau)=\sum_N\Lambda\left(\frac{\tau-b_N}{\zeta}\right)=\Lambda\left(\frac{\tau}{\zeta}\right)*\frac{1}{T}\text{Ш}\left(\frac{\tau}{T}\right) \tag{14}$$

where $*$ denotes convolution. Now, according to the Weiner theorem, the spectrum is given by,

$$S(f)=\int_{-\infty}^{\infty}\phi_x(\tau)\cdot\phi_\Pi(\tau)\cos\,2\pi f\tau\,d\tau \tag{15}$$

where we have tacitly assumed a stationary process, so that

$$\phi_x(t_1, t_2) = \phi_x(\tau).$$

Then by the convolution theorem we need to determine,

$$F[\phi_x(\tau)] * F[\phi_\Pi(\tau)]$$

where F signifies the Fourier transform. Let,

$$F[\phi_x(\tau)] = G(f) \tag{16}$$

and again referring to the convolution theorem,

$$F[\phi_\Pi(\tau)] = F\left[\Lambda\left(\frac{\tau}{\zeta}\right) * \frac{1}{T}\text{Ш}\left(\frac{\tau}{T}\right)\right]$$
$$= F\left[\Lambda\left(\frac{\tau}{\zeta}\right)\right] \cdot F\left[\frac{1}{T}\text{Ш}\left(\frac{\tau}{T}\right)\right]. \tag{17}$$

By the similarity theorem,

$$F[\Lambda(\tau/\zeta)] = \zeta \operatorname{sinc}^2 \zeta f \tag{18}$$

and

$$F\left[\frac{1}{T}\text{Ш}(\tau/T)\right] = \text{Ш}(Tf). \tag{19}$$

But

$$\text{Ш}(Tf) = \frac{1}{T}\sum_N \delta(f - N/T). \tag{20}$$

So that

$$S(f) = \frac{\zeta}{T}\sum_N G(f - N/T) \operatorname{sinc}^2 \zeta N/T. \tag{21}$$

So we see that $G(f)$ will be replicated on a set of impulses whose amplitudes are determined by the sinc function. We could isolate $G(f)$ and thereby separate the periodic and random components of the process by multiplying $S(f)$ by an appropriate rectangle function, which will separate the first period from the rest of the periodic train. It is of some interest to just briefly compare (9) and (21). To begin with, the assumption that the process is stationary would remove the sinc function in (9). In the previous section we assumed a continuous random process, whereas here we are concerned with a mixed process that describes the discrete output signals of a linear array due to random noise. Hence, the appearance of the multiplicative autocorrelation function and spectrum as described by (21). Thus, the two expressions [equations (9) and (21)] are, in fact, quite analogous.

Measurements

Given some random function, we can realize the power density spectrum by either analog or digital methods. The method is optional; the results should be equivalent. If we choose, as we have, the analog option, we will obviate the need for autocorrelating and transforming as necessitated by digital methods. That is to say, we will accept the rms voltage output of a wave analyzer (H.P. 3581 A/C) as the essential beginning of the operation to determine the power density spectrum. If we then divide that output by the square root of the analyzer's selected bandpass, we will have

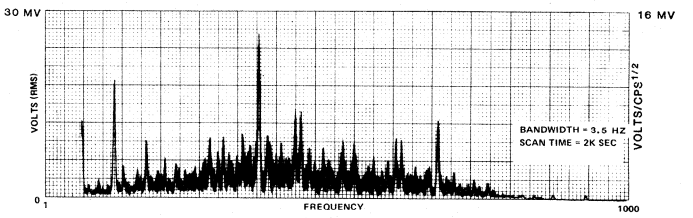

Fig. 2. The rms noise voltage and the corresponding root power spectrum are given as a function of frequency. The bandwidth is the calculated equivalent noise bandwidth. The 2K seconds refers to the sweep time of the analyzer for a record length of 10 seconds.

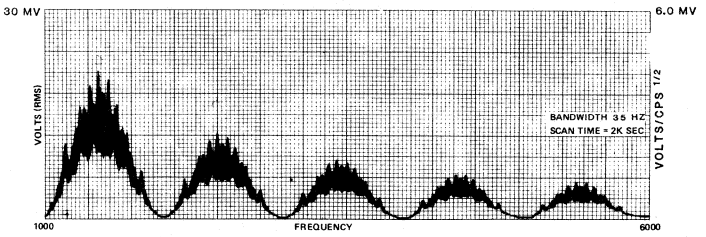

Fig. 3. The replication and the envelope formed by the sinc function for part of the periodic train as predicted by (21).

determined the root power spectrum whose units are $V/Hz^{1/2}$. Since the units of the power density spectrum are V^2/Hz, a further squaring operation is indicated. Here again we have two options. We can either pass the output of the wave analyzer through a squaring circuit and then divide by the bandpass, or simply rescale the ordinate so that we can read directly in terms of power. For most applications the root power spectrum suffices. Consequently, it is the spectrum usually reported in the literature.

With all this in mind, we return to (11) and Fig. 1 and agree to synchronously sample the pulse amplitudes d_{ij}, d_{ik}, $\ldots, d_{in}$, holding each value until the next signal amplitude appears. Clearly, holding $X(t)$ for a period T and multiplying by $\Pi(t)$ results in an equivalent $f(t)$, since $\Pi(t)$ would obliterate $X(t)$ outside the interval ζ. One further point, the particular form of $\Pi(t)$ is of no special consequence since it relates to the periodic component. With this in mind we have found it expedient in our case to collect nominally 10 000 samples of digitized data from a given element in computer memory. The contents of the computer memory are sequentially cycled through a digital-to-analog converter. The resulting analog signal is continuously cycled through a wave analyzer. Alternatively, the analog output of the array could have been passed through a SH circuit which is keyed to the time position of a given detector element and could have gone directly to the wave analyzer [4].

The results as predicted by (21) are shown in Fig. 2 and 3. It is quite clear from the figure that the noise in the LF region is suppressed. This very significant development is attributable to the double sampling signal processing [5] on the detector chip which effectively transforms an inherently nonstationary process to a stationary process. There is also further evidence gained by an independent statistical study which was concerned with the mean and the variance. This study supports the contention that the process is indeed stationary. The spectrum illustrated in Fig. 2 is, of course, the root power spectrum. The main intent of exhibiting Fig.

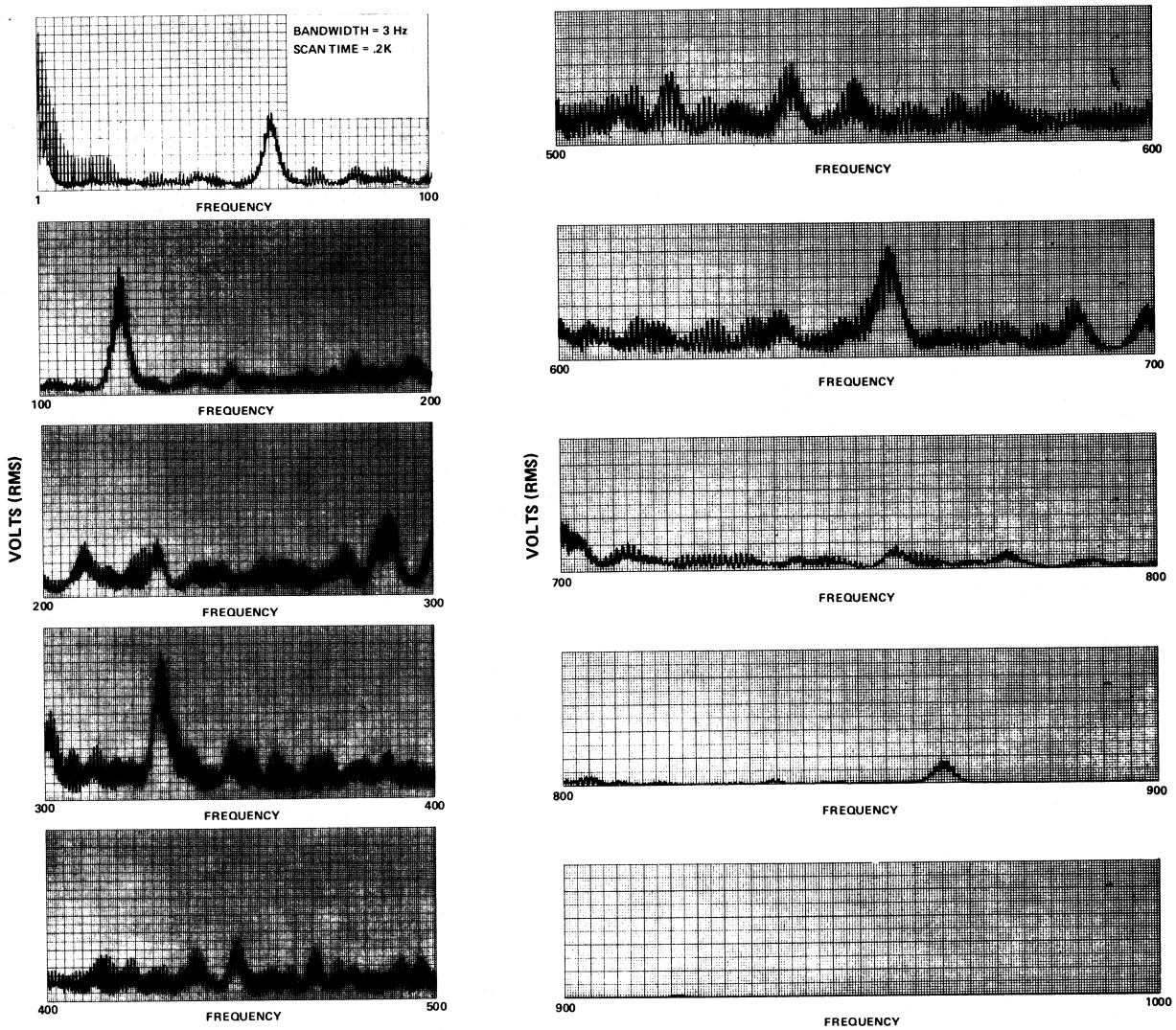

Fig. 4. An expanded view of the noise power spectrum. The extraneous 60 and 120 Hz pickup is clearly evident. Note the analyzer's frequency range begins at 15 Hz.

3 is to show the replication resulting from the periodicity, and the envelope formed by the sinc function. Fig. 4 offers a more detailed presentation of the spectrum for the indicated frequency range. We note the ubiquitous 60 Hz peak as well as some of the higher harmonics.

There are two relatively easy checks we can make to validate our measurements. First of all, it is a simple matter to cycle the analog signal through a true rms voltmeter. Consistently, we have found excellent agreement between the rms voltage readings and statistical determinations of the same quantity. We know, therefore, that the input to the wave analyzer is a proper representation of the original signal. It is also possible to validate the output. We recall that the area enclosed by the power spectrum is equal to the variance. To put it succinctly,

$$\sigma^2 = \int_{0+}^{\infty} G(f)\, df \tag{22}$$

where the notation $0+$ means that the integration begins just past the edge of the dc component. Here again, even a rather elementary numerical integration of the noise power spectrum is in very reasonable agreement with a statistical determination of the variance.

Conclusions

Essentially we have shown that once the output of a monolithic detector array has passed through a sample and hold circuit, determining the noise spectra reduces to the more familiar problem of measuring spectra of an elementary detector. We have also shown that the resultant spectra is multiplicative, and is replicated on a periodic train whose periodicity is determined by the line time.

References

[1] J. S. Bendat and A. G. Piersol, *Measurement and Analysis of Random Data*. New York: Wiley, 1966.
[2] F. Donati, "Finite-time averaged power spectra," *IEEE Trans. Inform. Theory*, vol. 17, pp. 7–16, Jan. 1971.
[3] R. N. Bracewell, *The Fourier Transform and It's Applications*. New York: McGraw-Hill, 1965.
[4] M. W. Finkel, R. J. Sullivan, and L. L. Thompson, "Procedures for the characterization of linear arrays," NASA/Goddard Space Flight Center X-Document, X-942-77-75, Apr. 1977.
[5] M. H. White, D. R. Lampe, F. C. Blaha, and I. A. Mack, "Characterization of surface channel CCD image arrays at low light levels," *IEEE J. Solid-State Circuits*, vol. SC-9, pp. 1–13, Feb. 1974.

Proposed Instrumentation for Analytical Video Stereoscopy of Extended Images

RODERICK R. REAL, MEMBER, IEEE

Abstract—**An approach to real-time photogrammetry is outlined using video techniques in order to combine precision coordinate control of stereo-related images with image enhancement and processing while viewing the stereo model, thereby facilitating photointerpretation in certain applications. One variant replaces the stereo optical paths of an analytical plotter with TV cameras, video signal processing and binocular displays; while a second has video disk inputs of stereo-related imagery.**

REMOTE measurement of large three-dimensional objects such as buildings or the earth's surface is conveniently performed by acquiring stereo-related images for subsequent processing. Advances in precision measurement within the optical models produced by pairs of stereo images have been due to ongoing developments in the field of photogrammetry [1]; known because of map products from aerial photographs and satellites, less well known but of increasing importance in such noncartographic applications as medicine [2], [3].

The technique of indirect measurement of complex objects has attained its highest precision and versatility with sophisticated instrumentation such as the analytical plotter [4], [5], Fig. 1. It affords the following solution in real time for the operator:

$$\text{Photo Coordinates} \begin{vmatrix} X_1 \\ Y_1 \\ X_2 \\ Y_2 \end{vmatrix} = T \begin{vmatrix} X \\ Y \\ Z \end{vmatrix} \text{Model Coordinates} \qquad (1)$$

where T is a transformation containing factors related to perspective, scale, orientation, and corrections for such errors as lens distortion and film shrinkage.

A video form of this instrument, which one may regard as a generalized stereoscope, is proposed for the following reasons.

1) To incorporate some features of electronic image processing on line and in real time with the coordinate control of the analytical plotter. An operator would be assisted in the photointerpretation of such imagery as terrain features or stereo medical X-ray records if he could control such parameters as intensity levels and contrast, intensity gradient enhancement or grey scale rendition by false color techniques. Image and annotation overlays and, at a more advanced level, the possibility of interactive editing of the image are additional possibilities. These operations would proceed under operator control while viewing the stereo model in order to accentuate otherwise overlooked details or patterns of importance. The transformed "enhanced" video images, with possible scale change, rotation or scan shaping could be recorded for future recall.

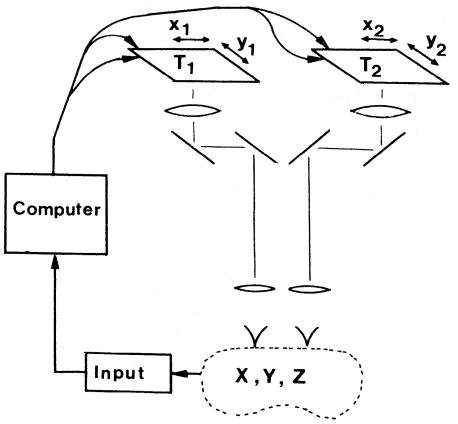

Fig. 1. Analytical plotter; a four axis coordinatograph with binocular optical channels that transduce homologous regions of stereo photographs T_1, T_2 onto the eyes of a human operator or automatic correlator under computer control. X, Y, Z is the perceived stereo model.

2) To develop a potentially lower cost analytical plotter for certain applications; one requiring less precision mechanics and optics where a large proportion of the manufacturing cost now resides.

3) To render certain photogrammetric transformations such as stereo orthophotos [6] into a form suitable for storage on video disk for purposes such as education.

4) Video techniques, in use for transmission of imagery from space, is also on trial as a complementary form of acquiring data of terrestrial features from aircraft [7].

The flexibility inherent in the video format such as image enhancement, scan conversion and, with increased complexity, interactive editing and annotation while viewing the stereo model is offset by the small spatial bandwidth of a single video frame compared to the usual optical field of view and further by the need to scan data already acquired in a high density storage medium such as photographs. Developments in low-cost high-density video storage in the form of the microprocessor-based video disk [8] with digital frame access somewhat compensates for the second disadvantage cited above. A video disk designed to accommodate

Manuscript received February 20, 1978.

The author is with the Photogrammetric Research, Division of Physics, National Research Council of Canada, Ottawa, Ont. K1A 0R6, Canada.

0018-9456/78/0900-0243$00.75 © 1978 IEEE

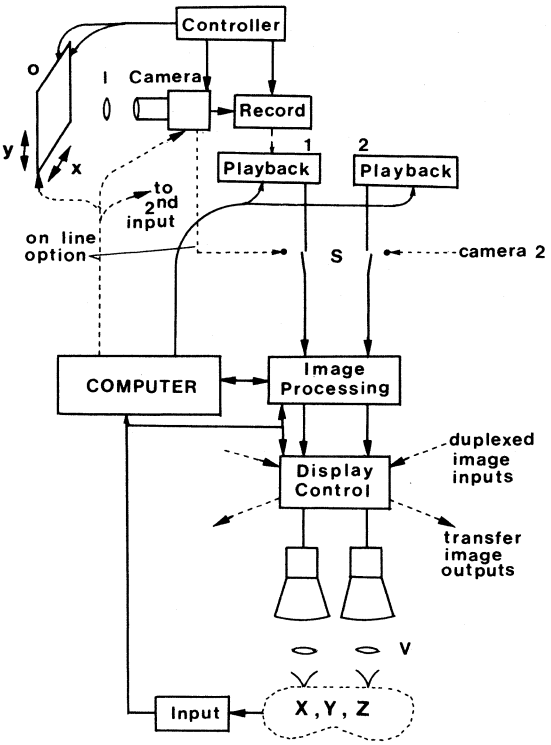

Fig. 2. Elements of the analytical video stereoscope combining features from Figs. 1 and 2. Switch S selects between on-line analysis of 2-D images (dotted connection) or video recordings 1 and 2 of these same stereo related images. O—object image plane, I—input optical image system, V—binocular viewer for the operator who perceives stereo model X, Y, Z.

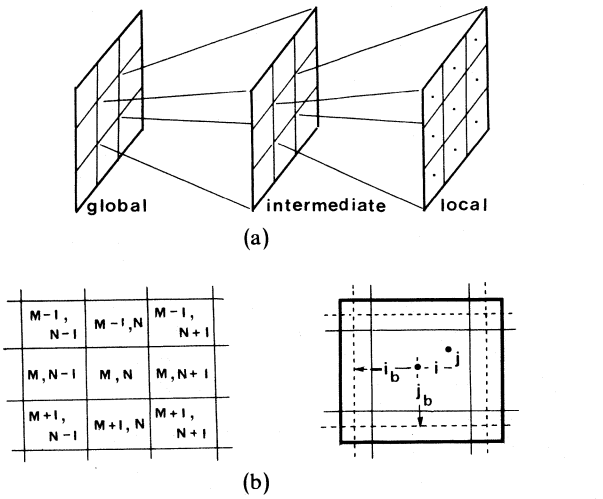

Fig. 3. (a) Image subdivision scheme for video recording of a 2-D image. (b) At left is a portion of the local framing matrix comprised of nonoverlapping TV frames. At right is a practical instance of overlapping redundant recording. A given point is distance i, j from the known center of the frame defined by the limits i_b, j_b set into the processor memory. Passing one of these limits automatically addresses the next frame and offsets it back to this boundary point.

a 30-min color TV program represents a storage capability in excess of 50 000 still frames of TV resolution. Furthermore, this capacity is likely to expand as high-density storage technology advances.

Two forms of videostereoscope incorporating the analytical features of that depicted in Fig. 1 are illustrated in Fig. 2. The analogous configuration replaces the optical train of Fig. 1 with solid-state TV cameras (the elements of which are geometrically precise) and twin-scanned displays viewed with binocular optics. As a variant the photocarriages can be replaced with two stationary tables retaining the stereo photographs while the TV cameras are positioned by coordinate servos over them under the control of the operator and computer. This latter appears to constitute a lower accuracy, less expensive approach to satisfy the growing need for a medical analytical plotter for stereo X-ray evaluation for example. Without much additional cost, some rudimentary image enhancement based upon filtering the video information can be included.

The second variation of Fig. 1 replaces the input photocarriage system with video disk playback units, Fig. 2, the information thereon derived from stereo video records of the original scene, or from scanning stereo photographs of the scene. Extended field high-resolution images must necessarily be subdivided into many TV frames for such recording and playback in a particular organized manner, the degree of subdivision and spatial resolution depending upon the application. As an example, Fig. 3(a) depicts a 23 cm × 23 cm aerial photograph subdivided in stages into a 100 × 100 grid to form final frames of about 2.5 mm square at photographic scale resolved to about 5 μm in a TV frame. Imaging and storing at different scale levels assists an operator in selecting regions of interest, globally, then in detail. The first two levels shown are selected by cursor or keyboard in order to assist pointing to the fine grid address.

Global and intermediate recording can be executed in an approximate imaging and positioning system, but the final large-scale recording must be done by imaging the input photograph accurately onto the solid-state camera by means of a coordinatograph imparting known displacements between frame exposures. A line array solid-state scanner may alternatively be used with continuous relative motion between the line array and the photograph and the video record recompiled to represent contiguous TV frames in the final recording. Assuming 50 percent overlap, one 23 cm × 23 cm black and white or color photograph can be stored on one video disk to a resolution of about 5 μm which, in terms of cost, density, and weight, could in time compare with the means now used to store aerial photographs: emulsion deposited upon glass.

As the coordinatograph and recording camera are relatively displaced by known increments over the photo area in a regular grid, the digitally addressed video disk recording frames are incremented until the recording is complete. After this is done in two stereo-related channels, the photo coordinates are latent in the video disks as

$$x_1, y_1 \rightarrow M_1, N_1; \pm i_1, \pm j_1$$
$$x_2, y_2 \rightarrow M_2, N_2; \pm i_2, \pm j_2 \qquad (2)$$

Photo Coordinates Video Coordinates

where M, N are the centers of stored TV frame number M, N and i, j are local excursions within the frame from those

centers. Subscripts 1 and 2 relate to the use of two video playback units, Fig. 2, one for each of the stereo pair.

Orientation procedure to attain a stereo model is conducted analogously to that of a conventional analytical plotter. For relative orientation usually several well-spaced points common to the overlap area of the stereo pair must be found and their relative position in the photographs entered into the computer to solve the six simultaneous expressions arising because of different camera orientation between successive aerial photographs. Under the control of photogrammetric programs written for orientation and other factors relating to T, expression (1), the computer executes the transformation T in real time in order to satisfy the relationship (1); in short, a form of mathematical projection used to update the photocoordinates with transformations and corrections to ensure the operator has a good stereo view from stereo imagery originally derived from random orientation and perspective in space but constrained to horizontal orientation for analysis, Fig. 1.

As the operator steers through a stereo model by incrementing model coordinates XYZ to the control computer, left and right display images are shifted with respect to the center of the displays which have a mark used as a measuring mark to determine relative height latent in X parallaxes between the left and right images. The amount of local shift within each frame is i,j, Fig. 3(b) (i_1,j_1,i_2,j_2). After a limit in i and/or j is reached, defining a local frame boundary, the next frame $M \pm 1$, $N \pm 1$, is indexed into position and after video blanking, frame centering and offsetting by i,j the viewer is now on the same point but in the next ongoing frame. Using designations in Fig. 3(b) as an example, boundary point M, N; $+i_b$, $-j$ translates to M, $N+1$; $-i_b$, $-j$ where suffix b is a boundary limit. This of course occurs independently in channels 1 and 2, Fig. 2. If random examination of the stereo model is required rather than describing a locus through the model, then the global and intermediate framing, Fig. 3(a), must be readdressed. Except for vertical frame photography, no stereo correlation is done at these smaller scales. In order to present as complete a field as possible as limits in i and j are reached, the recording should be highly redundant to reduce the size of the dotted frame, Fig. 3(b), when sufficient recording capacity exists.

Implementation of this control is possible by the type of circuit in Fig. 4. Coordinate position of the display is digital if a discrete array, or digitally derived analog signal for a cathode ray display. Assuming the latter, the four digital-to-analog (D/A) converters, one each for X and Y in each channel are run by reversible counters containing numbers originating from at least three signals.

1) Center of frame calibration: Each time a new frame is addressed, the video is blanked and a self-centering loop is activated, Fig. 4. Using counters to signal the center of the sweep in X and the central sweep in the Y raster, the video is unblanked to generate a luminous dot on the CRT. The center of each CRT contains a measuring mark comprised of a small four segment photoreceptor, the outputs of which are conducted via fine wires to one side of the CRT and

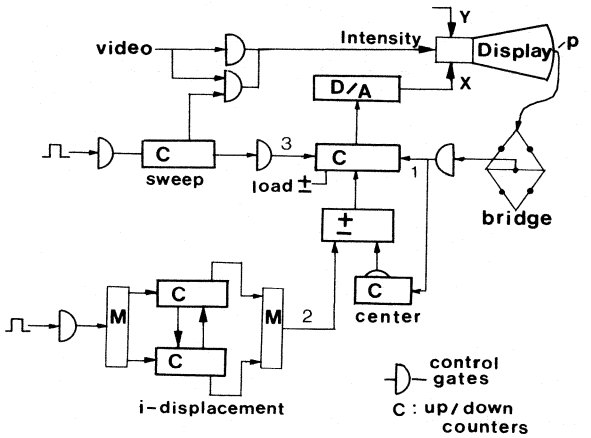

Fig. 4. Elements of display sweep control for the x sweep (y is similar). Numerals 1, 2, 3 correspond to sequences described in the text for automatic frame centering, local displacement and sweep respectively. D/A converter is operated from a counter containing at any time the sum of 1, 2, and 3. The i-displacement (j is the same) unit operates with a multiplexed (M) pair of counters such that when a frame boundary i_b is reached, this number is passed to the second counter while the first is free to receive new displacement data. p—photocell array.

connected into a bridge circuit, Fig. 4. During the self-center mode the bridge, if unbalanced, gates pulses into the centering counters (one each in X and Y) which drives the sweep into a position that balances the bridge, stops further pulse counting, then signals the next phase.

2) i, j offset: This number, entered from the boundary of the previous frame in the correct direction, is added or subtracted in parallel with the centering count in X and Y and the result passed to the D/A control counters. The time required to complete phases 1 and 2 depends upon the bandwidth of the control system and may cause a noticeable but single blink of the display involved.

3) Sweep signal: At this point the video can be unblanked and the sweep signal derived from counters, Fig. 4, incremented at the TV rate and run synchronously for the two recorder units. These are incrementally added to the centering and offset number already in the sweep control counters.

It is possible to compensate for known CRT system nonlinearity by calibrating and adjusting the sweep advance, then programming the compensation into the pulse stream supplying the sweep counters. This type of problem is not encountered when digitally addressed discrete imaging and display components are employed.

Maps, orthophotos, and annotated orthophotos or orthophoto maps may be recorded in color at various scales onto video disks with any degree of enhancement or exaggeration for playback on domestic TV sets; a possible educational application, (i.e., a video atlas). A cross index supplied with the disk enables any frame or frame sequence to be identified and addressed. Since the recorder may be programmed to operate in several modes, special effects are possible in which time-lapse sequences or moving picture sequences are interspersed with still frames.

A full stereo model video atlas display requires either two playback units, one with the orthophoto, one with the stereomate operated synchronously, or a single disk with the

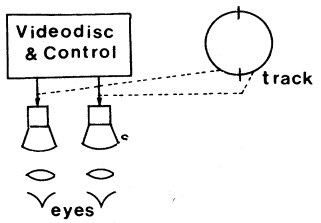

Fig. 5. Arrangement for stereo display from single video disk recording where each frame occupies one track that is time shared between the two stereo related video images.

information recorded as shown in Fig. 5. Assuming one complete track per frame, the orthophoto and stereomate each have half of the track, resulting in the reduction of Y resolution by half. The playback of course requires synchronous switching between two displays as shown, although a single-polarized display with synchronously switched PLZT goggles [9] is possible. The terrain coverage stored upon one disk depends upon the scale and detail required. To view other areas requires either changing the disk or, if access is to be rapid, having a multi-disk storage and control system.

In conclusion, the seeming incongruity in considering a video counterpart for a precision optically based instrument such as the analytical plotter is to achieve some real-time control of certain subjective image parameters for better photointerpretation while viewing the stereo model, to develop a lower cost instrument for certain applications and for deriving special recorded 3-D video displays such as a video atlas for educational purposes.

References

[1] M. M. Thompson, Ed., *Manual of Photogrammetry*. New York: American Society of Photogrammetry, 1966.
[2] V. Kratky, "Photogrammetry in scoliosis," *Photogrammetria*, vol. 31, pp. 195–210, 1975.
[3] V. Kratky, "Digital modeling of limbs in orthopedics," *Photogrammetric Eng. Remote Sensing*, vol. 41, pp. 741–752, 1975.
[4] Z. Jaksic, "Man–machine photogrammetric systems and system components," *Can. Surveyor*, vol. 27, pp. 308–319, 1973.
[5] R. R. Real and K. K. Lau, "Control system for the analytical processing of stereo images," *Rev. Sci. Instrum.*, vol. 48, pp. 1021–1027, 1977.
[6] T. J. Blachut and M. C. Van Wijk, "3-D information from orthophotos," *Photogrammetric Eng.*, vol. 36, pp. 365–374, 1970.
[7] ——, "Air Force TV camera has 140 degree view," *Optical Spectra*, vol. 11, p. 25, Oct. 1977.
[8] M. Yuhas, "Waiting for the disc," *Ind. Photogr.*, vol. 24, pp. 26–30, 1975.
[9] ——, "Distortion free 3-D viewing method developed," *Electro-Optical Systems Design*, vol. 7, p. 8, Oct. 1975.

Multiple-Beam Interferometry

G. MARSHALL MOLEN, MEMBER, IEEE

Abstract—**An optical interferometer is described in which spatial and temporal resolution of the plasma density are achieved simultaneously, thus circumventing a limitation of conventional interferometers. The instrument consists of a Twyman–Green interferometer illuminated by a CW He–Ne laser. The technique has proven to be particularly applicable to plasma events that lack reproducibility. An additional advantage is that the interferometer is easily adapted to real-time displays of the plasma density profile utilizing an automated process.**

Introduction

OPTICAL interferometry is routinely used for measuring changes in the optical path length of a medium. One such application is particle density diagnostics in gaseous plasmas using a dispersion function to relate the index of refraction of the plasma to the density of the various particle species. A novel interferometric technique has been developed that enhances the flexibility of the interferometer for these applications by providing simultaneous spatial and temporal resolution.

Conventional techniques, such as Mach–Zehnder and holographic interferometry [1], [2], are often used where spatial resolution is required. The methods are generally limited to a single interferogram taken at one instance during the event. Because of the rather limited reproducibility of many experiments, it is often desired to record the complete temporal evolution of the density profile during a single event. One approach is to use variable optical delays of portions of a single laser pulse to record several successive interferograms; however, this method is quite limited in the total delay time that can be obtained, as well as the number of exposures due to experimental limitations. Two notable exceptions are holographic cine-interferometry [3] and streak interferometry [4] where the fringes are recorded by

Manuscript received February 20, 1978. This work was supported by the Air Force Office of Scientific Research.

The author was with the Plasma Laboratory, Department of Electrical Engineering, Texas Tech University, Lubbock, TX. He is now with Old Dominion University, Norfolk, VA 23508.

0018-9456/78/0900-0246$00.75

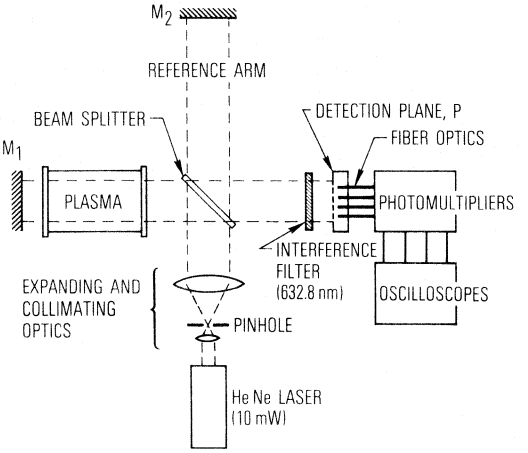

Fig. 1. Experimental arrangement for multiple-beam interferometer.

an image converter camera. The number of interferograms with the former method is generally limited to 3–5 by the camera while the latter is experimentally complex and fringe interpretation is often difficult.

At the other extreme, the much simpler coupled cavity interferometer is useful to record the temporal response of plasma events but at the sacrifice of spatial resolution [5]. The technique requires a separate laser and associated instrumentation for each spatial position. The interferometer described here incorporates the features of both types such that a continuous display of the fringe shifts is recorded at multiple positions using a single diagnostic laser.

Description of Interferometer

The experimental technique is described in Fig. 1 for a plasma vessel inserted in the diagnostic arm of the interferometer. The arrangement resembles a Twyman–Green interferometer in which the laser beam completes a double pass through the plasma before interferring with the reference beam. For applications to plasmas with azimuthal symmetry, the interferometer is aligned parallel to the axis of the plasma tube to measure the particle density integrated over the path lengths simultaneously for various radial positions. Other geometric configurations may require inversion techniques to unfold the plasma density.

The expanded collimated beam from a CW He–Ne laser operating at 632.8 nm is reflected into the plasma column by a beam splitter; a total reflector external to the plasma vessel reflects the beam back again through the plasma. The two arms of the interferometer are chosen to be approximately equal in length. Finite fringes corresponding to particular radial positions in the axisymmetric plasma occur at the detection plane P, because of the interference of the reference and diagnostic beams, and their movement is detected by fiber-optic light pipes which are strategically positioned. The plasma light is reduced to an acceptable level by an interference filter positioned in front of plane P so that the fringe modulation on each channel may be detected by photomultiplier tubes. Obviously, the number of channels is dictated by the required spatial resolution.

Templates are attached to each end of the plasma tube during the initial alignment procedure to facilitate the accurate identification of the radial position of each channel at the plane P. Once aligned, the static fringe spacing is chosen to be greater than the entrance apertures of the light pipes (e.g., 0.5 mm) by slightly tilting mirror M_2 in the reference arm of the interferometer. For this configuration, the frequency response is limited by the photomultiplier tubes and associated electronics.

The fringe shifts are interpreted by assuming that the plasma has reached a significant stage of ionization so that the refractive effects are primarily due to the free electrons. From the plasma dispersion relation for a collisionless plasma, the optical index of refraction is given by

$$\mu = [1 - \omega_p^2/\omega^2]^{1/2} \tag{1}$$

where ω_p is the electron plasma frequency and ω is the frequency of the electromagnetic wave with wavelength λ_0. As the laser light traverses the plasma region twice before interferring with the reference beam, the fringes will go through one cycle of modulation, or exhibit one fringe shift, each time the optical length $\int \mu\, dl$ changes by $\lambda_0/2$. Thus the effective length change due to the plasma in units of fringes $\chi(t)$ is

$$\chi(t) = \int_0^L \left[\frac{2(\mu - 1)}{\lambda_0}\right] dl = \frac{\lambda_0 r_e}{\pi} \int_0^L n_e(t)\, dl \tag{2}$$

where r_e is the classical electron radius, L is the length of the plasma, and $n_e(t)$ is the time dependent electron density. For $\lambda_0 = 632.8$ nm, a shift of one fringe corresponds to $\int n_e\, dl = 1.76 \times 10^{17}$ cm^{-2}.

Example of Application

The interferometer was used to measure the time dependent electron density profile of an axisymmetric plasma column where more conventional techniques had failed because of poor shot-to-shot reproducibility. The plasma was produced by a linear discharge in 1.3 Torr of hydrogen between two ring electrodes spaced 35 cm apart so as to give an initial density dip on axis. Radial losses to the walls of the 5 cm inside diameter (ID) tube were inhibited by a 0.33 T magnetic field. The discharge had a quarter-period of 6 μs and a corresponding peak current of 26 kA after which it was critically damped by a nonlinear resistor. Plasma temperatures of 2 eV were measured using line-to-continuum measurements of H_γ; Stark broadening of the line confirmed the magnitude of the density measured with the interferometer [6].

Fringe shifts were detected along a diameter of the tube, as shown in Fig. 2, at radial positions of 0, 5, 11, and 16 mm from the axis. Azimuthal symmetry was ascertained by comparisons with other locations at the same radii. The sensitivity is obtained from (2) assuming axisymmetric symmetry such that $\int n_e\, dl \approx n_e L$, where $L = 35$ cm; each fringe is calculated to correspond to a density of 5.03×10^{15} cm^{-3}. Axial density variations or small extensions of the plasma past the annular electrodes may introduce a slight error.

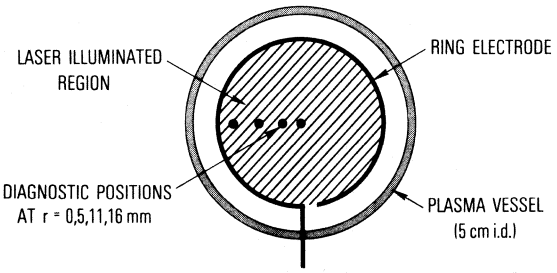

Fig. 2. End-on view of plasma vessel and laser illuminated region.

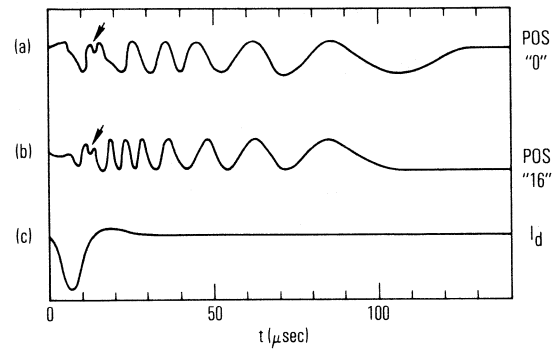

Fig. 3. Temporal fringe shifts at radial positions of (a) 0 mm and (b) 16 mm compared with (c) plasma discharge current I_d. Arrows denote fringe inflection.

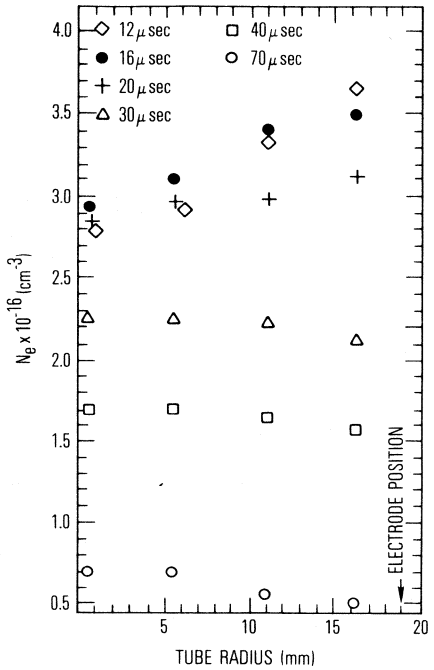

Fig. 4. Radial electron density profiles of the plasma column.

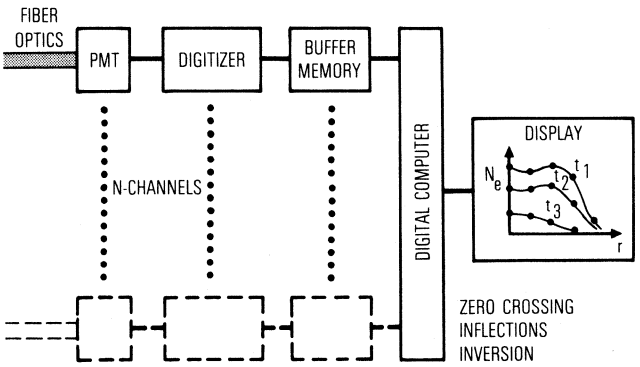

Fig. 5. Computer implemented interferometer.

Interference fringes are shown in Fig. 3 for two of the four channels (0 and 16 mm); the waveform of the plasma discharge current is also included to establish the time scale. A single inflection in the fringe shifts, as designated by the arrows in the figure, occurs immediately after the peak current corresponding to the transition from monotonically increasing to monotonically decreasing density. Because of difficulty in counting fringes during the formative stages of the plasma, each trace was analyzed by counting backward from $t = \infty$ to the inflection. The loss of the fringes at early times most likely results from angular deviations of the beam by refractive gradients in the plasma as well as bandwidth limitations of the electronics.

Radial electron density profiles are shown in Fig. 4 at several instances after the peak current for the fringes presented in Fig. 3 together with similar data at radial positions of 5 and 11 mm. The time delays are referenced to the initiation of the discharge current. As shown in the figure, a density minimum occurs on axis for early times in the life of the plasma because of the ring electrodes. The experimental accuracy is estimated by assuming that the fringes can be interpreted within 0.2 of a fringe shift. For this experiment, the uncertainty corresponds to a density of $\pm 1.0 \times 10^{15}$ cm^{-3} which is only 2.7 percent of the peak electron density.

Computer Implemented Interferometer

It is apparent from Fig. 3 that data reduction at successive time intervals for multiple channels can be exacting and tedious. These difficulties were alleviated by digitizing the oscilloscope data with an optical scanner interfaced with a minicomputer. A simple computer routine identified the zero crossings of the fringe shifts and calculated the position of the density inflections by identifying where the first and second derivatives were zero. A summation of the accumulated fringe shifts counted backward from $t = \infty$ to the desired moment, yielded the time dependent profile which was displayed on a plotter.

The interferometric technique is amendable to further automation using the scheme described in Fig. 5 so as to render essentially real-time displays of the plasma density profile. The electrical signals from the n-photodetectors are digitized by suitable A/D converters and subsequently stored in buffer memories thus avoiding photographic storage. The data processing technique is similar to that previously described except that additional computer routines may be introduced. One example would be the inclu-

sion of an Abel inversion routine to unfold the radial density profile for edge-on illumination of a plasma with cylindrical symmetry.

Acknowledgment

The author would like to acknowledge many valuable discussions with Prof. M. Kristiansen during the inception of this project. A note of appreciation is also extended to H. C. Kirbie for his assistance in assembling the interferometer.

References

[1] F. C. Jahoda, E. M. Little, W. E. Quinn, R. L. Ribe, and G. A. Sawyer, *J. Appl. Phys.*, vol. 35, p. 2351, 1964.
[2] F. C. Jahoda, R. A. Jeffries, and G. A. Sawyer, *Appl. Opt.*, vol. 6, p. 1407, 1967.
[3] F. C. Jahoda, *Appl. Phys. Lett.*, vol. 14, p. 341, 1969.
[4] G. M. Molen, H. C. Kirbie, and M. J. Bernstein, *Bull. Amer. Phys. Soc.*, vol. 19, p. 945, 1974.
[5] J. B. Gerardo and J. T. Verdeyen, *Proc. IEEE*, vol. 52, p. 690, 1964.
[6] G. M. Molen, M. Kristiansen, M. O. Hagler, and R. D. Bengtson, *Appl. Phys. Lett*, vol. 24, p. 583, 1974.

A Frequency-Lock System for Improved Quartz Crystal Oscillator Performance

FRED L. WALLS AND SAMUEL R. STEIN

Abstract—**The intrinsic noise of the best quartz crystal resonators is significantly less than the noise observed in oscillators employing these resonators. Several problem areas common to traditional designs are pointed out and a new approach is suggested for their solution. Two circuits are described which frequency lock a spectrally pure quartz crystal oscillator to an independent quartz crystal resonator. The performance of the composite system is predicted based on the measured performance of its components.**

Introduction

IN RECENT YEARS, tremendous advances have been made in the manufacture of ultrastable quartz resonators. Moreover, it is quite likely that further improvements in this area will be made within the next two years. Especially promising are the SC cut, TTC cut, and the various electrodeless AT and SC cut resonators [1]–[4]. The purpose of this paper is to point out some problems in the electronics design of traditional quartz-crystal oscillators and to introduce some new circuit concepts which will significantly reduce these problems.

Problem Areas

The traditional circuitry for a crystal-controlled oscillator uses the resonator inside of the oscillating loop as shown schematically in Fig. 1. A necessary condition for oscillation

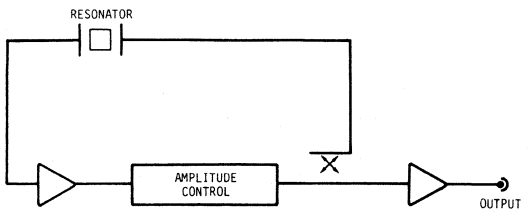

Fig. 1. Traditional quartz-crystal-controlled oscillator.

is that the phase shift around the loop be a multiple of 2π rad. A small phase fluctuation ϕ away from this state causes a fractional frequency change

$$y = \Delta\nu/\nu = \phi/2Q$$

where Q is the loaded quality factor of the resonator. In order to achieve a long-term fractional frequency stability of 10^{-13} with a resonator having a loaded Q of 2.5×10^6, the phase variations must be less than 5×10^{-7} rad. For standard coaxial cable with phase stability of approximately 100 ppm/°C, this corresponds to a temperature change of 1°C over a 5 cm length. Since nearly all components are phase sensitive, it is doubtful that the required stability around the oscillating loop can be achieved for extended periods of time.

The phase shift around the loop is also perturbed by output loading and pickup of stray signals. For example, a 20-percent change in the load resistance from the matched condition produces a reflected signal back into the oscillator

Manuscript received February 9, 1978.
The authors are with the Time and Frequency Division, National Bureau of Standards, Boulder, CO 80302.

output whose amplitude is 10 percent of the output voltage. The reflection changes the phase in the oscillating loop by an amount

$$\phi = (1/10)\beta \cos \theta$$

where β is the isolation from the output to the oscillating loop expressed as a voltage ratio and θ is the phase of the reflected signal relative to the unperturbed loop signal. In order to assure that $|\phi|$ is less than 5×10^{-7} rad for arbitrary θ, β must be less than 5×10^{-6} or -106 dB.

At the present time, crystal-controlled oscillators designed for good long term stability use either fifth overtone AT cut or FC cut resonators driven at approximately 0.1 to 1 μW of crystal dissipation [4], [5]. The relatively low power dissipation is used in order to avoid excessively large frequency shifts. This effect, due to nonlinear interactions within the crystal, is commonly called the amplitude to frequency effect (AF), and is typically of the order $\Delta v/v = 10^{-9}/\mu$W of crystal dissipation for 5-MHz fifth overtone AT cut crystals. Therefore, it is necessary to control the crystal dissipation to 10^{-4} μW in order to achieve stabilities of 10^{-13}. This required power stability then dictates a crystal dissipation of order 0.1 to 1 μW. The relatively low value of crystal dissipation required to achieve the good long term stability limits the signal-to-noise ratio or spectral purity to a relatively poor value compared to a hard-driven oscillator. However, the AF effect is reported to be about 100 times smaller in the new doubly rotated cuts like the SC, TTC, and electrodeless SC cut resonators [2], [3], and [6].

Finally, the frequency of the oscillator is usually adjusted with a tuning capacitance of approximately 25 pF for a 5 MHz unit. If the crystal has a Q of 2.5×10^6 and a motional resistance, $R_s = 70\ \Omega$, then the fractional frequency change due to a small change in the tuning capacitor C_L is

$$y = \frac{1}{2}\left(\frac{1}{\omega RQ}\right)\left(\frac{1}{C_L}\right)\frac{\Delta C_L}{C_L} \cong 4 \times 10^{-6}\,\frac{\Delta C_L}{C_L}$$

which can be derived from considering the *LCR* equivalent circuit of a quartz crystal. Thus in order to achieve a long-term stability of 10^{-13} the tuning capacitor must be constant to 6×10^{-7} pF, which is very difficult at best.

Possible Solutions

It is possible to attack all of these problems with a single circuit which uses the crystal in a frequency discriminator configuration instead of within an oscillating loop. Two possible realizations will be suggested which share the following principles: A crystal is operated at the optimum power dissipation for long-term stability while the required short-term stability is achieved with a second oscillator; the effect of the load capacitor is decreased an order of magnitude by increasing its value a factor of 10; load effects are minimized by using very-low-noise high-isolation buffer amplifiers; the effect of phase variations on the critical circuitry is reduced by using frequency or phase modulation in conjunction with a frequency-lock loop. The principles of operation are similar to the superconducting cavity-stabilized oscillator which is described in detail in the literature [7], [8].

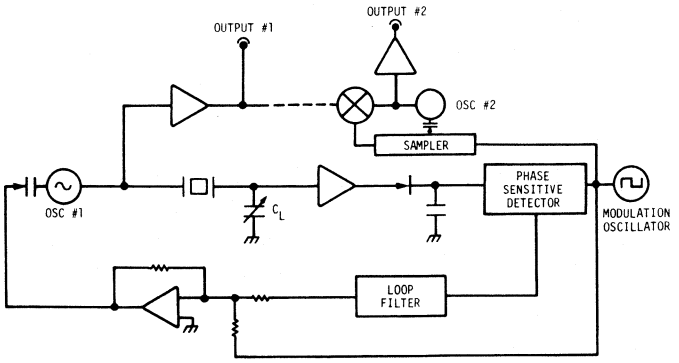

Fig. 2. Square-wave frequency-modulation system for locking a quartz-crystal oscillator with high spectral purity to a passive quartz resonator.

The first circuit is shown in Fig. 2. The quartz crystal is interrogated with a square-wave frequency modulated signal from oscillator 1. Transmission through the resonator converts the frequency modulation to amplitude modulation if the average signal frequency differs from the resonant frequency. A diode is used to detect the modulation envelope whose phase depends upon whether the average signal frequency is above or below the resonance. Thus a phase sensitive detector can be used to generate a feedback signal which will frequency-lock oscillator 1 to the quartz crystal.

The power dissipated in the quartz crystal should be set to approximately 10^{-7} W because of the amplitude to frequency effect. Since the crystal has a bandwidth of about 2 Hz, the spectral purity for Fourier frequencies above 1 Hz (the approximate cutoff frequency of the servo scheme) is determined by the performance of oscillator 1. The tuning capacitor C_L is increased an order of magnitude to 250 pF in order to reduce the sensitivity to the load capacitance and to swamp the stray capacitances which contribute to the total load capacitance. However, this implies that the resonator must be manufactured to closer tolerances than for traditional designs. The total electrical length of the transmission line connecting oscillator 1 to the diode demodulator via the crystal does not directly affect the frequency at which the system locks. However, dispersion in the transmission line does cause the lock frequency to deviate from the crystal resonance. Since the modulation frequency and its deviation is limited to about 1 Hz by the crystal Q, dispersive effects are smaller by a factor of 2×10^{-7} compared to the phase-stability problem of the traditional design. Finally, buffer amplifiers with isolation in excess of 120 dB and white phase noise floors $S_\phi < -170$ dB are easily constructed thereby reducing to insignificance the problem of coupling spurious signals into the resonator [9].

There are two major disadvantages to the circuit of Fig. 2. First, since the frequency of the modulation must be small compared to 2 Hz, the attack time of the feedback loop needs to be longer than about 0.16 s. This means that the stability of oscillator 1 may be worse than the passive crystal before the attack time is reached. Second, the direct output of the circuit has phase excursions of about 1 rad. Consequently, to

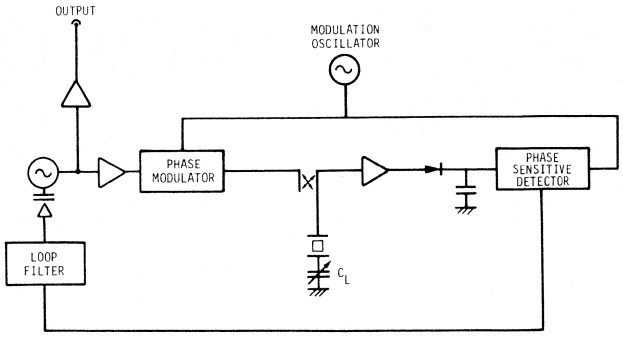

Fig. 3. Phase modulation system for locking an oscillator to a passive quartz resonator.

asynchronously realize a frequency stability of 10^{-13} it is necessary to average for 3×10^5 s or about 3 days. The latter problem may be overcome by phase-locking a oscillator 2 to oscillator 1 with a synchronous PLL. The loop filter for the PLL must average the phase difference between oscillators 1 and 2 over complete cycles of the modulation frequency in order to cancel most of the unwanted phase modulation.

This system appears to be quite complex and costly. A simpler system can be implemented which is based upon the same general principles, but which overcomes the two deficiencies just described. The simplified block diagram is shown in Fig. 3. Once again, the crystal dissipates about 10^{-7} W, C_L is approximately 250 pF and extensive use is made of low-noise isolation amplifiers. One major difference from the previous circuit is that the required modulation is accomplished by phase modulating the oscillator output rather than frequency modulating the oscillator itself. Consequently, a system output can be provided which is uncontaminated by the internal modulation frequency. The second significant difference is that the diode detector produces the modulation envelope of the signal which is reflected from the resonator rather than the signal transmitted through it. Thus the modulation frequency can greatly exceed the crystal bandwidth. The signal generated by this technique is proportional to the imaginary part of the reflection coefficient of the resonator which is, itself, linearly proportional to the frequency deviation from the center of the resonance. The heuristic explanation of this behavior is that the carrier reflects from the resonance but the sidebands are so far removed from the center that they effectively reflect from a short circuit (more detail is given in [7]). The advantage of the high modulation frequency which is possible in this system (for example, 200 Hz) is that the attack time of the frequency lock loop can be decreased by a factor of 200 compared to the case of the circuit in Fig. 2. This would make it possible to use one inexpensive component oscillator rather than the two high-quality oscillators needed in the previous example.

Expected Performance

The performance expected from the system suggested in Fig. 3 can be estimated from the measurements on the various components. Curve A of Fig. 4 shows the measured

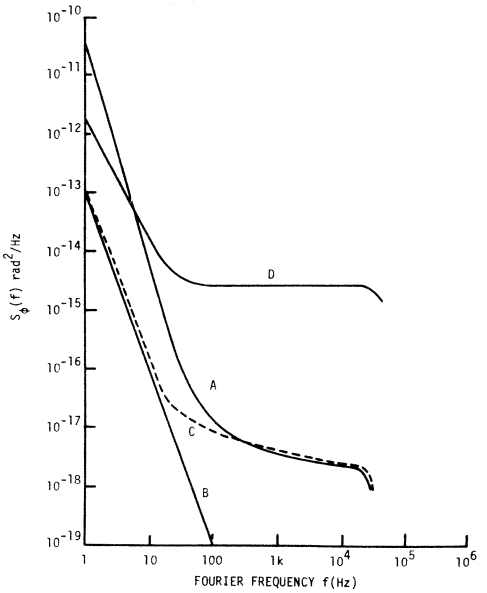

Fig. 4. Spectral density of phase noise for (A) a commercial high power 5 MHz oscillator, (B) a quartz crystal resonator measured passively, (C) the proposed system for locking A to B with 100 Hz unity gain frequency, and (D) a commercial low-power quartz-crystal oscillator.

spectral density of phase fluctuations $S_\phi(f)$ for a commercially available high power 5-MHz oscillator that would be suitable for the local oscillator. Note that its phase noise rises very rapidly close to the carrier, due primarily to the high drive level.

The frequency stability of commercial high-quality AT-cut quartz resonators has been measured using a passive phase bridge technique which has been previously discussed [10]. By evaluating three or more resonators in various pairs one can independently determine the stability of each resonator. Curve B of Fig. 4 shows the equivalent $S_\phi(f)$ for the best two of the four samples tested.

The use of a frequency-lock loop with a second-order loop filter (see, for example, [11]) should make it possible to achieve a system output with the phase noise shown in curve C of Fig. 4.

For comparison, the spectral density of phase for a commercial high quality, low-power 5-MHz quartz controlled oscillator is shown in curve D of Fig. 4. Note that the curve C, the system output, is significantly superior to curve D at all Fourier frequencies.

The corresponding time domain stabilities can be calculated from Fig. 4, and, assuming that the contribution to the phase noise from spurious pickup is insignificant, are given in Fig. 5. Again, note that the system output, curve C, is projected to yield excellent short term stability and long term stability. The frequency stability of such a system should exceed that of all available commercial standards for measurement times below 1000 s.

The frequency stability beyond 1000 s cannot be estimated from present measurements on the crystal resonators. However, from the above analysis we expect that the frequency stability of such a system should be superior to any present crystal-controlled oscillator, and further, that as

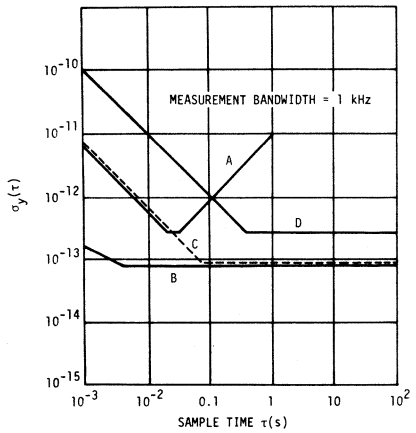

Fig. 5. The computed two-sample deviations corresponding to curves A, B, C, D of Fig. 4.

new quartz resonator types become available frequency drift and other long term frequency changes can be kept below 10^{-12}/week. The new crystal resonators are likely to exhibit much better turn-off turn-on retrace, lower hysteresis due to temperature cycling, and much lower acceleration sensitivity [2], [3].

References

[1] E. P. EerNisse, "Calculations on the stress compensated (SC cut) quartz resonator," in *Proc. 30th Annu. Symp. Frequency Control*, pp. 8–11, 1976. (Available from Electronics Industries Assoc., 2001 Eye St., NW, Washington, DC 20006.)

[2] J. A. Kusters, C. A. Adams, and H. Yosida, "TTC's-further developmental results," in *Proc. 31st Annu. Symp. Frequency Control*, pp. 3–7, 1977. (Available from Electronics Industries Assoc., 2001 Eye St., NW, Washington, DC 20006.)

[3] R. Besson, "A new electrodeless resonator design," *Proc. 31st Annu. Symp. Frequency Control*, pp. 147–152, 1977. (Available from Electronics Industries Assoc., 2001 Eye St., NW, Washington, DC 20006.)

[4] J. J. Gagnepain and F. L. Walls, "Fundamental properties of quartz crystal controlled oscillators," to be published.

[5] L. S. Cutler, "A frequency standard of exceptional spectral purity and long term stability," *Frequency*, vol. 1, pp. 20–27, 1962.

[6] J. J. Gagnepain, J. C. Poncot, and C. Pegeot, "Amplitude-frequency behavior of doubly rotated quartz resonators," in *Proc. 31st Annu. Symp. Frequency Control*, pp. 17–22, 1977. (Available from Electronics Industries Assoc., 2001 Eye St., NW, Washington, DC 20006.)

[7] S. R. Stein and J. P. Turneaure, "The development of the superconducting cavity stabilized oscillator," in *Proc. 27th Annu. Symp. Frequency Control*, pp. 414–420, 1973. (Available from the National Technical Information Service, Sells Building, 5285 Port Royal Road, Springfield, VA 22161.)

[8] S. R. Stein, "The superconducting-cavity stabilized oscillator and an experiment to detect time variation of the fundamental constants," Ph.D. dissertation, Stanford Univ., 1974. (Available from University Microfilms, 300 North Zeeb Road, Ann Arbor, Michigan 48106.)

[9] F. L. Walls, S. R. Stein, J. E. Gray, and D. J. Glaze, "Design considerations in state-of-the-art signal processing and phase noise measurement systems," in *Proc. 30th Annu. Symp. Frequency Control*, pp. 269–274, 1976. (Available from Electronics Industries Assoc., 2001 Eye St., NW, Washington, DC 20006.)

[10] F. L. Walls and A. E. Wainwright, "Measurement of the short-term stability of quartz crystal resonators and the implication for crystal oscillator design and applications," *IEEE Trans. Instrum. Meas.*, vol. IM-24, pp. 15–20, 1975.

[11] F. L. Walls and S. R. Stein, "Servo techniques in oscillators and measurement systems," NBS Tech. Note 692. (Available from Superintendent of Documents, U.S. Government Printing Office, Washington, DC 20402, SD Cat. No. C13.46:692.)

An Error Analysis for the Measurement of Satellite EIRP Using a Calibrated Radio Star

WILLIAM C. DAYWITT

Abstract—**An outline for the derivation of equations employed in a measurement and error analysis of satellite EIRP using a calibrated radio star is presented. A table showing analysis results at 7.55 GHz using Cassiopeia A for a satellite at 12° elevation angle is given. The quadrature sum of the systematic errors appearing in the table is 10.1 percent. Also presented is a curve of the systematic errors as a function of elevation angle showing a 7.3-percent minimum at high elevation angles.**

I. Introduction

THE NATIONAL Bureau of Standards has constructed a system designed to measure satellite EIRP using a calibrated radio star. The system operates off the IF patch panel of the downlink earth terminal (ET), and automatically controls the several measurement sequences.

The method employed in the earth-terminal measurement system (ETMS) is a modified version of the radio-star method [1] of measuring satellite EIRP (effective isotropic radiated power), the modification [2] allowing ET receiver gain fluctuations to be removed from the measurement and significantly reducing measurement error.

In addition to a digital voltmeter and accurately calibrated IF attenuators, the ETMS features a very accurate power bridge [3], and an improved solid-state noise source [4] of high stability. Combined, the components can routinely measure power ratios to a few hundredths of a decibel. The ETMS also incorporates well calibrated IF bandpass filters whose characteristics are combined with the observed ET passband characteristics by the computer software in the ETMS to obtain the overall noise bandwidth needed for the calculation of EIRP.

A measurement and error analysis for the 1–10-GHz frequency range to be reviewed in this paper is incorporated in the ETMS computer software. The analysis reveals additional errors and a higher atmospheric correction than previously calculated.

The relationship of the ETMS to the ET receiving system is shown in Fig. 1. The receiving system is represented by the ET antenna, cross-guide coupler, low-noise amplifier (LNA), downconverter, and IF patch panel. The ETMS consists of the solid-state noise source, and the power measurement and control console. The noise source is connected to the receiving system through the cross-guide coupler, and T_a is the noise temperature representing the noise power added to the system at the LNA when the noise source is turned on. The gain of the system from the antenna far field to the LNA is represented by G, and is the product of the antenna gain and the waveguide loss from the antenna to the LNA.

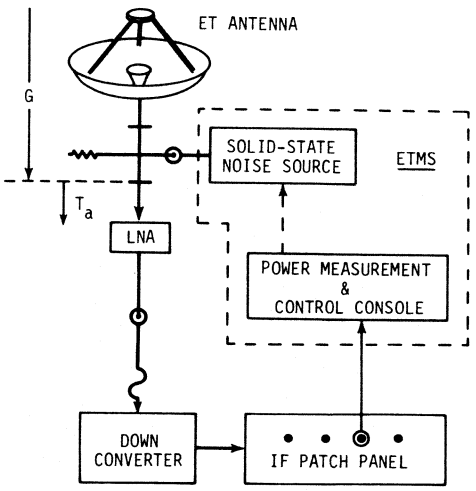

Fig. 1. Interface between the ETMS and the earth-terminal receiving system.

The noise source serves a double purpose in the EIRP measurement. The first is to eliminate gain fluctuations [2] from the LNA input to the power detector in the ETMS. This is accomplished by performing all power measurements in pairs, one measurement with the noise source turned off, followed immediately by the same measurement with the noise source turned on. The noise-source-off measurement is then normalized by the difference between the two measurements, thus eliminating the system gain (and consequently the possibility of gain fluctuations) between the LNA and the ETMS power detector from the power ratio. Besides the immediate benefit of removing these short-term gain fluctuations, measurements may now be compared accurately on a day-to-day basis. The second purpose is to provide a calibratable source of power by which the magnitude of the received satellite signal power can be measured. The calibration of this noise power is accomplished in the first step of the EIRP measurement by comparing the reduced noise temperature (T_a/G) of the noise source against the power from a calibrated radio star.

The EIRP measurement method employed by the ETMS involves two steps: 1) a radio-star calibration of the reduced

Manuscript received December 2, 1977. This work was supported in part by the U.S. Army Communications Command, Fort Huachuca, AZ.

The author is with the U.S. Department of Commerce, National Bureau of Standards, Boulder, CO 80302.

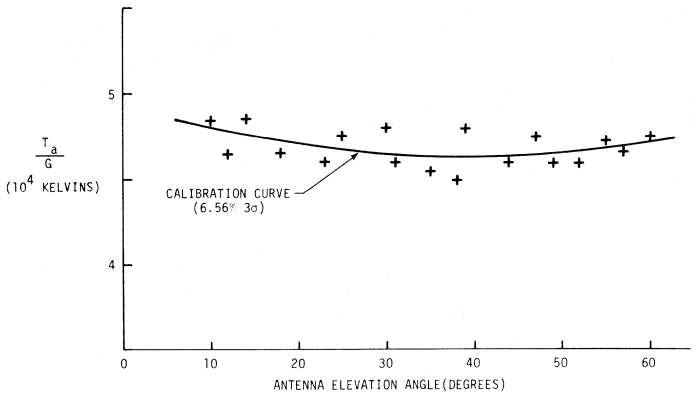

Fig. 2. T_a/G ET calibration curve.

noise temperature (T_a/G) of the solid-state noise source as a function of ET antenna elevation angle, and 2) the measurement of the available powers at the LNA input received from the satellite. The first step is performed by measuring the IF power from the ET receiving system as the radio star drifts through the mainbeam of the antenna. These measurements are performed at various elevation angles as the star traverses its path across the sky, and yield a set of T_a/G data points as depicted in Fig. 2. The least squares curve fit to these data points represents a calibration curve for the "front end" of the receiving system, and the solid-state noise source. The 6.5-percent value appearing in the figure represents random scatter (3σ) of the data points. The curve remains valid as long as T_a and G remain constant in time. Measurements performed on the noise source [4] show it to be stable to within ± 0.01 dB (1σ) over at least the time required to complete a set of EIRP measurements for a number of frequencies. The gain G is assumed to remain constant for this same period, an assumption that appears to be born out by experience. Once the calibration curve is established, the value of T_a/G for any satellite elevation angle can be easily determined by reading the value of T_a/G from the curve at that angle.

After obtaining the T_a/G calibration curve, the ET antenna is pointed at the satellite whose EIRP is to be measured, and a number of measurements of received satellite power are performed. The average of these measurements normalized by T_a yields a ΔY that can be used with the proper (at the satellite elevation angle) T_a/G value to determine the satellite EIRP from the equation

$$\text{EIRP} = \frac{k(T_a/G)\,\Delta f L\,\Delta Y}{Ae_1 \cdots e_7} \tag{1}$$

where k is Boltzmann's constant, Δf is the combined ET–ETMS noise bandwidth, L is the space loss $(4\pi r/\lambda)^2$ [5], r is the range from the ET antenna to the satellite transmit antenna, λ is the measurement wavelength, and A is the aspect angle correction [1]. e_1 through e_7 are near-unity correction factors analogous to the G/T correction factors described in an earlier publication [6]. Sequentially, these factors account for: 1) atmospheric transmission losses, 2) the angular extent of the received satellite signal as "seen" by the ET antenna, 3) frequency variations of the receiving system components across the receiver passband, 4) frequency variations of the downlink operating noise temperature across the receiver passband, 5) imperfect ET antenna pointing, 6) polarization mismatch between satellite signal and ET antenna, and 7) finite response time of the ETMS and instabilities in T_a.

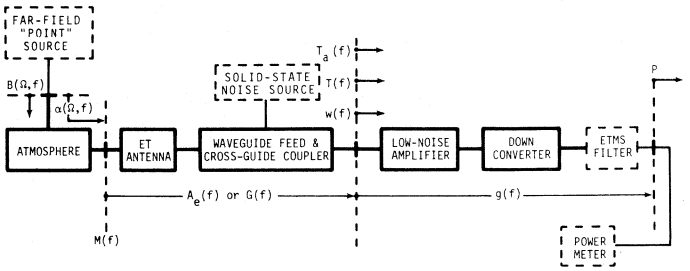

Fig. 3. Block diagram of a model representing the ET receiving system.

The theoretical development leading to (1) is outlined in the next section.

II. Theoretical Development

As mentioned earlier, the EIRP measurement performed by the ETMS is accomplished in two steps, obtaining the T_a/G calibration curve, and measuring the received satellite power. Before examining these two steps separately, basic equations used as a starting point for their theoretical descriptions will be presented. Although these equations and some of the approximations leading to the final working equations may be applicable over a wider frequency range, they are designed primarily for the 1–10-GHz frequency range.

A model of the ET receiving system is shown in the block diagram of Fig. 3. The system (including the atmosphere) is outlined in solid blocks. The far-field source is the satellite or radio star, depending at which the ET antenna is pointed, and $B(\Omega,f)$ is the corresponding brightness distribution [7]. Ω represents the pair of spherical polar angles with origin at the ET antenna and z axis along the center of the mainbeam, and f is the frequency. $\alpha(\Omega,f)$ is an operator representing the effects [8], [6] of gaseous absorption, refractive spreading, and tropospheric scattering on the incoming flux from the radio star or satellite. $M(f)$ is a mismatch factor [9] relating the polarization of the source radiation to the ET antenna polarization. $A_e(f)$ and $G(f)$ are the effective area and gain, respectively, of the combined antenna, waveguide feed, and cross-guide coupler. $T_a(f)$ is the noise temperature of the solid-state noise source as it appears at the LNA input. When the noise source is turned off the added noise $T_a(f)$ is zero. $T(f)$ is the noise temperature of the ET system and consists of cosmic background noise, atmospheric and man-made noise, ground noise, noise from I^2R losses in the antenna, waveguide feed, and cross-guide coupler, the effective input noise temperature of the LNA, and radiated satellite noise when the ET antenna is pointed at the satellite. $w(f)$ is the spectral power (power per unit bandwidth) corresponding to the sum of the spectral power from the

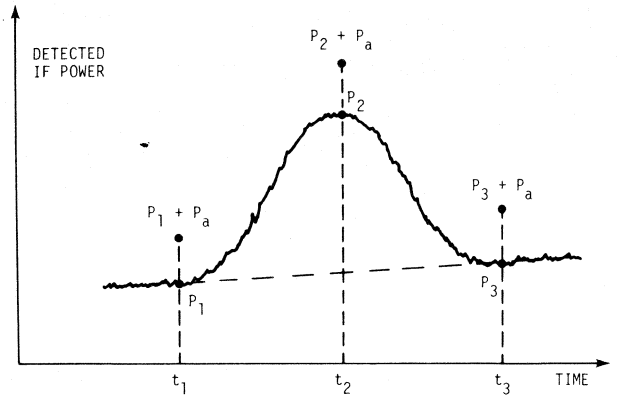

Fig. 4. IF power detected by the ETMS as a radio star traverses the ET antenna mainbeam.

far-field source $kT_a(f)$ and $kT(f)$. $g(f)$ is the ratio of the spectral power delivered to the power meter to the available spectral power at the LNA input. P is the total power delivered to the power meter.

The spectral power $w(f)$ is related to other parameters appearing in Fig. 3 by the equation

$$w(f) = k[T(f) + \text{“}T_a(f)\text{”}] + A_e(f)M(f) \cdot \int \alpha(\Omega, f)B(\Omega, f) \cdot P_n(\Omega - \Omega_0, f)\, d\Omega. \quad (2)$$

$P_n(\Omega - \Omega_0, f)$ is the normalized power pattern of the ET antenna, waveguide feed, cross-guide coupler combination, where the difference $\Omega - \Omega_0$ accounts for the fact that the antenna may not be pointing at the center Ω_0 of the far-field source. The quotation marks around $T_a(f)$ are a reminder that $T_a(f)$ is zero when the solid-state noise source is turned off. $d\Omega$ is the infinitesimal solid angle $\sin\theta\, d\theta\, d\psi$.

The power P detected by the ETMS is related to the spectral power $w(f)$ by the equation

$$P = \int w(f)g(f)\, df. \quad (3)$$

The form of (2) and (3) are a manifestation of the assumed linearity of the model in Fig. 3, and form the theoretical basis for the following description of the two-step measurement process leading to the EIRP equation (1).

A. Step One—T_a/G Calibration Curve

The power measurements performed by the ETMS to obtain T_a/G at a particular elevation angle are indicated by the heavy dots in Fig. 4. As a calibrated radio star passes through the center of the ET antenna mainbeam, the IF power detected by the ETMS describes a curve shaped somewhat as depicted in the figure. The slope of the baseline from t_1 to t_3 could be caused by a variation in the cosmic background surrounding the radio star, or a slow change in the ET receiver gain. Three pairs of power measurements are made, one at each time t_1, t_2, and t_3. At t_1, a measurement P_1 of the noise baseline is made, followed immediately by the same measurement $P_1 + P_a$ with the solid-state noise source turned on. The ratio y_1 $(= P_1/P_a)$ is then calculated to eliminate the receiver gain from consideration as previously described. Similar ratios y_2 $(= P_2/P_a)$ and y_3 $(= P_3/P_a)$ are calculated from measurements at t_2 and t_3. The measurement at t_2 corresponds to the radio star being in the center of the ET antenna pattern. The measurement at t_3 is another measurement of the noise baseline and which, with y_1, allows the value of the noise baseline at t_2 to be determined. By subtracting the noise baseline from the measurement at t_2, the IF power ratio difference Δy corresponding to the radio star can be determined from the equation

$$\Delta y = y_2 - (y_1 + y_3)/2. \quad (4)$$

The values of the measured powers in Fig. 4 can be related to the quantities in the block diagram of Fig. 3 through (2) and (3). For example,

$$P_2 = \int g(f)[kT(f) + A_e(f)M(f) \cdot \int B(\Omega, f)\alpha(\Omega, f)P_n(\Omega, f)\, d\Omega]\, df \quad (5)$$

and

$$P_a = \int g(f)kT_a(f)\, df. \quad (6)$$

The $B(\Omega, f)$ in (5) is the radio-star brightness distribution, and $M(f)$ (approximately equal to 1/2) is the corresponding mismatch factor.

Equations (5) and (6) with similar equations for the measurements at t_2 and t_3 can be combined to give a theoretical expression for the Δy of (4). When this is done and equated to Δy, the following equation can be derived:

$$\frac{T_a}{G} = \frac{\lambda^2 S}{8\pi k} \cdot \frac{k_1 \cdots k_7}{\Delta y}. \quad (7)$$

λ is the measurement wavelength, $S = B(\Omega, f)\, d\Omega$ is the radio-star flux density at frequency f, and k is again Boltzmann's constant. k_1 through k_7 are correction factors defined to give the functional form of (7) and are expressions containing a number of integrals. Under certain circumstances, these factors are close to unity, making accurate radio-star measurement of G/T or EIRP possible. Reduced expressions for the k_i's have been discussed in earlier publications [6], [12].

The value for T_a/G calculated from (7) pertains to a particular elevation angle. When this process is repeated for other elevation angles as the radio-star traverses its path across the sky, the data points in Fig. 2 from which the calibration curve is derived are generated. The T_a/G value needed to determine the satellite signal power is then obtained from the curve at the elevation angle of the satellite.

B. Step Two—Received Satellite Power Measurements

With the T_a/G calibration completed, the antenna is pointed at the satellite in order to measure the received signal power. Fig. 5 illustrates the resulting RF power

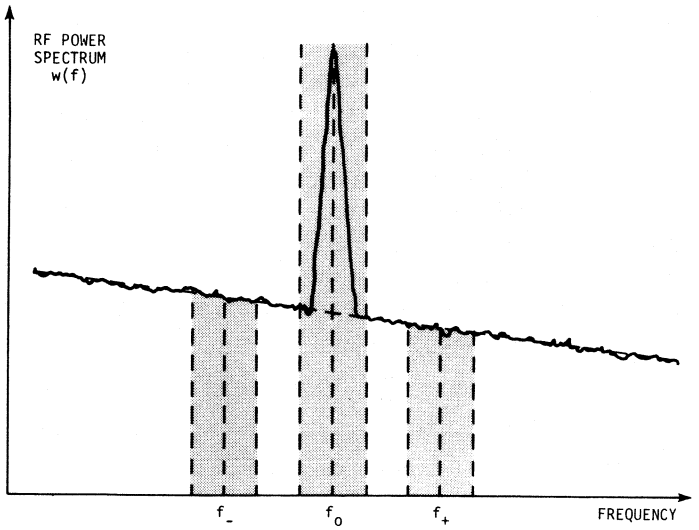

Fig. 5. A portion of the RF power spectrum as it appears at the low-noise amplifier input.

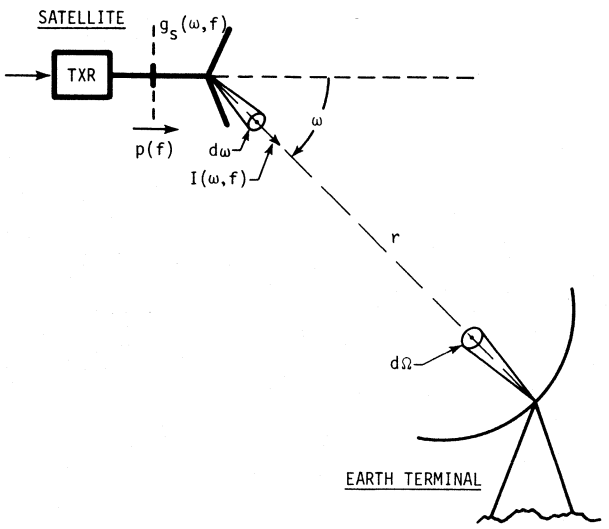

Fig. 6. Parameters used in the definition of satellite EIRP and the resulting power flux at the ET antenna aperture.

spectrum as it appears at the LNA input. In this example, the spectrum has a sloping noise baseline with the satellite signal appearing at the center frequency f_0. The shaded areas depict those frequencies passed by the limiting IF bandpass filter in the ETMS when the ET downconverter is tuned to f_-, f_0, or f_+, respectively. The corresponding IF powers P_-, P_0, and P_+ detected by the ETMS are related to this IF power spectrum by the equation

$$P_i = \int w(f) g_i(f)\, df, \qquad i = -, 0, + \tag{8}$$

where i indicates that the downconverter has been tuned to f_-, f_0, or f_+, respectively.

The procedure for normalizing these powers is different from the normalization procedure used in the T_a/G calibration, but is still done for the same purpose, to eliminate gain fluctuations. As previously discussed in the T_a/G measurement with the radio star y_1, y_2, and y_3 are calculated from pairs of power measurements with one member of each pair having the solid-state noise source turned on. With reference to Fig. 4, the magnitude of the added noise power P_a was large enough compared to the P_i ($i = 1, 2, 3$) that when P_i was subtracted from the measured power $P_i + P_a$ to obtain P_a, significant figures were not lost. However, in the measurement of satellite power (Fig. 5), P_0 and sometimes P_- and P_+ are sufficiently large compared to P_a to cause significant variation in the P_a determined from subtracting $P_i (i = -, 0, +)$ from $P_i + P_a$. This problem is circumvented by pointing the ET antenna away (in azimuth) from the satellite to obtain P_a (at f_-, f_0, and f_+) by measuring a noise baseline comparable in magnitude to the noise baseline in Fig. 4, and then normalizing P_i ($i = -, 0, +$) with the resulting P_a's. These P_a's are related to $T_a(f)$ and the receiver gain $g(f)$ by the equation

$$P_{ai} = \int k T_a(f) g_i(f)\, df, \qquad i = -, 0, + \tag{9}$$

where the subscript i signifies whether the ET downconverter has been tuned to f_-, f_0, or f_+.

The ratio difference ΔY of the received satellite signal at the LNA input is calculated from the equation

$$\Delta Y = y_0 - (y_- + y_+)/2. \tag{10}$$

With the Δy's of this equation replaced by their theoretical counterparts, (1) can be derived. Like the k_i's of (7), the e_i's are defined in such a manner as to obtain the functional form of (1). As in the T_a/G measurement, the utility of the radio-star method for measuring EIRP depends upon the e_i's being close to unity. The working equations for the e_i's used in the ETMS are to be found in [12].

In obtaining (1) from (10), a brief explanation of how the aspect angle correction A is defined in this analysis is helpful. Fig. 6 depicts a satellite signal being radiated to an earth terminal located in the direction of the spherical angles represented by ω from the center of the mainbeam of the satellite antenna. The spectral power $p(f)$ of the signal available at the output port of the satellite transmitter (TXR) is fed to the satellite antenna whose gain in the ω direction is $g(\omega, f)$. The resulting intensity $I(\omega, f)$ radiated into the infinitesimal solid angle $d\omega$ is

$$I(\omega, f) = p(f) g(\omega, f). \tag{11}$$

The aspect angle correction A is then defined here in terms of this radiated intensity by the equation

$$A \equiv \frac{\int I(\omega, f)\, df}{\int I(0, f)\, df} \tag{12}$$

where $I(0, f)$ is the intensity radiated in the boresight direction of the satellite antenna, and the integrals are evaluated across a narrow bandwidth centered on the center frequency f_0 of the signal. The denominator of (12) is the EIRP. The ratio in (12) reduces with negligible error to the normalized power pattern of the satellite antenna at the center frequency f_0.

TABLE I
ERROR IN MEASURING EIRP AT 7.55 GHz AND 12° ELEVATION ANGLE

SOURCE OF ERROR	SOURCE MAGNITUDE AND UNCERTAINTY	RESULTING PERCENT ERROR IN EIRP
1. Y-Factor Ratio	10 ± 0.029 dB	0.66
2. Cassiopeia A Flux Density	586 ± 26 fu	4.46
3. Space Loss $(4\pi r/\lambda)^2$	202 ± 0.006 dB	0.14
4. Noise Bandwidth	5 MHZ ± 19 kHz	0.38
5. Atmospheric Transmission	1 ± 0.0702	7.02
6. Star Shape	0.899 ± 0.0070	0.81
7. Component Frequency Dependence	1 ± 0.0073	0.73
8. Downlink Noise Temperature Variation	1 ± 0.0001	0.01
9. ET Antenna Pointing	1 ± 0.0131	1.31
10. Polarization Mismatch	1 ± 0.0056	0.56
11. System Time Response & T_a Instability	1 ± 0.0023	0.23
12. Aspect Angle Correction	0 ± 0.25 dB	5.29
13. Frequency	7.55 ± 0.00 GHz	0.00
QUADRATURE SUM OF SYSTEMATIC ERRORS		10.1%
14. Random Error From T_a/G Measurement	-33.2 ± 0.28 dB(3σ)	6.56
15. Random Error From Received Satellite Power	± 0.57 dB(3σ)	14.10
TOTAL QUADRATURE ERROR		18.5%

III. Error Analysis

Examination of (1) and (7) reveals that there are twenty-one possible sources of systematic EIRP error. However, since Δy and ΔY, and the e_i's and k_i's are related, the number of sources reduces to thirteen. These thirteen sources of error are listed in the first column of Table I. This table was prepared for an ET operating at 7.55 GHz with an 18-m antenna looking at a synchronous satellite at 12° elevation above the horizon. The source magnitudes and uncertainties listed in column two reflect this choice. The error in EIRP resulting from the various uncertainties are listed in the third column. Typical random errors generated during T_a/G and received satellite power measurements are given in rows 14 and 15.

The Y-factor ratio uncertainty (0.029 dB) is calculated from the ratio of y appearing in (4) to the ΔY appearing in (10), although the 10-dB magnitude applies to Y only. The uncertainty is mainly due to calibration errors in the IF attenuators in the ETMS, the errors due to the power bridge being considerably smaller.

The Cassiopeia A flux-density uncertainty (26 fu) (fu stands for flux units, one flux unit being equivalent to 10^{-26} W m^2/Hz/steradian) represents a careful but not quite state-of-the-art flux density calibration [9]. This uncertainty and the corresponding 4.46-percent EIRP error appears difficult to reduce at the present time.

The 0.006-dB uncertainty in the space loss is due to range (r of Fig. 6) uncertainty which was assumed to be the daily range variation of the satellite used in the example.

The composite ET receiving system-ETMS noise bandwidth is determined at each ET from previously measurement parameters of the ETMS filters and the gain slope of the ET passband.

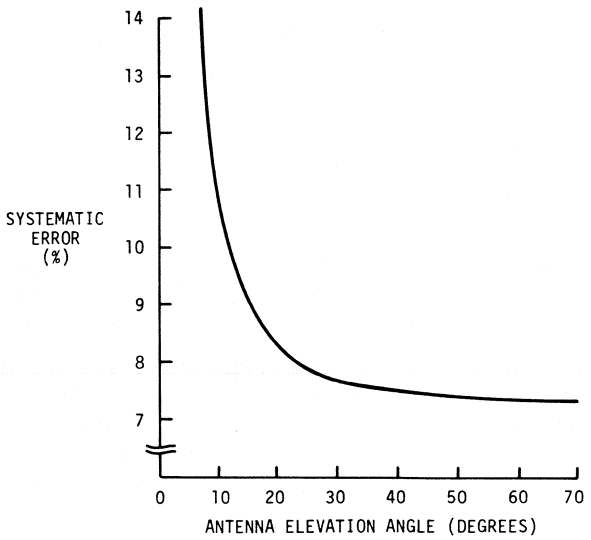

Fig. 7. Total quadrature systematic EIRP error at 7.55 GHz versus ET antenna elevation angle.

The uncertainties listed in rows 5 through 11 were calculated from the k_i/e_i ratios for i equal to 1–7, respectively. Most of the ratios shown in column 2 are unity because like correction factors tend to cancel each other. The exception is the star-shape correction factor ratio (0.899) where e_2 is always unity because the satellite subtends a vanishingly small solid angle at the ET antenna, and the radio star does not.

The atmospheric transmission error (7.02 percent) varies with elevation angle, giving the total EIRP error a characteristic shape shown in Fig. 7. Table I is a breakdown of this curve at 12° elevation angle. Uncertainties in the k_1/e_1 ratio arise mainly from unpredictable variation in the atmo-

spheric temperature, pressure, and water-vapor density profiles between the T_a/G and received satellite power measurements. The large magnitude of this error (7.02 percent) is due in great part to a lack of measurement data and analysis concerning the tropospheric scattering effect [6], [8]. The error could probably be reduced with even a modest effort in this area. The basis for errors 6 and 7 have been previously discussed [6].

The error due to downlink noise temperature variations includes uncertainties arising from cosmic background variation around the calibrated radio star, and from portions of the satellite signal (if the signal carrier is modulated) appearing in the f_- and f_+ frequency bands (see Fig. 5) reserved for the baseline noise measurements. The satellite signal was assumed to be unmodulated for these calculations, accounting for the small 0.01-percent error.

The 1.31-percent error from antenna pointing inaccuracies is essentially twice the value when pointing at either the radio star or satellite, and is calculated using an assumed pointing uncertainty of 5 percent of the antenna half-power-beamwidth.

The polarization mismatch error was calculated assuming axial ratios for the ET and satellite antennas of 0.5 and 0.05 dB, respectively.

The time constant of the ETMS is sufficiently short and causes no appreciable EIRP error. The 0.23-percent error in row 11 is due entirely to the T_a instability.

The normalized power pattern of the satellite transmit antenna is needed to determine the aspect angle correction. The 5.29-percent EIRP error is the result of an aspect angle uncertainty obtained from the literature [1]. The application of emerging spherical near-field scanning techniques [10], [11] to satellite antenna measurements should significantly reduce this error.

The quadrature sum of the systematic errors in Table I is 10.1 percent, and is dominated by errors resulting from uncertainties in the Cassiopeia A flux density, the atmospheric transmission factor, and the aspect angle correction. Representative values for the random errors generated during the measurement of T_a/G and received satellite power increase this quadrature error to 18.5 percent.

Further information concerning details of the measurement and error equations is available [12], [13].

IV. Conclusions

The measurement of EIRP as performed by the ETMS has been described, and an outline of the derivation of the equations leading to the error analysis presented. The results of this analysis are given in Table I and Fig. 7.

The results show a 10-percent quadrature systematic EIRP error for a 12° elevation angle, increasing to 19 percent (3σ) with addition of the random errors generated during the measurement.

At 12° elevation angle, the total systematic error is dominated by errors resulting from uncertainties in the radio-star flux density, the atmospheric transmission factors, and the aspect angle correction. It appears that the latter two uncertainties might be significantly reduced with presently available knowledge and measurement techniques.

Acknowledgment

The author would like to thank D. Bathker and A. Freiley of the Jet Propulsion Laboratories, and T. Bremer, M. Kanda, D. Wait, and J. Wakefield of the NBS Laboratories for a number of helpful discussions.

References

[1] E. E. Steinbrecher and L. F. Gray, "A computer controlled satellite signal monitoring system," *COMSAT Tech. Rev.*, vol. 1, no. 1, Fall 1971.

[2] C. T. Stelzried, "The JPL total power and noise adding radiometers," NBS High Frequency and Microwave Noise Seminar, May 1970, unpublished.

[3] N. T. Larsen and F. R. Clague, "The NBS type-II power measurement system," in *Proc. 1970 ISA Annu. Conf.*, Philadelphia, PA, *Paper No. 712-70*, vol. 25, Part 3, Oct. 1970.

[4] M. Kanda, "An improved solid state noise source," *MTT Symp. Dig.*, Cherryhill, NJ, June 1976.

[5] *Satellite Communications Reference Data Handbook*, Defence Communications Agency, July 1972.

[6] W. C. Daywitt, "Error equations used in the NBS precision G/T measurement system," *Nat. Bureau Standards Internal Note 76-842*, Sept. 1976.

[7] J. D. Kraus, *Radio Astronomy*. New York: McGraw-Hill, 1966.

[8] H. Yokoi, M. Yamada, and T. Satoh, "Atmospheric attenuation and scintillation of microwaves from outer space," *Astron. Soc. Japan*, vol. 22, no. 4, p. 511, 1970.

[9] M. Kanda, "An error analysis for absolute flux density measurements of Cassiopeia A," *IEEE Trans. Instrum. Meas.*, vol. IM-25, no. 3, p. 173, Sept. 1976.

[10] P. F. Wacker and A. H. Newell, "Advantages and disadvantages of planar, circular cylindrical, and spherical scanning and description of the NBS antenna scanning facilities," presented at the Workshop on Antenna Testing Techniques, European Space Research and Technology Center of the European Space Agency, Noordwijk, The Netherlands, June 6–8, 1977.

[11] F. H. Larsen, "Probe correction of spherical near-field measurements of a satellite model," presented at the Workshop on Antenna Testing Techniques, European Space Research and Technology Center of the European Space Agency, Noordwijk, The Netherlands, June 6–8, 1977.

[12] W. C. Daywitt, "Error equations used in the NBS earth terminal measurement system," *NBSIR 78-869*, Dec. 1977.

[13] ——, "Atmospheric propagation equation used in the NBS earth terminal measurement system," *NBSIR* 78-883, Apr. 1978.

An RMS Digital Voltmeter/Calibrator for Very-Low Frequencies

HOWARD K. SCHOENWETTER, SENIOR MEMBER, IEEE

Abstract—**A portable rms digital voltmeter (DVM) has been developed at NBS to support vibration measurements over the ranges of 0.1 to 50 Hz and 2 mV to 10 V. A self-contained calibrator provides for self-calibration and may be used for calibrating other VLF voltmeters. The calibrator basically consists of a Kelvin–Varley divider fed by a reference voltage (either dc or sinewave generated by a ROM–DAC combination). A multijunction thermal converter (MJTC) was selected as the sensing device in the rms/dc converter of the DVM since its low ac/dc difference facilitates calibration of the ac calibrator. Factors affecting accuracy and response time are analyzed. The DVM response time is 40 s for the lowest input frequency. Its accuracy (percent of reading) is 0.1 percent above 0.5 Hz and 5 mV and 0.2 percent below these values. The ac calibrator accuracy is 0.02 percent. Measurement accuracy improves by a factor of about 4 for transfer measurements (comparing input voltages with ac calibrator voltages). Means for extending this accuracy to 0.01 percent are discussed.**

I. Introduction

CALIBRATED vibration transducers (accelerometer–amplifier systems) are required in calibration laboratories and test facilities to determine the acceleration of vibration exciters, tables and fixtures. At very-low frequencies (VLF's), particularly below 10 Hz, the major source of error in calibrating these transducers (both reference standards and test items) has been the error in measuring the output voltage from the transducer [1], [2]. This is because the measurement error of the few commercial voltmeters (that measure VLF's) ranges from a few tenths of a percent to over 1 percent, depending upon the voltage and frequency. Furthermore, calibration of these voltmeters is difficult since no commercial ac voltage calibrator operates below 10 Hz. Voltage measurement errors are very significant since their contribution to transducer calibration uncertainty is added at each level of the calibration hierarchy.

To meet present and expected future requirements of vibration and other very low frequency measurements, a portable rms digital voltmeter (DVM) was designed to measure voltages from 2 mV to 10 V over the frequency range of 0.2 Hz to 50 Hz.[1] Since the means for calibrating the voltmeter to the required accuracy below 10 Hz did not exist, an ac voltage calibrator was also developed and incorporated into the same instrument. This calibrator, covering the frequency range of 0.2 Hz to 50 Hz,[2] is intended not only for calibration of the companion voltmeter but also for the calibration of other voltmeters. In addition, the calibrator facilitates transfer measurements.

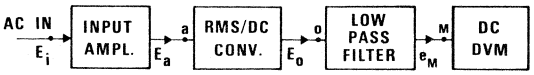

Fig. 1. RMS digital voltmeter used in ac voltmeter/calibrator.

The accuracy objective for the voltmeter was 0.1 percent of reading above 2 Hz and 5 mV and 0.25 percent of reading for lower frequencies and voltages. As explained in the next section, the minimum response time obtainable in rms voltmeters is directly proportional to the period of the input voltage. Commercial rms DVM's require 15–20 periods for a response to within ± 0.1 percent of the input change. This extrapolates to 150–200 s for 0.1 Hz. Since slow response limits an instrument's usefulness, the design objective also was to decrease the response time below these figures as much as was practicable.

II. RMS Voltmeter Design

A. Design Considerations

The rms voltmeter designed for this instrument follows the conventional approach shown in Fig. 1. In describing the operation of this circuit and the following circuits, rms and instantaneous values will be represented by upper and lower case letters, respectively. The ac input voltage E_i is amplified to a voltage level E_a suitable for the rms/dc converter and converted to a unidirectional voltage E_o. The converter transfer characteristic E_o/E_a is ideally a constant, adjustable to unity.[3] Since the input voltage to the converter e_a is sensed by a square-law device, the converter output e_o consists of a dc component E_{dc} and a ripple component e_r whose rms value is E_r; hence,

$$E_o = \sqrt{E_{dc}^2 + E_r^2} \simeq E_{dc}(1 + E_r^2/2E_{dc}^2). \quad (1)$$

If the amplifier gain is G and $E_o/E_a = 1$, then $E_o = E_a = GE_i$. For accurate measurement of E_i, the voltmeter reading should be E_o/G; however, the dc DVM responds to E_{dc} (since it is average-responding) and displays the value E_{dc}/G. Therefore, it is seen from (1) that the ripple value E_r causes a fractional error of $E_r^2/2E_{dc}^2$ in the displayed voltage.

Manuscript received February 20, 1978. This work was supported in part by the Calibration Coordination Group of the Department of Defense.

The author is with the Electricity Division, National Bureau of Standards, Washington, DC 20234.

[1] The design was later modified to extend the range to 0.1 Hz.

[2] The design was later modified to extend the range to 0.1 Hz.

[3] In practice, E_o/E_a varies somewhat with the frequency of the input voltage. This rms/dc conversion error will be discussed in later sections.

Thus ripple filtering is required in the converter to limit this rms/dc conversion error to an acceptable level. This constraint still allows a relatively large peak-to-peak value of e_r and would, if not reduced, cause intolerable fluctuations in the displayed voltage. These fluctuations, in effect, reduce the DVM accuracy. Therefore, a low-pass (LP) filter is used to reduce the peak ripple (in e_M) to an acceptable level.

If the input voltage e_i is a waveform with a crest factor greater than 1 (e.g., a sinewave), the time constants in the converter and LP filters must be increased in direct proportion to the period of e_i in order to maintain acceptable ripple levels. Consequently, the minimum rms voltmeter response time is proportional to the period of e_i. For a given frequency (and a given voltmeter design), response time can only be decreased by decreasing the filter time constants, resulting in increased voltmeter error (including fluctuations in the displayed voltage). Thus a tradeoff exists between minimum response time and minimum voltmeter error.

B. Error Budget

The error budget of 0.1 percent above 2 Hz was allocated as follows:

rms/dc conversion error	0.02%
calibration errors	0.03%
temperature effects/°C	0.02%
gain-offset drift/30 days	0.03%

The error budget of 0.25 percent below 2 Hz included the above items, plus the following:

rms/dc conversion error from ripple (E_r)	0.05%
rms/dc conversion error from sensing element	0.05%
peak fluctuations in displayed voltage	0.05%

Much smaller fluctuations (0.01–0.02 percent) in the displayed voltage are desirable when using the voltmeter for ac/ac transfer measurements where the input voltage is measured by comparison with a calibrator voltage of approximately the same frequency. The gain-offset error budget was not considered critical since corrections are readily made (2 adjustments) using the voltage calibrator.

C. Detailed Design

1) Input Amplifier: The input amplifier is direct-coupled and has gains from 0.5 to 2500, selectable in 12 ranges of 1–2–5 gain sequence. The amplifier consists of two cascaded low-noise low-drift operational amplifiers with buffering to provide high-input impedance and power capability with low distortion at its output. The sequence of voltage ranges limits the nominal input range over which the rms/dc converter must operate from 2 to 5 V. Reed relays in DIP configuration are used for range switching. The frequency response for all gain ranges is flat from dc to 50 Hz to within 0.01 percent or better.

2) RMS/DC Converter:[4]

a) General description: The rms/dc converter in this instrument (Fig. 2) is a feedback type, employing a differential multijunction thermal converter (MJTC) for the sensing element.[5] The differential MJTC contains two matched MJTC's connected so that the dc components of their outputs oppose each other. The outputs $e_1(t)$ and $e_2(t)$ have dc components E_{d1} and E_{d2} proportional to the input power to heater elements H_1 and H_2, respectively. Therefore,

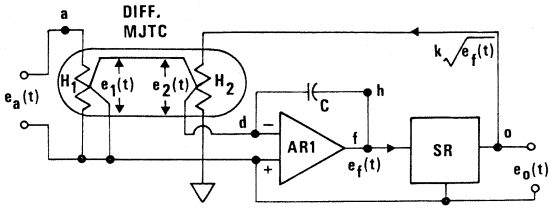

Fig. 2. Functional block diagram of rms/dc converter.

$$E_{d1} = K_1 E_a^2 / r_1 \quad \text{and} \quad E_{d2} = K_2 E_o^2 / r_2 \tag{2}$$

where E_a and E_o are the rms values corresponding to $e_a(t)$ and $e_o(t)$, K_1 and K_2 are constants of proportionality and r_1 and r_2 are the resistance values of H_1 and H_2. It will be shown later that the circuit is constrained to allow only negative feedback, i.e., the voltage fed back to H_2 always tends to decrease the difference between E_{d1} and E_{d2}. If the loop gain is very large, $E_{d1} - E_{d2} \simeq 0$. Equating the expressions in (2), $E_o^2 \simeq K_1 r_2 E_a^2 / K_2 r_1$ or

$$E_o \simeq \sqrt{K_1 r_2 / K_2 r_1}\, E_a. \tag{3}$$

Hence, E_o is proportional to E_a, the rms value of the input voltage $e_a(t)$. To simplify later discussions, it is assumed that $K_1/r_1 = K_2/r_2 \equiv B$, i.e., $K_1 r_2 / K_2 r_1 = 1$.

Equation (3) is also valid if square-rooting circuit SR is omitted and point f connected to point o. However, omitting circuit SR causes the rms/dc converter circuit to be nonlinear, since the MJTC in the feedback loop has a nonlinear transfer characteristic ($E_{d2} = BE_o^2$). This nonlinearity, in turn, causes the response time of the converter to be different for input step increases than for input step decreases [7], [8]. This effect can be removed by placing a squaring amplifier between points f and h [8], [9], or by linearizing the converter circuit using circuit SR, as shown in Fig. 2. The latter method has the advantage of maintaining constant dc loop gain, independent of E_o.

b) Detailed description: Circuit details of the rms/dc converter are shown in the upper part of Fig. 3. As explained in the next section, resistor $R1$, matched to the resistance of heater H_1 (~ 1 kΩ), is used to reduce the low-frequency ac/dc difference of the MJTC input section.[6] Resistor $R2$ is added to equalize the rms values of the input and output voltages. Adding these resistors decreases the effective value of B by a factor of 4. (See statement following (3) for definition of B.)

Amplifier AR1 is a low-noise chopper-stabilized amplifier which provides high loop gain. The circuit SR (Fig. 2)

[4] Bibliographies on rms/dc converters may be found in [3] and [4].

[5] The MJTC is described in [5]. Differential MJTC's have been used previously in rms/dc feedback converters operating above 50 Hz [6].

[6] The ac/dc difference is defined as $\delta = (Q_a - Q_d)/Q_d$ where Q_a and Q_d are the ac and dc inputs which produce the same thermal converter output (dc component only).

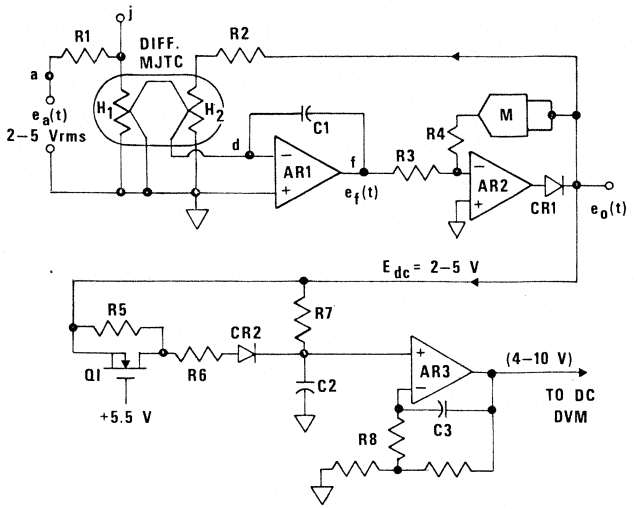

Fig. 3. RMS/dc converter and signal conditioner.

consists of amplifier AR2 and multiplier M, which functions as a squaring circuit in the AR2 feedback loop. The constant k of the SR circuit's transfer characteristic ($e_0 = k\sqrt{e_f}$) is adjusted by the value of $R3$. Diode CR1 restricts the feedback voltage $e_0(t)$ to positive values (negative feedback only).

c) Sensing element: An MJTC was selected for the sensing element of the rms/dc converter because of its negligible ac/dc difference over a large part of the 0.1–50 Hz frequency range. It will be shown later that this factor is important for the calibration of the ac calibrator.

For input frequencies sufficiently high that negligible temperature variation of the thermal converter heater occurs during a cycle (because of the heater thermal time constant), deviation from square-law response has no effect on δ and the ac/dc difference is very small. At very-low frequencies (VLF's), the heater temperature varies with instantaneous input power and external filtering is necessary to smooth the output voltage. Lack of square-law response now increases δ. It is shown in Appendix I that the low-frequency ac/dc difference of a thermal converter (TC), caused by lack of square-law response, is

$$\delta_m = b'I^2m^2/4 \tag{4}$$

where I is the rms value of the input current and m is the ratio of peak to average value of the output electromotive force (EMF) (before external filtering is applied). Constant b' is a measure of the TC's deviation from a square-law response, may be of either sign, and can be determined from dc measurements (see (A.3) and (A.12)).

Resistor $R1$ (Fig. 3), matched to the resistance of heater H_1, reduces δ_m in two ways: 1) It minimizes the dependence of input power on small cyclic resistance changes [10] which decreases b', and 2) it reduces δ_m by decreasing I to a full-scale value of 2.5 mA (rated current for the MJTC is 5 mA). The value of b' should be specified so that $\delta_m \leq 0.1$ percent for $m = 1$. For the MJTC used in this instrument, m is approximately 0.6 and 0.1 at 0.1 and 1 Hz, respectively. Therefore, $\delta_m \leq 0.04$ percent at 0.1 Hz and causes and equivalent error in rms/dc conversion, which is within the allocated error budget. At 1 Hz, $\delta_m \leq 10$ ppm and decreases to zero below 10 Hz. The ac/dc difference from other causes (such as Thompson and Peltier effects) is less than 1 ppm up to 10 kHz [10], [11], and is expected to be constant over the voltmeter's frequency range.

The rms/dc converter has essentially the same ac/dc difference as the MJTC if its output ripple is negligible (maximum filtering used). Consequently, the ac/dc difference of the rms voltmeter (input applied to the TC DIRECT terminals) changes less than 10 ppm from 1 to 10 Hz and is negligible above 10 Hz. This voltmeter characteristic is very useful in calibrating the ac calibrator.

In the following discussions, each section of the differential MJTC is treated as a device with a single time constant, represented by the 0–63 percent step response. The MJTC used in this instrument has time constants of approximately 1 s for each section, represented by the symbol τ_1. Therefore, the transfer characteristics for the MJTC may be written

$$e_1(t) = Be_a^2(t)/(1 + \tau_1 p) \tag{5}$$

and

$$e_2(t) = Be_0^2(t)/(1 + \tau_1 p) \tag{6}$$

where $p \equiv d/dt$ and B is a dimensional constant defined earlier (see statement following (3)).

d) Accuracy and response time: Since it is most difficult to meet the accuracy and response time objectives at the lowest frequencies, the converter design requirements will be examined at 0.1 Hz. The transfer characteristics for the circuit of Fig. 2 are derived in Appendix II-A for the critically damped and overdamped cases. These cases correspond to circuit conditions of $\omega_0^2 = b^2$ and $\omega_0^2 < b^2$, where $b \equiv 1/\tau_1$, $\omega_0^2 \equiv Bk^2/\tau_1 RC$, R is the MJTC output resistance, and C is the integrating capacitance.

The response of the critically damped circuit to an input $e_a(t) = \sqrt{2}\, V_i \sin \omega t$ is given in (A.21). The transient and steady-state parts of that equation are

$$e_0(t)_t \simeq \tfrac{1}{2}bte^{-bt}V_i \tag{7}$$

and

$$e_0(t)_{ss} \simeq \left(1 - \frac{X^2}{16} - \frac{X}{2}\cos 2\omega t\right)V_i \tag{8}$$

where

$$X \equiv b^2/(b^2 + 4\omega^2) \quad \text{and} \quad \omega \equiv 2\pi f.$$

The second term of (8) represents the rms/dc conversion error caused by ripple and is 0.12 percent at 0.1 Hz. The response time is obtained by equating (7) to $0.0005V_i$ and is 18.2 s.[7]

The error budget of 0.05 percent for conversion error from ripple can be met by decreasing ω_0^2 (increasing C or decreasing k), resulting in an overdamped circuit. The response of the overdamped circuit to $e_a(t) = \sqrt{2}\, V_i \sin t$ is given in

[7] Unless stated otherwise, "response time" refers to the time required for the output voltage to reach its final value ±0.05 percent of the voltage change.

(A.23) (applicable for $\omega_0 < 0.95b$). The transient and steady-state parts of that equation are

$$e_0(t)_t \simeq \frac{\omega_0^2 \exp\{-[b - \sqrt{b^2 - \omega_0^2}]t\}}{4\sqrt{b^2 - \omega_0^2}[b - \sqrt{b^2 - \omega_0^2}]} V_i \quad (9)$$

and

$$e_0(t)_{ss} \simeq \left(1 - \frac{Y^2}{16} - \frac{Y}{2}\cos 2\omega t\right) V_i \quad (10)$$

where $Y \equiv \omega_0^2/[2\omega\sqrt{4b^2 - 2\omega_0^2 + 4\omega^2}]$. The second term of (10) represents conversion error from ripple.[8] Equating this term to $0.0005V_i$ yields $\omega_0^2 = 0.67b^2$ at 0.1 Hz, the value of ω_0^2 which will reduce the conversion error to 0.05 percent. Substituting this value for ω_0^2 into (9) and equating it to $0.0005V_i$ give 34 s for the response time. Since this increase in response time was considered unacceptable, a circuit was designed to compensate for ripple error, thus making it feasible to use the critically damped converter. This ripple error compensating circuit is part of the signal conditioner circuit described later.

3) Low-Pass Filter: The filtering following the converter must reduce the peak ripple to 0.05 percent and should have less than 0.05 percent transient overshoot for input voltage steps to the rms/dc converter. In the worst case of $f = 0.1$ Hz, the ripple from the converter must be reduced by a factor of 136. These are minimum requirements (see error budget) and can be met by 1) LP filtering, 2) integration over an integral number of periods of ripple or 3) by a combination of LP filtering and fixed period integration. Method 2) was considered to be somewhat beyond the scope of this project.[9] Comparison of the other two methods (Appendix II-B) was limited to filters whose poles are all real and equal. The comparison shows that method 1) has the shorter response time if the filter has 5 or more poles. However, method 3) is more appropriate for ac/ac transfer measurements, since the fluctuations in the voltage indication are zero for frequencies of 0.05, 0.1, 0.15, $\cdots$, Hz (includes calibrator frequencies) and are less for most other frequencies. For this reason, method 3) was used to perform the filtering and consists of a 2 pole LP filter and an integrating dc DVM. The filter is part of the signal conditioner circuit, described next.

4) Signal Conditioner: The signal conditioner (lower half of Fig. 3) consists of a 2-pole LP filter, a ripple error compensating circuit, and a voltage follower (AR3) with a gain of 2. The output of the rms/dc converter $e_0(t)$, consisting of dc and ripple components E_{dc} and e_r, is applied to the signal conditioner for attenuation of e_r and correction and amplification of E_{dc}.

The attenuation factor of the LP filter (sections $R7$–$C2$ and $R8$–$C3$) is[10]

$$\frac{4\omega^2 + \alpha^2}{\alpha^2} \quad (11)$$

where $\alpha \equiv 1/(R7)(C2) = 1/(R8)(C3)$. As indicated in Appendix II-B2, a maximum ripple attenuation factor of 11.7 is required in the LP filter at $f = 0.125$ Hz (ripple frequency = $2f$). This corresponds to $\alpha = 0.48$. Larger α (smaller time constants) are used for $f > 0.5$ Hz.

The ripple error compensating circuit consists of $Q1$, $R5$, $R6$, and $CR2$. This circuit compensates for rms/dc conversion error (from excessive ripple e_r) by injecting a positive charge on $C2$ during the positive half cycles of e_r. The amplitude of e_r is proportional to E_{dc}. Therefore, because of the nonlinear $V - I$ characteristic of diodes, $CR2$ presents an increasing impedance to ripple as E_{dc} decreases. This effect is compensated by $Q1$ which is biased so that its drain-source resistance decreases as E_{dc} decreases. The compensating circuit reduces conversion error at the lowest frequencies to well below the 0.05-percent objective.

In addition to functioning as an active filter, AR3 serves to amplify E_{dc} to the 4–10 V level required for the dc DVM. The overall temperature coefficient of the rms DVM is compensated to within ± 0.015 percent/°C by using a Sensistor in the feedback circuit of AR3.

5) DC Digital Voltmeter: The dc digital voltmeter consists of a voltage-to-frequency (V/F) converter and a frequency counter with digital display. The V/F converter has an input voltage range of 0 to 10 V (only the 4–10 V range is used) and a transfer characteristic of 1000 Hz/V. Since the number displayed by the frequency counter must be proportional to the input voltage, the pulse rate output of the V/F converter is effectively scaled inversely to the gain (scaling) of the input amplifier and the integration period (either 1 or 10 s). This is accomplished by pulse rate scaling of 1, 2, and 5 (using a counter) and decimal point selection. The ripple attenuation factor (versus frequency) of the integrating dc DVM, and its effective response time are given in Appendix II-B2.

III. Calibrator Design

The error budget for the rms DVM allocated 0.03 percent for calibration errors. Since up to 0.01 percent calibration uncertainty results from lack of resolution in the displayed voltage, 0.02 percent was the accuracy objective for the ac calibrator.

The voltage calibrator consists of a compact 7-digit Kelvin–Varley (K–V) divider fed by a reference voltage of 1 V (either ac or dc) and buffered at its output by a voltage follower with selectable gains of 1 and 10. The frequency response of the K–V divider (set to all fives) and buffer amplifier is flat to within 0.005 percent through 50 Hz. The measured nonlinearity of the K–V divider is 0.005 percent for a dial setting of 0020000 (2-mV output), decreasing to 0.002 percent or less at 1000000 and above. The 1-V dc reference is derived from a precision 10-V reference supply.

The ac (sinewave) reference is shown in Fig. 4. The sinewave is generated by a 7-bit counter–ROM–DAC combination so that 128 input pulses are required per sinewave cycle. The necessary input frequencies are obtained using a clock frequency of 6400 Hz and scaling it 5, 25, 50, 100, 250, and 500 times using a series of counters. The amplifier is designed to have an output of 1-V rms and sufficient filtering to reduce the contribution of all harmonics generated by the

[8] The second term of (8) and (10) corresponds to the second term of (1).

[9] A long-range program is underway at NBS to develop an all-digital system for measuring and analyzing VLF waveforms in time periods approaching the theoretical minimum.

[10] Attenuation factor is defined here as the reciprocal of the transfer characteristic.

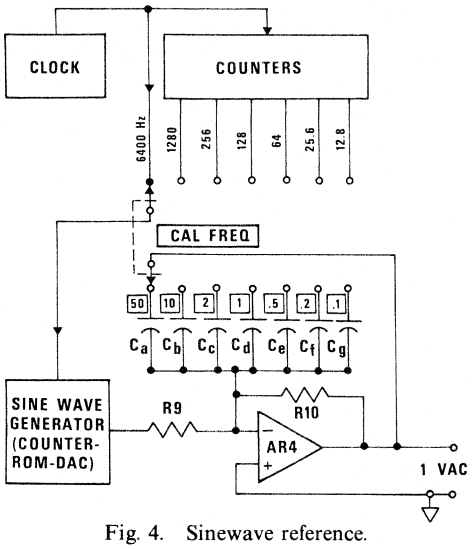

Fig. 4. Sinewave reference.

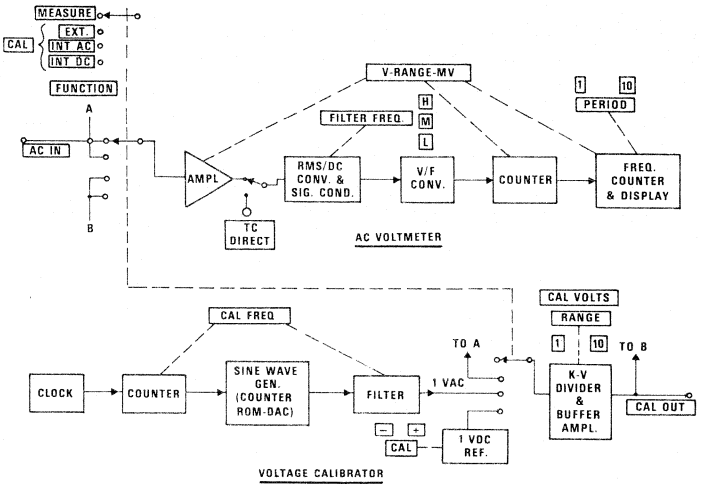

Fig. 5. Simplified block diagram of ac voltmeter/calibrator.

digital-to-analog converter (DAC) to less than 20 ppm. Capacitances C_a, C_b, $\cdots$ are chosen so that capacitance $\times$ frequency = a constant (to within 0.2 percent). Therefore, attenuation of the fundamental and harmonic components remains constant for all calibrator frequencies. Also, the phase shifts of the harmonics are essentially the same for all calibration frequencies. The circuit was designed to have a small output amplitude sensitivity to a change in capacitance or frequency and is approximately 27 ppm per percent change.

The flatness (constancy) of the ac calibrator voltage with frequency was determined by using the ac voltmeter (input connected to the TC DIRECT terminals) to measure 1, 2, 10, and 50-Hz calibration voltages at the 5-V level. The voltage indications for 1, 2, and 10 Hz fell within a 20 ppm range; however, each reading had an uncertainty of 20 ppm because of lack of resolution. As described earlier, the change in the ac/dc difference of the voltmeter over this range is < 10 ppm. Therefore, the worst case difference between the 1, 2, and 10-Hz calibration voltages is 70 ppm. The voltage indication for 50 Hz was 40 ppm less than for 10 Hz, probably because of the finite risetimes and small glitches between steps in the DAC output. Since the range of measured amplitudes for 1, 2, and 10 Hz was less than 70 ppm, these factors evidently have little effect on the calibrator output in this frequency range. More important, there is no reason to believe that these factors or any others have a more adverse effect from 0.1 to 1 Hz than in the 1–10 Hz range. Hence, it is unlikely that the calibration voltages from 0.1 to 10 Hz fall outside a 70 ppm range. Since the ac/dc difference of the ac voltmeter is too large to accurately compare the calibrator voltages from 0.1 to 1 Hz, a special "viewing circuit" developed for another project [12] was used to compare the peak-to-peak values of the calibrator voltages from 0.1 to 10 Hz. The measured values fell within a 38-ppm range, adding confidence to the 70-ppm range assigned above. Basing differences between the rms values of voltages on the differences between the peak-to-peak values appears to be valid since all necessary precautions were taken to insure that the wave shape is the same for all frequencies. The calibration voltage at 50 Hz is easily trimmed (by decreasing C_a of Fig. 4 slightly) to be the same as at 10 Hz. Thus since the ac calibrator voltage is essentially independent of frequency, it is sufficient to calibrate it at only one frequency.

Fig. 6. AC voltmeter/calibrator.

The ac calibrator is temperature compensated to within ± 0.005 percent/°C, using a Sensistor in series with $R9$ of the amplifier. For dc voltages, the calibrator temperature coefficient is within ± 0.0025 percent/°C (average of both polarities). Calibration and overall accuracy of the calibrator will be discussed in a later section.

IV. Voltmeter/Calibrator Description

A. Operation

Fig. 5 is a functional block diagram of the ac voltmeter/calibrator and Fig. 6 is a photograph of the instrument showing the front panel controls and connectors.

When the FUNCTION switch is in the MEASURE mode, the instrument functions as a voltmeter and measures voltages applied to the AC IN terminals. The same is true in the CAL-EXT position, except that now the input voltage is also applied to the K–V divider; therefore, this voltage can be multiplied by any factor up to 10 and outputed at the CAL OUT terminals. This mode of operation permits wave shapes and frequencies other than those provided in the internal calibrator to be used as a reference. With the FUNCTION switch set to either the CAL-INT AC or CAL-INT DC positions, calibration voltages determined by the K–V divider and associated RANGE switch appear at

the CAL OUT terminals and are applied to the input of the voltmeter. The calibration voltages are limited to ±10-V dc or 7-V ac. Selection of the calibration frequency is by the CAL FREQ switch. The dc calibrator is intended to be used primarily as a means of calibrating the ac calibrator and is very accurate at 1 V and larger. Offsets in the direct-coupled amplifiers of the voltmeter and calibrator limit the smallest dc voltage at which they can be used with good accuracy to 0.1 V.

Measurement accuracy is determined by the accuracy of the voltmeter when it is used to measure voltages directly. However, measurement accuracy approaches the accuracy of the ac calibrator when the voltmeter is used as a transfer device (i.e., the voltmeter is used to compare the input voltage with the calibrator voltage at the nearest frequency—two measurements). For example, if the indicated value E_i' of the input voltage is dialed into the calibrator, yielding an indicated value E_c', the correct value of the input voltage is $2E_i' - E_c'$.

The FILTER FREQ (H, M, L) switch selects appropriate filtering for different frequency ranges and the PERIOD (1, 10) switch selects the integrating period. It is shown in Appendix II-B2 that maximum filtering results in a response time of about 37 s. With minimum filtering (including a 1-s integration period), the response time is approximately 19 s. This response was thought to be acceptable for general use; however as shown in Appendix II-C, it can be shortened by modifying the converter circuit.

B. Calibration

Use of low-drift film resistors and other components eliminates the need for frequent calibrations of the instrument. However, the self-contained calibrator makes it a simple matter to recalibrate the instrument any time the accuracy is in question.

The dc calibrator serves as the basic voltage reference for the instrument. It is calibrated against laboratory standards at the 1- and 5-V levels of the 1- and 10-V ranges, respectively.[11] The average of both polarities is used. Since the ac/dc difference of the MJTC (and the rms/dc converter) is very small at 1 Hz and above (< 10 ppm), the ac voltmeter (input connected to the TC DIRECT terminals) can be used as a transfer voltmeter to compare ac and dc calibrator voltages. Calibration of the ac calibrator is performed at 10 Hz, and consists of adjusting the ac reference so that the ac and dc voltages are equal at the 5-V level. The ac calibrator is then used for adjusting the gain and offset of the signal conditioner and the gain ranges of the input amplifier.

C. Overload Protection

The input amplifier is given instantaneous protection against peak voltages in excess of ±16 V by diode-coupled current sinks of 5-A capacity. Sustained overdrive blows a fuse, disconnecting the amplifier. Applying calibrator voltages to the thermal converter (via the TC DIRECT terminals) cannot damage it. However, the voltmeter can be used for high frequency measurements if driven at the TC DIRECT input by an external wide band amplifier. For this reason, the current sinks were also diode-coupled to point j of Fig. 3. Sustained overdrive may damage or open resistor $R1$ but will not damage the MJTC.

D. Performance Specifications

A brief list of the ac voltmeter/calibrator performance specifications follows.

Input signal range: 2 mV to 10 V in 12 ranges (1–2–5 sequence)

Frequency range: 0.1–50 Hz

Accuracy, percent of reading (23 ± 1°C): 0.1 percent for 0.5–50 Hz, 5 mV–10 V; 0.2 percent for 0.1–50 Hz, 2 mV–10 V

Response time (see footnote 7): Approximately 40 s for 0.1–0.5 Hz range, decreasing to 20 s for 2 Hz and above (see Appendix II-C)

Temperature coefficient of voltmeter: ±0.015 percent/°C

Calibration voltages: 0 to 7-V ac and 0 to ±10-V dc, with 7 place resolution

Calibration frequencies: 50, 10, 2, 1, 0.5, 0.2, 0.1 Hz

Calibration accuracy (23 ± 1°C): For dc voltages in range of 1–10 V, ±0.005 percent (average of both polarities). For ac voltages, ±(0.02 percent + 0.4 μV)

Temperature coefficient of calibrator: For dc voltages, ±0.0025/°C (average of both polarities). For ac voltages, ±0.005 percent/°C

Transfer accuracy: Voltmeter accuracy is improved by a factor of 4.

V. Conclusions

An rms DVM has been developed for measuring VLF's which represents an improvement of 4 to 5 times over existing equipment with respect to response time and worst case accuracy. Extensive circuit analysis (Appendix II) facilitated the choice and design of the circuits employed.

A self-contained calibrator, providing both ac and dc calibration voltages, is used for 1) calibration of the companion DVM, 2) calibration of other very low frequency voltmeters, and 3) very-high accuracy measurements, using the DVM as a transfer instrument. After initial calibration against a laboratory standard, the dc calibrator serves as the basic voltage standard for the instrument. The calibration of the ac calibrator is based on three methods: a) the transfer of the dc calibrator accuracy to the ac calibrator, using the DVM as an ac/dc transfer instrument, b) theoretical considerations, and c) peak-to-peak amplitude measurements. Theory is developed in Appendix I which relates the ac/dc difference of a TC to its lack of square-law response and the measured output ripple. Using this theory, it is shown that the ac/dc difference of the DVM is less than 10 ppm above 1 Hz but increases rapidly as the frequency is decreased. Therefore, method a) is used from 1 Hz to 50 Hz and b) below 1 Hz. Method c) is applicable to the entire frequency range and is used as an independent check on the other two methods.

The ac calibrator accuracy is 0.02 percent of dialed voltage + 0.4 μV; DVM accuracy (percent of reading) is 0.1 percent above 0.5 Hz and 5 mV and 0.2 percent below these

[11] Trim adjustments facilitate calibration of all circuits.

values. However, when the input voltage is measured by comparison with a calibrator voltage of approximately the same frequency (ac/ac transfer measurement), measurement accuracy improves by a factor of about 4.

By upgrading or changing a few components, it appears feasible to increase the ac calibrator accuracy to 50 ppm and the accuracy of ac/ac transfer measurements to 0.01 percent or better.

The DVM has a very-high input impedance (input impedance of FET voltage follower) for all ranges except the 10-V range (for which it is 200 kΩ). Therefore, it is a simple matter to extend the DVM voltage range using an external, single ratio, resistive voltage divider. Using a 1000/1 divider extends the range to 5 kV and changes the displayed voltage from millivolts to volts. Transfer measurements (ac/ac) are made the same way as before; however, their accuracies are derated by the uncertainty of the divider ratio.

Appendix I
Thermal Converter Characteristics

The transfer characteristic of a TC can be represented by a power series in I^2

$$E = \sum a_n I^n, \qquad n = 2, 4, 6, \cdots \tag{A.1}$$

on dc and ac for frequencies sufficiently high that temperature rise θ does not vary during a cycle. If the frequency is so low that $e(t)$ follows $[i(t)]^2$ without significant delay or attenuation, then

$$e = \sum a_n i^n. \tag{A.2}$$

The temperature coefficients of electrical resistivity and thermal conductivity, and the variation of the EMF versus θ characteristic cause a_4 to be significant. The a_6 and higher terms are usually smaller. Thus at VLF's,

$$e \simeq ai^2 + ab'i^4 = ai^2(1 + b'i^2). \tag{A.3}$$

For multijunction TC's, $b'i^2 \ll 1$. If $i = \sqrt{2}I \sin \omega t$, (A.3) becomes

$$e = a(I^2 - I^2 \cos 2\omega t) + \frac{ab'I^4}{2}(3 - 4 \cos 2\omega t + \cos 4\omega t) \tag{A.4}$$

The average value of e over one cycle of i (i.e., a period $T = 2\pi/\omega$) is

$$E_a = \frac{1}{T}\int_0^T \left(aI^2 + \frac{3ab'I^4}{2} + \text{cosine terms}\right)dt = aI^2 + \frac{3ab'I^4}{2}. \tag{A.5}$$

With dc applied, $E_d = aI^2 + ab'I^4$. Therefore, for the same I,

$$\frac{E_a - E_d}{E_d} = \frac{ab'I^4/2}{aI^2 + ab'I^4} \simeq \frac{b'I^2}{2}. \tag{A.6}$$

The conventional ac–dc difference δ is defined by

$$\delta = \left.\frac{I_a - I_d}{I_d}\right|_{E_a = E_d} \text{ which equals } \left.-\frac{1}{2}\frac{E_a - E_d}{E_d}\right|_{I_a = I_d} \tag{A.7}$$

from which[12]

$$\delta_l = -\frac{b'}{4}I^2 \tag{A.8}$$

where δ_l denotes the limiting low frequency ac/dc difference caused by lack of square-law response.

The constant b' can be evaluated from dc measurements. Let a dc of rated value (I_r) be applied to the TC. Its measured output EMF E_{dr} can be equated to

$$aI_r^2(1 + b'I_r^2) = E_{dr}. \tag{A.9}$$

Let the applied current be reduced to $I_r^2/\sqrt{2}$. If the TE has a perfect square-law characteristic, the output voltage is now $E_{dr}/2$. This is numerically equal to

$$\frac{aI_r^2}{2}(1 + b'I_r^2) \equiv E_s. \tag{A.10}$$

The actual measured voltage, however, should be equated to

$$\frac{aI_r^2}{2}\left(1 + \frac{b'I_r^2}{2}\right) \equiv E_d. \tag{A.11}$$

Therefore,[13]

$$b' \simeq \frac{2(E_s - E_d)}{E_d I_r^2}. \tag{A.12}$$

When a low-frequency sinewave is applied to a TC, the ratio m of peak ripple to average output EMF ranges (approximately) from 1 at very low frequencies to zero at high frequencies. Lack of square-law response has no effect on the ac/dc difference δ when $m = 0$ and a maximum effect when $m = 1$. (Equation (A.8) represents the case of $m = 1$.) The effect on δ for the case $0 < m < 1$ is considered next.

Equation (A.3) may be written as

$$e = ai^2 + ab'i^4 \equiv e_1 + \frac{b'}{a}e_1^2 \tag{A.13}$$

where $e_1 \equiv ai^2$. If $i = \sqrt{2}I \sin \omega t$ and τ is the TE time constant, it can be shown that

$$e_1 = aI^2(1 - m \cos 2\omega t) \tag{A.14}$$

where $m \equiv 1/\sqrt{1 + 4\omega^2\tau^2}$. Substituting (A.14) into (A.13) and following the same procedure as in (A.5) to (A.8) yields

$$\delta_m \simeq -\frac{b'm^2}{4}I^2 \tag{A.15}$$

where δ_m designates the low-frequency ac/dc difference (as a function of m) caused by lack of square-law response.

Appendix II

A. Transfer Characteristics of RMS/DC Converter

From Fig. 2

$$Cpe_f(t) = \frac{e_1(t) - e_2(t)}{R} \tag{A.16}$$

[12,13] These derivations were suggested by F. L. Hermach, NBS, in a private communication.

and

$$e_0(t) = k\sqrt{e_f(t)}. \tag{A.17}$$

Substituting (A.17) into (6) and then (5) and (6) into (A.16) gives

$$\tau_2 p e_f(t) = \frac{Be_a^2(t)}{1+\tau_1 p} - \frac{Bk^2 e_f(t)}{1+\tau_1 p}, \tag{A.18}$$

where $p \equiv d/dt$, B, and k are dimensional constants, τ_1 is the time constant for each thermal converter section, R is the output resistance of the thermoelement, and $\tau_2 \equiv RC$. Rearranging (A.18)

$$\left(p^2 + \frac{1}{\tau_1} p + \frac{Bk^2}{\tau_1 \tau_2}\right) e_f(t) = \frac{B}{\tau_1 \tau_2} e_a^2(t). \tag{A.19}$$

Let $2b \equiv 1/\tau_1$ and assume the system is critically damped, i.e., $1/4\tau_1^2 = Bk^2/\tau_1\tau_2$. Then, if an input voltage $e_a(t) = \sqrt{2}\, V_i \sin \omega t$ is applied at $t = 0$ and the initial conditions are zero,[14] the solution to (A.19) is

$$e_f(t) = \frac{V_i^2}{k}\left[1 - (1+bt)e^{-bt} + \frac{b^3 t e^{-bt}}{(b^2+4\omega^2)} - \frac{b^2(4\omega^2 - b^2)e^{-bt}}{(b^2+4\omega^2)^2} - \frac{b^2}{b^2+4\omega^2}\cos(2\omega t + \phi)\right] \tag{A.20}$$

where $\omega = 2\pi f$ and $\phi = \tan^{-1} 4b\omega/(b^2 - 4\omega^2)$. All of the transient terms except $bt \exp(-bt)$ can be omitted without causing significant error in the calculated response time (see footnote 7 for definition). Also, the phase angle is not needed. Applying these simplifications to (A.20), substituting in (A.17) and using a binomial series approximation yields[15]

$$e_0(t) \simeq V_i\left[1 - \frac{b^4}{16(b^2+4\omega^2)^2} - \tfrac{1}{2}bte^{-bt} - \frac{1}{2}\frac{b^2}{b^2+4\omega^2}\cos 2\omega t\right]. \tag{A.21}$$

The second term is the rms/dc conversion error caused by ripple.

If $Bk^2/\tau_1\tau_2 < 1/4\tau_1^2$, the circuit of Fig. 2 is overdamped and the solution to (A.19) contains transient terms in both $\exp(-b + \sqrt{b^2 - \omega_0^2})t$ and $\exp(-b - \sqrt{b^2 - \omega_0^2})t$, where $\omega_0^2 \equiv Bk^2/\tau_1\tau_2$. If ω_0 is less than about $0.95b$, the $\exp(-b - \sqrt{b^2 - \omega_0^2})t$ terms have little effect on the response time and can be omitted. Retaining only the largest transient term as before, the solution to (A.19) for an input $e_a(t) = \sqrt{2}\, V_i \sin \omega t$ is

$$e_f(t) \simeq \frac{V_i}{k}\left[1 - \frac{\omega_0^2 \exp[-(b - \sqrt{b^2-\omega_0^2})t]}{2\sqrt{b^2-\omega_0^2}(b - \sqrt{b^2-\omega_0^2})} - \frac{\omega_0^2 \cos 2\omega t}{2\omega\sqrt{4b^2 - 2\omega_0^2 + 4\omega^2}}\right] \tag{A.22}$$

Substituting (A.22) into (A.17) and approximating as before,[16]

$$e_0(t) \simeq V_i\left[1 - \frac{\omega_0^4}{64\omega^2(4b^2 - 2\omega_0^2 + 4\omega^2)} - \frac{\omega_0^2 \exp[-(b^2 - \sqrt{b^2-\omega_0^2})t]}{4\sqrt{b^2-\omega_0^2}(b - \sqrt{b^2-\omega_0^2})} - \frac{\omega_0^2 \cos 2\omega t}{4\omega\sqrt{4b^2 - 2\omega_0^2 + 4\omega^2}}\right]. \tag{A.23}$$

B. Ripple Filtering and Response Time

1) LP Filtering: As mentioned in the text, filtering must reduce the ripple in $e_0(t)$ by a factor of 136 at $f = 0.1$ Hz. The tradeoffs between number of poles and response time will be examined for LP filters whose poles are all real and equal.

If a unit voltage step is applied to an n-pole filter whose transfer function is $\alpha^n/(s+\alpha)^n$, the transient term which largely determines the response time for $\alpha t > 10$ is[17]

$$\frac{(\alpha t)^{n-1}}{(n-1)!} e^{-\alpha t}. \tag{A.24}$$

The response time is obtained by equating this expression to 0.0005. The attenuation factor for this filter[18] is

$$\frac{[(4\omega^2 + \alpha^2)^{1/2}]^n}{\alpha^n}. \tag{A.25}$$

Using (A.24) and (A.25), and adjusting α to hold the attenuation factor constant at 136, the calculated response times are 35, 30, 27, 26, and 25 s for n equal to 4, 5, 6, 7, and 8, respectively. Corresponding values for α are 0.385, 0.51, 0.62, 0.72, and 0.81.

The overall response time of the rms/dc converter plus filter will be computed for the 4 and 5 pole filters. Using the transient term in (A.21) as the forcing function, the response of the 4 pole filter is

$$\mathcal{L}^{-1}\left\{\frac{1}{2}\frac{b}{(s+b)^2}\cdot\frac{\alpha^4}{(s+\alpha)^4}\right\} \simeq \frac{b\alpha^4}{12}\frac{[(b-\alpha)^3t^3 - 6(b-\alpha)^2t^2 + 18(b-\alpha)t - 24]e^{-\alpha t}}{(b-\alpha)^5} \tag{A.26}$$

where $b = 0.5$ and $\alpha = 0.385$. For the 5-pole filter, the response is

$$\mathcal{L}^{-1}\left\{\frac{b\alpha^5}{2(s+b)^2(s+\alpha)^5}\right\} \simeq \mathcal{L}^{-1}\left\{\frac{\alpha^6}{2(s+\alpha)^7}\right\} \simeq \frac{(\alpha t)^6}{2(6)!}e^{-\alpha t} \tag{A.27}$$

[14] For response time determinations, initial conditions can be considered zero if the input has been zero for at least 20 s.

[15] This approximation is acceptable for the ranges of t and ω applicable to response time and rms/dc conversion error (or ripple) calculations, respectively.

[16] This approximation is acceptable for the ranges of t and ω applicable to response time and rms/dc conversion error (or ripple) calculations, respectively.

[17] Symbol s is the Laplace transform variable.

[18] Reciprocal of its transfer function. See footnote 10.

where $\alpha = 0.51$. The computed response times using the 4 and 5 pole filters are 38 and 34 s, respectively.

2) LP Filtering Plus Integration: A second approach to the filtering requirement is to perform part of the filtering by integration in the dc voltmeter. If the integration period is T_i, perfect filtering of the ripple frequency ($2f$) occurs for input frequencies of $f = n/2T_i$, where $n = 1, 2, 3, 4, \cdots$. Minimum filtering occurs for $f = (n + \frac{1}{2})/2T_i$ and, depending upon the phase of the ripple relative to the start of the integration period, approaches a minimum attenuation factor of $2\pi f T_i$. If $T_i = 10$ s, its minimum value is 7.85 at $f = 0.125$ Hz. (It is convenient to use integration periods of 1 and 10 s in the dc DVM.) Using (A.21), the peak ripple from the converter at 0.125 Hz is $V_i/21.74$. Therefore, the attenuation factor required for the LP filter is $2000/(7.85)(21.74) = 11.7$. According to (A.25), a 2 pole filter with $\alpha = 0.48$ meets this requirement. A good approximation to the overall response time t_f of the converter plus this filter results if we average their time constants ($b = 0.50$, $\alpha = 0.48$) and equate (A.24) to 0.0005.

$$\frac{1}{2}\frac{(0.49t_f)^3}{6}e^{-0.49t_f} = 0.0005 \tag{A.28}$$

from which $t_f = 26$ s. The factor of $\frac{1}{2}$ is introduced by the SR circuit. (See (A.21).)

The integrator can start integrating at some time t_1 prior to t_f without exceeding a residual transient value of 0.05 percent. Integrating the most significant transient in the filter output over a 10-s period (starting at $t = t_1$), taking its average and equating to 0.0005:

$$T(t_1) \equiv \frac{1}{10}\int_{t_1}^{t_1+10}\frac{(\alpha t)^3}{12}e^{-\alpha t}\,dt = 0.0005$$

$$T(t_1) = \frac{1}{10}\cdot\frac{\alpha^3}{12}\left\{-\frac{e^{-\alpha t}}{\alpha^4}\left[(\alpha t)^3 + 3(\alpha t)^2 + 6(\alpha t) + 6\right]_{t_1}^{t_1+10}\right\}. \tag{A.29}$$

Only the highest degree term for the lower integration limit needs to be retained, yielding

$$T(t_1) \simeq \frac{1}{10\alpha}\left[\frac{(\alpha t_1)^3}{12}e^{-\alpha t_1}\right] = 0.0005. \tag{A.30}$$

Setting α equal to 0.49 and solving for t_1 gives 21.6 s. There is no simple method of synchronizing the integrator with t_1. If integration starts at t_1, the ac voltmeter response time is $22 + T_i = 32$ s. If it starts before t_1, two integration periods are required and the response time approaches 42 seconds. Therefore, the average response time is 37 s.

C. Improved Converter Response Time

For the upper decade or so of input frequencies, response time is limited by the time constant τ_1 of the MJTC. This can effectively be shortened by placing a resistance r in series with capacitance C (Fig. 2). Equation (A.16) now becomes

$$\frac{Cp}{1 + rCp}e_f(t) = \frac{e_1(t) - e_2(t)}{R}. \tag{A.31}$$

Substituting (A.17) into (6) and then (5) and (6) into (A.31) gives

$$CRpe_f(t) = (1 + rCp)\frac{Be_a^2(t)}{(1 + \tau_1 p)} - \frac{Bk^2 e_f(t)}{(1 + \tau_1 p)}. \tag{A.32}$$

Rearranging (A.32) and letting $\tau_2 \equiv RC$ and $\tau_3 \equiv rC$,

$$\left[p^2 + \frac{1}{\tau_1}\left(1 + \frac{Bk^2\tau_3}{\tau_2}\right)p + \frac{Bk^2}{\tau_1\tau_2}\right]e_f(t) = \frac{B}{\tau_1\tau_2}(1 + \tau_3 p)e_a^2(t). \tag{A.33}$$

Let $2b \equiv (1/\tau_1)(1 + [Bk^2\tau_3/\tau_2])$, $\omega_0^2 \equiv Bk^2/\tau_1\tau_2$ and assume that $b^2 = \omega_0^2$. Also, let $e_a(t)$ in (A.33) be a unit step. Then, solving for $e_f(t)$ and substituting into (A.17) yields[19]

$$e_0(t) \simeq 1 - \tfrac{1}{2}(1 + bt - b^2\tau_3 t)e^{-bt}. \tag{A.34}$$

If $\tau_3 = 0$ (i.e., $r = 0$), equation (A.33) reduces to (A.19). Let $e_a(t)$ be a unit step and solve (A.19) for $e_f(t)$. Substituting this result into (A.17) gives[20]

$$e_0(t) \simeq 1 - \tfrac{1}{2}(1 + bt)e^{-bt}. \tag{A.35}$$

The circuits represented by (A.34) and (A.35) have response times largely determined by the factor $\exp(-bt)$. However, the b in (A.34) is $(1 + Bk^2\tau_3/\tau_2)$ times larger than the b in (A.35). Therefore, adding a resistance r in series with capacitance C (Fig. 3) shortens the response time by nearly a factor of $(1 + Bk^2\tau_3/\tau_2)$.

Let $e_a(t) = \sqrt{2}\,V_i \sin \omega t$ in (A.33). Solving for the steady-state value of $e_f(t)$ and substituting into (A.17) results in[21]

$$e_1(t)_{ss} \simeq \left(1 - \frac{Z^2}{16} - \frac{Z}{2}\cos 2\omega t\right)V_i \tag{A.36}$$

where $Z \equiv b^2\sqrt{1 + 4\omega^2\tau_3^2}/(4\omega^2 + b^2)$. This equation shows that adding r moves the -3-dB point of the ripple attenuation versus ripple frequency characteristic up by at least a factor of $(1 + Bk^2\tau_3/\tau_2)$, and changes the slope of the attenuation characteristic from -12 dB/octave to -6 dB/octave. (Compare (A.36) with (8).)

Acknowledgment

The author is grateful to B. A. Bell for helpful suggestions on the manuscript and to F. L. Hermach for helpful discussions on thermal converters.

References

[1] R. S. Koyanagi, "Development of a low-frequency-vibration calibration system," *Experimental Mechanics*, vol. 15, no. 11, p. 3, Nov. 1975.

[2] R. S. Koyanagi and J. D. Pollard, "Piezoelectric accelerometer low-frequency response by signal insertion methods," NBSIR 74-597, pp. 3–4, May 1975 (Final Report).

[3] F. L. Hermach, "ac–dc comparators for audio-frequency current and voltage measurements of high accuracy," *IEEE Trans. Instrum. Meas.*, vol. IM-25, pp. 489–494, Dec. 1976.

[4] *Nonlinear Circuits Handbook*. Norwood, MA: Analog Devices, Inc., 1974.

[5] F. J. Wilkins, T. A. Deacon, and R. S. Becker, "Multijunction thermal

[19,20,21] See footnote 15.

converter," *Proc. Inst. Elec. Eng.*, vol. 112, no. 10, Oct. 1965.
[6] L. G. Cox and N. L. Kuster, "An automatic rms/dc comparator," *IEEE Trans. Instrum. Meas.*, vol. IM-23, pp. 322–325, 1974.
[7] H. Handler, "A hybrid circuit rms converter," in *IEEE Int. Solid State Circuit Conf. Dig.*, vol. 14, p. 190, Feb. 1971.
[8] W. E. Ott, "A new technique of thermal rms measurement," *IEEE J. Solid State Circuits*, vol. SC-9, pp. 374–380, Dec. 1974.
[9] J. B. Folsom, "Measuring true rms ac voltages to 100 MHz," *Hewlett-Packard J.*, vol. 23, no. 7, p. 17, Mar. 1972.
[10] F. L. Hermach, "An investigation of multijunction thermal converters," *IEEE Trans. Instrum. Meas.*, vol. IM-25, pp. 524–528, Dec. 1976.
[11] F. J. Wilkins, "Theoretical analysis of the ac/dc transfer difference of the NPL multijunction thermal converter over the frequency range of dc to 100 kHz," *IEEE Trans. Instrum. Meas.*, vol. IM-21, pp. 334–340, Nov. 1972.
[12] H. K. Schoenwetter, "A high speed, low noise 18 bit digital-to-analog converter," to be published.

VHF Loop Antenna Loss Measurements

KENNETH M. UGLOW, SENIOR MEMBER, IEEE

Abstract—**The product of the loss ratios of two very small loop antennas, oriented such that their axes coincide, is given approximately by**

$$L_1 L_2 = A(1.5)^{-2}(1 + k^2d^2)^{-2}(kd)^6$$

where L_1 and L_2 are the dissipative power loss ratios of the loops, d is the spacing between the loops, and $k = 2\pi/\text{wavelength}$. A is the insertion loss measured between the ports of the two loops including their matching networks. The loops are assumed to be impedance-matched to the generator and to the load, respectively.

A relationship is developed which takes into account the effects of the receiving loop current on the transmitting loop mesh. This makes possible measurements with more closely spaced loops than otherwise, without incurring intolerable errors. The minimum useful spacing depends on the loss ratios, being greater for more efficient antennas. For small antennas with practical loss ratios, the measurements can be made on the laboratory bench or in production test without special antenna test facilities. A more nearly exact field expression due to F. M. Greene is utilized for loops of appreciable size.

I. Introduction

WHEN USING loop antennas for signal reception at very high frequencies where receiver noise limits sensitivity, we strive to obtain the greatest available signal power by minimizing the dissipative loss in the loop and its impedance-matching network. Although the loop may be intentionally mismatched to the receiver input for an optimum noise figure, it is useful to be able to measure the efficiency of the antenna when connected to a matched load. For small loops with practical losses, this measurement can be made "on the bench" without an antenna range or special facilities such as the "bear trap" described in [1].

There are attractions to making these measurements on the bench. The distances used can be small (say less than a foot at 150 MHz). If we use a reasonable receiver as the detector, the field strengths needed are so low that we do not annoy other services in the vicinity. The field strength drops off so rapidly with distance that objects nearby (such as test equipment, people, walls, etc.) may not create reflections strong enough to be annoying. The potential advantages for production testing are obvious.

The sensitivity of receivers with built-in loops can also be measured on the bench. This is done using a transmitting loop whose efficiency has been evaluated using the measurement and calculation procedure described in this paper. The magnetic field due to the transmitting loop in terms of signal generator available power, loop efficiency, and distance between transmitting and receiving loops is derived in Appendix A. The receiver sensitivity in terms of electric field strength (microvolts per meter) is readily obtained from the magnetic field measurement.

The technique involves making insertion loss measurements in the manner described by Yokoshima [2]. In our approach, however, we take the view that the antennas have been impedance matched to, say, a 50- or 75-Ω system. Also, instead of deriving Yokoshima's "loop antenna factor" we derive directly the product of the power loss ratios of the two antennas. If the antennas are somewhat mismatched to the system impedance, the losses measured include the mismatch losses.

Manuscript received November 21, 1977.
The author is an Independent Research Consultant, Box 2260, Sarasota, FL 33578.

0018-9456/78/0900-0268$00.75

II. Discussion

The analysis on which this method is based is a bit lengthy. Since mathematical expositions frequently obscure understanding, it may be well to point out the key physical principles. The magnetic field strength of the transmitting loop is proportional to the product of current and loop area. The voltage induced in the receiving loop is proportional to magnetic field strength and loop area. The ratio of receiving loop voltage to transmitting loop current is the mutual impedance between the loops, a complex function of distance between loops and the product of the loop areas. The loop areas are then expressed in terms of the radiation resistances of the loops.

The radiation resistances can be expressed in terms of loop efficiencies and total equivalent resistance in the transmitting and receiving circuit meshes. The product of the two loop-loss ratios is then expressed in terms of mutual impedance and mesh resistances. The insertion loss between signal generator and detector is determined by these same quantities, which are replaced by the insertion loss which is measurable. We then find the product of the loop-loss ratios in terms of measured insertion loss and a complex function of distance (spacing between loops). Using efficiency or loss in each of the loops, along with the radiation resistance (related to the far field), we avoid needing to know transmitting loop current or receiving loop voltage, which at VHF require difficult measurements.

III. Measurement Procedure

The procedure requires two or three loop antennas. If only two are available, the results will give the product of the loss ratios of the two antennas. If they can be assumed identical, the loss due to each one will be the square-root of the overall loss ratio (or one half the loss expressed in decibels). If a third antenna is available, each of the other two can be used with the third to determine the difference between their decibel losses. Knowing the sum and the difference of the decibel losses, we can solve for each individually.

Fig. 1 is a schematic diagram of the measurement setup. The planes of the two loops are parallel, and their axes coincide. The solid lines show the connections for transmitting by way of the loops. The broken line indicates a direct connection between the generator and the detector. With the direct connection, the the signal-generator attenuator is adjusted to give a reference reading on the detector meter. Connections are then made through the loop path, and the attenuator is readjusted to achieve the reference meter reading. The difference between the attenuator settings (in decibels) is the insertion loss due to the matching networks, loops, and transmission path. Measurements should be made for various distances d between the centers of the loops.

The power P_2 at the detector input is that value which produces the reference level reading. The power P_1 at the signal generator output is that required to produce the reference level reading when transmitting through the loops. In the following discussion, we will be speaking of available

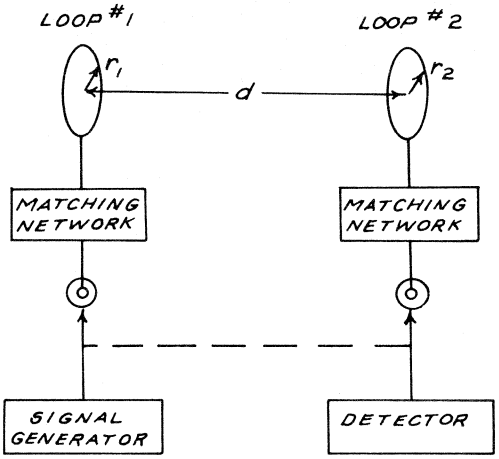

Fig. 1. Measurement setup.

powers and will assume that the detector impedance is matched to the signal generator impedance, thereby skirting a discussion of mismatch loss evaluation. When the detector is matched to the generator, the loss ratios determined by this procedure include mismatch losses at the interfaces between the antenna ports and the generator/detector ports.

IV. Calculation Procedure

Having made measurements of insertion loss between the ports of two loops, we can calculate the product of their losses $L_1 L_2$ with the following relationships:

$$L_1 L_2 = k^6/(1.5Fx)^2 \tag{1}$$

where

$$k = 2\pi/\lambda \quad \text{m}^{-1} \tag{2}$$

λ = wavelength m

$$x = (1/A)^{1/2}, \text{ approximately} \tag{3}$$

A = measured insertion loss (power ratio) less than unity.

The exact definition of x is

$$x = -2\cos a + [(1/A) - 4\sin^2 a]^{1/2}. \tag{3a}$$

The angle a is given by

$$a = (\pi/2) - kd + \tan^{-1} kd \quad \text{rad.} \tag{4}$$

The factor F describes the variation of axial magnetic field with distance along the loop axis. For loops small compared to the wavelength and compared to the spacing between loops

$$F = (1 + k^2d^2)^{1/2}/d^3, \text{ approximately} \tag{5}$$

where d is the distance between loops in the same units as the wavelength. For circular loops, F. M. Greene [3] has developed a more exact field expression, including averaging of the field over the area of the receiving loop, from which

$$F = \left[1 + \frac{15}{8}\left(\frac{r_1 r_2}{D^2}\right)^2 + \frac{315}{64}\left(\frac{r_1 r_2}{D^2}\right)^4 + \cdots\right] \cdot (1 + k^2D^2)^{1/2}/D^3 \tag{5a}$$

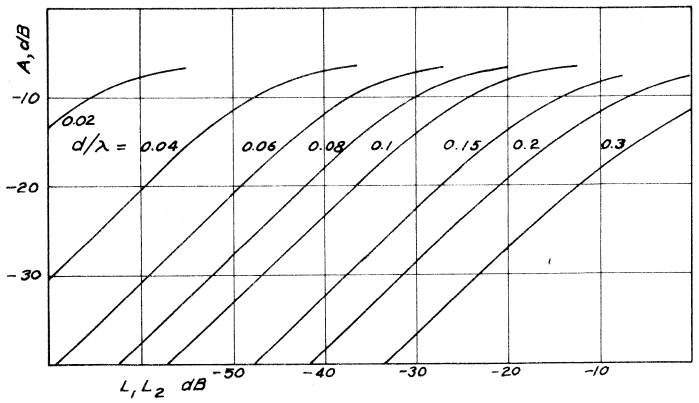

Fig. 2. Approximate insertion loss versus loss product.

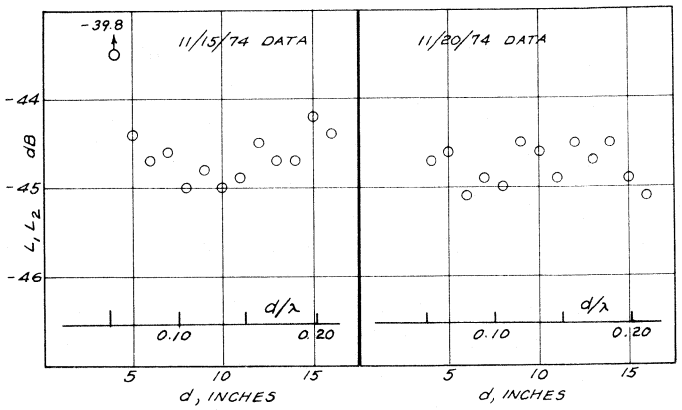

Fig. 3. Loss product from measured data.

where

$$D = (d^2 + r_1^2 + r_2^2)^{1/2} \text{ m.} \quad (6)$$

r_1 is the radius of one loop and r_2 is the radius of the other loop. Greene states that (5a) is correct to within 0.2 percent, provided $r_1 r_2 / D^2$ is 1/16 or less and kD is less than unity.

Fig. 2 shows the nature of the relationship between insertion loss and loss product for various loop spacings. It does not include the effect of nonzero loop size, and therefore is very inaccurate at small spacings. The minimum insertion loss, based on the derivation in Appendix A, is -6 dB, regardless of the loss ratio. This corresponds to unity coupling between the loops.

The working equations are derived in Appendix A. Appendix B presents plots of the effects of approximations (3) and (5) in order to be able to judge when these simpler working equations suffice for the needs at hand. The plots also permit correction for the use of (3) and (5).

V. Measurement Results

We have very little experimental data to back up our analysis, and are unaware of others who have taken this approach. In 1974, the author constructed two 1.125-in square loops in order to test some of the ideas contained in this paper. At that time, there was no procedure for taking into account the mutual impedance effects, his development being based on field theory. The data from these tests were recently analyzed to find the loss product for the two loop antennas including their matching networks. The frequency used was 156.425 MHz. No special design was used to minimize the losses. The results are plotted in Fig. 3 for two series of measurements.

There is some recollection of erratic behavior at the closest loop spacing, but this was not discussed in the laboratory notes. In the first series, the point at 4-in spacing is about 5 dB away from the rest of the group. In the second series, this point is consistent with the rest of the group. We have since discovered that a narrow-band receiver used as the detector could cause undetected errors due to signal generator mistuning, but this does not rule out the possibility of some other unrecognized physical effect.

The setups for the two series were different in several respects. The first series was made on the laboratory bench with several items of equipment within a foot or so of the antennas. The detector had unknown input impedance, and also had the possibility of multivalued input–output transfer. The signal generator had 2-dB dial increments, and was read to 0.5 dB. In the second series, the detector was a wide-band receiver with input padding. A second receiver monitored the frequency to detect interference. The attenuator was read to 0.2 dB. The clearance between antennas and adjacent structures (except for the antenna supports) was three feet or greater.

For the first series, the mean value of $L_1 L_2$ is -44.66 dB, with a sample standard deviation of 0.25 dB, discarding the wild point at 4-in spacing. For the second series, the mean is -44.77 dB; the sample standard deviation is 0.23 dB. Considering the limitations of the author's laboratory, this consistency is gratifying, and appears to validate the circuit analysis. Validation is still needed, however, for low-loss antennas where the radiation resistance is a substantial portion of the mesh resistance.

VI. Measurement Sensitivity

When the measured insertion loss, in decibels, is more negative than, say, -20 dB, the calculated loss product is approximately proportional to the numerical insertion loss A. Under such conditions, 1-dB error in measuring insertion loss results in about 1-dB error in the calculated loss product $L_1 L_2$. As we bring the loops closer than the spacing which produces -20-dB insertion loss, the loss product error becomes more sensitive to insertion loss error. We have derived the partial derivative of the log loss product with respect to the log insertion loss, which we call G. For small errors, the decibel error in loss product is G times the decibel error in insertion loss. The results, obtained with numerical differentiation, are plotted in Fig. 4.

G is a function of the insertion loss A and the quantity x defined earlier, which in turn depends on the phase angle of the mutal impedance and hence distance in wavelengths. Distance in wavelengths is the parameter for the curves of G versus insertion loss. If the insertion loss is more negative than -9 dB for the spacings of less than 0.1 wavelength, the error ratio G will be less than about 2, which should be tolerable. When these conditions are obtained, the loss product is more negative than -20 dB. For a pair of antennas as used in pocket receivers, we might expect loss products between -30 and -50 dB.

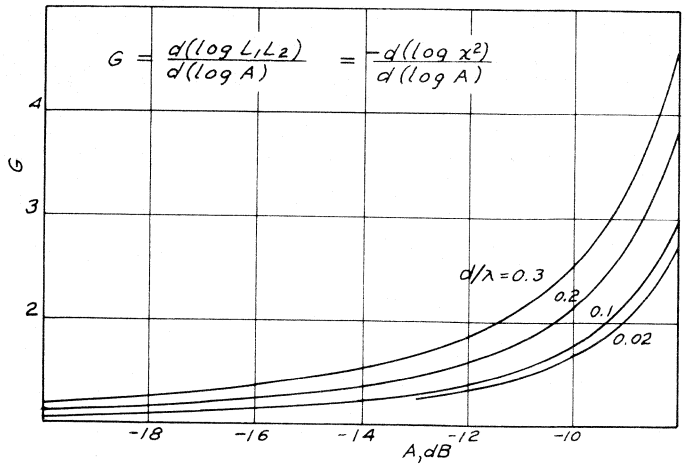

Fig. 4. Sensitivity to insertion loss errors.

If we were to obtain efficiencies giving −10-dB loss product, for example, we would expect about −12-dB insertion loss for D equal to 0.2 wavelengths which give a tolerable value of G. On the other hand, measurements for a wide range of spacings larger than 0.2 wavelength will require more care than in the lossy case above, with respect to disturbances from equipment and structures in the vicinity of the antennas. If the spacing is reduced to, say, 0.1 wavelength, we would expect the insertion loss to flatten out below 0.15 wavelengths, resulting in large values of G.

The derivation of G does not depend on the form of the factor F, which depends on loop size. It does, however, depend on the phase angle, which we know accurately for only negligibly small loops. Therefore, this discussion should be viewed as somewhat qualitative, to provide cautions. The actual sensitivity in a given situation can be determined by calculating the loss product for the observed value of insertion loss and again for that value plus an increment representing possible measurement error. The same may be done for uncertainties in the spacing d, particularly where multiturn loops are used which have appreciable thickness in the axial direction.

Appendix

A. Derivations

Slater [4, p. 233] gives us the radial magnetic field of a small loop, in complex form. Taking into account the phase shift with respect to distance, we find the complex field H along the loop axis

$$H = (I_1 A_1/2\pi)F \angle b \quad \text{(complex) rms A/m} \tag{7}$$

where

I_1 rms current in loop (complex) A

A_1 transmitting loop area m^2

$$F = (1 + k^2d^2)^{1/2}/d^3 \quad m^{-3} \tag{8}$$

d distance along loop axis m

$$k = 2\pi/\lambda \tag{9}$$

λ wavelength m

$$b = -kd + \tan^{-1} kd \quad \text{rad.} \tag{10}$$

For circular loops of appreciable size, Greene [3] has developed a field expression which includes the average of the magnetic field over the area of the receiving loop. Based on his work, a more nearly exact expression for F is

$$F = \left[1 + \frac{15}{8}\left(\frac{r_1 r_2}{D^2}\right)^2 + \frac{315}{64}\left(\frac{r_1 r_2}{D^2}\right)^4 + \cdots\right] \cdot (1 + k^2D^2)^{1/2}/D^3 \tag{11}$$

where

$$D = (d^2 + r_1^2 + r_2^2)^{1/2} \text{ m.} \tag{12}$$

r_1 is the radius of one loop, r_2 the radius of the other. We do not have an exact value of phase angle b for this case.

The voltage induced in the receiving loop V_2 is given by

$$V = 2\pi f(\mu\text{H})A_2 \angle \pi/2 \quad \text{(complex) rms V} \tag{13}$$

f radio frequency Hz

μ permeability of vacuum, $4\pi \cdot 10^{-7}$ H/m

A_2 receiving loop area m^2.

The phase angle $\pi/2$ and the factor $2\pi f$ are due to the voltage's being proportional to the time derivative of the flux.

Slater [4, p. 234] gives us the radiation resistance of the small loops from which we derive

$$A_1 = (6\pi R_{r1})^{1/2}(\lambda/2\pi)^2(\mu/\varepsilon)^{1/4} \quad m^2 \tag{14}$$

R_{r1} radiation resistance of transmitting loop, ohms

ε permittivity of vacuum, $8.854 \cdot 10^{-12}$ F/m.

Similarly

$$A_2 = (6\pi R_{r2})^{1/2}(\lambda/2\pi)^2(\mu/\varepsilon)^{1/4} \quad m^2 \tag{15}$$

R_{r2} radiation resistance of receiving loop.

The complex mutual impedance Z_m from (7) and (13) is given by

$$Z_m = V_2/I_1 = f\mu A_1 A_2 F \angle a \quad \text{(complex) ohms} \tag{16}$$

$$a = b + \pi/2 = (\pi/2) - kd + \tan^{-1} kd \quad \text{rad.} \tag{17}$$

Substituting the expressions for A_1 and A_2 from (14) and (15) and noting that $f\lambda = (\mu\varepsilon)^{-(1/2)}$, the speed of light in vacuum

$$Z_m = 3(R_{r1}R_{r2})^{1/2}(1/k)^3 F \angle a. \tag{18}$$

Fig. 5 is a simplified equivalent circuit representing the two loops inserted between the signal generator and the load. The load resistance R_L equals the signal generator resistance R_g. R_{r1} is the radiation resistance and R_{d1} is the loss resistance of the transmitting loop, transformed to the port connected to the signal generator. The net circuit reactance is made zero in matching the generator. Similar definitions and conditions apply to the receiving loop, for which the subscript 2 is used. For matched conditions

$$R_L = R_g = (R_{r1} + R_{d1}) = (R_{r2} + R_{d2}) = R/2 \tag{19}$$

where R is defined as the total resistance in each mesh.

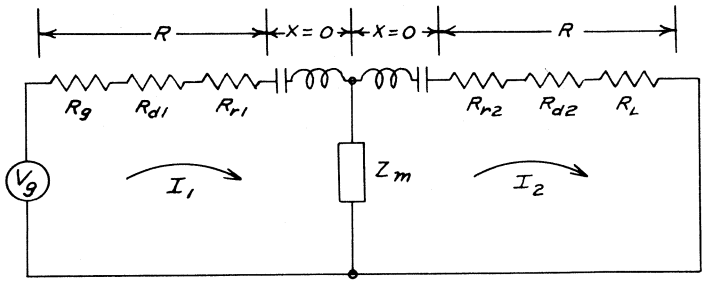

Fig. 5. Equivalent circuit for loop transmission.

The efficiency of each loop is defined as a power loss ratio. For the transmitting loop, the ratio L_1 is

$$L_1 = R_{r1}/(R_{r1} + R_{d1}) = 2R_{r1}/R \tag{20}$$

and for the receiving loop

$$L_2 = R_{r2}/(R_{r2} + R_{d2}) = 2R_{r2}/R. \tag{21}$$

We can now replace the radiation resistances (unknowns) in the expression (18) for Z_m by the following:

$$R_{r1}R_{r2} = L_1 L_2 R^2/4 \tag{22}$$

$$Z_m = (3/2)R(L_1 L_2)^{1/2}(1/k)^3 F \angle a. \tag{23}$$

For convenience, we define a scalar ratio x as follows:

$$x = |R/Z_m| = (2/3)(L_1 L_2)^{-(1/2)}k^3/F \tag{24}$$

from which we obtain (1):

$$L_1 L_2 = k^6/(1.5Fx)^{-2}. \tag{25}$$

We now proceed to find x as a function of the measured insertion loss, again using the equivalent circuit of Fig. 2, from which

$$I_2/V_g = (2R + R^2/Z_m)^{-1} \tag{26}$$

$$= R^{-1}(2 + x\angle -a)^{-1} \quad \text{(complex)}. \tag{27}$$

Next, we derive the insertion loss. The signal generator available power P_1 is given by

$$P_1 = |V_g|^2/4R_g = |V_g|^2/2R \quad \text{(scalar)}. \tag{28}$$

The power P_2 delivered to the load is given by

$$P_2 = |I_2|^2 R_L = |I_2|^2 R/2 \quad \text{(scalar)}. \tag{29}$$

The insertion loss A is the ratio of these powers

$$A = P_2/P_1 = |I_2/V_g|^2 R^2 \quad \text{(scalar)}$$

$$= |2 + x\angle -a|^{-2} = |2\angle a + x|^{-2}$$

$$= [(2\cos a + x)^2 + (2\sin a)^2]^{-1}. \tag{30}$$

This is a quadratic in x, one of whose solutions is

$$x = -2\cos a + (A^{-1} - 4\sin^2 a)^{1/2} \tag{31}$$

which is the working equation (3a). A is the measured insertion power loss ratio and a is the phase angle of the mutual impedance given by (17), a function of the loop spacing in wavelengths.

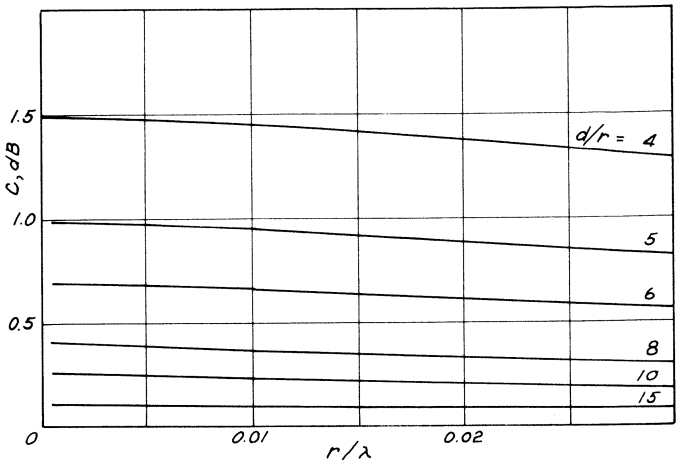

Fig. 6. Correction for size of circular loops.

Although we have stated previously that the measured efficiency includes impedance-mismatch losses, we did not include mismatch in the simple equivalent circuit. When Z_m is very small compared to the circuit resistances, the effect of mismatch will be as stated. We have not proven, however, that this is valid for all loop spacings and efficiencies. Calculation of $L_1 L_2$ for a wide range of spacing (say from $d = 0.05$ to $d = 0.25$) should detect possible errors due to this and other effects, because $L_1 L_2$ is independent of d.

We can find the axial magnetic field of the transmitting loop knowing the signal generator available power and the loop efficiency. The power radiated by the loop P_t:

$$P_t = |I_1|^2 R_{r1} = P_1 L_1 \quad \text{W} \tag{32}$$

$$R_{r1} = (k^4/6\pi)(\mu/\varepsilon)^{1/2}A_1^2 = 19.986k^4 A_1^2 \quad \text{ohms}. \tag{33}$$

From (32) and (33), we obtain the rms magnetic moment:

$$|I_1|A_1 \approx (P_1 L_1/20)^{1/2}(1/k)^2 \quad \text{(scalar)}. \tag{34}$$

Substituting in (7) gives

$$|H| = (P_1 L_1/20)^{1/2}(1/k)^2 F/2\pi \quad \text{rms A/m}. \tag{35}$$

B. Approximations

Substituting (3) and (5) in (1) gives the following simple form for calculating the loss product from measured values of d and A:

$$L_1 L_2 = A(1/1.5)^2(kd)^6/(1 + k^2 d^2). \tag{36}$$

This ignores the nonzero loop size and the first term in parentheses in (27).

The effect of ignoring loop radius is plotted in Fig. 6 for two loops of equal radius. The factor C in decibels is to be added to $L_1 L_2$ in decibels when $L_1 L_2$ is calculated from (36). $L_1 L_2$ (in decibels) is negative. C is positive, therefore, including Greene's relationship gives a more favorable value for $L_1 L_2$.

The second approximation we refer to as the mutual impedance correction. Equation (36) can be derived from field theory alone without considering the reaction of I_2 on

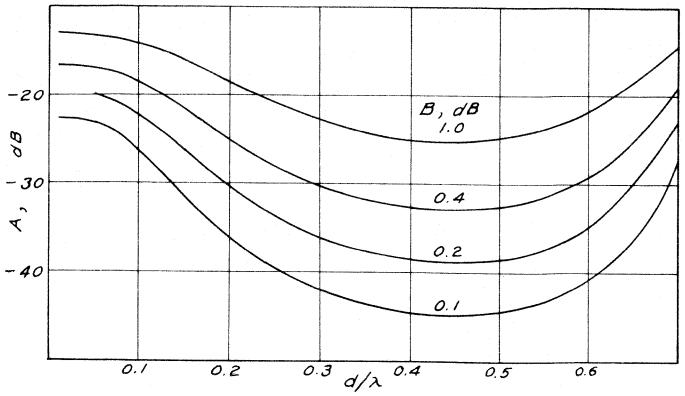

Fig. 7. Correction for mutual impedance effect.

the transmitting loop mesh, and therefore may need correction. The needed correction in decibels is plotted in Fig. 7. It is positive over the range plotted, but is not so for all spacings because it depends on the phase angle of Z_m. A positive decibel value for the correction B indicates a more favorable (less negative decibel) value for $L_1 L_2$ than that given by (36).

Note that the mutual impedance phase angle was derived on the basis of negligibly small loop size. We do not have the effect on phase angle due to nonzero size but believe it to be small.

References

[1] D. Mitchell and K. G. Van Wynen, "150-MC personal radio signaling system," *IRE Trans. Veh. Commun.*, vol. VC-10, pp. 57–70, Aug. 1961.
[2] I. Yokoshima, "Absolute measurements for small loop antennas for RF magnetic field standards," *IEEE Trans. Instrum. Meas.*, vol. IM-23, pp. 217–221, Sept. 1974.
[3] F. M. Greene, "NBS field-strength standards and measurements (30 Hz to 1000 MHz)," *Proc. IEEE*, vol. 55, no. 6, pp. 970–981, June 1967.
[4] J. C. Slater, *Microwave Transmission*, 1st ed. New York: McGraw-Hill, 1942.

Bandpass Filter Comparator for Confirming the Absence of Serious Internal Voids in Wood Poles

A. DOUGLAS SHAW

Abstract—**Structural timber is frequently exposed to weather and is thus subject to decay and consequential strength loss which eventually requires the replacement of the affected member. When decay is internal, destructive investigation is the only direct way of detecting it. This is obviously undesirable and a frequently used alternative is to tap each member with a hammer. A conclusion is reached by listening to the sound emitted. Because this sound is composed of many different frequencies which vary in magnitude and spectrum from one member to another, the result of the test is uncertain. Research has revealed that a definite sonic frequency range exists for a class of members such as poles used for electricity distribution purposes. Part of this range is common to all members regardless of condition, but there is another part which is greatly affected by the presence of hollowness or decay. A double bandpass filter arrangement has been constructed to register the presence and magnitude of frequencies relating to hollowness or decay and to measure this magnitude against the magnitude of frequencies always present. The member under test is excited by a series of blows of equal force and a ratio established between the signals from each filter, the *A* low ratio indicates a solid section. A high ratio indicates that the section may be hollow or decayed.**

Manuscript received January 24, 1978; revised May 17, 1978.
The author is with the Retail Supply Branch, Hydro-Electric Commission of Tasmania, Tasmania, Australia.

I. Introduction

THE CRUDE but time-honored method of declaring electricity distribution and communication poles safe, whereby the inspector strikes the pole with a hammer and listens to the note emitted, was the point at which investigations commenced. One must not be too critical of this old method as it has served the industry well since its inception. It can however, be seen as being somewhat wasteful and occasionally risky because the region of doubt is rather large, and intuition on the part of the inspector seems to play a role in determination of pole condition.

0018-9456/78/0900-0273$00.75 © 1978 IEEE

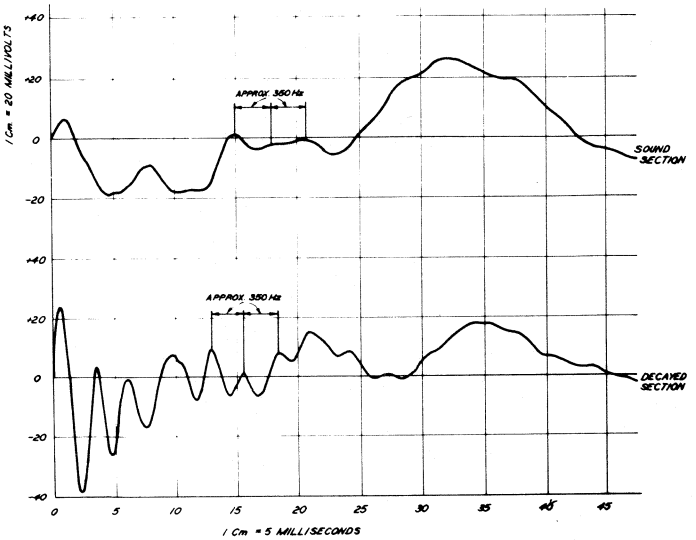

Fig. 1. Oscillographs of pole cross sections.

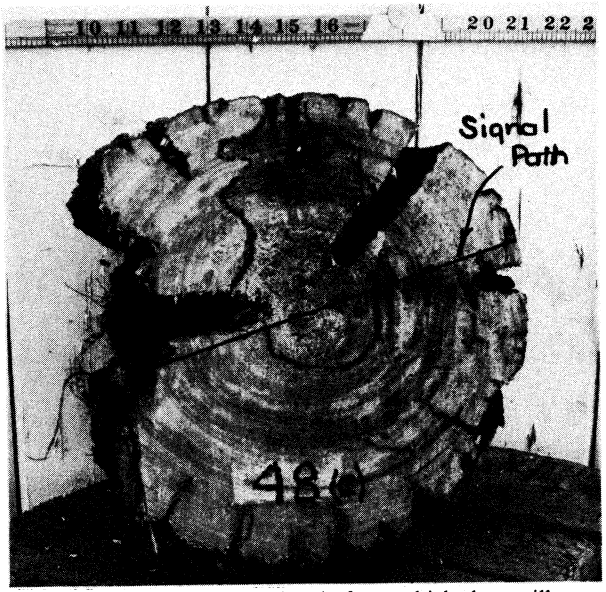

Fig. 2. Cross section of decayed pole from which the oscillographs of Fig. 1 were obtained.

II. Basic Investigations

The species of poles investigated were Eucalyptus Globulus and Eucalyptus Obliqua and the aim of preliminary investigations was to examine the aural differences by which the inspector reaches his decisions. It was soon apparent, by using oscilloscope methods, that sound poles did produce traces which were usually different from those generated when significant hollows or regions of decay were present. Fig. 1 is a typical example, the upper trace relating to the good part of a pole and the lower trace relating to a seriously decayed portion of the same pole which is shown in Fig. 2.

It will be seen from Fig. 1 that there is a large amplitude frequency around 350 Hz present in the lower trace and also a suggestion of the same frequency in the upper trace.

An accelerometer and a tunable bandpass filter with meter and memory, and having a range from 20 to 2000 Hz, were used for detailed examination of the signals from good and deteriorated poles. There appeared to be no clear

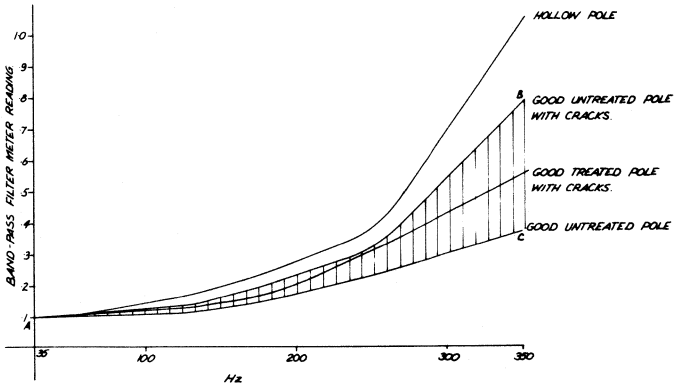

Fig. 3. Graphs of signal response for various classes of pole.

relationship between pole condition and graphical features above 400 Hz. However, below 400 Hz, amplitudes of various frequencies were seen to be related to pole condition in a fairly regular manner. When the carpenter's hammer was replaced with an electromagnetic hammer delivering a continuous stream of precisely controlled blows, the situation clarified further. The results are shown in Fig. 3 where graphs for all sound poles are found to be contained within the envelope *ABC*.

These results suggest that the response to frequencies up to about 140 Hz is similar in all poles regardless of defects, whereas beyond this and increasingly up to 350 Hz, there are marked amplitude changes which correspond to good poles and deteriorated ones. The results were independent of the zone of test, provided that sampling did not occur lower than 100 mm above the ground line, the proximity of which appeared to have a damping effect at higher frequencies. In addition, the results lost consistency if the position of the hammer relative to the listening point departed too far from a diameter or too far from a right angle measured axially along the pole.

III. Prototype for Field Use

The consistency of results justified an extended investigation to test their validity over a larger sample of poles. Accordingly, a simple double bandpass filter comparator of active filters was constructed, one filter to operate at 100 Hz and one to operate at 350 Hz. 100 Hz was selected for the frequency of the lower filter because, according to Fig. 3, it was still low enough to produce wide differences between the amplitude of frequencies in the region of 400 Hz and yet contained a consistently low variation of amplitude for all specimens regardless of class. 350 Hz was selected for the higher filter as this was well clear of the region where random results commenced above 400 Hz, yet produced high amplitudes when compared with those at 100 Hz.

The drive device was a simple squarewave multivibrator amplifier which supplied an electromagnetic hammer attached solidly to the pole by a 75-mm nail and operated at 40 Hz. The frequency of operation of the amplifier was selected so that there would be no interference between this frequency and the filter frequencies in regard to the possible effects of harmonics on the shape of the curves as defined in Fig. 3. The signal was detected by a piezoelectric transducer

TABLE I

DISTRICT	RATIO BELOW 1:8		RATIO ABOVE 1:8	
	POLE SECTIONS GOOD	POLE SECTIONS BAD	POLE SECTIONS GOOD	POLE SECTIONS BAD
Burnie	113	0	0	0
Devonport	360	0	119	34
George Town	210	0	9	1
Hobart	1 266	0	15	8
Longford	310	0	212	45
Sorell	70	0	0	0
TOTAL	2 329	0	355	88

attached to the pole in similar fashion to the transmitter, both devices being on opposite ends of the same diameter through the pole. The signal was switched in turn to the 100- and 350-Hz filters and thence to a metering arrangement.

In all, 250 poles were examined and the data obtained yielded the result that a ratio less than 1:8 between the relative amplitudes of the 100- and 350-Hz parts of the signal always denoted a structurally safe pole, while ratios greater than 1:8 occasionally denoted a structurally unsound pole.

IV. Full-Scale Investigation

Using the parameter of the 1:8 ratio as the criterion for detecting a good pole, and a "Q" factor of 12 for the filters, three more instruments were constructed for in-depth investigation.

The 100-Hz filter circuit was given a gain of 8 which, for fixed input to the filters, had the effect of leaving the meter needle stationary at a selected datum point on the meter scale when switching from low to high filter at this ratio. This device made it simple for pole inspectors to interpret the result after a test, the needle being on the left of the datum below the critical ratio and to its right if above it.

During the 250-pole investigation, it had been necessary to check at 90° through two diameters of the plane of each test position. This requirement became apparent as it was noticed occasionally if only a single check was made that the eccentricity of an internal void, whether caused by shakes or decay, affected the meter reading. This variability was revealed as a low reading when a higher one would have been more probable, having regard to the shape and extent of the void as revealed by careful auger assessment.

To account for this in the extended trials, inspectors were instructed to make two checks at right angles, and the higher value of the two was taken as the result and recorded. Each pole section was then carefully augered to determine its actual condition as in the previous trials.

In all, 1386 poles were inspected at random throughout Tasmania, each pole being examined at 750 and 125 mm above ground, thus giving tests for 2772 pole sections. The results of the survey are contained in Table I. The following consolidated figures are derived from this table.

1) Total pole sections tested: 2772.

2) Pole sections having a ratio less than 1:8 (the auger test showed that *all* of these sections were good): 2329, being 84 percent of the total.

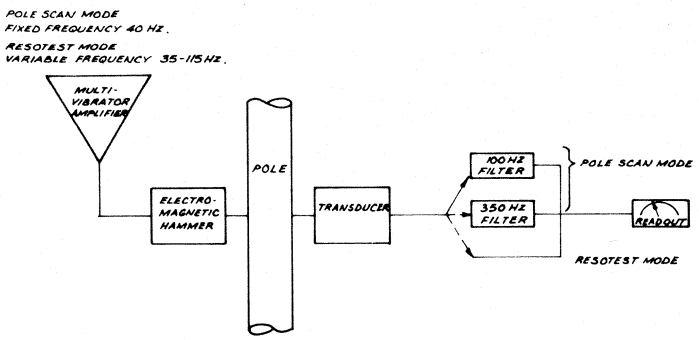

Fig. 4. Schematic arrangement of modified Resotest components.

3) Pole sections having a ratio greater than 1:8: 443, being 16 percent of the total.

4) Auger tests on these 443 sections showed:

a) Good sections: 355, being 80 percent of the high ratio group.

b) Bad sections: 88, being 20 percent of the high ratio group.

During these extended trials, it was determined also that test results were unaffected by various types of pole top arrangement, the class of pole, whether treated or not, or the position of testing on the pole up to a man's height above the ground, except that close proximity to the ground line should be avoided as previously mentioned. It was found important, however, to temporarily remove attachments such as guards and covers in the region of the test.

V. Implications for Users of Overhead Power and Communications Distribution Systems

The foregoing facts as revealed by basic investigations and field trials may be utilized to screen poles quickly and isolate those which may possess defects from those where defects are not present or are insignificant. Usually, most poles would pass the test and leave a small percentage of poles to be examined further by other means. The virtue of such a screening system rests on the fact that, in any properly maintained distribution network, most poles are in good condition at any one time and it therefore has practical value, particularly if utmost simplicity of method can be achieved.

VI. Integration of a Double Bandpass Filter Comparator with an Instrumental (Resotest) Decay Detection System

The author has been involved for many years in the general problems created by decay in wood poles and has been responsible for development of an instrument (Resotest) [1] for establishing the existence of structurally serious internal defects. This system has been operating in Tasmania for several years.

In effect, all that was necessary to combine the two functions of positive identification of poles with and without serious internal defects was to add two filters to the existing Resotest circuitry with appropriate additions to switching, and perform some minor circuit modifications.

Fig. 4 is the modified schematic arrangement of the Resotest instrument to enable incorporation of the neces-

sary filters. This, of course, was a mere convenience as both systems are intimately related and could be applied directly by pole inspectors during their routine duties.

As pole inspectors are relatively few and their duties do not frequently impinge directly on the day-to-day activities of linesmen, whose main concern is that the poles on which they work are secure, the filter comparator (which has been named Polescan) stands on its own. Such a separate instrument could be much simpler in its construction and therefore cheaper. Efforts are now being directed towards instruments of this type which should be cheap enough for distributing to linesmen in liberal quantities.

VII. Performance of the Integrated Resotest/Polescan System

In summary, the statistics produced from Table I are the following.

1) Over a very large sample of power distribution poles, Polescan classified 84 percent as good poles.

2) Of the poles rejected by Polescan, additional testing by the more sophisticated Resotest system would separate the good poles (80 percent) from the bad poles (20 percent).

3) The time for examination of a single cross section by Polescan was 3–5 min.

The combined Resotest/Polescan system has been in general use as a standard system for only six months using twenty instruments throughout Tasmania. There have been no difficulties and the system appears to be achieving the results which it promised.

Acknowledgment

The author wishes to thank his colleagues for their encouragement and unstinting assistance during the progress of trials and investigations and the Commissioner of the Hydro-Electric Commission of Tasmania, J. R. Ashton, for his kind permission to publish this paper.

References

[1] A. D. Shaw, "Sonic vibration technique for rot detection in wood pole," *IEEE Trans. Instrum. Meas.*, vol. IM-23, p. 240, Sept. 1974.

A New Way in the Development of Electronic Electrometers with a Varicap-Diode Modulator

HARI HERSCOVICI

Abstract—**In this paper, the theoretical studies and adopted technical solutions relative to an electronic electrometer with a varicap-diode modulator are described. The electrometer has an input resistance of 10^{14} Ω at 1-V input. The use of this electrometer technique and the performance limitations which may be obtained are analyzed. In order to overcome the usual input resistance of the varicap-diode modulator, reverse polarization of the bridge diodes is used. This provides an increase in input modulator resistance of about 15 times.**

I. Introduction

TECHNICAL DEVELOPMENT has set for the technician's use (in 1960) the measurement device called a varicap diode or varactor. This realization had a favorable acceptance and a large and quick spread because of the small price, the circuit's simplicity, and the high performance. The varicap diode appeared at the time of strong progress in bipolar transistors and devices with small input resistance.

The varicap diode based upon the p–n junction capacitance variation of the silicon diode, under a direct voltage applied on the junction terminals, is used in amplifier circuits similar to the vibrating capacitor, but the varicap-diode modulator is supplied with relatively high frequency alternating voltage (1–50 kHz) and this allows the design of very stable and reliable amplifiers [1]–[8]. The development of this varicap-diode amplifier in the hybrid integrated circuit technique allowed the development of some high performance products.

In the past years, the electrical measurement field has been enriched with some other devices such as unipolar transistors with junction or, and especially, with the insulated gate. These devices are also developed in hybrid integrated

Manuscript received March 26, 1974; revised May 18, 1978.

The author was with the Research Laboratory of Process Control Instrumentation of the Institute for Research and Design for Automation, Bucharest, Romania. He is now with the Research and Development Department of the Cordis Corporation, Miami, FL.

0018-9456/78/0900-0276$00.75

TABLE I

Parameter	FET	MOS-FET	VARICAP
Common mode input resistance	typ. 10^{12} Ω max. 10^{14}	10^{15} Ω protected 10^{16} Ω unprotected	10^{14} Ω
Input capacitance	1...5 pF	15 pF	2...3 pF
Temperature drift of the input offset voltage	typ. 10 μV/°C min. 1 μV/°C max. 30 μV/°C	200 μV/°C	typ. 10 μV/°C min. 1 μV/°C max. 30 μV/°C
Bias current	typ. 5...30 pA opt. 0.1...0.5 pA exc. 0.01 pA	0.002 pA protected 0.001 pA unprotected	0.01 pA
Temperature drift of the bias current	typ. 0.02 pA/°C min. 0.001 pA/°C max. 3 pA/°C	0.0002 pA/°C protected 0.0001 pA/°C unprotected	0.001 pA/°C
Voltage noise	typ. 3...10 μV exc. 0.125 μV max 20 μV	100 μV	10 μV
Current noise	10^{-13} A	10^{-15} A	10^{-15} A

TABLE II

Parameter / Input device	FET	MOS-FET	VARICAP	Vibrating capacitor	Electrometer tube
Input impedance	fair	large	large	very large	large
Voltage stability	good	poor	good	excellent	poor
Current stability	poor	excellent	good	excellent	good
Frequency bandwidth	wide	wide	narrow	narrow	wide
Overload protection	easy	difficult	easy	easy	easy
Common mode rejection	good	good	excellent	excellent	poor
Microphonics stability	good	good	good	good	poor'
Warm-up	fast	fast	fast	fast	slow
Size	small	small	small	large	large
Price	medium	medium	medium	high	medium

circuit techniques and the electrometrical performances obtained were very high.

Electrometrical integrated circuits in hybrid techniques now represent the industrial products with the highest known performances. Study of these products allows us to establish a correct idea about the level of performance as to the inherent limitation of each technique. Only the products with common-mode input resistance over 10^{12} Ω are retained in this study. Also, we have analyzed only the most important performances that describe the electrometric amplifier qualities [9]–[14].

Examining the performances of these products, we may construct Table I. In the same manner, we may compare the semiconductor device electrometers against the "classic" ones with vibrating capacitor or electrometric tube [13]. We make this analysis in Table II, at the same time extending the study to larger and different performances.

It is very interesting to find among the semiconductor electrometers that, although with MOS-FET realized remarkable points relative to the input resistance and the bias current, the only products which have all optimal performances are those with a varicap diode modulator. Especially for industrial applications, the varicap diode modulator electrometer remains the most satisfactory instrument at the actual technical level. This instrument is also superior to the vibrating capacitor relative to the size and especially to the price.

II. Varicap Diode Modulator Limitations

The main varicap diode electrometer limitation consists of the maximal 10^{14}-Ω input resistance value (Table I) limitation due to internal diode resistance, and internal diode resistance decreasing because of the use of modulators with alternating voltage supply. The diode internal resistance is a consequence of its voltage-current characteristic. This characteristic is determined, in the small applied voltage area, by the carrier generation–recombination phenomenon in the junction passing and surface regions.

Studies of this phenomenon show that the alloyed silicon diode equation may be written [16], [18] as

$$I = \alpha I_g \left(\exp \frac{qU_a}{mkT} - 1 \right) \tag{1}$$

where

- I the junction current,
- U_a the junction direct applied voltage,
- q/kT the diode thermic voltage (25 mV at 17°C),
- m a diode characteristic coefficient,
- I_g the generation–recombination current in the passing region,
- α a coefficient which describes the junction surface phenomenon and the metallurgical deviations from the nominal junction area.

Studies and measurements on a great number of alloyed silicon diodes with abrupt junctions (DZ 308) show that for a great number of diodes we may consider

$$m = 1.6 \cdots 2$$

$$I_g = 4.8, 10^{-11} \text{ A}$$

$$\alpha = 0.5 \cdots 6.$$

The diode resistances, both static R_{is} and dynamic R_{id}, become comparable for very small applied voltages $U_a \leq 5$

mV and thus represent an internal resistance characteristic element

$$R_{iso} = R_{ido} = R_{io} = \frac{25m}{\alpha I_g} \tag{2}$$

The R_{io} value results between 1.4×10^{11} and 2×10^{12} Ω, which is a variation of about an order of magnitude for the same diode type.

For a higher applied voltage value U_a,

$$R_{is} = R_{io} \frac{(U_a/25m)}{\exp(U_a/25m) - 1} \tag{3}$$

and

$$R_{id} = R_{io} \cdot \exp\left(-\frac{U_a}{25m}\right) \tag{4}$$

the diode resistance has decreases strongly compared to the origin value; for example, for $U_a = 60$ mV, there results $R_{is} = 0.4R_{io}$ and $R_{id} = 0.2R_{io}$.

The second diode resistance limitation is due to the modulator alternating voltage regime in which, because of the diode nonlinear characteristic, an autopolarization current is produced with the effect of changing the diode operating point towards the diode direct current region, thus decreasing the internal resistance. In this region, the diode internal resistance decreased also because we must consider the dynamic resistance which, in the direct current domain, is smaller than the static one by about an order of magnitude.

We have shown [17], [18] that the ratio of the combined regime diode resistance to the direct current regime resistance, at the same applied voltage U_a, is

$$\frac{R_{io}}{R_{is}} = \frac{\exp(-(U_a/25m)}{1 + \sum_{k=1}^{n} \frac{(V/50m)^{2k}}{(K!)^2}} \cdot \frac{\exp(U_a/25m) - 1}{(U_a/25m)} \tag{5}$$

which, for diodes with $m = 1.6$, may produce (at the same voltage $U_a = 60$ mV) the value $R_{io} = 0.3R_{is} = 0.12R_{io} = 1.7 \times 10^{10} \cdots 2.5 \times 10^{11}$ Ω (obviously for smaller voltages of U_a, the input resistance will be larger).

The varicap diode bridge modulator resistance, being half of each diode resistance, there results, theoretically, an input resistance of the order of minimum 10^{10} Ω and maximum 10^{11} Ω.

The input resistance increase is usually obtained with series negative feedback amplifiers. With this circuit, it is possible to increase the input resistance by about 10^2–10^3 times, the last value being possible practically using integrated circuit operational amplifiers.

A second method consists of the introduction of an initial adjustable polarization, which will compensate for the diode autopolarization voltage [4], reseting the operating point to the origin.

The third method for increasing the varactor electrometer input resistance—in our opinion, more efficient—consists of the introduction of a reverse polarization on the bridge modulator diodes.

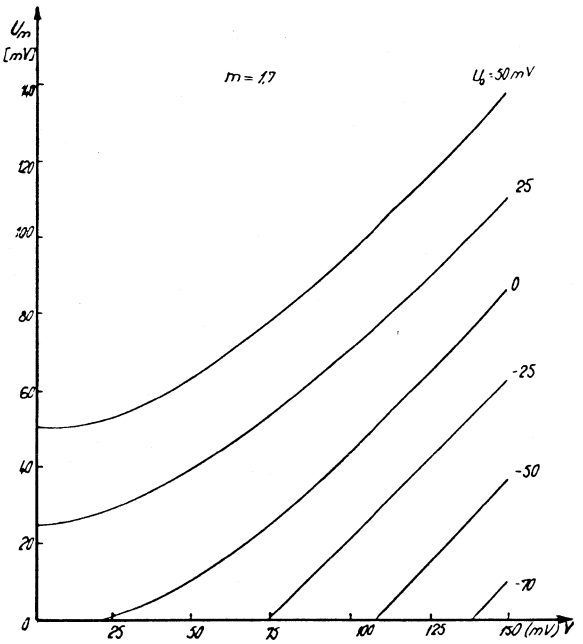

Fig. 1. Diode voltage autopolarization as a function of the applied direct and alternative voltage.

It is shown [17] that the ratio of the dynamic resistance of a polarized diode to the same diode resistance in the usual combined regime, or in the regime with autopolarization voltage compensation, is

$$\frac{R_{id}}{R_{ic}} = \exp\frac{U_m - U_p}{25m} \tag{6}$$

respectively,

$$\frac{R_{id}}{R_{is}} = \exp\left(-\frac{U_p}{25m}\right) \tag{7}$$

where U_m is the autopolarization voltage due to the average rectified current (Fig. 1).

At convenable reverse polarization, $U_m = 0$, relations (6) and (7) show a diode resistance increasing by more than an order of magnitude.

It results also in the input resistance limits of the varicap diode electrometer being found between $R_i = 10^{13}$ Ω and $R_i = 10^{15}$ Ω.

Diode reverse polarization in the modulator bridge has practical construction difficulties with negative consequences on the circuit function (stray capacitances due to the large size of the polarization source, insufficient stability of that source, etc.). These difficulties may be overcome by the use of an integrated voltage regulator as a polarization source. This solution assures both a high performance stability and a miniature size.

III. Electrometer with Reverse-Polarized Varicap Diode Modulator

In Fig. 2 is shown the principal diagram of an electronic electrometer developed on this principle by the author.

It may be seen that the modulation–demodulation amplifier is composed of the characteristic elements of such

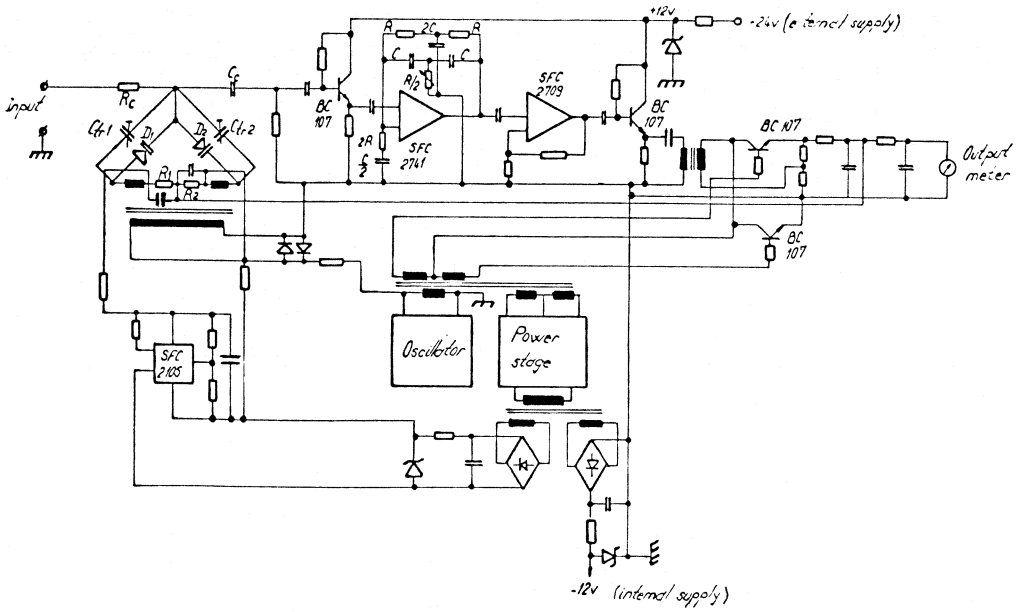

Fig. 2. Principal diagram of the reverse-polarized diode modulator electronic electrometer.

an amplifier, its output being closed on a total negative feedback circuit.

The varicap diode modulator is first characterized by the reverse polarization of the diodes. In two of the bridge arms, the varicap diodes are connected together with the trimmer capacitors for bridge equalization. In the other two arms, there are the symmetrical windings of the transformer secondary, series with the resistances R_1 and R_2 of strictly equal value, to which is applied the polarization voltage $2U_p$.

The polarization voltage is supplied by an integrated regulated voltage model SFC 2105 and applied to the R_1 and R_2 resistance terminals through a voltage-divider circuit, in order to obtain

$$U_p = -160 \text{ mV}.$$

The supply voltage of the regulator is obtained by rectification from the modulator alternating source. This modulator alternating voltage source is defined by

$$V = 100 \text{ mV}$$

$$f = 10 \text{ kHz}.$$

From the same source, by a power stage, we obtain also the -12 V for the integrated circuit supply. The alternative voltage amplifier has the following characteristics. The first amplifier stage is realized with an integrated operational amplifier type SFC 2741 with an RC double T bridge in the feedback loop, tuned to the 10-kHz work frequency. The amplifier bandwidth is about 100 Hz and the gain about 400. The feedback is equipped with high stability RC components.

The second amplifier stage is realized with an integrated operational amplifier type SFC 2709. This stage gain is about 300. Its output is connected to the demodulator stage by a follower as a buffer stage. The whole alternating voltage gain is about 120 000.

The demodulator output voltage represents the output of the modulation–demodulation amplifier and it is brought back to its input to realize the negative feedback. The resulting closed loop amplifier gain is about 1000.

The electrometer experimentation has been performed with the modulator equipped with Zener type DZ 308 silicon diodes used as varicap diodes and with ITT-BAY 35 type professional varicap diodes.

The measurements indicated the following main performances.

Unlinearity error

$$\leq 1 \text{ mV for } U_i \leq 600 \text{ mV}$$

$$\leq 1 \text{ mV for } U_i \leq 825 \text{ mV}$$

$$\leq 1.5 \text{ mV for } U_i \leq 1000 \text{ mV}.$$

Input resistance at 25°C ambient temperature

$$\geq 2.10^{13} \text{ for } U_i \leq 825 \text{ mV}$$

$$\geq 10^{13} \text{ for } U_i \leq 1000 \text{ mV}$$

$$\geq 10^{14} \text{ for } U_i \leq 850 \text{ with BAY 35 diodes}.$$

Input offset current at 25°C ambient temperature

$$\leq 0.5 \times 10^{-12} \text{ A with DZ 308 diodes}$$

$$\leq 10^{-13} \text{ A with BAY 35 diodes}.$$

Temperature drift of the input offset voltage between 0 and +57°C

$$\pm 60 \ \mu\text{V/°C}.$$

Temperature drift of the input offset current

$+20 \cdots +57$°C

$$\leq 0.65 \times 10^{-12} \text{ A/10°C with DZ 308 diodes}$$

$$\leq 0.16 \times 10^{-12} \text{ A/10°C with BAY 35 diodes}$$

$+20 \cdots 0°C$

$\leq 1.4 \times 10^{-12}$ A/10°C with DZ 308 diodes.

Temperature input resistance variation between 0 and +57°C; reduces by about one half for each ±10°C rise in temperature.

IV. Conclusions

The performance obtained with popular DZ 308 type diodes is close to that obtained with professional type BAY 35 varicap diodes, the main differences being in the input resistance and in the temperature drift of the input offset current.

Such good results are due principally to the reverse polarization of the modulator bridge diodes, which increases at least 15 times the modulator input resistance, at the same time decreasing the offset current due to the diode rectifying effect.

The maximal input resistance obtained with the BAY 35 diodes is, however, smallest at the theoretical upper limit obtained, although it is equal to that of the hybrid integrated circuits (see Table I). At the same time, the temperature drift of the offset current is larger than that of the products in Table I.

The input resistance may be increased by technical means [4] and also by associating the diode reverse-polarization method with integrated circuit techniques. We suppose that the two ways will allow the development of some varicap diode electrometers with internal resistances even above 10^{15} Ω. Offset current drift decrease is also possible using integrated circuit techniques, this being the only possible way to obtain identical diodes in the modulator bridge [18].

References

[1] J. Registrar, "Silicon junction diodes as variable capacitors," *Electron. Eng.*, vol. 33, no. 406, 1971.
[2] L. Micio and A. Gilly, "Gleichspannungsaverstarker mit kapazitatsdioden fur kleine eingangsleistungen," *Elektronik*, no. 9, pp. 263–265, 1963.
[3] E. Schoninger and F. Seibt, "Elements semi-conducteurs pour les amplificateurs de tension continue de grande sensibilite," *Rev. Siemens*, no. 3, 1965.
[4] J. Bajon, "L'amplification parametrique en electrometrie," *L'Onde Electrique*, vol. 49, fasc. 3, pp. 535–543, May 1969.
[5] J. Bajon, "Caracteristiques d'un dispositif electrometrique a varactor," *Electron. Lett.*, vol. 4, no. 8, pp. 161–163, Apr. 19, 1968.
[6] R. Stere, "Measuring modulators and demodulators with semiconductor devices," Ph.D. dissertation, Polytechnic Institute, Bucharest, Romania, ch. 3, pp. 3.1–3.27, June 1972.
[7] R. Stere, "Etude d'un modulateur à diodes varicap utilisées dans les amplificateurs de courant continu à grande impédance d'entrée," *Rev. Roumaine Sci. Tech., serie Electrotechnique et Energetique*, tome 14, no. 1, 1969.
[8] W. Roisman, "Very large input resistance modulator, with voltage regulator diodes used as varicap diodes," *Automat. Electron.*, vol. 11, no. 2, pp. 62–69, Mar./Apr. 1967.
[9] Documentation ANCOM, England, Mar. 1970.
[10] Documentation Optical Electronics, U.S., 1970–71.
[11] Documentation Ohmic–Bourns, France, 1971.
[12] Documentation TEKELEC–Airtronic, France, Jan. 1970.
[13] Documentation Analog Devices, U.S., 1969.
[14] Documentation Burr–Brown, U.S., 1971.
[15] A. G. von Nie, "Measuring currents down to 10^{-17} A with a low noise level by means of a dynamic capacitor electrometer," *IEEE Int. Convention Rec.*, part B, 1967.
[16] H. Hersocvici and E. Luca, "Une nouvelle interprétation de quelques phénomènes èlectroniques de la jonction semi-conductrioe abrupte PN," *Buletinul Institut. Politehnic din Iasi*, tom. XIX, fasc. 1–2, 1973.
[17] ——, "Some aspects of the silicon diodes resistance in varicap utilization in combined regime of direct and alternative voltage," *Buletinul Institut. Politehnic Iasi*, tom. XIX, fasc. 3–4, 1973.
[18] H. Herscovici, "Some contributions on the study and the use of the semiconductor silicon diodes for some electronic electrometers development, Ph.D. dissertation, Polytechnic Institute, Iassy, Dec. 1973.

A Precise Instrument for Measuring Water Waves

ARTURO G. SANCHOLUZ, MEMBER, IEEE

Abstract—**A novel design of an electronic instrument used for measuring water waves is presented. The instrument, which operates in conjunction with a twin-wire conductance probe, effectively computes the conductance by analog division. Lead-wire voltage drops, which are largely responsible for distortion in wave peaks, are subtracted from the voltage-proportional input signal. In addition, the unit incorporates a front-panel control to compensate for changes in water conductivity.**

The instrument exhibits a linear calibration curve over a very large range, regardless of the length and size of the interconnecting cable.

I. Introduction

HYDRAULIC MODELS have become an important method in predicting and analyzing the action of waves in a variety of Civil Engineering structures. These models, as well as more theoretical studies in the field of gravity waves, pose the general problem of measuring and accurately recording water surface height as a function of time.

A number of different techniques to generate an electrical magnitude related to instantaneous water height have been developed and extensively tested in the past [1]–[4]. Among these, the float transducer, the capacitance probe, and the twin-wire conductance probe have been adopted by most experimenters. However, when extended linearity and high-frequency response are desirable, the twin-wire conductance probe has proven to have a superior performance [4] and consequently this method was adopted here.

The instrument to be described in this paper has been developed at the Venezuelan National Hydraulics Laboratory, to be used in connection with several research projects concerned with coastal defense structures. These investigations required that wave amplitudes ranging from ± 5 to ± 30 cm be measured and recorded at a number of points in a hydraulic model. To accomplish this purpose, it was necessary to develop an instrument offering a suitable linear calibration to facilitate data analysis and, at the same time, capable of operating at long distances from the transducer. The equipment uses a twin-wire probe as a sensing device, and an electronic circuit that incorporates an analog divider to produce an output that varies linearly with the depth of immersion of the probe.

First, a brief review on the principle of operation of the twin-wire probe will be given to provide the reader with a better understanding of some of the problems associated with the technique. Then, the details of the transducer and measurement circuit will be discussed and the experimental results will be analyzed. Finally, the significance of the instrument as well as its advantages and limitations will be summarized.

Manuscript received August 3, 1977.

The author is with the Laboratorio Nacional de Hidráulica, Caracas, 101 Venezuela.

II. Principle of Operation

Neglecting end effects [3], the electrical conductance G between two parallel rods partially immersed in water can be expressed as

$$G = \frac{I}{V} = \frac{C}{\rho} h \tag{1}$$

where V denotes the voltage drop across the probe, I the current flowing through the circuit, ρ the resistivity of the water, h the depth of immersion, and C is a constant depending on the geometry of the rods. The resistivity of the water is not constant and varies with temperature in approximately 2 percent per °C. Hence, at least for a constant temperature, (1) shows that the conductance between the rods results directly proportional to the depth of immersion of the probe.

Early designs of water wave measuring instruments [3] have been based upon energizing the transducer with a constant amplitude alternating voltage and measuring the current I as an indication of the instantaneous wave height. These realizations, however, were affected by at least three important sources of error. Due to the relatively low probe impedances involved (a typical 60-cm twin-wire probe, when fully immersed in fresh water, has a resistance of the order of 35 Ω), the small current sensing resistor normally connected in series with the transducer represented an appreciable source impedance. As a consequence, the voltage drop across the transducer could not be maintained constant for all water levels causing large waves to be underestimated. Interconnecting cables had to be kept short because they contributed to the same degenerative effect on the wave crests. Finally, any amplitude variation in the oscillator output appeared directly as a change in wave height. A more recent circuit proposed by Fryer *et al.* [5], has attempted to overcome the two first limiting factors by applying a combination of positive and negative feedback around the driver amplifier but the scheme still depends critically upon the amplitude of the energizing voltage. The circuit to be presented in this work surmounts the disadvantages of previous realizations and at the same time offers the possibility of restoring the original calibration when the conductivity of the water changes. It also eliminates the interconnecting cable limitation by subtracting from the input the instantaneous voltage drop along the cable. The main feature of the realization is that effectively

0018-9456/78/0900-0281$00.75

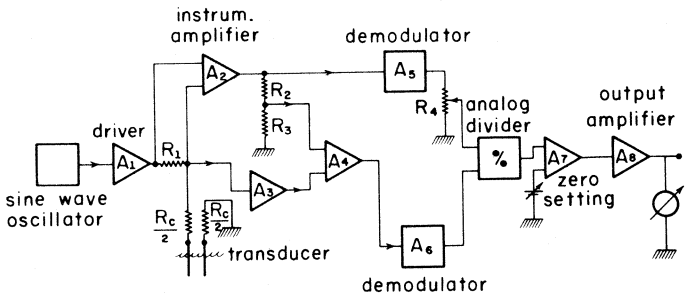

Fig. 1. Simplified diagram of the electronic circuit.

computes the conductance as the quotient I/V by means of an analog divider.

III. Circuit Description

Fig. 1 shows a block diagram of the circuit employed. The transducer was energized by means of an FET-controlled Wien bridge oscillator followed by a driver amplifier. The oscillator frequency is not critical but has to be of a few kHz to minimize polarization effects at the water–transducer interface. A frequency of 2 kHz is a good compromise between polarization and the undesirable capacitive susceptance appearing in parallel with the conductance. The driver, A_1, was incorporated to act as a buffer between the oscillator and the load composed of R_1 in series with the transducer. Resistors $R_c/2$ represent the probe-electronics cable. The nominal output voltage, V_0, of amplifier A_1 was set at 0.5 V.

The probe itself consisted of two 3-mm stainless-steel rods, 600 mm long, and 12 mm apart. Two Lucite pieces, one at each end of the rods, were used to maintain the rods parallel. The upper Lucite piece was attached to a 17-mm stainless-steel rod used for mounting the transducer. A picture illustrating the complete transducer assembly is shown in Fig. 2.

IV. Cable Compensation

A simplified diagram for amplifiers A_1, A_2, A_3, and A_4 is depicted separately in Fig. 3 in order to explain the technique used to correct for cable resistance. Neglecting the input currents to the amplifiers, it can readily be seen that

$$V_2 = V_1 - IR_c \tag{2}$$

and

$$V_0 - V_1 = IR_1 \tag{3}$$

Letting A_i for $i = 1$ to 6 denote, respectively, the voltage gain of each stage appearing in Figs. 1, 3, and 4, it follows that

$$V_4 = V_3\left(\frac{R_3}{R_2 + R_3}\right) = A_2 IR_1\left(\frac{R_3}{R_2 + R_3}\right). \tag{4}$$

Thus, V_6 can be expressed as

$$V_6 = A_3 A_4\left\{V_1 - \frac{A_2}{A_3} R_1\left(\frac{R_3}{R_2 + R_3}\right) I\right\}. \tag{5}$$

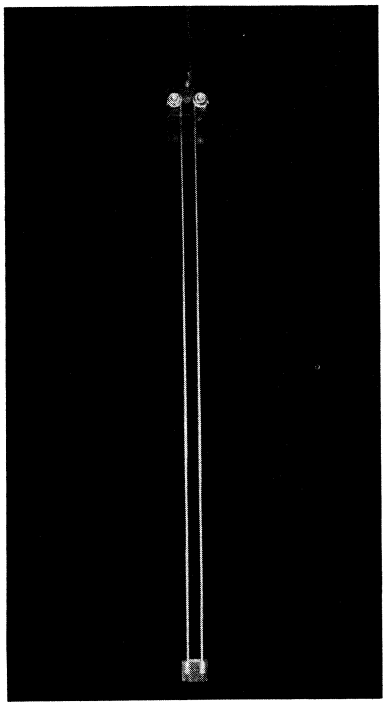

Fig. 2. The twin-wire conductance transducer.

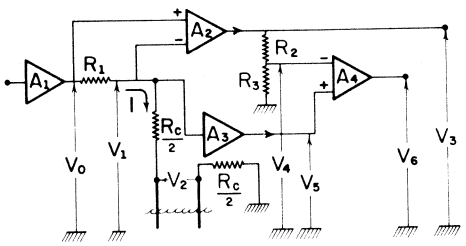

Fig. 3. Detailed block diagram of amplifiers A_1, A_2, A_3, and A_4.

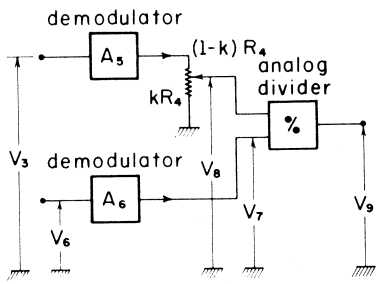

Fig. 4. Detailed block diagram of rectifiers and analog divider.

Comparing (2) and (5) and provided the condition

$$R_c = \frac{A_2}{A_3} R_1\left(\frac{R_3}{R_2 + R_3}\right) \tag{6}$$

it is evident that

$$V_6 = A_3 A_4 V_2. \tag{7}$$

Gains A_2 and A_3 and the value of resistor R_1 are mainly determined by conditions imposed by the following stages. Yet, it is possible to modify the ratio R_2/R_3 within ample limits in order to satisfy (6). Thus, V_6 results directly proportional to the instantaneous voltage across the probe, V_2, regardless of the value of R_c. In practice (see Fig. 5),

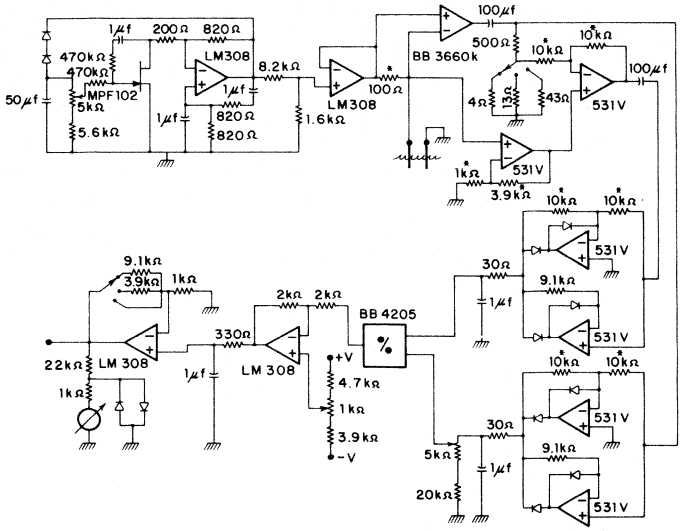

Fig. 5. Complete circuit diagram. A ±15-V regulated power supply, not indicated, is included with the unit. Asterisk denotes 1 percent resistors. Other resistors are 5 percent. All diodes are MPN3401.

different resistors are switched in place of R_3 to accommodate for the different values of R_c corresponding to each of the standard lengths of cable (5, 15, and 50 m).

V. Computation of the Conductance

Signals V_3 and V_6 are sent to the demodulator circuits A_5 and A_6, respectively, as indicated in Fig. 4. These circuits, which rectify and demodulate the signals going into the divider, have approximately equal voltage gains A_5 and A_6, respectively, both slightly less than one. Even though the divider has a frequency response extending well beyond 2 kHz, it was necessary to rectify and demodulate the incoming signals prior to their arrival. Otherwise, the output of the divider would have been undefined for the zero crossings of the signal in the denominator.

Using (4) and (7) and by inspection of Fig. 4 the following relations are obtained

$$V_7 = A_3 A_4 A_6 V_2 \tag{8}$$

$$V_8 = k A_2 A_5 R_1 I. \tag{9}$$

In addition, the specifications of the divider state that

$$V_9 = 10 \frac{V_8}{V_7}. \tag{10}$$

Therefore, combining (8), (9), and (10) the output of the divider can be written as

$$V_9 = \frac{10 A_2 A_5 R_1}{A_3 A_4 A_6} k \frac{I}{V_2}. \tag{11}$$

Substituting (1) for I/V_2 in (11) and rearranging:

$$V_9 = \frac{10 A_2 A_5 R_1 C}{A_3 A_4 A_6} \left(\frac{k}{\rho}\right) h. \tag{12}$$

Hence, the output of the divider results proportional to the instantaneous depth of immersion h. Moreover, since (12) contains the quotient k/ρ this suggests the possibility of compensating water conductivity changes by means of potentiometer R_4.

VI. Compensation for Conductivity Changes

Equation (12) indicates that the output from the divider will be independent of the conductivity of the water provided the quotient k/ρ is maintained constant. The method used for doing this is described next.

Prior to calibrating the instrument at the beginning of each experiment, potentiometer R_4 is set at approximately its center value. During the calibration, a particular depth of immersion is chosen as a reference level and the output voltage at this point is recorded. Since the calibration is linear and goes through zero, changes in water conductivity will change the slope of the calibration curve, so that the output voltage at the reference level will differ from the value originally recorded. Hence, by returning the probe to the reference level and adjusting potentiometer R_4 until the indicator is brought back to the recorded level, the original calibration will then be restored. Because changes in water temperature rarely exceed ±5°C during short time intervals, in the final circuit potentiometer R_4 has been replaced by a fixed resistor in series with a smaller variable resistor. In this manner, changes of ±10 percent in the resistivity can be easily compensated.

VII. Experimental Results and Discussion

Fig. 5 shows the complete circuit diagram for the instrument. Coupling capacitors have been used between stages to eliminate dc drifts at critical points such as the inputs to the demodulators. Two final stages are connected in cascade after the divider. The first of them is a zero suppression stage that derives the offset voltage from the power supplies. A 1-kΩ potentiometer enables the user to position the zero anywhere in the scale. The last stage is a variable gain amplifier which provides sensitivities of approximately 0.1, 0.5, and 1 V/cm, respectively. A low-pass filter having a cutoff frequency of 500 Hz has been included at the input of this stage and a diode-protected galvanometer at its output.

The frequency response of the instrument has been determined experimentally. The probe was replaced by a FET connected as a voltage-controlled resistor and a square wave was applied to the gate causing the drain-source resistance to switch between 100 Ω and 1 kΩ. In this manner, changes of conductance at the transducer for an ideal 25-cm step function type of wave were simulated. The frequency response is mainly controlled by the demodulators time constants and was found to be −3 dB at 45 Hz, this upper limit being more than adequate for the inherently low-frequency water waves.

The influence of amplitude variations in the oscillator on the calibration was determined by varying the oscillator output in ±20 percent. No significant changes (less than 0.1 percent) could be observed in the output of the instrument. Induced noise at line frequency was kept within reasonable limits by proper grounding and shielding techniques. If necessary, higher rejection at line frequency can be achieved changing the characteristics of the low-pass filter at the input of the final stage.

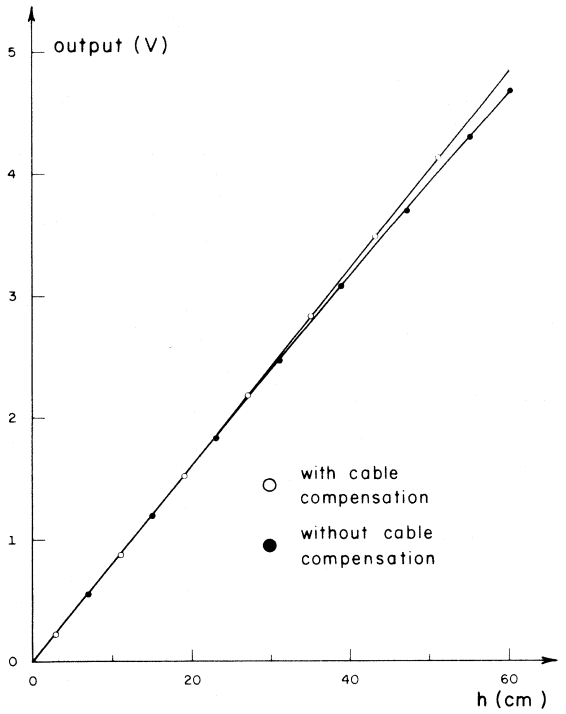

Fig. 6. Two typical static calibration curves using a 600-mm transducer and a 50-m 20-AWG shielded pair cable. Open dots denote with cable compensation. Closed dots denote without cable compensation.

Fig. 6 shows a static calibration curve obtained for the instrument when connected to the transducer by a 50-m 20-AWG cable. The transducer employed was similar to the one depicted in Fig. 2. The degree of parallelism in the stainless-steel rods, and not the instrument itself, proved to be the limiting factor as far as linearity is concerned. This was ascertained by a separate test in which the transducer was replaced by a resistance decade box. Improper parallelism in the rods is caused by two factors: alignment errors in the holes drilled through the supporting pieces and lack of straightness in the rods themselves. In our case, the second factor was preponderant because highly straight rods were unavailable in Venezuela at the time of manufacturing the transducer. At this point, the possibility of using stainless-steel wires under tension was considered in an attempt to overcome the difficulty. However, due to their smaller radii, wires favor capilarity effects which in turn introduce hysteresis errors between run up and run down calibrations. The size of the meniscus depends on the diameter and the finish of the wires, but in all cases is in the order of millimeters and would affect severely the dynamic performance of the instrument. The idea of employing wires had to be rejected and it was decided to buy a large stock of rods and select only those being acceptably straight for manufacturing the probes.

The calibration curve obtained for the same transducer with the cable compensation circuit disconnected ($R_3 = 0$ in Fig. 3) is also shown in Fig. 6. By comparison, a good idea of the sort of improvement to be expected can be gained.

VIII. Conclusion

An electronic instrument for measuring water waves has been presented. The design incorporates an integrated analog divider, an instrumentation amplifier, and a number of inexpensive operational amplifiers.

The instrument offers a highly linear calibration curve. This is particularly noticeable when long cables are run to the transducer. Nevertheless, special care is needed in selecting the rods and manufacturing the transducer to insure a suitable degree of parallelism.

The calibration is affected in less than 0.1 percent by amplitude variations of ± 20 percent in the oscillator output. Although changes in water conductivity can not be ignored, a front panel control and a simple procedure are provided to restore calibration.

Acknowledgment

The financial support offered by the Venezuelan National Hydraulics Laboratory which made this work possible is gratefully acknowledged. Special thanks are due to Dr. W. Kimberly of the Electrical Engineering Department of the Simon Bolivar University for his many comments and suggestions in preparing the manuscript.

References

[1] C. G. Whittenbury, E. A. Huber, and G. S. Newell, "Instrument for measuring water waves," *Rev. Sci. Instrum.*, vol. 30, no. 8, pp. 674–676, Aug. 1959.

[2] D. G. Fink, *Electronic Engineers' Handbook*. New York: McGraw-Hill, 1975, pp. 10-49–10-52.

[3] H. G. Farmer and D. D. Ketchum, "An instrumentation system for wave measurement, recording and analysis," in *Proc. 7th Conf. Coastal Engineering* (Univ. California, Berkeley), 1960.

[4] D. K. Fryer and M. J. Wilkie, "The simulation in the laboratory of random seas and their effects," in *Conf. Proc. Instrumentation in Oceanography* (Bangor, Wales, U.K.), Sept. 1975.

[5] D. K. Fryer and M. S. W. Thomas, "A linear twin wire probe for measuring water waves," *J. Phys. E: Sci. Instrum.*, vol. 8, pp. 405–408, Aug. 1975.

A Combined Total Reflection-Transmission Method in Application to Dielectric Spectroscopy

STANISLAW S. STUCHLY, SENIOR MEMBER, IEEE, AND MIROSLAW MATUSZEWSKI

Abstract—**A combined total reflection–transmission method for permittivity measurements at radio and microwave frequencies is described. Analytical expressions for the dielectric constant and the loss factor of a sample, viewed as a two-port in the transmission system, in terms of the measured scattering parameters are given. The uncertainty of measurements of the dielectric constant and the loss factor is discussed and a method of selecting an optimum sample length is suggested.**

INTRODUCTION

VARIOUS METHODS for measuring the permittivity of dielectrics have been summarized in [1] and a comprehensive list of references and a general review can be found in an excellent survey paper by Bussey [2]. The measurement methods for dielectrics can be generally divided into two groups: transmission line methods and resonant methods.

The resonant methods which can be applied only in the frequency domain, usually assure very good accuracy, but are difficult and time consuming when applied in a broad range of frequencies.

The transmission line methods, on the other hand, can be applied in both frequency and time domain, and are most suitable for broad-band measurements. A comprehensive review of the transmission line methods in the frequency domain can be found in [3] while the time domain methods are summarized in [4].

The transmission line methods can be further divided into the total reflection and total transmission methods [4]. In both cases the permittivity of the sample is expressed in terms of the measured values of the complex reflection and transmission coefficients, respectively, although analytical expression for the permittivity are not available, and numerical methods are being used.

In a combined transmission–reflection method originally suggested by Nicolson and Ross [5] for time-domain measurements of dielectric materials, the permittivity of a sample is uniquely related to the reflection and transmission coefficients. The method is applicable in both frequency and time domains, and in principle can be used in a very broad frequency range, provided that the coefficients are measured with acceptable accuracy. Since broad-band network analyzers are available in both frequency [6] and time domain [7], the combined transmission–reflection method is an effective tool for broad-band measurements of the dielectric properties of materials; including swept-frequency and time-domain measurements. It should be pointed out, that although the uncertainty obtainable by this method can not approach that achievable with narrow-band frequency-domain resonant methods, bandwidths of several decades are feasible with a single basic sample configuration. The method is, therefore, best suited for materials whose properties change relatively slowly with frequency, and also, as will be shown later, rather for lossy materials (e.g., $\tan \delta \geq 0.1$).

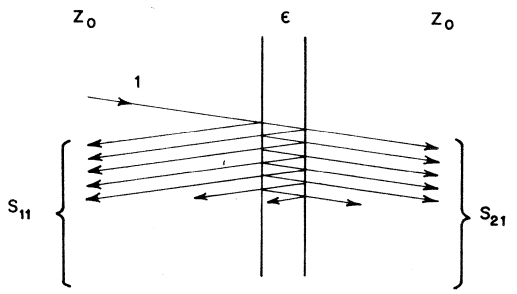

Fig. 1. Configuration of the dielectric sample.

THEORY

The structure shown in Fig. 1 represents a dielectric sample placed in the coaxial line. The sample can be viewed as a two-port characterized by the scattering coefficients S_{11} and S_{21}. The scattering coefficients can be further expressed in terms of the sample properties by the following equations [4]

$$S_{11}(i\omega) = \rho(i\omega)\,\frac{1 - \exp\{-(2l/c)i\omega[\varepsilon(i\omega)]^{1/2}\}}{1 - \rho^2(i\omega)\exp\{-(2l/c)i\omega[\varepsilon(i\omega)]^{1/2}\}} \quad (1)$$

$$S_{21}(i\omega) = \frac{[1 - \rho^2(i\omega)]\exp\{-(l/c)i\omega[\varepsilon(i\omega)]^{1/2}\}}{1 - \rho^2(i\omega)\exp\{-(2l/c)i\omega[\varepsilon(i\omega)]^{1/2}\}} \quad (2)$$

where

$$\rho(i\omega) = \frac{1 - [\varepsilon(i\omega)]^{1/2}}{1 + [\varepsilon(i\omega)]^{1/2}}$$

Manuscript received November 8, 1977. This work was supported by the National Research Council of Canada and Agriculture Canada.

The authors are with the Department of Electrical Engineering, University of Ottawa, Ottawa, Ont. K1N 6N5, Canada.

0018-9456/78/0900-0285$00.75 © 1978 IEEE

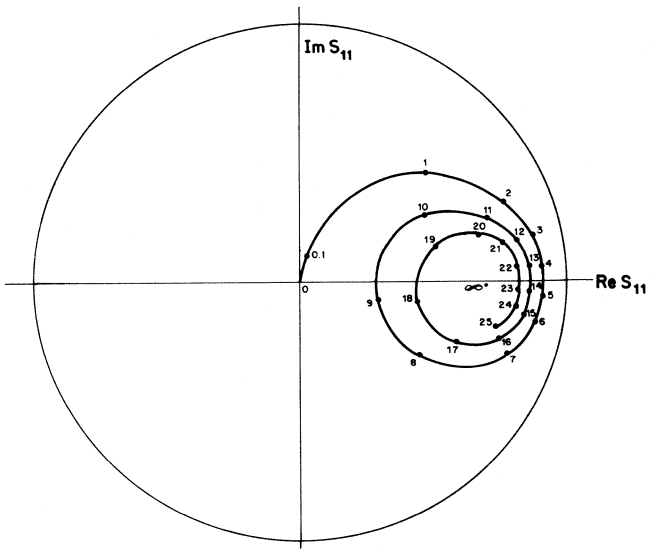

Fig. 2. Complex reflection coefficient $S_{11}(i\omega)$ as a function of the length of the sample, expressed in hundredths of the free space wavelength, for a dielectric characterized by $\varepsilon' = 30$ and $\varepsilon'' = 3$.

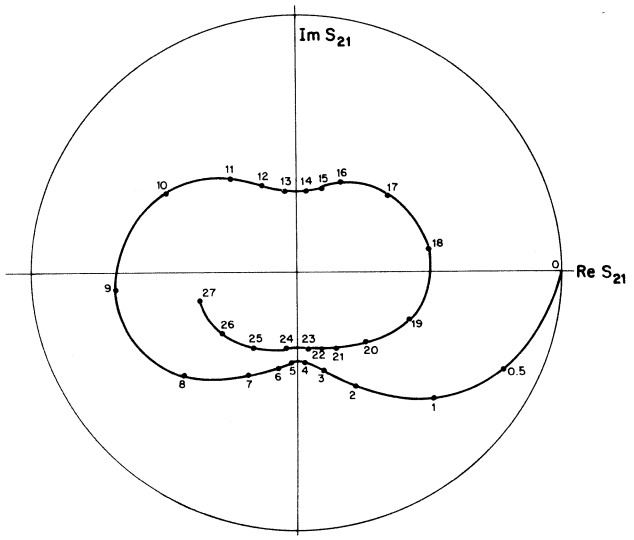

Fig. 3. Complex transmission coefficient $S_{21}(i\omega)$ as a function of the sample, expressed in hundredths of the free-space wavelength, for a dielectric characterized by $\varepsilon' = 30$ and $\varepsilon'' = 3$.

and l is the length of the sample, c is the speed of light in vacuum, $\varepsilon(i\omega)$ is the permittivity of the sample and ω is the angular frequency.

Before undertaking any further steps it is interesting to analyze the behavior of the scattering coefficients $S_{11}(i\omega)$ and $S_{21}(i\omega)$ as a function of the length of the sample and its dielectric properties. Figs. 2 and 3 show the behavior of $S_{11}(i\omega)$ and $S_{21}(i\omega)$, respectively, as a function of the length of the sample of a dielectric characterized by $\varepsilon' = 30$ and $\varepsilon'' = 3$.

The complex reflection coefficient varies from $|S_{11}(i\omega)| = 0$ for $l/\lambda = 0$ to $|S_{11}(i\omega)| = \rho$ for $l/\lambda = \infty$ (infinite sample), further $\arg S_{11}(i\omega) = 0$ for $(l/\lambda) \times (\varepsilon'^2 + \varepsilon''^2)^{1/4} = n/4$, where n is an integer.

The complex transmission coefficient $S_{21}(i\omega)$, on the other hand, changes from $|S_{21}(i\omega)| = 1$ for $l/\lambda = 0$ to $|S_{21}(i\omega)| = 0$ for $l/\lambda = \infty$ (infinite sample), while $\arg S_{21}(i\omega) = 0$ for $(l/\lambda)(\varepsilon'^2 + \varepsilon''^2)^{1/4} = (n + 1)/4$ and $\arg S_{21} = |\pi/2|$ for $(l/\lambda)(\varepsilon'^2 + \varepsilon''^2)^{1/4} = n/4$, where n is an integer.

As will be shown later, these relationships have important implications in the uncertainty analysis.

Equations (1) and (2) cannot be solved in closed form in a general case, although several approximate methods were suggested [4]; also numerical solutions are possible [4]. Nicolson and Ross [5] have shown that by combining (1) and (2) it is possible to express $\varepsilon(i\omega)$ in terms of $S_{11}(i\omega)$ and $S_{21}(i\omega)$ in closed form. Following their procedure, (1) and (2) can be presented as

$$S_{11}(i\omega) = \frac{(1 - Z^2(i\omega))\rho(i\omega)}{1 - \rho^2(i\omega)Z^2(i\omega)} \tag{3}$$

$$S_{21}(i\omega) = \frac{(1 - \rho^2(i\omega))Z(i\omega)}{1 - \rho^2(i\omega)Z^2(i\omega)} \tag{4}$$

where $Z(i\omega) = \exp\{-(l/c)i\omega[\varepsilon(i\omega)]^{1/2}\}$.

In order to solve (3) and (4) for $\varepsilon(i\omega)$ it is necessary to eliminate $\rho(i\omega)$ or $Z(i\omega)$, and although both ways give a solution for $\varepsilon(i\omega)$, the first way gives ambiguous results for samples longer than certain value, while the other does not.

Rearranging (3) to eliminate $\rho(i\omega)$

$$Z^2(i\omega) = \frac{1 - S_{11}(i\omega)/\rho(i\omega)}{1 - S_{11}(i\omega)\rho(i\omega)} \tag{5}$$

and substituting (5) to (4)

$$S_{21}^2(i\omega) = 1 - S_{11}(i\omega)[\rho(i\omega) + \rho(i\omega)^{-1}] + S_{11}(i\omega)^2 \tag{6}$$

which leads to the final equation

$$\varepsilon(i\omega) = \frac{[1 - S_{11}(i\omega)]^2 - S_{21}^2(i\omega)}{[1 + S_{11}(i\omega)]^2 - S_{21}^2(i\omega)}. \tag{7}$$

A similar result using a different approach was obtained by Altschuler [1].

Equation (7) allows to calculate unambiguously the permittivity of the test material[1] from the measured complex scattering coefficients $S_{11}(i\omega)$ and $S_{21}(i\omega)$. Although the normalized length of the sample l/λ does not appear explicitly in (7), both scattering coefficients depend on l/λ as evident from (1) and (2).

Using the second way one rearranges (4) to eliminate $Z(i\omega)$

$$\rho^2(i\omega) = \frac{1 - S_{21}(i\omega)Z^{-1}(i\omega)}{1 - S_{21}(i\omega)Z(i\omega)} \tag{8}$$

and substituting (8) to (3)

$$S_{11}^2(i\omega) = 1 - S_{21}(i\omega)[Z(i\omega) + Z^{-1}(i\omega)] + S_{21}^2(i\omega) \tag{9}$$

which leads to the final equation

$$\varepsilon(i\omega) = -\lambda^2/(4\pi^2 l^2)\ \text{arc cosh}^2\left[\frac{1 + S_{21}(i\omega) - S_{11}(i\omega)}{2S_{21}(i\omega)}\right]$$

which is ambiguous for $l \geq \lambda/\{8\varepsilon'[1 + (1 + \tan 2\delta)^{1/2}]\}^{1/2}$.

[1] Computer programs in APL are available from the authors.

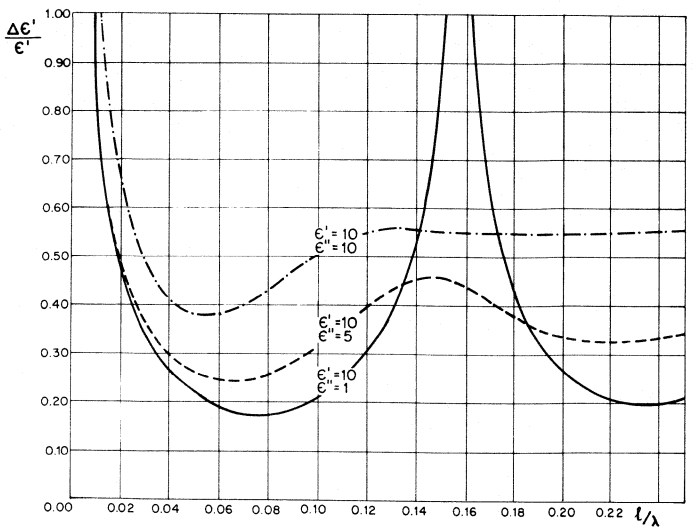

Fig. 4. The relative uncertainty of measurement of the dielectric constant ($\Delta\varepsilon'/\varepsilon'$) as a function of the normalized sample length (l/λ) for dielectrics characterized by a dielectric constant $\varepsilon' = 10$ and different loss factors; scattering coefficients $S_{11}(i\omega)$ and $S_{21}(i\omega)$ measured by a HP 8410B network analyzer.

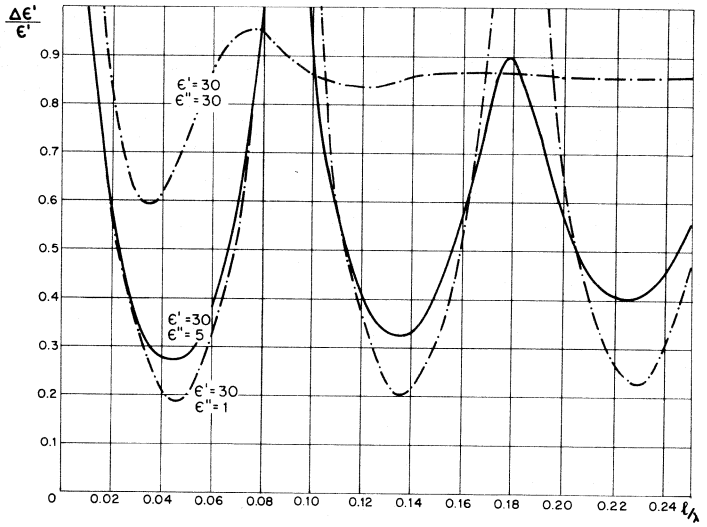

Fig. 5. The relative uncertainty of measurement of the dielectric constant ($\Delta\omega'/\varepsilon'$) as a function of the normalized sample length (l/λ) for dielectrics characterized by a dielectric constant $\varepsilon' = 30$ and different loss factors; scattering coefficients $S_{11}(i\omega)$ and $S_{21}(i\omega)$ measured by a HP 8410B network analyzer.

Uncertainty Analysis

For a given test material and a given frequency of operation the only parameter to be selected by the user is the length of the sample. It is, therefore, essential to develop an appropriate method for selection of the sample length. In any real experiment it is quite natural to select a sample length which gives minimum uncertainty.

The relative uncertainty of measurement of a function of n variables expressed as $R(x_1, x_2, \cdots, x_n)$ is given by [8]

$$\Delta R/R = \{[(\partial R/\partial x_1)(w_1/R)]^2 + [(\partial R/\partial x_2) \cdot (w_2/R)]^2 + \cdots + [(\partial R/\partial x_n)(w_n/R)]^2\}^{1/2} \quad (11)$$

where $w_1, w_2, \cdots, w_n$ are the uncertainties in $x_1, x_2, \cdots, x_n$, respectively.

In the specific case discussed in this paper in order to calculate the uncertainties in the dielectric constant $\Delta\varepsilon'/\varepsilon'$ and the loss factor $\Delta\varepsilon''/\varepsilon''$, it is necessary to calculate the partial derivatives, $\partial\varepsilon'/\partial|S_{11}|$, $\partial\varepsilon''/\partial|S_{21}|$, $\partial\varepsilon'/\partial\phi_{11}$, and $\partial\varepsilon''/\partial\phi_{21}$ as well as assume certain uncertainties in measurement of $S_{11}(i\omega)$ and $S_{21}(i\omega)$ in a selected measurement system.

Due to the analytical complexity of (7) the partial derivatives of ε' and ε'' were calculated numerically[2] for several values of ε' and ε'', while the uncertainties in $S_{11}(i\omega)$ and $S_{21}(i\omega)$ were taken for a HP 8410B network analyzer as suggested by the manufacturer.

The relative uncertainty of measurement of the dielectric constant $\Delta\varepsilon'/\varepsilon'$ as a function of l/λ is shown in Figs. 4–6, while the uncertainty in the loss factor $\Delta\varepsilon''/\varepsilon''$ is depicted in Fig. 7.

Closer analysis of Figs. 4–7 reveals an empirical relationship between the uncertainties in the dielectric constant and the loss factor which can be expressed as

$$\Delta\varepsilon''/\varepsilon'' \cong (\varepsilon'/\varepsilon'')(\Delta\varepsilon'/\varepsilon') \quad (12)$$

[2] A computer program in APL is available from the authors.

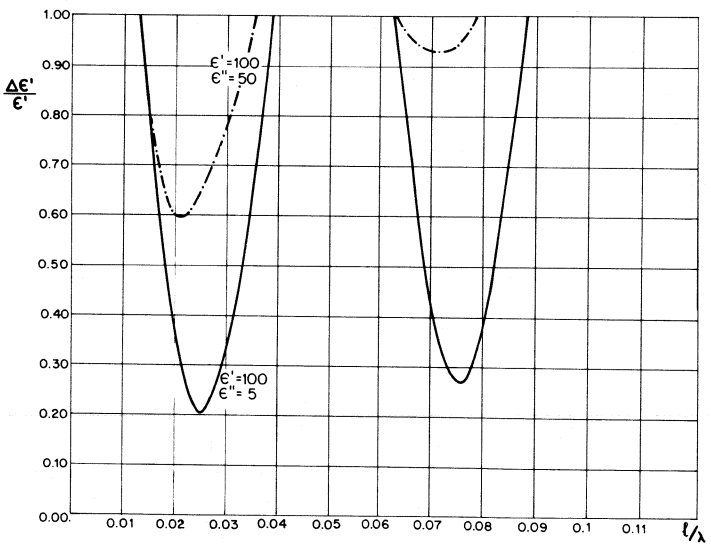

Fig. 6. The relative uncertainty of measurement of the dielectric constant ($\Delta\varepsilon'/\varepsilon'$) as a function of the normalized sample length (l/λ) for dielectrics characterized by a dielectric constant $\varepsilon' = 100$ and different loss factors; scattering coefficients $S_{11}(i\omega)$ and $S_{21}(i\omega)$ measured by a HP 8410B network analyzer.

which is equivalent to

$$\Delta\varepsilon'' \cong \Delta\varepsilon' \quad (13)$$

and indicates that the relative uncertainty in the loss factor is large for low loss materials $\tan\delta = \varepsilon''/\varepsilon' < 1$.

Further analysis of Figs. 4–7 allows also to find an empirical expression for the normalized sample length l/λ which gives minimum experimental uncertainty,

$$l/\lambda = 1/4\,|\varepsilon(i\omega)|^{-(1/2)}. \quad (14)$$

A graphical presentation of (14) is given in Fig. 8.

Discussion and Conclusions

It has been shown that combining (3) and (4) leads to a relatively simple equation, (7), which allows to compute the

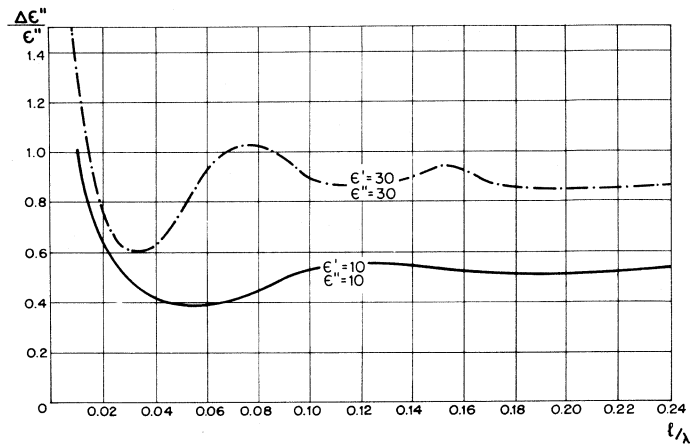

Fig. 7. The relative uncertainty of measurement of the loss factor ($\Delta\varepsilon''/\varepsilon''$) as a function of the normalized sample length (l/λ) for different dielectrics as indicated in the figure; scattering coefficients $S_{11}(i\omega)$ and $S_{21}(i\omega)$ measured by a HP 8410B network analyzer.

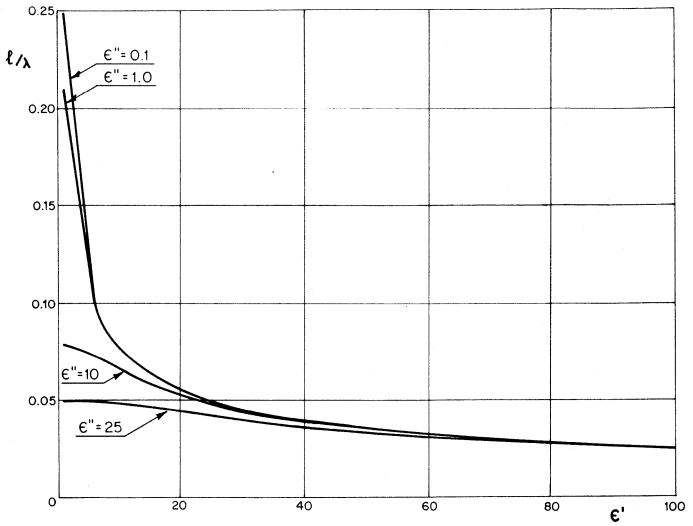

Fig. 8. Optimum normalized length of the sample (minimum uncertainty) as a function of the dielectric constant for different loss factors.

permittivity of the test material when the values of the reflection coefficient, $S_{11}(i\omega)$, and the transmission coefficient $S_{21}(i\omega)$ are known.

Equation (7) allows also to calculate the experimental uncertainty in the dielectric constant $\Delta\varepsilon'/\varepsilon'$ and the loss factor $\Delta\varepsilon''/\varepsilon''$ as a function of the relative sample length. This is not possible in the total reflection method (3) nor in the total transmission method (4), because $\varepsilon(i\omega)$ cannot be expressed in a closed form.

Although it is difficult to determine analytically a sample length giving minimum experimental uncertainty, an empirical relationship, (14), is satisfactory for the majority of practical applications.

Figs. 4–7 allow to determine the frequency range in which the experimental uncertainty remains below certain assumed value. The estimated uncertainty for an experimental system with a network analyzer is relatively large, particularly for the loss factor of low-loss materials, but can be considerably improved if an automated network analyzer is utilized.

The combined total reflection–transmission method allows to measure the permittivity of materials in a wide frequency range. Time- or frequency-domain methods can be used to measure the reflection and transmission coefficients from which the permittivity is computed.

References

[1] H. Altchuler, "Dielectric constant," in *Handbook of Microwave Measurements*, vol. 3, M. Sucher and J. Fox, Eds. Brooklyn, NY: Polytechnic Press, 1963, ch. 9, p. 502.

[2] H. E. Bussey, "Measurement of RF properties of materials—A survey," *Proc. IEEE*, vol. 55, pp. 1046–1053, 1967.

[3] W. B. Westphal, "Techniques of measuring the permittivity and permeability of liquids and solids in frequency range 3 Hz to 50 GHz," M.I.T., Lab. Insul. Res., Tech. Rep. 36, 1950.

[4] M. J. C. van Gemert, "High-frequency time domain methods in dielectric spectroscopy," *Philips Res. Rep.*, vol. 28, pp. 530–572, 1973.

[5] A. M. Nicolson and G. F. Ross, "Measurement of the intrinsic properties of materials by time domain techniques," *IEEE Trans. Instrum. Meas.*, vol. IM-19, pp. 377–382, Dec. 1970.

[6] Hewlett-Packard Application Note 117-1, June 1970.

[7] W. L. Gans and J. R. Andrews, "Time domain automatic network analyzer for measurement of RF and microwave components," NBS Tech. Note 672, 1975.

[8] J. P. Holman, *Experimental Methods for Engineers*. New York: McGraw-Hill, 1971, p. 38.

A Laboratory Setup for Simulating an N-Hop 2-PSK Direct Regenerative System

KJELL AAMO

Abstract—**A circulating test loop setup for simulating an N-hop 2-PSK direct regenerative system in the laboratory, is described. A 2-PSK direct regenerator at carrier frequency $f_c = 2$ GHz and bit-rate $f_b = 50$ Mbit/s is designed and included in the test loop. The N-hop transmission is simulated by allowing a 2-PSK sequence of 16 bit to enter the test circuit and to circulate N times through the regenerator and a mini-coax loop of 500-ns delay.**

In direct regenerative systems the "pulses" are only partially regenerated. Therefore, the influence of *one* regenerator on the noise and the error-rate of the *entire system* cannot be exactly calculated, even if the characteristics of *that* regenerator are completely known. It is necessary to treat the system as a connected whole. This is rather comprehensive and requires many assumptions and approximations. The actual laboratory simulation setup will therefore be of great practical importance, and a valuable tool for investigating the influence of different parameters from a *system point of view*. The influence on for instance the error rate of the entire system caused by heavy rain attenuation on one or two repeater sections, cochannel and intersymbol interference, additive noise, time varying channels, etc., can be studied. The mode of operation of the test setup is illustrated by experiments.

I. Introduction

THE REASON why digital transmission has become so successful—compared to analog transmission—is the immunity of the digital signal against noise. This is owing to the fact that "the pulses" are regenerated at definite points along the route of transmission. This means that the noise is suppressed relative to the signal at the repeater stations. Thus the accumulation of noise is prevented, and the signal is avoided from subsequently being lost in the noise.

Different methods exist for this noise reduction. Due to the progress in solid-state technology at microwave frequencies, there has been a growing interest attached to the actual method of *direct regeneration*. It is named so because the regeneration takes place *directly* on the carrier frequency (or intermediate frequency). Mainly three different solutions are suggested in the literature. Ohwaku *et al.* [1] report an experimental 4-PSK regenerator based on "the sampling/slice principle," operating at 30 MHz intermediate frequency with a bit rate of about 7 Mbit/s. Fukeda and Kurosaki [2] describe "the parametric oscillator principle," and the last of the three solutions, based on a degenerate parametric amplifier, is discussed by Ohta and Hata [3]. Their method is assumed to be the most suitable at microwave frequencies, and is the one to be used in the present work. In addition [4] and [5] discuss two related variants.

Circuit simplicity as well as economy weigh heavily *for* the application of direct regeneration compared to base band regeneration which is used in the digital radio-relay systems in operation today (1977). The latter systems require a complete transceiver including detection and modulation at every regenerator station.

A theoretical treatment of a direct regenerative system, however, is far more comprehensive than that of a baseband system. This is attributable to the fact that the output signal of a direct regenerator is always encumbered with a small amount of noise. (A baseband regenerator output is free from noise, but has surely a certain amount of error bits. Here it is distinguished between noise and bit-error). Concerning the actual 2-PSK system for instance, the statistical phase fluctuations owing to noise are strongly compressed in the regenerator, but there will always be a certain amount of phase jitter (PM-noise) at its output. The influence of *one* regenerator therefore depends on the succeeding part of the transmission chain, and as a consequence the entire system has theoretically to be treated as a whole.

The laboratory simulation setup described here will thus be of great practical importance in the study of direct regenerative systems. Answers to many questions concerning both the regenerators (bandwidth limitations, nonlinearities, gain variations, etc.) and the transmission paths (additive noise, rain attenuation, cochannel, and intersymbol interference, etc.) are thus found more easily and exactly by laboratory simulation than by time-consuming theoretical calculations with many assumptions and approximations.

The actual system is simulated by letting a 16 bit—50 Mbit/s sequence (320-ns duration) circulate N times through the regenerator and a transmission loop of 500-ns delay. A logic circuit controls the setup and makes it possible to study the signal after a certain number of circulations. Band limited white noise may be added inside or outside the loop and the influence of varying different parameters may be studied.

It has not been the purpose of the present work to display in detail the many investigations which are possible by means of the test loop, but to present some experiments which illustrate the mode of operation of the simulation setup.

II. The Direct Phase Regenerator

The main components of the regenerator (Fig. 1) are a reflection-type (tunnel diode) phase-coherent degenerate parametric amplifier (PA) where the phase fluctuations are reduced, an injection-locked transistor oscillator (ILO)

Manuscript received May 3, 1977; revised September 7, 1977.

The author is with the Division of Telecommunication, Norwegian Institute of Technology, 7034 Trondheim-NTH, Norway.

0018-9456/78/0900-0289$00.75

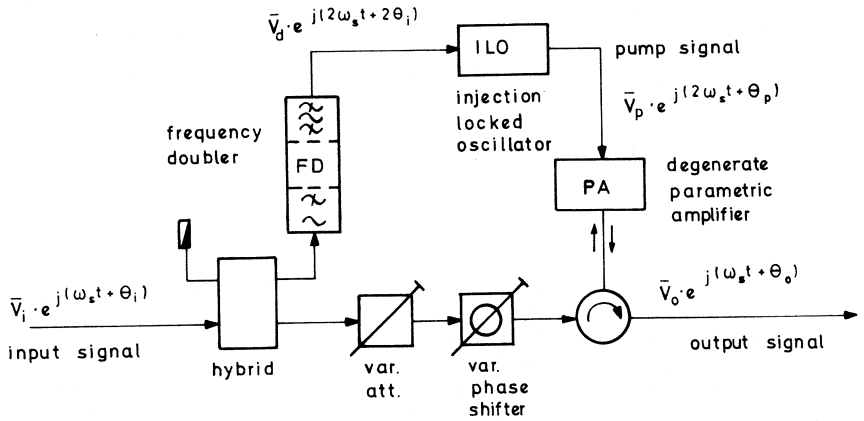

Fig. 1. Schematic diagram of the 2-PSK direct regenerator.

acting as a narrow-band filter/amplifier for the pump signal and finally a frequency doubling (FD) circuit where the 2-PSK modulation is removed, giving a locking signal to the ILO at twice the signal frequency. If the pump frequency is *exactly* twice the signal frequency the amplifier is a phase-coherent degenerate PA. Particular amplifier properties occuring under this condition are utilized in the phase regenerative process [6].

The basic relation between the *i*nput, *o*utput, and *p*ump phases (Fig. 1) of the phase-coherent degenerate PA is given by [3, p. 87] and [6]

$$\tan\left(\theta_o - \frac{\theta_p}{2}\right) = A \cdot \tan\left(\theta_i - \frac{\theta_p}{2}\right), \qquad 0 < A < 1. \quad (1)$$

In practice the parameter A, which is mainly determined by the magnitude of the pump signal, can easily be set to the interval 0.02 – 0.05.

As seen from (1) the desired input–output phase relation as illustrated in Fig. 2, requires a constant pump phase θ_p. The generation of this clean pump signal takes place in the FD/ILO circuit. Because phase coherence between the pump and the information signals is an indispensable condition for the phase regenerative effect, the pump signal must be derived from the input signal, which is modulated and contaminated by noise. The 2-PSK modulation is removed in the FD, but in return the statistical phase deviations—the phase noise—is doubled. Owing to the fact that the locking range ($2\,\Delta f$) of the ILO is narrow compared to the bandwidth of the received signal, this phase noise together with modulation rests are suppressed in the ILO. Actually $2\,\Delta f$ (< 2 MHz) corresponds to only a few percent of the bit rate (50 Mbit/s). Supposing that θ_p is constant, an input phase deviation $\Delta\theta_i$ is reduced to $\Delta\theta_o$ at the output, as illustrated in Fig. 2. The PA is set to the operating point (origo of Fig. 2) by means of the variable phase shifter shown in Fig. 1.

By linearizing (1) together with the input/output phase relation of the ILO given by [7], *the phase noise power improvement factor* of the entire regenerator is found to be

$$C = \left|\frac{\theta_o}{\theta_i}\right|^2 = \frac{1 + A^2 \cdot (f_m/\Delta f)^2}{1 + (f_m/\Delta f)^2} \quad (2)$$

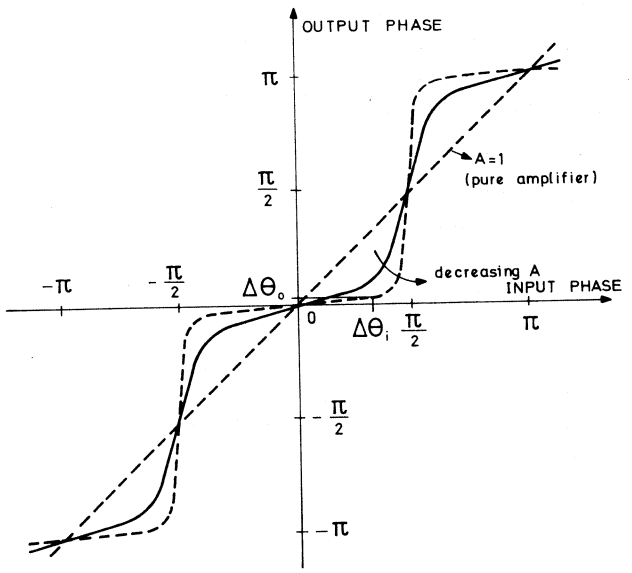

Fig. 2. The input–output phase characteristics of the direct regenerator with A as a parameter. The reduction of an input phase deviation $\Delta\theta_i$ to $\Delta\theta_o$ at the output is illustrated.

where $2\,\Delta f$ is the locking range of the ILO and f_m is the video noise frequency.

Equation (2) shows that the case of $A = 1$, which corresponds to the pure amplifier line of Fig. 2, makes $C = 1$. The case of $A = 0$, which corresponds to the ideal staircase characteristics, makes C identical to the noise power suppression factor of the ILO [7]. For all values of $A < 1$ the noise is more suppressed the more its frequency deviates from the center frequency and the narrower the locking range of the ILO is adjusted. It is easily seen that if no noise suppression takes place in the pump circuit, the output phase fluctuations will follow those at the input, and no phase regeneration occurs.

In addition to the reduction of the quadrature noise component (phase noise), it is essential to emphasize that if the PA is operated in the large signal mode, also the in-phase component will be suppressed. Such a "constant output" regenerator is of great interest from a practical point of view, because (with $A < 0,2$) it gives nearly the same error rate as a baseband type [8].

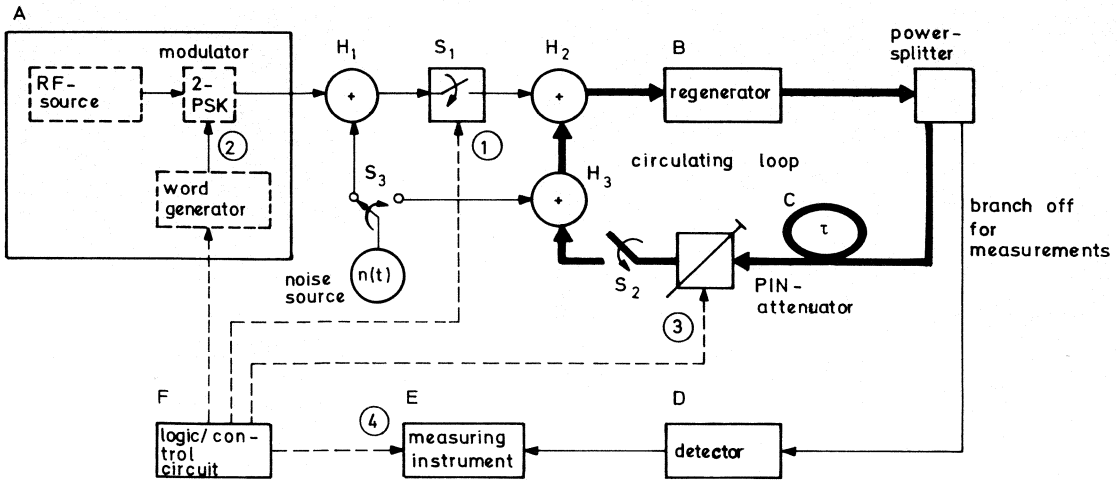

Fig. 3. Block diagram of the circulating test loop setup. The control signals at ①–○ are shown in Fig. 4.

III. The Circulating Test Loop Setup

This section describes the mode of operation of a laboratory setup, named *the circulating test loop*, for simulating an N-hop radio-relay line. The description is based on the block diagram of Fig. 3.

The test circuit is divided into six fundamental blocks:

- *A* The generator block (RF and modulation)
- *B* The circuit under test (actually the 2-PSK regenerator)
- *C* The transmission medium (with variable delay and attenuation plus "branch off" possibilities for measurements)
- *D* The detector (differentially coherent detector)
- *E* The measuring instrument (actually an oscilloscope)
- *F* The logic circuit (controls the test loop).

The N-hop transmission is simulated by generating a 2-PSK-word which is allowed to circulate N times through the regenerator and the loop. The loop is controlled by logic circuits, which make it possible to study the pulse sequence and the noise contribution after an arbitrary number of circulations.

In the actual experiments which demonstrate the mode of operation of the test loop, a 16 bit–50 MHz word generator is used to give a 2-PSK sequence of $16 \cdot 20$ ns $= 320$-ns duration. This sequence, whose pattern may be "arbitrarily" chosen by the setting of the word generator, enters the loop through the switch S_1 and the hybrid H_2, as shown in Fig. 3. S_1 is closed to allow the desired pulse sequence to enter the loop. S_1 must be opened *before* the front of the sequence arrives at H_2 after the *first* circulation in the loop.

As appears from Fig. 3, band limited white noise may be added to the signal both outside (H_1) and inside (H_3) the loop. In order to make measurements, half of the signal is branched off in the power splitter. A low-noise amplifier (not shown in Fig. 3) is included in the loop in order to compensate for the total attenuation. The closed-loop gain is set to unity by means of a variable attenuator (neither shown in Fig. 3). The gain of the PA is set to about 10 dB.

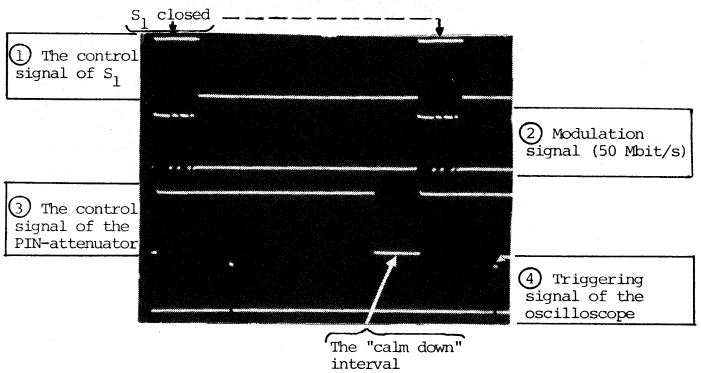

Fig. 4. The control signals at the points ①–④ of the test setup of Fig. 3. Horizontal scale: 400 ns/div.

With reference to Fig. 3 the logic/control circuit generates the following sequence:

1) The switch S_1 is closed. $(t = 0)$

2) The word generator is trigged in order to transmit a 16 bit–50 Mbit/s sequence to the 2-PSK modulator. The PIN-attenuator is set for minimum attenuation. A PSK-sequence now enters the loop through the switch S_1. $(t \approx 10$ ns$)$

3) In the course of about 320 ns the PSK-sequence has passed S_1, which is opened at $t \approx 450$ ns. (S_1 must be opened before the front of the PSK-sequence arrives at H_2 after the first circulation in the loop.) The loop delay $\tau \approx 500$ ns. $(t \approx 450$ ns$)$

4) The oscilloscope is trigged after a time delay of $k \cdot \tau$ $(k = 1, 2, \cdots, N)$ to display the detected signal plus noise after the kth circulation. $(t \approx k \cdot 500$ ns$)$

5) The PIN-attenuator is excited for maximum attenuation after a time interval of $N \cdot \tau$. This interval of great attenuation must be > 500 ns in order to make the loop "calm down" before S_1 closes and the word generator is trigged for a repeating sequence. $(t \approx N \cdot 500$ ns$)$

The different signals at the points ①–④ of Fig. 3 are shown in the picture of Fig. 4, where $N = 5$ and $k = 2$ are chosen.

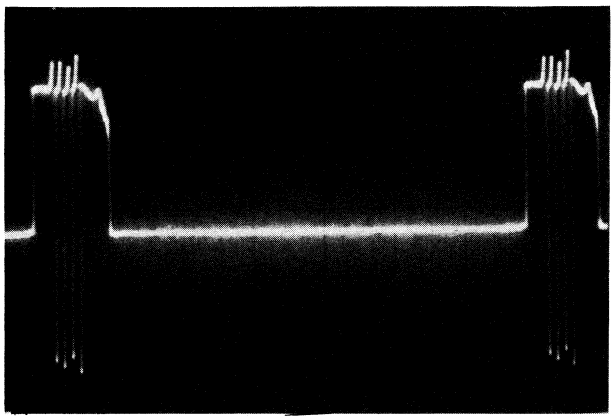

(a)

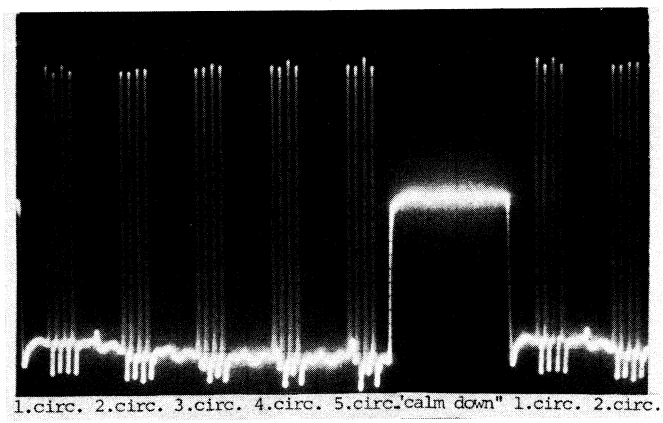

Fig. 5. An illustration of the mode of operation of the circulating test loop, showing the detector output in the case of: (a) Open loop (S_2 open), i.e., the pulse sequence is prevented from circulation. (b) Closed loop (S_2 closed). The pulse sequence of the (a) picture is allowed to circulate five times through the regenerator. Then the "calm down" interval of about 800 ns appears, after which the whole sequence is repeated. Horizontal scale: 500 ns/div.

IV. Illustrations of the Mode of Operation of the Circulating Test Loop

The mode of operation of the test loop is illustrated best by using an oscilloscope as the measuring instrument (E) of Fig. 3, because display pictures of the detector output (D) of Fig. 3 tell more than words and curves in this case. For reasons, which are not discussed here, the DPSK mode of detection is most conveniently used in the circulating loop experiments.

Fig. 5(a) shows the output of the detector in the case of open loop (S_2 open). The word generator is set to give a DPSK-detected output of four pulses. These are situated in the interval of time during which the switch S_1 is closed, as shown in the picture. (This time interval of about 450 ns corresponds to the positive pulse in the upper trace of Fig. 4). Because S_2 is open, circulations are impossible, and the detector shows no output signal until S_1 is closed and the word generator is trigged once more.

In Fig. 5(b) S_2 is closed. The DPSK-sequence shown in (a) is now allowed to circulate in the loop. In the present case N is chosen to be *five* circulations. The pulse pattern therefore

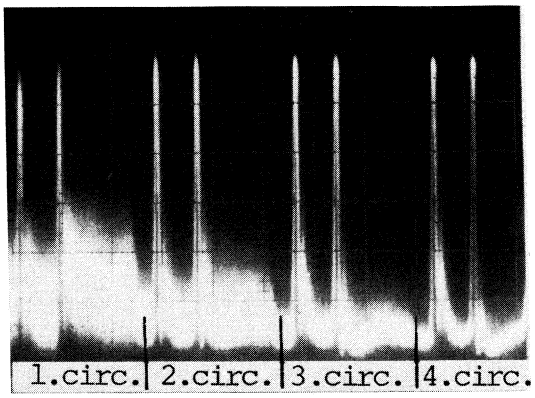

Fig. 6. Two signal pulses plus in-phase noise through four circulations in the test loop. The regenerator is operated in the "constant output" mode. Note the reduction of noise from one circulation to the next. Horizontal scale: 200 ns/div.

appears five times, as shown. After those five circulations the PIN-attenuator is switched to maximum attenuation, in order to make the loop "calm down" before a new sequence starts, as discussed in Section III. This is indicated by the time interval of about 800 ns of Fig. 5(b), showing a detector output of zero voltage. (The same "calm-down" period is found in the third trace of Fig. 4, showing the control signal of the PIN-attenuator). The unity gain of the loop is confirmed by the equal magnitude of the pulses from one circulation to the next. This is adjusted by a variable attenuator in the loop.

As a final illustration of the test setup, the noise-reduction qualities of the regenerator is demonstrated. While simulating a transmission system, S_3 is switched to the right-hand position (Fig. 3) because noise power surely adds in each repeater section of an N-hop link. For the actual illustration, however, band limited (1968–2032 MHz), white noise is added to the signal *outside* the loop (S_3 in left-hand position). The signal sequence (two pulses in Fig. 6) plus noise thus enter the loop during a time interval of about 450 ns, after which the generator block (A) of Fig. 3 is shut off by S_1, as described in Section III. The signal plus noise are now allowed to circulate in the loop, and Fig. 6 shows the successive reduction of noise during *four* circulations through the regenerator. Owing to the mode of operation of the detector, in-phase and quadrature noise are measured separately. In order to display *both* signal pulses *and* noise in the same picture, which is believed to give the best illustration, the detector is adjusted so that the noise shown in Fig. 6 is approximately pure in-phase noise. The "constant output" mode of operation of the regenerator is therefore chosen during this exemplification. (It remains to say that also from a practical point of view the "constant output" regenerator is of great interest to be investigated in the test loop setup, because exact theoretical calculations are impossible for such a system consisting of more than *one* regenerator (2-hop) [8].)

Fig. 6 shows that while the noise is reduced from one circulation to the next, the magnitude of the two signal pulses remains unchanged, confirming the unity gain setting

of the loop. The two pulses of the first regeneration seems to be a bit smaller, but this is owing to the great amount of noise which makes the top of these pulses rather diffuse. More exact measurements by means of a true rms-meter have shown that under the actual condition of large signal operation (PA input ≈ -24 dBm), in-phase noise is reduced about 9 dB in the regenerator, while the quadrature noise reduction is about 13 dB. The latter is greater than 17 dB under small signal condition. In this case, of course, in-phase noise is not affected. During these measurements $2\,\Delta f \approx 1.5$ MHz and the input carrier-to-noise ratio is 5 dB, corresponding to an input rms phase deviation of about 25°. The noise bandwidth is 64 MHz.

It is beyond the scope of the present work to carry through a lot of measurements which are possible by means of the test circuit. We will finally, however, give some ideas on investigations which can be carried out.

Heavy-rain attenuation on one or two repeater sections of an N-hop system can be simulated. This is accomplished by extending *that* part of the logic circuit (F) in Fig. 3 which controls the PIN-attenuator. In the previous examples the PIN-attenuator is just utilized as an ON/OFF switch. It may, however, easily be operated to give greater attenuation during one or two circulations than during the rest of the circulations, and in this way simulate heavy rain attenuation between certain regenerators in the transmission path. The electronically controlled attenuator may also be used in order to simulate some sort of fading in the system as well as other types of time varying channels.

The influence of interference on the system is another investigation that can be done by means of the test setup. A narrow-band filter included in the loop will distort the "pulses" and thus result in intersymbol interference. The degree of interference is determined by the filter bandwidth relative to the bit-rate of the system. Cochannel interference can be simulated by allowing a 2-PSK sequence, suitably attenuated relative to the main circulating sequence and different from this one, to enter the loop and thus add to the original signal during its *second* circulation. Error-bit measurements after the Nth hop will give valuable informations on system performance relative to interference. Also these measurements require an extended control circuit.

In addition the influence on the system caused by all sorts of variations and alternations within the regenerator as well as the transmission paths can be studied (changing parts of the regenerator or interchanging the entire regenerator, varying channel filters, gain, signal levels, etc.).

V. Conclusion

A circulating test loop setup for simulating an N-hop regenerative radio-relay system is examined. This test circuit is a valuable tool especially for investigating *direct* regenerative systems, where a theoretical treatment is very comprehensive and necessitates extensive use of approximations and limitations.

To illustrate the mode of operation of the test loop the oscilloscope is the most convenient measuring instrument (E, Fig. 3). For more quantitative measurements an error bit counter, a true rms meter, etc., are more appropriate.

Acknowledgment

The author is grateful to Prof. T. Schaug-Pettersen, Division of Telecommunication, The Norwegian Institute of Technology, for valuable discussions, and to Dr. ing. H. Hanebrekke, at the same Division, for critically reading the manuscript. He is also greatly indebted to Dr. ing. J. Torp, Electronics Research Laboratory (ELAB), The University of Trondheim, for his advices and his willingness of discussing problems during the laboratory experiments.

References

[1] S. Ohwaku, M. Hata, and N. Kondo, "Experiments on direct regeneration of PCM phase-modulated signal," *Electron. Commun. Jap.*, vol. 49, no. 11, pp. 318–326, Nov. 1966.

[2] H. Fukeda and T. Kurosaki, "Experimental studies on phase-recognition method in carrier stage of 4-phase PM system," *Electron. Commun. Jap.*, vol. 49, no. 10, pp. 19–27, Oct. 1966.

[3] T. Ohta and M. Hata, "Parametric amplifier having phase-regenerative effect," *Electron. Commun. Jap.*, vol. 53-B, no. 4, pp. 85–93, Apr. 1970.

[4] M. Hata and T. Iwano, "Direct regenerative phase-locked loop: A new carrier synchronization system," *Electron. Commun. Jap.*, vol. 52-A, no. 9, pp. 15–21, Sept. 1969.

[5] S. Komaki, O. Kurita, and T. Memita, "GaAs MESFET regenerator for phase-shift-keying signals at the carrier frequency," *IEEE Trans. Microwave Theory Tech.*, vol. MTT-24, pp. 367–372, June 1976.

[6] L. Blackwell and K. Kotzebue, *Semiconductor-Diode Parametric Amplifiers*. Englewood Cliffs, NJ: Prentice-Hall, 1961, ch. 3, pp. 72–79.

[7] M. E. Hines, J. Collinet, and J. G. Ondria, "FM-noise suppression of an injection phase-locked oscillator," *IEEE Trans. Microwave Theory Tech.*, vol. MTT-16, pp. 738–742, Sept. 1968.

[8] E. Myrseth, "Reléstasjoner for faseskiftmodulerte (PSK) radiolinjer over 10 GHz" (in Norwegian), *Telektronikk*, nr. 1, 1974.

Short Papers

A/D Controller for Acquisitions of Signals with Different Sampling Periods

J. KISHON AND SERGE GRACOVETSKY, MEMBER, IEEE

Abstract—**Efficient data acquisitions from analog signals of very different bandwidths require that each analog signal be sampled at a different rate. This paper proposes an A/D controller which has been implemented on an Analogic 5800 data acquisition system. The host computer is a PDP 11/45 with a DR11-C interface (see Fig. 1).**

Essentially, this programmable controller sorts out the sequencing of eight different analog channels. The sampling rate of each channel is independently set by software from 10 to 255 μs in 1-μs increments. Once the controller is programmed, it will control the A/D itself.

The host computer programs the controller according to the user's instructions. The sampling rate of each analog channel may be independently set by software from 10 to 250 μs. Then the controller sets out the appropriate sequencing of the data collections on the analog channels, sorts out conflicts, and sees that information is stored properly in the host computer.

I. Introduction

Some experiments require the simultaneous data collections of analog signals of widely different bandwidths. The cost of storage of digitized information makes it uneconomical to sample all signals at an identical rate since the slower signals could be sampled less often.

This work presents a solution to this problem. It has been implemented on a PDP 11/45 machine and an Analogic 5800 A/D converter. Our contribution has been the design of a programmable controller for the A/D. It basically works as follows. The user sets the desired sampling rates of up to eight analog channels within, say, a Fortran program. The 11/45 will then program the A/D controller to properly sort out the acquisition sequence. At this stage, the controller can take over the control of the A/D.

II. Operational Principles

Because the sampling periods of the analog channels are set independently by the user, it is possible that, at a given time, two or more channels need to be sampled. The main task of the controller is to resolve the priority between the eight analog inputs. Whenever a conflict occurs, a channel will be sampled if: 1) he makes a request, and 2) the time left for the next conversion to be made is the smallest of all channels. The general organization is indicated in Fig. 2. The sampling periods are loaded into the data registers. These registers are eight bits wide, giving a capacity of 255. The data register (D reg) is connected to a present down-counter and the output of the counter is connected to a tri-state eight-bit latch (TS latch).

As shown, all the TS latches are connected to a single eight-bit bus which is the comparator bus.

One side of the comparator (side A) is connected to the bus. The other side (side B) is connected to a register which holds the smallest channel period (CMP reg). Each counter output (zero detect output) is connected to a sample-and-hold amplifier, and the convert request flag (CR flag).

Manuscript received December 6, 1977.

The authors are with the Department of Electrical Engineering, Concordia University, Montreal, P.Q., Canada.

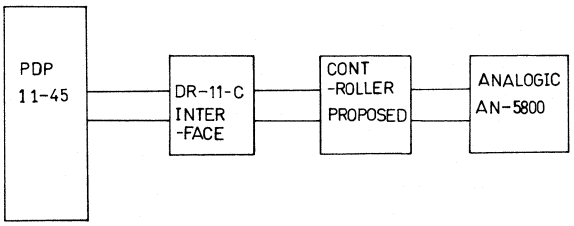

Fig. 1. General organization of the controller.

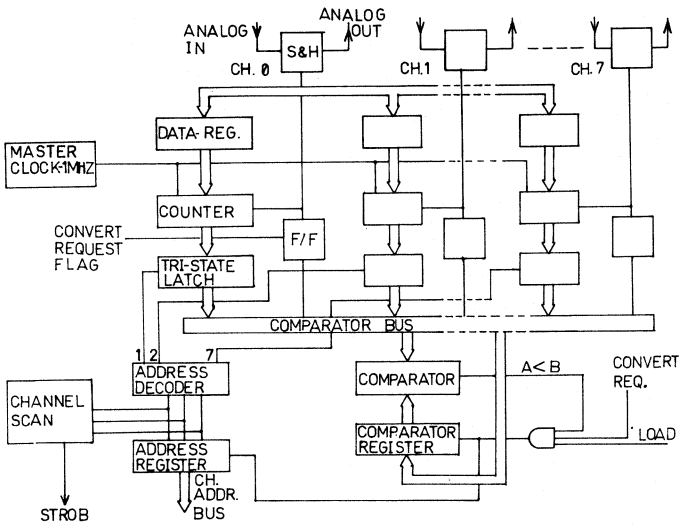

Fig. 2. Detailed block diagram of the controller.

III. Operation Sequence

1) The controller is initialized by the computer which clears all registers and flags. It loads 255 in the CM reg.

2) The sampling period of each channel is loaded into the data registers.

3) A START command is sent by the computer.

The master clock which is a 1-MHz clock, is downcounting all the counters at the same time.

Each counter divides the master clock by the number which is in the corresponding D reg (divided by the sampling period). Each time a counter downcounts to zero, a sample-and-hold pulse (S–H pulse) is generated. The analog signal is sampled and held.

The CR flag is set, and the counter presets to the D-reg value. The S–H pulses of each channel are generated periodically at the sampling period rate.

While this is going on, the TR latches are being updated every 10 μs. These latches hold the present value of the counters for comparison. Each time the TS latches are updated, a compare cycle will start. This cycle lasts for 10 μs.

In the compare cycle, all eight TS latches starting from #0 up to #7 will be compared to the CM reg (which was initialized to 255).

0018-9456/78/0900-0294$00.75

If the TS latch is smaller than the CM reg and the CR flag is set, the CM reg will be updated with the content of the TS latch. At the same time, the address reg will be updated with the channel number corresponding to the TS latch.

At the end of the compare cycle, the channel address is ready and a strobe pulse is generated. The strobe pulse starts the A/D conversion cycle, and at the same time it clears the CR flag of the channel that was selected for conversion. (If 2 CR's are made with no strobe pulse, an error flag will be set to indicate that the bandwidth is too high.)

The data transfer between the A/D to the computer is done in a wait-loop manner, i.e., in the program, the CPU continuously tests a flag and when the A/D completes a conversion, the flag is set and the CPU reads the signal value (12 bits) with the channel address in the three most significant bits. When memory is full, the computer stops the controller and starts processing the data.

IV. Conclusion

This paper has proposed a programmable controller for A/D data acquisition systems. The sampling rate of each channel may be different, allowing optimum use of storage capacity whenever simultaneous acquisition of analog signals of widely different bandwidths is required.

References

[1] *PDP 11/45 Operating Manual DR11-C Interfaces*, Digital Equipment Corp., Maynard, MA.
[2] Analogic Corporation 5800 A/D Series, MA.

A Digital Frequency Meter for Measuring Low Frequencies

M. P. MATHUR

***Abstract*—A new technique of measuring low frequencies accurately has been described. The whole scheme can be implemented using TTL integrated circuits.**

Digital measurement of low frequencies poses certain problems, especially if it is desired to measure the frequency with an accuracy of one percent or so and in reasonably short time, which may be of the order of a second. An obvious and direct method to measure the frequency is to feed a signal of unknown frequency to a digital counter through a gate which opens for 1 s and then read the counter. This basic scheme is shown in Fig. 1.

The major disadvantage of the above scheme is that the counter will only register a change if the change in the input frequency is in integral number and will ignore all fractional changes. The fractional changes are quite important in low frequencies. For example, if 50 Hz is to be measured and if frequency changes from 50 Hz to 50.5 Hz, the change is one percent which may not be ignorable, and the frequency 50.5 can be measured by keeping the gate open for, say, 10 s so that the counter receives 505 pulses and

Manuscript received February 23, 1978.
The author is with the Department of Electrical Engineering, Regional Engineering College, Kurukshetra, Haryana, India.

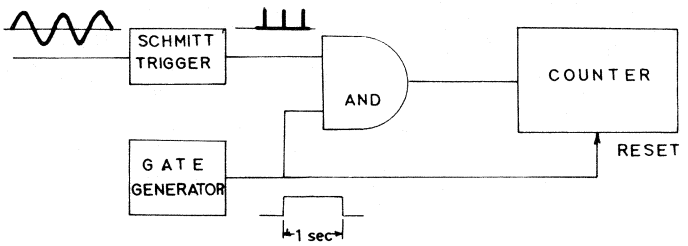

Fig. 1.

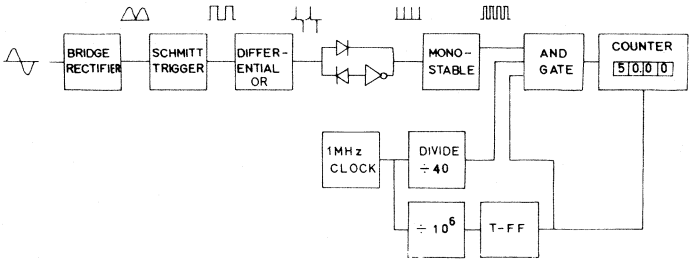

Fig. 2.

reads 505, which may be interpreted as 50.5 Hz. The disadvantage of the above scheme is that the measuring time has considerably increased.

In the scheme described below, while measuring time is reduced back to 1 s, the accuracy is increased. It will be seen that now it is possible to register the change of 0.25 Hz, while the measuring time is reduced back to 1 s. The scheme is shown in Fig. 2 and works as follows. If the input wave is sinusoidal, then by help of a bridge rectifier, it is rectified. Then, by help of a Schmitt trigger, it is converted into pulses. It can be seen that, for every cycle, there will be two square pulses which can be made of $T/4$ duration, where T is the time period of the input sinewave. The square wave is fed to a differentiator which is followed by a network of diodes and inverters so that, at the output of the network, four positive impulses are obtained for every one cycle. Each impulse is used to trigger a monostable multivibrator and, hence, for each impulse, there is one pulse of fixed predetermined duration, say δ, and therefore for every one cycle, there are four pulses of duration δ such that δ is less than $T/4$. In 1 s, there are $4f$ pulses of duration δ and thus a gate can be made to open for $4f\delta$ s in 1 s. The gate is fed with a fixed frequency N Hz and, hence, in $4f\delta$ s, $4f\delta N$ pulses will pass through the gate in 1 s, which can be fed to a counter. Reading of the counter can be interpreted directly in terms of input frequency. The gate pulse in 1 s and N-Hz frequency input can be derived from a crystal-controlled oscillator for an accurate work.

Example: Suppose we are interested in measuring 50 Hz, which means that $T = 20$ s. The pulsewidth at the output of the Schmitt trigger will be 5 ms and, hence, the four positive impulses at the input of the monostable multivibrator will be 5 ms apart. The monostable is designed to give a 1-ms pulse when it is triggered and, hence, at the output of the monostable, there will be $4 \times 50 = 200$ pulses/s, each of 1-ms duration. If a triple input AND gate is fed with the output of the monostable, 1-s gate pulse, and 25 kHz frequency source, then the gate will effectively open for

0018-9456/78/0900-0295$00.75 © 1978 IEEE

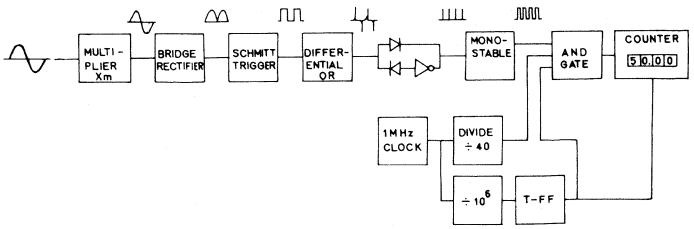

Fig. 3.

200 ms in 1-s duration and 200 × 25 = 5000 pulses will appear at the output of the AND gate which can be made to register by counter and can be made to display 50.00. If the input frequency changes to 50.25 Hz at the output of monostable multivibrator, there will be 4 × 50.25 = 201 pulses of 1-s duration. Thus the gate will be effectively open for 201 ms in 1-s duration and at the output of the AND gate, there will be 201 × 25 = 5025 pulses, and these will be displayed as 50.25, and so on.

In the above scheme, the accuracy of 0.25 Hz is obtained. The accuracy can be further improved if the signal of an unknown frequency is fed to a frequency multiplier which multiplies the input frequency by an integral number m and as a result an output signal of mf frequency is obtained, and if this signal of frequency mf is processed in the manner described above, the accuracy of measuring scheme will improve by factor m. In the above example, it will be possible to register and display a change in the input frequency by an amount 0.25/mHz. Fig. 3 shows the complete scheme of the system with improved frequency.

Electrolyte Conductivity Apparatus

LOUIS A. ROSENTHAL, SENIOR MEMBER, IEEE

Abstract—**The resistance of an electrolytic cell is measured by passing a square-wave constant current and amplifying/rectifying the voltage developed. A differential recorder provides a record of the conductivity in dynamic mixing studies. The apparatus is extremely simple and reliable and amenable to multiprobe studies.**

I. Introduction

In the study of various mixing salinity problems, the need for a simple multiprobe apparatus arose. A satisfactory procedure for evaluating salinity is through a conductivity or resistivity measurement by means of a cage or point electrode [1], [2]. Details of the design and preparation of such probes are available [3]. To capture the dynamics of a mixing experiment, the signals available from the probes should be recorded on a multichannel strip-chart recorder. The apparatus to be described provides a probe resistivity signal to such a typical recording system. Because of its simplicity, multiple probes can be readily accommodated. In principle, the application is not limited to electrolyte conductivity and any parameter presented as a resistance variation can be treated in the same analog manner.

Manuscript received March 10, 1978. This work was supported in part under NSF Grant ENG73-03545-A01.

The author is with the Department of Electrical Engineering, College of Engineering, Rutgers University, Piscataway, NJ 08854.

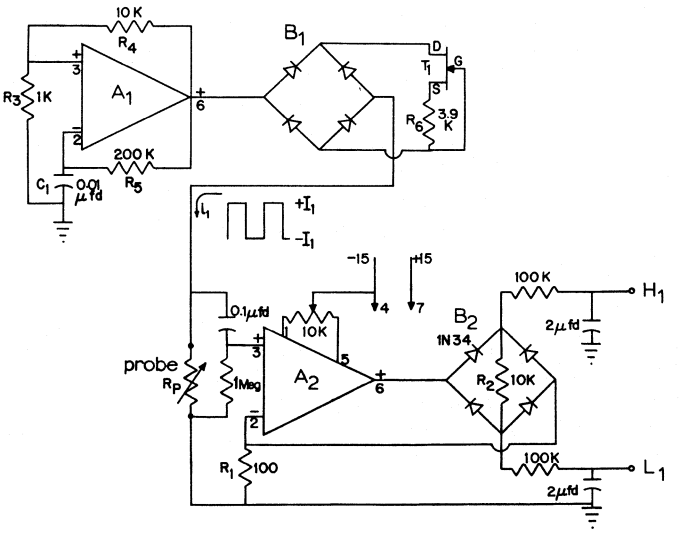

Fig. 1. A complete circuit diagram is shown. Amplifiers A_1 and A_2 are 741 and T_1 is 2N5457. Each channel requires a current drive (B_1) and amplifier-rectifier (A_2) circuits. Amplifier terminals are for a can configuration.

II. Circuit Design

The apparatus consists of a square-wave constant current source driving the probe resistance. The voltage across the probe is amplified, rectified, and filtered prior to the recorder. This is a basic carrier type ohmmeter and the novelty is in the simple mode of accomplishing the conversion. A single probe channel is depicted in Fig. 1, and for each additional channel, the current drive (B-1) and amplifier rectifier (A-2) circuits have to be duplicated.

Amplifier A_1 is employed as a free-running multivibrator and provides a square wave output that swings between the saturation levels ± 13 V at a period that roughly follows

$$T \simeq 2R_5C_1 \ln [2(R_3/R_4) + 1]. \quad (1)$$

Actually, slew rate and transition times together with input leakage currents tend to increase the period. For the parameters shown, the measured period was 1.04 ms ($f = 960$ Hz).

The full-wave bridge rectifier B-1 employing general-purpose junction rectifiers is a bilateral constant current converter in conjunction with the FET (T_1) circuit. An N channel depletion mode device is employed with a large amount of source (R_6) degeneration to provide a constant current of 200 μA independent of the drive voltage [4]. The bridge rectifier merely makes the constant current characteristic bilateral. Thus the current i_1 is a square-wave signal independent of the probe resistance. This is an excellent waveform for ease of rectification. Electrolyte conductivity cells must be excited with ac to prevent polarization, and current drive is a way of minimizing ohmic nonlinearities. Adjusting R_6 is a means of setting the channel sensitivity and correcting for conductivity cell constant differences.

The ac voltage drop appearing across the probe R_P is applied to amplifier-rectifier A_2. This is a well-established voltmeter circuit arrangement and the voltage across $R_2(V_{R_2})$ is R_2/R_1 times the full-wave rectified value of the input voltage. For the square-wave current drive of amplitude I_1, the output voltage follows

$$V_{R_2} = I_1 R_P R_2 / R_1. \quad (2)$$

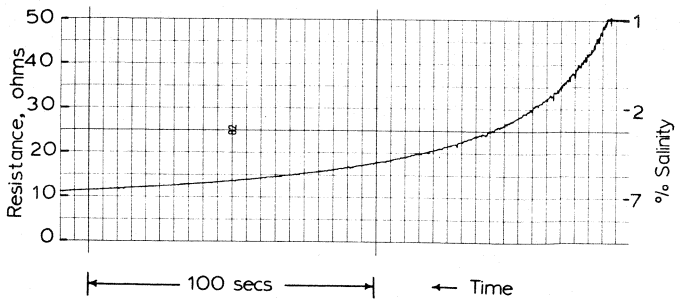

Fig. 2. The dynamic mixing of 1- and 15-percent salt solutions is recorded by a single probe. Probe resistance decreases from 50 Ω at 1 percent. The recorder sensitivity was 20 mV/div which is equivalent to 1 Ω/div.

For $I_1 = 200\ \mu A$, $R_2 = 10$ K, and $R_1 = 100$, the overall sensitivity follows

$$V_{R_2} = 20\ \text{mV}/\Omega. \tag{2a}$$

Since the A_2 amplifier is limited to ± 13 V, the maximum cell resistance that can be accommodated, as shown, is 650 ohms. By adjusting the cell current and cell geometry, it is possible to set the apparatus for a wide experimental range. Linearity was excellent except for the region of 0–5 ohms. The full-wave bridge rectifier *B*-2 employs IN34 or equivalent point contact rectifiers. Junction rectifiers have a zero conduction region before cut-in and when installed in the feedback loop would fail to produce dc feedback stabilization. For "in specification" 741 operational amplifiers, the indicated null balance arrangement will provide proper zero balance conditions. Note that the balance must be set at terminal 6, the output, since the drop across R_2 is unidirectional. No drift or instability has been observed in the performance.

The voltage across R_2 is the desired output signal. Two low-pass filters remove any ac components and the differential signal can be passed on to a recorder. Most recorders provide differential input and the signals H_1 and L_1, together with the common ground, feed the typical recorder (i.e., Gould/Brush 260). The recorder range of sensitivities, calibrated and uncalibrated, and the zero suppression feature make the overall system very flexible.

III. Experimental Observation

As an example of the single channel behavior, a recording of a mixing experiment is presented. Starting with a 1-percent (by weight) salt solution in a vessel, a metering pump feeds a 15-percent solution, and another pump extracts the same quantity. The vessel salinity in the limit will approach 15 percent. Fig. 2 is the recorded mixing. At 1-percent salinity, the probe has a resistance of 50 Ω and after 200 s is slowly moving towards the asymptote. Note that the resistance is not a linear function of salinity and at 2-percent salinity, the probe resistance is close to 30 Ω. There is fluctuation noise due to mixing which is also related to the conductivity field seen by the probe. The efficacy of mixing can be examined by comparing the indicated mixing curves under different agitation conditions. This apparatus will be the basis for a variety of mixing salinity studies.

Acknowledgment

The efforts of S. G. Thangam of the Department of Mechanical, Industrial, and Aerospace Engineering, in evaluating this method are appreciated.

References

[1] C. H. Gibson and W. H. Schwartz, *J. Fluid Mech.*, vol. 16, p. 357, 1963.
[2] D. M. Sheppard and H. W. Doddington, *Rev. Sci. Instrum.*, vol. 48, no. 3, Mar. 1977.
[3] S. J. Khang and T. J. Fitzgerald, *Ind. Eng. Chem. Fundam.*, vol. 14, no. 3, 1975.
[4] B. Botos, Motorola Application Note AN-462.

A Comparison of the United Kingdom National Standards of Microwave Power in Waveguide and Coaxial Lines

PETER J. SKILTON AND A. E. FANTOM

***Abstract*—A series of comparisons at 8.2 GHz between bolometric waveguide power standards and 50-Ω coaxial line calorimetric standards resulted in differences, with respect to the waveguide standard, of +0.20 to −0.06 percent during 12 comparisons and combined estimated 95-percent confidence limits of ±0.35 percent.**

I. Introduction

The United Kingdom national standard of waveguide power at 8.2 GHz consists of four regularly compared WG16 (WR90) bolometer mounts whose efficiency is known from microcalorimeter calibrations [1]. Since 1973, these have been used in the national RF and microwave standards division of the Royal Signals and Radar Establishment (RSRE) to fulfill the British Calibration Service traceability program.

The national standards of power in a 50-Ω coaxial line are held at the National Physical Laboratory (NPL). Recently, the frequency range covered was extended from dc-6 to dc-8.2-GHz using a new dual-load dry calorimeter [2], so that a comparison at 8.2 GHz between the two fundamentally different types of standard became possible.

Three coaxial line power meters, all fitted with GR900 precision connectors, were compared with the waveguide standards. These were:

1) an NPL primary standard calorimeter designated III(2),
2) a similar device designated III(3),
3) a secondary traveling standard comprising a commercial dry load calorimetric power meter (NRS)[1] previously calibrated at NPL against the III(3) calorimeter.

II. Method of Comparison

The comparison was performed at RSRE using a WG16-tuned transfer instrument similar to that described by Engen [3] and calibrated in terms of the waveguide power standard. To enable GR900 equipped power meters to be connected to the transfer instrument, three WG16-to-GR900 adaptors were calibrated by RSRE using the technique described in [4]. The results of this calibration enabled the efficiency of each adaptor to be calculated when terminated in each of the three coaxial power meters, so that

Manuscript received March 13, 1978.

P. J. Skilton is with the Royal Signals and Radar Establishment, Malvern, Worcestershire, England.
A. E. Fantom is with the National Physical Laboratory, Teddington, Middlesex, England.

[1] The use of a Rhode and Scwarz NRS power meter should not be construed as implying any recommendation (or criticism) of the device.

TABLE I
SUMMARY OF POWER COMPARISON RESULTS

NPL Power Meter	via	Number of Measurements	Percentage Difference		Percentage uncertainty (95% limits)			
			Average	Standard Deviation	RSRE Bolometer and transfer Instrument	Adaptor Efficiency	NPL Power Measurement	TOTAL
III (2)	A 1	4	-0.02	0.09	0.25	0.10	0.18	0.32
III (2)	A 2	4	0.09	0.08	0.25	0.08	0.18	0.32
III (2)	A 3	4	0.01	0.05	0.25	0.09	0.19	0.34
III (3)	A 1	4	0.15	0.01	0.25	0.11	0.22	0.35
III (3)	A 1	3	-0.06	0.02	0.25	0.12	0.22	0.35
III (3)	A 1	4	0.00	0.05	0.25	0.11	0.22	0.35
III (3)	A 1	4	0.20	0.04	0.25	0.11	0.22	0.35
III (3)	A 2	4	0.08	0.02	0.25	0.09	0.22	0.34
III (3)	A 3	4	0.18	0.05	0.25	0.08	0.22	0.34
NRS*	A 1	4	-0.01	0.03	0.25	0.09	0.20	0.34
NRS*	A 1	4	-0.03	0.02	0.25	0.09	0.20	0.34
NRS*	A 2	4	0.00	0.02	0.25	0.08	0.20	0.34

* NRS calibrated with respect to the III (3) calorimeter

the adaptor loss could be taken into account. The results of measurements using eight different combinations of adaptor ($A1$, $A2$, or $A3$) and power meter, some being repeated, are given on the left of Table I. The percentage difference is defined as

$$\left(\frac{\text{NPL power} - \text{RSRE power}}{\text{RSRE power}}\right) \times 100.$$

III. Comparison Uncertainty

The right-hand side of Table I lists and combines the three principle sources of uncertainty in the comparison. They are as follows.

1) RSRE bolometer and transfer instrument: the main contribution is an uncertainty of ±0.2-percent (95-percent confidence limits of a Gaussian distribution in the microcalorimeter [1]) determination of bolometer mount efficiency, but also included is the uncertainty in the instrument calibration in terms of the waveguide standard and that in the subsequent power measurement.

2) Adaptor efficiency: the uncertainty in this term is derived in [4] in terms of the component uncertainties in the adaptor evaluation. It is a function of the voltage reflection coefficient of the coaxial power meter terminating the adaptor.

3) NPL power measurement: this uncertainty comprises the uncertainty in the effective efficiency of the calorimeters or NRS meter, uncertainty in their dc sensitivity, and noise in their output.

Since all three uncertainties are derived at the same confidence level (95 percent), are independent, and of similar magnitude, they may be combined by calculating the root-sum of their squares [5].

IV. Discussion of Results

Following the comparison in March 1977, an examination of the calorimeters at NPL revealed a minor electrical fault in the III(2) calorimeter. Although not affecting the accuracy, this would have the effect of increasing its susceptibility to electrical interference in the laboratory and would explain the relatively large standard deviations obtained with this device. The extreme values of average difference obtained when using the III(3) calorimeter with adaptor $A1$ appeared to be associated with the temperature dependence of the sensitivity of the calorimeter when used in a laboratory whose temperature was controlled to 1.5°C. This error may be insignificant when using a source which can be switched from RF to dc, so as to reduce the interval between these measurements, but such an arrangement was not possible for the waveguide transfer instrument used.

V. Conclusions

The results of this comparison of waveguide and coaxial power standards were well within the estimated uncertainty limits, thus providing increased confidence in both standards. The average differences from nine sets of measurements with the NPL calorimeters varied from +0.20 to −0.06 percent with respect to the RSRE waveguide standard, with an average difference of +0.07 percent and combined uncertainty limits of typically ±0.35 percent.

Acknowledgment

The authors wish to acknowledge the help given by J. Hansen-Addy of NPL and R. M. Embleton of RSRE during the comparison.

References

[1] G. F. Engen, "A refined x-band microwave microcalorimeter," *J. Res. Nat. Bur. Stand.*, vol. 63, no. 1, July–Sept. 1959.
[2] A. E. Fantom, "An improved coaxial calorimetric RF power meter for use as a primary standard," NPL Rep. DES 45, 1978.
[3] G. F. Engen, "A transfer instrument for the intercomparison of microwave power meters," *IRE Trans. Instrum.*, pp. 202–208, Sept. 1960.
[4] P. J. Skilton, "A technique for measuring the efficiency of waveguide to coaxial line adaptors," this issue, pp. 231–234.
[5] C. F. Dietrich, *Uncertainty, Calibration and Probability*. London, England: Adam Hilger, 1973.

Digital Generation of a Nonlinear Time-Base

J. J. HILL

***Abstract*—A method of generating nonlinear time-bases is described. The approximation may be either step or piecewise linear and involves using a READ-ONLY memory as a look-up table to store digitally the shape of the required function.**

The case of a logarithmic time-base is considered in detail.

Introduction

There are many applications in the display of time varying quantities where a nonlinear rather than a linear ramp time-base is required. Logarithmic time-bases are usually generated using some form of analog, nonlinear circuitry [1] but such circuits often have temperature drift problems. Novel digital implementations may be found for certain functions. Franklin used a digital difference analyzer to generate a hyperbolic law time-base for radar

Manuscript received February 21, 1978.
The author is with the Department of Electrical, Electronic, and Control Engineering, Sunderland Polytechnic, Chester Road, Sunderland, SR1 3SD, England.

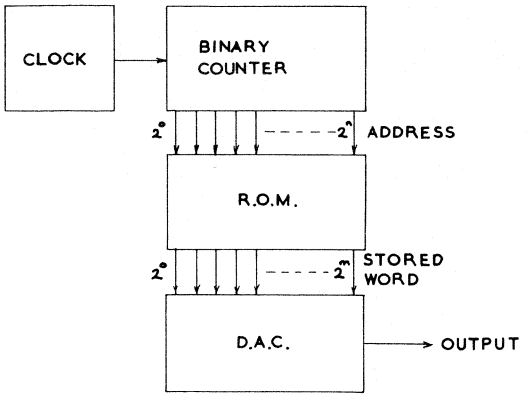

Fig. 1. Step approximation circuit.

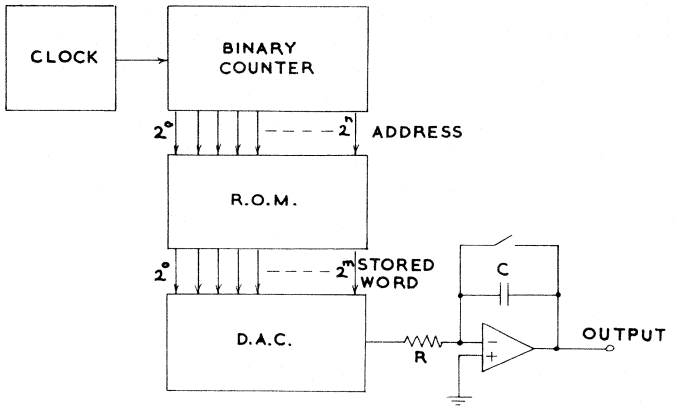

Fig. 2. Piecewise linear approximation circuit.

applications [2]. The logarithmic time-base may also be generated digitally [3]. An alternative approach which may be used to generate time-bases of any shape is considered here, where a READ-ONLY memory (ROM) is used to store digitally the shape of the nonlinear time-base.

Step Approximation Circuit

In a recent communication [4] the use of ROM storage for generating Gaussian pulses was described. This circuit, shown here in Fig. 1, is easily used for generating nonlinear time-bases. The $2^n \times m$ bit ROM operates as a look-up table which stores binary coded samples of the required function. The counter in Fig. 1 is used to address the ROM and thus as the counter counts through its n-bit binary sequence each sample is addressed in turn and read out through the digital-to-analog converter (DAC) to produce a step approximation to the required time-base shape.

The problem with this method of approximation, particularly over a wide range, is that rapidly changing functions give rise to rapidly changing sample values and hence leads to large departures from the true function between the clocking instants.

Piecewise Linear Approximation Circuit

An improved result may be obtained by approximating the required function in a piecewise linear manner. In this case the circuit is modified to that shown in Fig. 2 which operates by varying the rate of integration of an op-amp integrator. The ROM look-up table is used to store the difference between successive samples of the nonlinear time-base. As the counter addresses, in turn, each storage location of the $2^n \times m$ bit storage capacity ROM, the binary coded sample is read out through the DAC to produce a step changing voltage level which when integrated gives the piecewise linear approximation to the required function.

Flyback occurs when the integrator is reset by discharging the capacitor through the switch shown in Fig. 2.

At slow time-base speeds the charge loss from the integrator capacitor should not be significant. For this reason an op-amp with a low input bias current should be used.

The magnitude of the time-base output voltage is dependent on the CR time constant and the clock rate. Thus a disadvantage of this circuit is that changing the time-base scan rate, which is achieved by varying the clock rate, will result in a different output voltage level. However, the circuit is suitable for switched time-base speeds in which case the integrator time constant can be switched in unison with the clock period to maintain a constant output voltage.

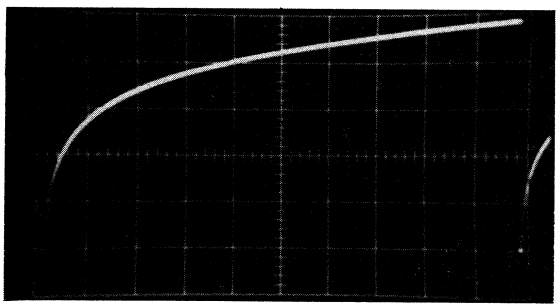

Fig. 3. 255 segment approximation to a logarithmic time-base.

Logarithmic Time-Base

As an example of the application of the piecewise linear approximation circuit the ROM was programmed to enable a logarithmic function to be generated. In this case the stored coefficients are given by

$$X_l = K_1 \log_{10} [1 + K_2(l + 1)] - X_{l-1}$$

where $0 \leq l \leq 2^n - 2$ and $X_{-1} = 0$. If this recurrence relationship is used to compute the coefficients and the rounded value of X_{l-1} used to compute the next value, X_l, then errors due to rounding will not accumulate over the range of the log function. The largest value of X_l occurs when $l = 0$. Hence the coefficient K_1 is chosen to given $X_0 = 2^n - 1$. Thus

$$K_1 = \frac{2^n - 1}{\log_{10} (1 + K_2)}.$$

The constant K_2 is chosen to define the range over which the log function operates.

Using a 256×8 bit ROM which stores 2 decades of the function the constants are evaluated as $K_1 = 183.2$ and $K_2 = 0.3922$.

The response of the circuit was displayed on an oscilloscope, photographed and is shown in Fig. 3. Because the approximation consist of 255 segments the result appears as a smooth curve. On the 256th segment the integrator is reset to zero.

Conclusions

This correspondence has described two methods of generating a nonlinear time-base. Although the results have been restricted to the case of a logarithmic function the method is easily used to generate time-bases of other shapes.

The step approximation circuit is useful if the departure from nonlinearity is small and if the step approximation nature of the

waveform will not lead to problems. A better approximation may be obtained by using the piecewise linear circuit of Fig. 2.

Acknowledgment

The author wishes to acknowledge stimulating discussions with Dr. D. Otway of Sunderland Polytechnic.

J. H. Jones is thanked for making available the facilities of the Department of Electrical, Electronic and Control Engineering, Sunderland Polytechnic.

References

[1] J. V. Wait, L. P. Huelsman, and G. A. Korn, *Introduction to Operational Amplifier Theory and Applications*. New York: McGraw-Hill, 1975, pp. 195–200.
[2] D. P. Franklin, "Digital generation of a hyperbolic-law time-base," *Electron. Circuits Syst.*, vol. 1, no. 3, pp. 85–87, Apr. 1977.
[3] W. N. Trump and L. Fowler, "A logarithmic time base generator or counter," *Rev. Sci. Instrum.*, vol. 45, no. 5, pp. 714–716, May 1974.
[4] J. J. Hill, "A simple digital pulse-shaping circuit," *Proc. IEEE*, vol. 65, p. 1517, Oct. 1977.

Measurement of Impedance by Cross-Coupler and Sliding Short at Microwave Frequencies

DEVENDRA K. MISRA, MEMBER, IEEE

Abstract—**A technique for measuring the impedance at microwave frequencies using cross-coupler and a sliding short has been described in this paper. The theory behind the measurements is given and it has been shown that this arrangement is a complete substitute of the slotted line technique.**

I. Introduction

A technique to determine the impedance of a load at microwave frequencies using directional coupler and adjustable short-circuit has been reported by Chandra *et al.* [1], which actually describes the VSWR measurements only. The work reported by Jha *et al.* [2] is also limited to the VSWR measurements. In this paper, the author presents a precise theory of the impedance measurement by a cross-coupler and shows that this arrangement is a substitute for the slotted-line method. The results of VSWR and location of first minima, needed for determination of an unknown impedance, have been verified.

II. Theoretical Considerations

Consider the circuit arrangement as shown in Fig. 1. The power P_{in} fed by the source at port 1 of the coupler, is divided into two parts at the center 0 of it. The power coupled to the auxiliary arm will flow towards port 3 (assuming infinite directivity) and it will be reflected back from the sliding short connected at the port at a distance d from 0. After reflection, a part of this power will flow

Manuscript received April 21, 1978.
The author is with the Department of Electronics Engineering, Institute of Technology, Banaras Hindu University, Varanasi-221005, India.

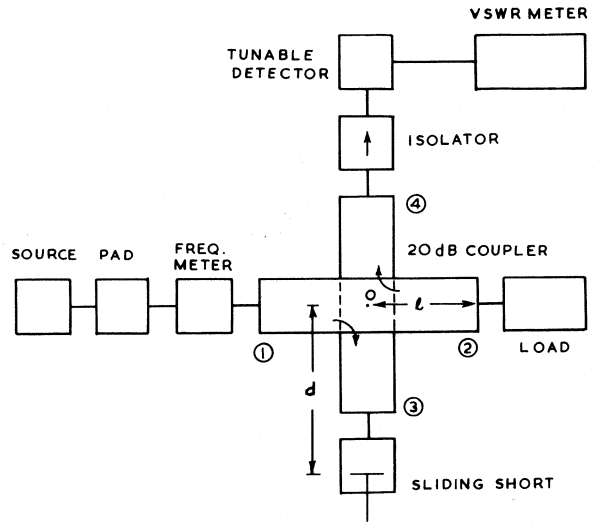

Fig. 1. Experimental arrangement for VSWR measurement using a cross coupler and waveguide sliding short.

towards port 4. The electric field at the reference 0 due to this power may be written as

$$\vec{E}_4' = -Q\{P_{in}\alpha(1-\alpha)\}^{1/2} \exp[-j(2\beta d - \delta)] \tag{1}$$

where Q is the proportionality constant, α the coupling coefficient of the coupler, δ the arbitrary phase shift introduced by the coupling apertures, and β is the propagation constant in the guide.

The remaining power in the main guide will travel a distance l from 0 and depending upon the value of the reflection coefficient of the load, it will be reflected back by it. A part of this reflected power will be coupled to the auxiliary guide which will go towards port 4. The electric field $\vec{E}_4''$ in the auxiliary guide at the reference 0 due to this reflected power, may be written (neglecting the relatively small power recoupled from the auxiliary to main guide) as,

$$\vec{E}_4'' = Q\{P_{in}\alpha(1-\alpha)\}^{1/2} \exp[-j(2\beta l - \delta)]. \tag{2}$$

Therefore, the amplitude of the electric field $\vec{E}_4$, emerging from port 4 may be found from (1) and (2) as

$$|\vec{E}_4| = |\vec{E}_4' + \vec{E}_4''|$$
$$= E_0[1 - 2\rho \cos\{2\beta(l-d) - \chi\} + \rho^2]^{1/2} \tag{3}$$

where

$$E_0 = -Q\{P_{in}\alpha(1-\alpha)\}^{1/2} \tag{4}$$

and

$$\rho e^{j\chi} = \Gamma. \tag{5}$$

From (3), it may be seen that $|\vec{E}_4|$ will change by the change in d and it will have the maximum value $|\vec{E}_4|_{max}$ as,

$$|\vec{E}_4|_{max} = E_0[1+\rho] \tag{6}$$

when

$$2\beta(l-d) - \chi = m\pi, \qquad \text{where } m = 1, 3, 5. \tag{7}$$

Similarly, the minimum amplitude $|\vec{E}_4|_{min}$ may be found as,

$$|\vec{E}_4|_{min} = E_0[1-\rho] \tag{8}$$

when

$$2\beta(l-d) - \chi = n\pi, \qquad \text{where } n = 0, 2, 4. \tag{9}$$

0018-9456/78/0900-0300$00.75

TABLE I
FREQUENCY = 9.53 GHz

Attenuator Position in dB	VSWR			Position of First Minima From the Load in cm	
	Cross-Coupler Method	Calculated	Slotted-Line Method	Cross-Coupler Method	Slotted-Line Method
1	8.6	8.73	8.5	2.164	2.13
2	4.6	4.42	4.6	2.114	2.06
3	2.95	3.01	3.1	2.069	2.02
6	1.70	1.67	1.65	1.935	1.89
8	1.38	1.38	1.28	1.868	1.79
10	1.24	1.22	1.12	1.61	1.73
15	1.08	1.07	1.02	--	--

Thus, from (6) and (8) one gets,

$$S = \frac{|E_4|_{\max}}{|E_4|_{\min}} = \frac{1+\rho}{1-\rho} = \text{VSWR}. \tag{10}$$

Thus this arrangement works identical to the slotted line system [3]. In this, the maxima and minima are obtained by adjusting the length d at port 3 and recording the reading of matched square law detector connected at port 4 of the coupler.

III. Experimental Arrangement and Results

The experimental arrangement of a 20 dB cross coupler for measuring the VSWR and the position of first minima of an unknown load is shown in Fig. 1. However, for the present measurements, a variable attenuator (0–20 dB) with one end terminated by a waveguide short, was used as an unknown load. Before starting the measurements, the detector was tuned for maximum output. The VSWR of the load was measured by adjusting the sliding short positions for maximum and minimum output of the detector at port 4. For measuring the position of first minima from the load, the port 2 was first short circuited and the sliding short at port 3 was adjusted for minimum output at port 4. Then the short at port 2 was replaced by the unknown load and the sliding short was readjusted for the minima by moving the plunger inwards (i.e., decreasing d). The difference between the two settings of the sliding short is equal to the position of first minima from the load.

The measured VSWR and the positions of first minima are verified by the well-known slotted line technique [4]. The two VSWR values are also compared with the theoretically calculated results, using the following relation,

$$\text{Attenuation (in dB)} = 10 \log \frac{S+1}{S-1} \tag{11}$$

where S is the VSWR of the load. The results are given in Table I.

IV. Conclusion

The results obtained by this method are shown in Table I along with the calculated, and experimental values obtained by slotted-line method, which shows quite a good agreement. The small differences in the values are expected due to observational errors and calibration accuracies of the variable attenuator used as an unknown load.

This method seems to be very useful for the measurements at high power and frequencies. As mentioned before, this cross-coupler, and sliding short method can easily be used for the measurements in place of the slotted section arrangement. Also, the sliding short usually has relatively more precise calibration, the phase informations determined by this method are more accurate. However, the directivity of the coupler limits the lower range accuracy of the VSWR.

Acknowledgment

The author wishes to thank Dr. N. C. Vaidya, Senior Professor and Head of the Department of Electronics Engineering, BHU for his valuable help and encouragement.

References

[1] K. Chandra, R. Parshad, and R. C. Kumar, "Measurement of impedance at microwave frequencies using directional coupler and adjustable short circuit," *Proc. Inst. Elec. Eng.*, vol. 114, no. 11, pp. 1653–1655, 1967.
[2] R. K. Jha and V. K. Garg, "Voltage standing wave ratio measurement by cross coupler," *Int. J. Electron.*, vol. 29, no. 2, pp. 179–183, 1970.
[3] M. Sucher and J. Fox, Eds., *Handbook of Microwave Measurements*, vol. I, ch. II. New York: Polytechnic, 1963.
[4] F. E. Terman and J. M. Pettit, "Electronic measurements," Kogakusha Co. Ltd., pp. 145–147, 1952.

A Simple High-Resolution Measurement of Motor Shaft Speed Variations

YISHAY NETZER

***Abstract*—A simple method is presented for displaying the instantaneous speed variations in closed-loop or open-loop motor speed regulating systems. The measurement is sampled in nature and is easily adapted to phase-locked-loop systems.**

Motor speed regulating systems can be divided into two major categories: 1) classical tachometer feedback type, and 2) phase-locked-loop (PLL) type.

When ultimate performance is needed, only the latter type should be considered. This is since this method provides zero average speed error. The average speed is determined by the input pulse rate.

The above distinction should be treated carefully however, since although the average error is zero, there are always instantaneous speed variations. These may result from transient load variations or motor torque ripple which are not compensated for by the relatively slow response of the loop. Error may result also from instabilities in the closed loop.

The above variations in speed can be detected by measuring the time period between successive feedback pulses; this can be accomplished by a digital counter or a delayed sweep oscilloscope. However, those methods are deficient in that only random readings are obtained which are not related to one another.

The suggested method is better than the method above in that it gives a continuous display of the changing period from which the speed as a function of time can be inferred.

The method is based on successively measuring the time interval between each of two feedback pulses from the controlled load, converting the interval into a proportional voltage, and displaying

Manuscript received October 3, 1977.
The author is at 20 Gilboa Street, Haifa, Israel.

0018-9456/78/0900-0301$00.75

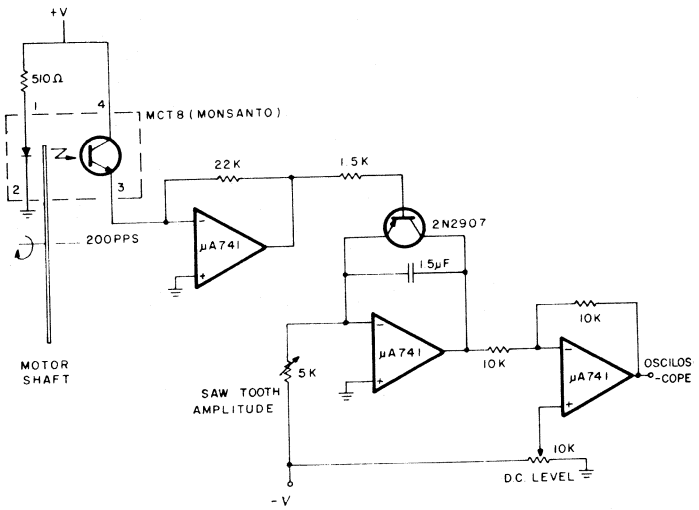

Fig. 1.

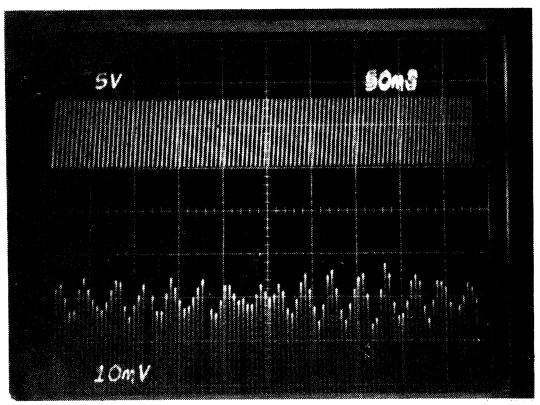

Fig. 2.

the pulsetrain obtained on an oscilloscope screen. Referring to Fig. 1, feedback pulses from the controlled shaft are optically generated, amplified by the first amplifier, and applied to a resettable ramp generator so that each ramp now has an amplitude proportional to the interpulse time duration. The third amplifier is used to level shift the envelope of the waveform to near ground potential so that high magnification can be effected without overloading the oscilloscope. Very high resolution can thus be obtained.

The photograph in Fig. 2 illustrates the application of the method. It was taken from a miniature synchronous–hysteresis-type motor with a low inertia load. The upper trace is the sawtooth waveform which is approximately 7 V peak to peak. The lower trace is a magnified portion of the waveform. It clearly shows that the apparently smooth speed is, in fact, slightly irregular; the main ripple component is approximately seven times the rotation duration. This "hunting" is typical in this type of motor. In comparison, a typical PLL-stabilized induction motor with approximately similar dimensions showed an order of magnitude lower than instantaneous speed variations, whereas a brushless dc motor was found to have a practically smooth angular velocity. It should be emphasized that similar readings could not be taken from the output of the loop filter because of the comparatively slow loop response.

Active Foldback Resistive Circuits

LOUIS A. ROSENTHAL, SENIOR MEMBER, IEEE

Abstract—**A two-terminal circuit provides a low resistance until the current exceeds a designed level. At this point, it switches to a high resistance limiting the current. The circuit can be restored to its low resistance state only by returning the current to near zero.**

There is often a need for a fast-acting current limiting circuit breaker that will protect a circuit from excessive current flow [1], [2]. A novel simple circuit has been developed for this purpose where the circuit provides a low resistance up to a fixed current level. Upon exceeding this current, the circuit becomes a high resistance limiting the current flow to some low level. By returning the current to near zero, it is possible to restore the circuit to its low resistance state. There is a small insertion loss that must be tolerated corresponding to the current passing and sensing mechanism.

Fig. 1 is the circuit arrangement. Transistors T_1 and T_2, as a Darlington pair, pass the load current in the active state since resistor R_2 will bias the circuit into conduction. Load current through the resistor R_1 produces a voltage drop which, at a critical current, will break down the $T_3 - T_4$ circuit. The base of T_2 is thereupon pulled down to the low forward drop of the $T_3 - T_4$ circuit and the Darlington conduction path is opened. Breakdown of the $T_3 - T_4$ circuit changes the conduction state. As shown, this circuit can be replaced by a typical four-layer breakdown diode (e.g., SUS 2N 4987) except that the trigger voltage level would be fixed at about 8 V. As shown, the three diodes (D_n) hold off conduction in T_4 until 1.8 V appears at the emitter of T_4. At the onset of conduction, T_3 in a regenerative manner pulls the entire circuit drop down to one diode drop (V_{BE}). For each additional silicon diode in the D_n string, the threshold (V_f) is increased 0.45 V. Since the voltage at the base of T_2 must be at least two diode drops (i.e., $2V_{BE}$) to start conduction; no current flows through R_1, and R_2 essentially limits the current flow.

Fig. 2 shows the circuit states and the foldback resistance paths. Starting from the origin and ignoring an offset of two diode drops (due to $T_1 - T_2$), current increases along conductance line G_1 according to

$$G_1 = 1/(R_1 + R_2/\beta_1\beta_2) \tag{1}$$

where $\beta_1\beta_2$ are the respective current gains for T_1 and T_2. At the foldback or breakdown point corresponding to "A," the current is

$$I_A = (V_f - 2V_{BE})/R_1 \tag{2}$$

where V_f is the breakdown voltage of the $T_3 - T_4$ circuit and V_{BE} is a typical active base-emitter voltage drop (i.e., 0.6 V). The voltage drop at the foldback point is I_A/G_1 and greater than V_f by $I_A R_2/\beta_1\beta_2$. A typical value for $\beta_1\beta_2$ would be 2500.

Upon breakdown, the circuit jumps to point "B" corresponding to a conductance G_2 where

$$G_2 = 1/(R_2). \tag{3}$$

Increasing or decreasing the voltage produces movement along the line 0–C. To restore the circuit to the G_1 state, the current has

Manuscript received October 7, 1977.

The author is with the Department of Electrical Engineering, College of Engineering, Rutgers University, Piscataway, NJ 08854.

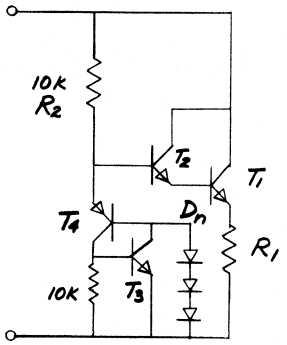

Fig. 1. The circuit diagram is shown. Transistors are T_2, T_3 = 2N718, T_1 = 2N3585, T_4(PNP) = 2N2862. D_n is a series string of three general-purpose silicon diodes.

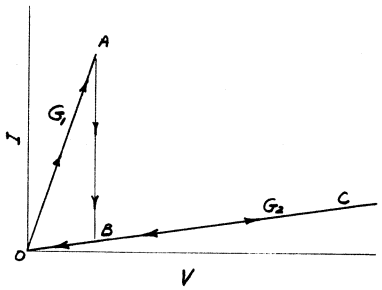

Fig. 2. The resistance paths are shown. Low resistance region (G_1) will change to a high resistance region (G_2) at a trip point "A." Returning to the origin will reset the resistance back to the original low level.

to be dropped below the holding current for the $T_3 - T_4$ circuit and this practically corresponds to the origin "0" region.

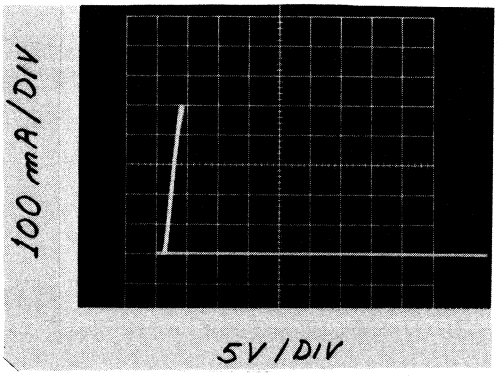

Fig. 3. A curve-tracer portrait of the circuit of Fig. 1 with R_1 = 0.9 ohms displays the two resistance regions. The insertion voltage drop is 4 V.

Fig. 3 is a "curve tracer" presentation of a typical circuit for which R_1 is 0.9 Ω. The current trip point is 500 mA, G_1 = 0.2 mho, and the insertion voltage drop is 4 V including a 2-V_{BE} offset. During the off state, the G_2 conductance (10^{-4}) is not discernible. The circuit is sufficiently simple so that scaling and design variations are obvious.

Since the resistance change can produce inductive energy effects, a reverse conduction diode or equivalent can be placed across T_1. By placing the circuit in a full-wave rectifier bridge, it is possible to obtain ac current trip performance.

References

[1] *SCR Manual*, 5th ed., General Electric Semiconductor Products Dept., Syracuse, NY, 1972, p. 210.
[2] "ISO-Switch," Ohmic Instruments, St. Michaels, MD.

Correspondence

Comments on "Optimization of the Wheatstone Bridge Sensitivity"

EIJIRO TAKAGISHI

In the above paper,[1] Maisel mentioned that S_{max}, the optimum value of a normalized voltage sensitivity, attains 0.25 at its upper limit, but the same result was made public more than forty years ago by J. Krönert [Messbrücken und Kompensatoren, Band I, 1935, equation (146)].

In dealing with the optimization of the relation between S_{max} and P_{TN}, a normalized power input, Maisel adopted for the said S_{max} the value of S, in which N satisfies (7). This point of view is, however, not right strictly speaking, as is made clear in the following. In Fig. A1, a curve S is drawn by the aid of (3), as is the case in Fig. 2 of the paper, and it contacts at a point C with a horizontal line parallel to the axis N. Thus this point C represents the optimum state mentioned above. Now, let a dotted line P_{TN} be drawn by aid of the equation for P_{TN} in Table I of the paper so as to pass through the point C, and another dotted line $\boldsymbol{P}_{TN}$ be a similar one but contacting with the curve S at a point $\boldsymbol{C}$. Then, the relation $\boldsymbol{P}_{TN} < P_{TN}$ will be evident to hold by numerical calculations. Since this point $\boldsymbol{C}$ means the optimum state under the condition of a given $\boldsymbol{P}_{TN}$, contrary to the point C adopted by Maisel independently of P_{TN}, it is clearly much more reasonable to prefer the said point $\boldsymbol{C}$ in the analysis of the present subject.

Before dealing with this analysis, I will comment on the contents of the present paper of Maisel, which dealt with the point C.

1) The numerical values read off Figs. 3 and 4 of the paper at S_{max} do not agree with those (marked *) calculated from (3) as Table AI shows. Why?

2) Equation (6) must be corrected as (perhaps a misprint)

$$M = \{K(1 - N^2) - N^2\}/N^2.$$

3) Maisel illustrated graphically the existence of a minimum value of P_{TN} at a certain value of S_{max} and mentioned that this optimum point can be determined by setting dP_{TN}/dS_{max} equal to zero, but its result was not shown by him. Then I will show it, for reference, as follows:

$$\mathring{S}_{max} = [\{(1 + 2K) - \sqrt{1 + K}\}/(3 + 4K)]^2 \tag{A1}$$

$$\mathring{P}_{TN} = \frac{K(1 + 2\sqrt{1 + K})^2}{2\sqrt{1 + K}\{(1 + 4K)\sqrt{1 + K} - 1\}} \tag{A2}$$

the mark ∘ on the symbols meaning the optimum state mentioned above. Some results of calculation made by use of these equations are shown in Table AII.

Such an optimum state as above exists so far as the said point C is concerned and disappears in a rigorous analysis of the present subject as will be proved theoretically in the following.

Now we know that the following equation holds at the point $\boldsymbol{C}$

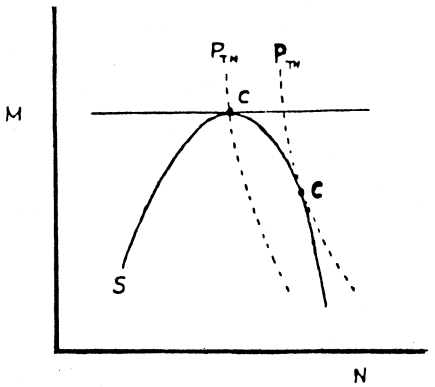

Fig. A1. Graph illustrating two kinds of contact points on an S contour.

TABLE AI

Fig.	K	M	N	S_{max}	
3	10	30	0.3	0.05	0.10*
"	"	3	0.64	0.15	0.21*
4	100	25	0.43	0.1	0.2 *

TABLE AII

K	$\mathring{P}_{TN}$	$\mathring{S}_{max}$	Remarks
1	0.8536	0.05132	Fig.5
10	0.6508	0.1691	" 6
100	0.5498	0.2245	" 7

after mathematical treatment by use of (3) and the equation for P_{TN} shown in Table I of the paper:

$$[\boldsymbol{P}_{TN} \cdot N + (P_{TN} - 1)][K(1 - P_{TN}) + (1 + K)\boldsymbol{P}_{TN} \cdot N^2] = N[(1 + K)\boldsymbol{P}_{TN} \cdot N + K(P_{TN} - 1)]. \tag{A3}$$

This becomes a cubic equation with respect to N as follows:

$$N^3 + a_2N^2 + a_1N + a_0 = 0 \tag{A4}$$

where

$$a_2 = 1 - \left(\frac{2}{\boldsymbol{P}_{TN}}\right)$$

$$a_1 = \left(\frac{K}{1 + K}\right)\left\{\left(\frac{1}{\boldsymbol{P}_{TN}}\right)^2 - 1\right\}$$

$$a_0 = -\left(\frac{K}{1 + K}\right)\left\{1 - \left(\frac{1}{\boldsymbol{P}_{TN}}\right)\right\}^2. \tag{A5}$$

S in this state, being designated by S_{max}, is

$$S_{max} = \frac{\{(1 + N)\boldsymbol{P}_{TN} - 2N\}}{K(\boldsymbol{P}_{TN} - 1)(1 + N)^3}. \tag{A6}$$

Manuscript received March 17, 1978.
The author is at 25-26, 3-Chome, Kamikitazawa, Setagayaku, Tokyo 156, Japan.
[1] J. E. Maisel, *IEEE Trans. Instrum. Meas.*, vol. IM-26, pp. 17-21, Mar. 1977.

0018-9456/78/0900-0304$00.75 © 1978 IEEE

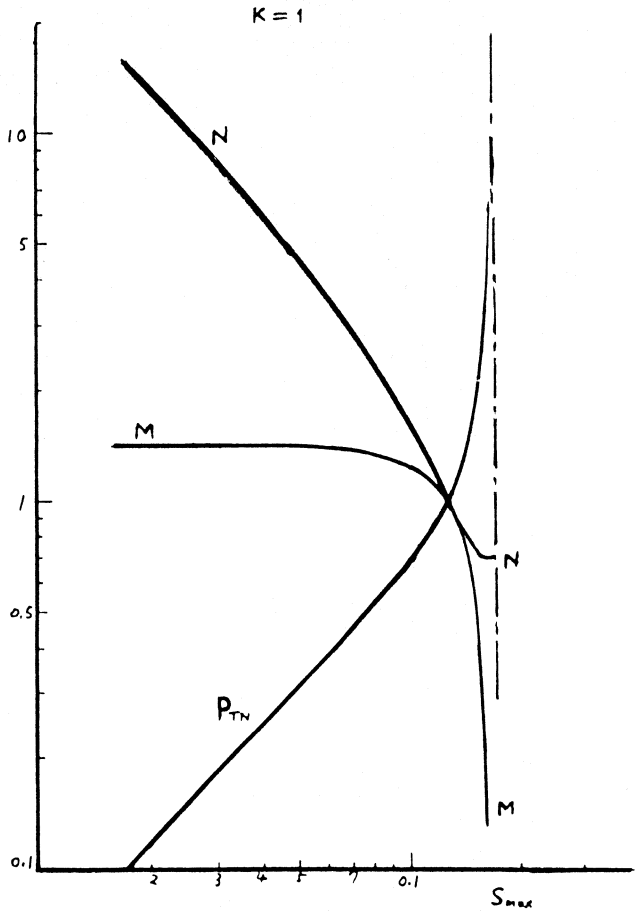

Fig. A2. Optimum characteristics with respect to the point C.

TABLE AIII

K	$\mathring{P}_{TN}$	$\mathring{S}_{max}$	M	N
1	0.8536	0.1144	1.141	1.198
10	0.6508	0.2101	2.149	1.252
100	0.5498	0.2405	5.239	1.166

In a special case of $P_{TN} = 1$, directly from (3)

$$N = M = 1 \tag{A7}$$

and from (3)

$$S_{max} = \frac{1}{4}\left(\frac{K}{1+K}\right). \tag{A8}$$

In another special case of $P_{TN} = \infty$, similarly,

$$N = \sqrt{\frac{K}{1+K}} \tag{A9}$$

$$M = 0 \tag{A10}$$

$$S_{max} = K/\{\sqrt{K} + \sqrt{1+K}\}^2. \tag{A11}$$

By aid of these equations, we can elucidate the numerical relations between N and S_{max}, the result being shown in Fig. A2 for the case of $K = 1$. Comparing the curve P_{TN} in this figure with the curve 1 for P_{TN} in Fig. 5 of the paper, we see a distinct difference between them, i.e., no minimum phenomena of P_{TN}. This holds for other values of K as well. Also, if we calculate the values of S_{max} obtainable at the point C, Table AIII is achieved, which shows much

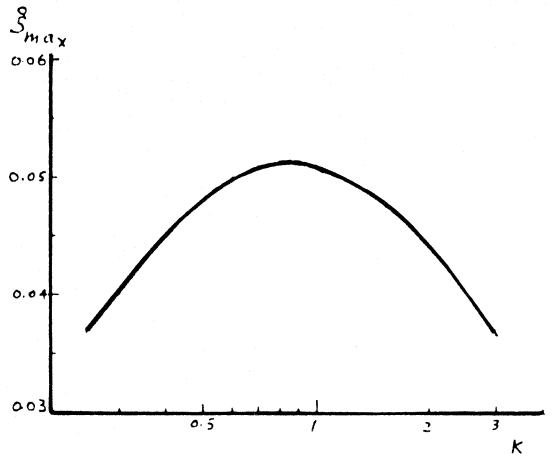

Fig. A3. Graph showing the existence of optimum K.

TABLE AIV

K	$\mathring{P}_{TN}$	S_{K-max}	M	N	P_{TN-MIN}	S_{K-max}
0.5	0.9083	0.0481	13.35	0.1835	0.948*	0.034*
1.0	0.8536	0.0513	9.657	0.2929	0.853*	0.050*
2.0	0.7887	0.0441	8.196	0.4227	0.700*	0.050*
3.0	0.7500	0.0370	8.00	0.5000	0.593*	0.039*

better results than those in Table AII, and this fact also agrees with the relation $P_{TN} < P_{TN}$ mentioned in illustrating Fig. A1.

Lastly, I wish to add some comments also on the earlier paper by Maisel which dealt with a current sensitivity since it was referred to in his present paper. It is to be noted that in the earlier said paper, also, the point C was dealt with.

1) Equation (3) must be corrected as (4) in the present paper, and accordingly, (4) as follows:

$$S_{k-max} = 1/(\sqrt{M+1+K} + \sqrt{K})^2. \tag{A12}$$

2) Equation (5) must be corrected as

$$\frac{S_k}{S_1} = \frac{1+K}{1+KX}. \tag{A13}$$

Accordingly, Figs. 4 and 5 of the paper need rewriting and the content of the section "Power Distribution" must also be altered.

3) Since the optimum relation between S_{max} and P_{TN} is dealt with in the paper merely by a graphical method, I will show its mathematical results below:

$$\mathring{S}_{max} = \frac{1}{K}\left[\frac{(1+2K) - \sqrt{1+K}}{(3+4K)}\right]^2 \tag{A14}$$

$\mathring{P}_{TN}$ = the same as (2)

$$M = 2(1+K)\,\frac{\{(1+4K)\sqrt{1+K} - 1\}}{\{(1+2K) - \sqrt{1+K}\}^2} \tag{A15}$$

$$N = \frac{1}{\sqrt{1+K}}\,\frac{\{(1+2K) - \sqrt{1+K}\}}{\{(5+4K) + 4\sqrt{1+K}\}^{1/2}}. \tag{A16}$$

These equations serve to make clear the behaviors in further details as Table AIV and Fig. A3 show.

The numerical values (marked *) were obtained graphically by Maisel. Based on these figures, he concluded that the optimum value of K lies between unity and two. This conclusion, however, is wrong due to the graphical method's error and it must be

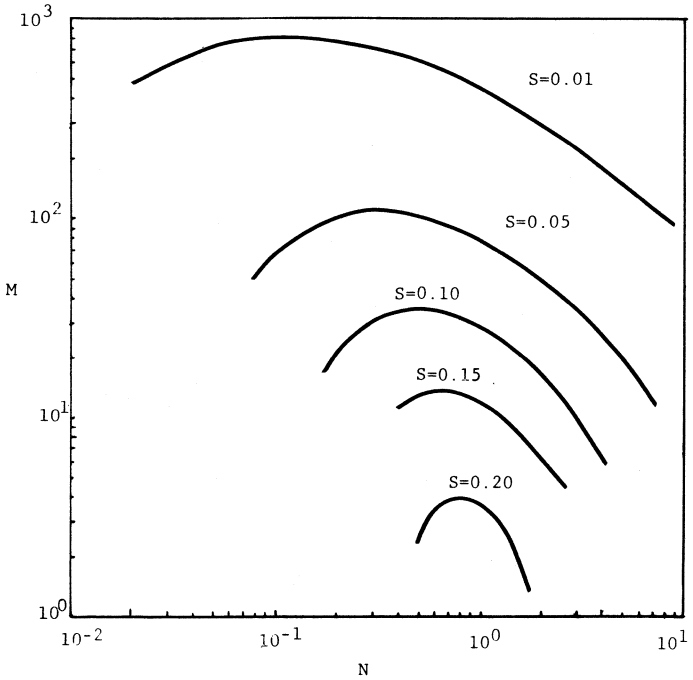

Fig. A4. Curves of constant bridge sensitivity ($K = 10$).

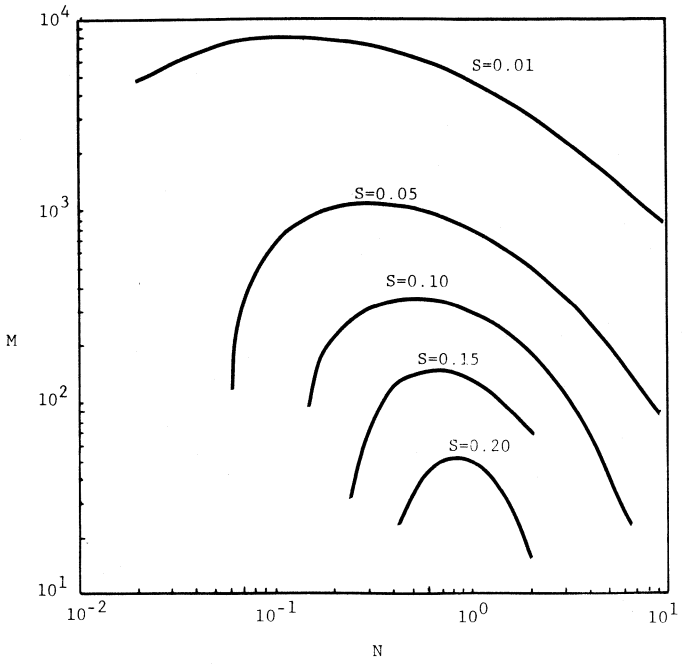

Fig. A5. Curves of constant bridge sensitivity ($K = 100$).

corrected as "nearly equal to 0.8" as Fig. A3 shows. If a far more precise value of K is necessary, we may calculate it using (A14) by the cut-and-try method, the results being: $K = 0.8653$, $\tilde{S}_{max} = 0.05157$, $P_{TN} = 0.8661$, $M = 10.2$, and $N = 0.2678$.

4) Although I pointed out in the above some errors found in Maisel's course of analysis on the state of the point C, the analysis ought to be made substantially with respect to the state of the point C, as already examined in case of voltage sensitivity; and there is no doubt that there appears to be no minimum characteristics of P_{TN} such as concluded by Maisel.

Reply[2] *by James E. Maisel*[3]

I agree that E. Takagishi's approach for determining the normalized power input at maximum bridge sensitivity will produce the most favorable results.

In regard to Figs. 3 and 4 in the original article, I must apologize for the scaling error. Figs. A4 and A5 in this correspondence represent the corrected set of curves for Figs. 3 and 4, respectively.

[2] Manuscript received May 30, 1978.
[3] J. E. Maisel is with the Electrical Engineering Department, Cleveland State University, Cleveland, OH 44115.

Contributors

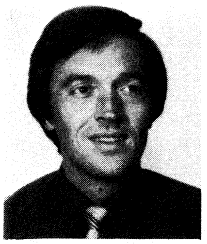

Kjell Aamo was born in Malvik, Norway, on June 3, 1942. He received the degree of Siv.ing. (M.Sc.) from the Division of Physical Electronics, Norwegian Institute of Technology, Trondheim, Norway, in 1968, and the degree of Lic.techn. (Ph.D.) from the Division of Telecommunication, Norwegian Institute of Technology, University of Trondheim, Trondheim, Norway, in 1976.

He is currently an Assistant Professor at the Division of Telecommunication, Norwegian Institute of Technology, where he is engaged in laboratory courses covering high-frequency and microwave measuring techniques. During the last couple of years his research interests have been directed towards digital microwave radio-relay systems and gigabit transmission.

✣

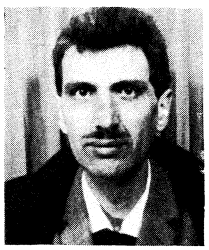

Etienne Boileau was born in Mulhouse, France, in 1933. He studied physics at the University of Paris, Paris, France.

He entered the higher teaching administration as an Assistant in the University of Paris, Paris, France, in 1960. He studied the statistical fluctuations of single-mode lasers experimentally and developed a model which gives all the moments of such amplitude stabilized signals. This work was accepted as his doctoral dissertation in 1970. He obtained five years of detachment at the University of Algiers where he gave courses on thermodynamics. He is now Maître-Assistant in Electronics at Paris XI University, where he is working on some aspects of spectrum analysis.

✣

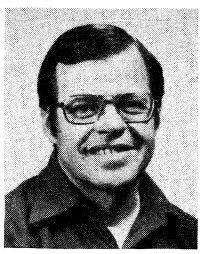

William C. Daywitt was born in Denver, CO, on September 30, 1935. He received the B.S. degree in engineering physics in 1958, and the M.S. degree in applied mathematics in 1959, both from the University of Colorado, Boulder, where he is currently doing graduate work towards the Ph.D. degree in physics.

He joined the staff of the National Bureau of Standards in October, 1959. He has worked in the field of microwave noise where he was engaged in developing systems, standards, and techniques for use in microwave noise measurements.

✣

Mitchell W. Finkel received the B.S. degree from American University, Washington, DC, and the M.S. degree from George Washington University, Washington, DC.

For the past several years, he has been principally concerned with detector evaluation. Prior to that, he worked in the general area of optical instrumentation and measurement.

Hari Herscovici, photograph and biography not available at the time of publication.

✣

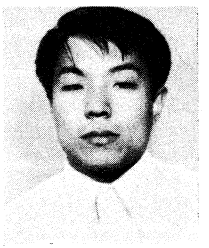

Toshiyuki Iida was born in Wakayama, Japan, on May 8, 1949. He received the B.E. and M.E. degrees in nuclear engineering from Osaka University, Osaka, Japan, in 1973 and 1975, respectively. He is currently working towards the Ph.D. degree in the area of nuclear instrumentation at Osaka University.

He is a member of the Atomic Energy Society of Japan.

✣

Takemi Inoue (S'67–M'69), for a photograph and biography please see page 201 of the June 1978 issue of this TRANSACTIONS.

✣

Gregory J. Johnson was born in Sydney, Australia, in 1923. He received the B.Sc. and M.Sc. degrees from the University of Sydney, Sydney, Australia, in 1952 and 1960, respectively.

He joined the National Measurement Laboratory (then the National Standards Laboratory) in 1951, where he worked on problems associated with the absolute ohm determination. He joined the University of New South Wales in 1960 where he is now Associate Professor in Electrical Engineering. He spent 1967 as a Research Scientist in the Absolute Measurements Section of the National Bureau of Standards and was for six months in 1972 Visiting Research Officer at the National Research Council of Canada.

✣

Miroslaw Matuszewski, photograph and biography not available at the time of publication.

✣

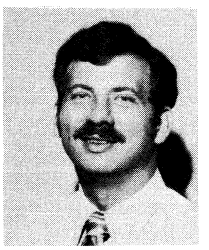

G. Marshall Molen (S'69–M'74) was born in Greenville, TX, on February 22, 1945. He received the B.S.E.E., M.S.E.E., and Ph.D. (electrical engineering) degrees from Texas Tech University, Lubbock, in 1968, 1969, and 1974, respectively.

As a student, he conducted research in gas lasers, plasma diagnostics, and optical data processing; and he studied CO_2 laser refraction and heating effects in a magnetized plasma column for his Ph.D. degree. In 1974 he joined the Weapons Effects Department of The Aerospace Corporation where he conducted basic research in plasma focus devices and CO_2 laser-plasma interactions. In 1976 he joined ESCO Manufacturing Company in Greenville, TX, as the Director of Research and Development where he was involved in the development of subsea electrical equipment and engineering for the utility and oil industries. He is presently an Associate Professor in the Electrical Engineering Department at Old Dominion University in Norfolk, VA, where he is pursuing research in pulsed power.

Dr. Molen is a member of American Physical Society, Tau Beta Pi, Eta Kappa Nu, Sigma Xi, and Phi Kappa Phi.

Toshio Nemoto (M'63), for a photograph and biography please see page 114 of the March 1978 issue of this TRANSACTIONS.

✠

Juraj Poliak was born in Czechoslovakia in 1940. He received the Dipl. Ing. degree in electrical engineering from the Technical University of Brno, Brno, Czechoslovakia, and Doctor degree from the Université Paul Sabatier, Toulouse, France, in 1962 and 1971, respectively.

From 1963 to 1965, he was in the Czechoslovakia Academy of Sciences in Bratislava and he joined the Technical University, Bratislava, Czechoslovakia. In 1969 he joined the Laboratoire d'Automatique et de ses Applications Spatiales du CNRS in Toulouse, France, and since 1971 he has been in the Ecole Polytechnique Fédérale, Lausanne, Switzerland. His principal field of interests is measurements, transducers, and instrumentations.

✠

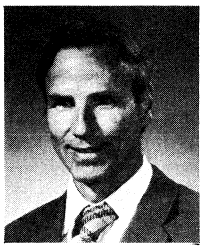

Roderick R. Real (S'55–M'57) was born in Saskatoon, Sask., Canada, on May 21, 1931. He received the B.Sc. degree in electrical engineering from the University of Saskatchewan, Saskatoon, Sask., Canada, in 1953, and the M.Eng. degree in communications electronic engineering from McGill University, Montreal, P.Q., Canada, in 1957.

From 1953 to 1955, he was with the Northern Electric Company, Montreal, P.Q., Canada, working in high-tension cable design. From 1957 to 1964, he worked on various communication devices at the Radio and Electrical Engineering Division of the National Research Council (N.R.C.) of Canada, Ottawa, Ont., Canada. Since then, he has been with the N.R.C.'s Division of Physics, working on problems associated with photogrammetric data processing and instrumentation.

Mr. Real is a member of the Professional Engineers of Ontario, Canada.

✠

Arturo Sancholuz (M'76) was born in Bahia Blanca, Argentina, on May 20, 1946. He received the Diploma in Electrical Engineering from Universidad de La Plata, La Plata, Argentina, in 1969, and the M.S. degree in instrumentation and M.S. degree in electrical engineering from the University of Iowa, Iowa City, in 1974 and 1975, respectively.

From 1969 to 1972, he was a Research Engineer at La Plata University, working primarily on fluid mechanics instrumentation. He was an Assistant Research Scientist at the Institute of Hydraulic Research of the University of Iowa from 1975 to 1976. He is currently Head of the Instrumentation Division at the National Hydraulic Laboratory of Venezuela, Caracas, Venezuela.

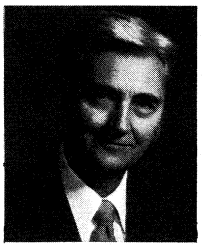

Howard K. Schoenwetter (M'54–SM'75) was born in Klemme, IA, in 1922. He received the B.S. degree in physics from the University of Iowa, Iowa City, in 1946, the M.S. degree in physics from Georgia Institute of Technology, Atlanta, in 1949, the M.S. degree in electrical engineering from the University of Illinois, Urbana, in 1953, and the D.Sc. degree in electrical engineering from George Washington University, Washington, DC, in 1972.

He developed electronic instrumentation for nuclear physics experiments, commercial laboratory test equipment and telemetering equipment (FM, PDM, PCM) for flight testing aircraft and missiles during 1949–1965. He was Chief Engineer of the Instrumentation Section, Martin-Marietta Corporation, Denver, CO, during 1960–1962 and of General Devices, Inc., Princeton, NJ, during 1962–1965. Since 1967, he has been with the Electricity Division, National Bureau of Standards, Washington, DC, developing instrumentation for precision high-speed voltage measurements.

Dr. Schoenwetter is a member of Sigma Pi Sigma, Pi Mu Epsilon, and a number of ANSI and IEEE Standards committees.

✠

A. Douglas Shaw was born in Camberwell, Victoria, Australia, on July 18, 1924. He received a diploma in electrical engineering from the Caulfield Institute of Technology, Caulfield, Australia, in 1952.

From 1957 to 1970, he was Metropolitan Mains Engineer in the Retail Supply Branch of the Hydro-Electric Commission of Tasmania, Tasmania, Australia, where he was responsible for the design, maintenance, and construction of overhead and underground mains in Hobart. In 1970, he was appointed Development Engineer of the Retail Supply Branch. His principal activities are technical investigations and research into all matters likely to have an impact on electricity distribution systems.

Mr. Shaw is a member of the Institution of Engineers, Australia, and the Association of Professional Engineers, Australia.

✠

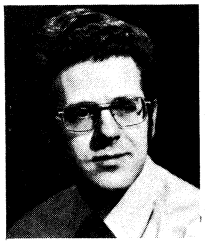

Peter J. Skilton was born in Bexley, England, on February 22, 1947. He received the B.Sc. honours degree in applied physics from the City University, London, England, in 1970.

Before and during his degree course he worked in the Avionics division at the Royal Aircraft Establishment, Farnborough, England, and since the completion of the course has been employed in the Microwave Standards division at the Royal Signals and Radar Establishment, Malvern, England, where he has worked on systems for the measurement of waveguide attenuation and waveguide power standards.

✠

Samuel R. Stein, for a photograph and biography please see page 116 of the March 1978 issue of this TRANSACTIONS.

Stanislaw S. Stuchly (M'70–SM'72) was born in Lwow, Poland, on November 20, 1931. He received the B.Sc. degree from the Technical University, Gliwice, Poland, and the M.Sc. degree from the Warsaw Technical University, Warsaw, Poland, both in electrical engineering, in 1953 and 1958, respectively, and the Ph.D. degree from the Polish Academy of Sciences, Warsaw, Poland, in 1968.

From 1953 to 1959, he was a Research Engineer in the Industrial Institute for Telecommunications, Warsaw, Poland. From 1959 to 1963, he was with Warsaw Technical University. In 1963, he joined UNIPAN—Scientific Instruments, subsidiary of the Polish Academy of Sciences. From 1970 to 1976, he was with the University of Manitoba, Winnipeg, Man., Canada. Since 1977, he has been an Associate Professor in the Department of Electrical Engineering, University of Ottawa, Ottawa, Ont., Canada.

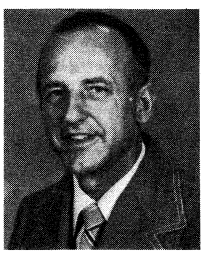

Robert Sullivan received the B.S. degree from Indiana Institute of Technology, Fort Wayne.

Currently Manager of the Sensor Evaluation Hybrid Computer Laboratory at Nasa/Goddard; he has worked on computer software systems, digital and analog hardware with emphasis on computer interfacing hardware for automatic data acquisition, control, and display.

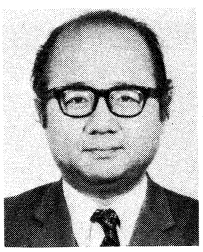

Kenji Sumita was born in 1930. He received the M.S. degree in physics and the Ph.D. degree in nuclear engineering from Osaka University, Osaka, Japan, in 1953 and 1966, respectively.

From 1953 to 1956, he was a Research Fellow of Central Research Institute of Electric Power Industry Japan. From 1956 to 1964, he worked at Japan Atomic Energy Research Institute. In 1964, he became an Associate Professor of Osaka University, and since 1975 he has been a Professor of Osaka University.

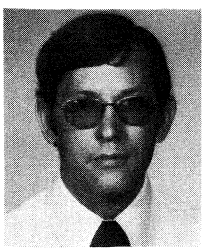

Leslie L. Thompson was born in Albuquerque, NM, on January 11, 1944. He received the B.S. and M.S. degrees in electrical engineering from the University of Maryland, College Park, in 1966 and 1969, respectively.

He has been employed at NASA/Goddard Space Flight Center, Greenbelt, MD, since 1966. For the last seven years, he has been responsible for the development of advanced discrete, hybrid, and monolithic detector technologies for earth observation remote sensors. In addition, he is responsible for sensor systems design utilizing these advanced technologies.

Mr. Thompson is a member of Phi Eta Sigma, Eta Kappa Nu, Tan Beta Pi, and the Society of Photo-Optical Instrumentation Engineers (SPIE).

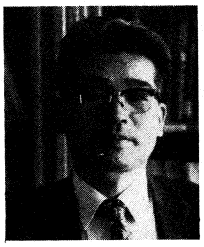

Tasuku Takagi (M'66) was born on March 31, 1932. He received the B.E. degree from the Kyushu Institute of Technology, Kitakyushu, Japan, in 1955, and the Doctor of Engineering degree in 1960 from Tohoku University, Sendai, Japan.

He joined the Department of Electrical Communications of Tohoku University in 1963 as an Associate Professor and became Professor in 1976. His research interests are in the field of instrumentation and measurement applying electronics and pattern recognition hardware.

Dr. Takagi is a member of the Institute of Electrical Engineers of Japan, the Institute of Electronics and Communication Engineers of Japan, the Institute of Television Engineers of Japan, the Japan Society of Medical Electronics and Biological Engineering, the Society of Instrument and Control Engineers, and the Japan Society of Applied Physics.

✣

Kenneth M. Uglow (S'42–A'45–SM'54) received the B.S. and M.S. degrees in electrical engineering from the University of Maryland, College Park, in 1943 and 1948, respectively.

He was engaged in microwave radar development at the General Electric Company, where he studied mathematics and electromagnetic theory in their advanced engineering program. He was engaged in analytical work and development of radio systems, measurements, and telemetry for high-altitude sounding rockets and ballistic missile guidance at the Naval Research Laboratory. In 1953, he began independent research, consulting, and development work in electronic equipment and systems. In 1958, he joined Electro Mechanical Research, Inc., as Director of Research and Engineering, and later became Chief Scientist. In 1967, he returned to independent research and consulting. His work has included noise and communication theory, nonlinear distortion, antennas, propagation, multiplex transmission, radio interferometry, electronic instrumentation, satellite subsystems for astronomy, data collection, air traffic control and navigation, design review, and malfunction analysis. He has developed a short course in frequency modulation which he teaches periodically in Sarasota, FL, and at other facilities.

Mr. Uglow is a member of Phi Eta Sigma, Phi Kappa Phi, Tau Beta Pi, Eta Kappa Nu, and is a Registered Professional Engineer in the State of Maryland and the District of Columbia.

✣

James R. Wait (SM'56–F'62) received the B.A.Sc., M.A.Sc., and Ph.D. degrees from the University of Toronto, Toronto, Ont., Canada, in 1948, 1949, and 1951, respectively.

After spending some time prospecting in Arizona, he turned his attention seriously to electromagnetics in 1952 at the Radio Physics Laboratory, Ottawa, Ont., Canada. In 1955, he accepted an offer from the National Bureau of Standards, and since then has been with their Boulder Laboratories, Boulder, CO. His principal affiliation is currently with the National Oceanic and Atmospheric Administration; in addition, he is also a Fellow of the Cooperative Institute for Research in Environmental Sciences as well as Professor Adjoint in the Department of Electrical Engineering of the University of Colorado, Boulder. He also acts as Consultant to the Office of Telecommunications.

Dr. Wait was elected to the U.S. National Academy of Engineering and became Fellow of the Institution of Electrical Engineers (IEE) in 1977.

Naoaki Wakayama was born in 1935 and received the B.E. degree from the Musashi Institute of Technology in 1959. He joined the Japan Atomic Energy Research Institute in 1960 and developed advanced nuclear instrumentation systems for the JMTR, FBRs, and a pulse reactor, NSRR. Since 1969, he has been in charge of the development of high temperature fission counter-chambers. He is a Principal Research Engineer of the JAERI and a member of the Atomic Energy Society of Japan.

✣

Fred L. Walls was born in Portland, OR, on October 29, 1940. He received the B.S., M.S., and Ph.D. degrees in physics from the University of Washington, Seattle, in 1962, 1964, and 1970, respectively.

From 1970 to 1973, he was a Post-Doctoral Fellow at the Joint Institute for Laboratory Astrophysics, Boulder, CO, engaged in research on ion storage techniques and applications. Since 1973, he has been a Staff Member of the Time and Frequency Division of the National Bureau of Standards, Boulder, CO. He is presently engaged in research and development of crystal-controlled oscillators, multiplier chains, hydrogen maser devices, and standards based on ion storage.

Dr. Walls is a member of the American Physics Society.

✣

Hideshi Yamagishi was born in 1945. He finished Kashiwazaki Technical High School in 1964, then joined the JPDR division of the JAERI, where he was engaged in the construction and operation of the JPDR reactor. He moved to the Reactor Instrumentation Laboratory of the same institute in 1974 and was concerned with the development of nuclear power transient monitoring system for the NSRR. He is also concerned with the development of high temperature fission chambers. He is a member of the Atomic Energy Society of Japan.

✣

Kyohei Yamamura, for a photograph and biography please see page 202 of the June 1978 issue of this TRANSACTIONS.

An Invitation To Membership

There is no better time than now to join an IEEE technical Group/Society. Membership gives you ready access to meetings and conferences in your areas of interest, and to the prime movers in engineering, science, and business.

The Transactions and the Newsletter — both included in your Group/Society fee — keep you abreast of the latest developments in your field. And, as an IEEE member, you may choose from a wide offering of Standards, products and services (books, conference records, employment surveys, short courses, and other helpful aids) — all at greatly reduced member rates.

Payments Required

Admission Fee (only if not an IEEE member) . . . $10.00

Plus
50% ☐ or 100% ☐ of:

IEEE Membership Dues: for U.S.A. $45.00, for Canada $42.00, for elsewhere $35.00 . . . . _____

Group/Society Fee (see below) . . . . . _____

Payment . . . . . $_____

Keep this for your records.

If you are a student, see your IEEE counselor or write for Student Membership brochure.

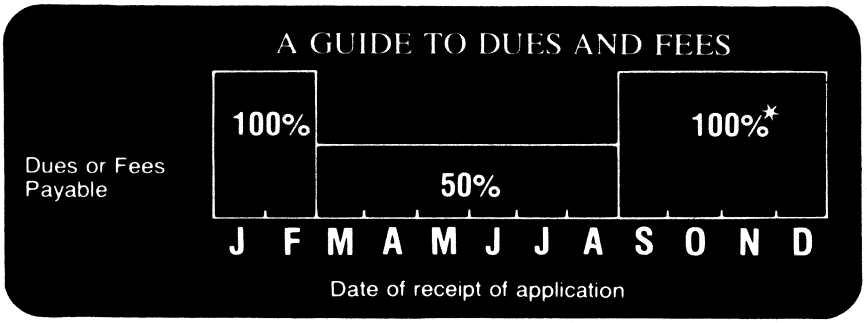

*Includes dues for entire following year.

Membership Application

23-1

Please check appropriate boxes:

Admission fee ☐ $_____

Membership dues payments
50%☐ 100%☐
USA ☐ $_____
Canada ☐ $_____
Elsewhere ☐ $_____

G/S fee ☐ $_____

Payment enclosed $_____

Make check payable to IEEE.

Please mail to:
IEEE Service Center
445 Hoes Lane
Piscataway, N.J. 08854

IEEE
INSTRUMENTATION AND MEASUREMENT SOCIETY
FEE: $5.00 PER YEAR

I am applying for the following as indicated:

☐ I am an IEEE member. Please enroll me in this Group/Society. IEEE member No. _____

☐ IEEE membership plus the above Group/Society membership.

☐ IEEE membership only.

Your Signature _____ Date _____

First Name _____ Middle Initial(s) _____ Last Name _____

Street Address _____

City _____ State/Country _____ Postal Code _____

APPLICANTS FOR IEEE MEMBERSHIP PLEASE COMPLETE THE FOLLOWING INFORMATION:

ENDORSEMENT (Name one individual, preferably an IEEE member, who knows you professionally.)

Endorser's Name (Please print full name) _____

Address (if not an IEEE member) _____

IEEE member?
☐ Yes ☐ No.
If yes, please indicate IEEE member No. _____

Research, Design and Development Engineers:

Reduce Your Literature-Searching Time By Up To 80%

IEEE Journals on Microfilm comprise an Information System that provides amazingly quick access to much of the fundamental literature of modern electrical/electronics engineering.

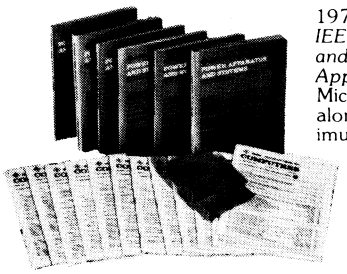

1976 printed issues of *IEEE Trans. on Computers* and *IEEE Trans. on Power Apparatus and Systems*. Microfilm editions, shown alongside, require a minimum of storage space.

Each and every IEEE periodical may now be purchased on roll microfilm on a yearly update basis, beginning with the 1976 issues. This includes ALL 34 of the *IEEE Transactions*, the three *IEEE Journals — Solid State Circuits, Quantum Electronics*, and *Oceanic Engineering* — the *Proceedings of the IEEE* and *IEEE Spectrum*. Micro filmed volumes of IEEE periodicals are ready by June following the publication year. All yearly issues of a given periodical are usually contained in a single cartridge or reel. In full text. Not a word or illustration is omitted.

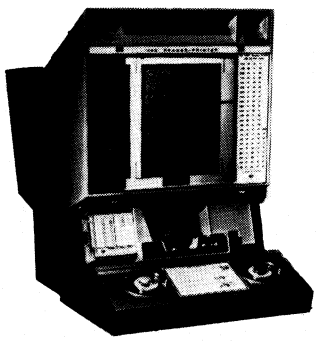

IEEE microfilm is compatible with all currently available equipment. Comes in your choice of 16mm (on cartridge, magazine or reel) or 35-mm reel.

And if your research activities cover a multitude of electrical/electronics engineering disciplines, we've provided worthwhile incentives toward the purchase of ALL IEEE Group/Society *Transactions* and *Journals* on film: 37 periodicals on a yearly update basis. At a 12% saving under their individual list prices. Plus a FREE copy of our ANNUAL COMBINED INDEX TO IEEE PUBLICATIONS for that year.

IEEE microfilm is available on either positive or negative film.

Also available on roll microfilm — all IEEE BACKFILES! These include the *Transactions* published by both the Institute of Radio Engineers (IRE) *and by the American Institute of Electrical Engineers (AIEE)* and the AIEE's *Electrical Engineering*. Our predecessor societies date back to 1884 and it's all here. Every article and paper in every issue of every journal they published. And all easy to locate on handy, inexpensive, trouble-free microfilm. Handsome discounts are available to libraries on purchases of the complete backfiles of each publication, and there are added bonuses for purchasers of full backfiles — FREE microfilmed cumulative COMBINED INDEXES OF THE IRE (1913-1958) or of the AIEE (1884-1959) as appropriate.

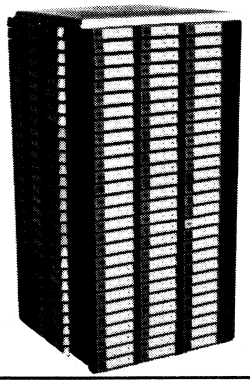

All IEEE journals published between 1884 and 1975 can be housed in the carrousel measuring only 16¼" × 16¼" × 42"—the equivalent of over 80 feet of shelf space.

We have a brochure which fully describes our IEEE journals on microfilm, along with list prices, discounts, free bonuses-everything. If you're interested in learning more about IEEE microfilm, send for brochure No. F-15 today.

Mail your request to:
IEEE,
Attention:
J. D. Broderick,
345 East 47th Street,
New York, N.Y. 10017.

THE INSTITUTE OF ELECTRICAL AND ELECTRONICS ENGINEERS, INC.

IEEE Instrumentation and Measurement Society

Transactions

'itor
:orge B. Hoadley
:p. Elec. Eng.
)rth Carolina State Univ.
ıleigh, NC 27650
19)-737-2283

Editor Designate
ANDREW R. CHi
NASA-Goddard Space Flight Cent.
Code 810
Greenbelt, MD 20771
(301)-982-2502

Editor for Automated Instrumentation
Fred Liguori, 9251
Naval Air Eng. Center
GSED, Naval Air Station
Lakehurst, NJ 08733
(201)-323-2842/3

Newsletter

Editor
S. Clark Wardrip
Timing Syst. Sect.
NASA Goddard Space Flight Cent.
Greenbelt, MD 20770
(301)-982-6587

On January 1, 1979, Mr. Chi will become Editor and Mr. Hoadley will become Editor Emeritus. New Manuscripts may now be sent to Mr. Chi.

Invitation For Papers

Individuals are invited to submit manuscripts and Correspondence items for publication in the IEEE TRANSACTIONS ON INSTRU-ENTATION AND MEASUREMENT. A manuscript, together with an abstract of not more than 200 words (Correspondence abstracts should t be more than 50 words), a biographical sketch, and a photograph of the author, may be sent directly to the Editor of this TRANSAC-ONS.

For suggestions regarding manuscript preparation, authors should consult "Information for IEEE Authors," available on request from : IEEE Editorial Department, 345 East 47 Street, New York, N. Y. 10017. Particular points are to be observed.

1) Manuscript should be easily read and should be spaced so that instructions to the typesetter can be added. Double-spacing typing on 8½- × 11-inch pages with 1-inch margins all around is satisfactory.
2) Drawings for figures should be of high contrast. India ink on white paper or tracing paper is excellent.
3) Drawings for figures should not have detail in them so small that a magnifying glass will be needed to see the detail after a drawing has been reduced in size. Large schematic diagrams are especially troublesome in this respect, and should not be used unless they are really necessary.
4) The typist should follow the arrangement used in a recent issue of this TRANSACTIONS, especially for capitalization and punctuation of titles and footnotes.
5) A separate list of captions for the figures should be prepared.
6) Drawings and photographs of figures should be separate from the body of the manuscript.

If an author wishes to present his paper at a conference, he should send it directly to the conference management. He may simultaneously ıd it to the Editor for publication unless the conference reserves publication rights. The author should advise the Editor that one paper s been submitted for a conference presentation and should notify further the acceptance or rejection of the paper by the conference man-ement.

The quality of this TRANSACTIONS can be only as good as the membership of the Society makes it by contributing papers reporting new d interesting phases of instrumentation.

Page Charges

The first five (four for special issues) are printed without any page charge. For every page beyond this limit, there is an Overlength Page ıarge of $100 per page. As a guide to estimating the printed length of a manuscript, 15 pages typed double-spaced (3 lines per inch) with te type (12 characters per inch) with the typed area 6.4 inches by 9.3 inches will print close to five pages, if there are no figures. To estimate ures determine the height of the figure when the original is reduced to 3.5 inches and add 0.6 inch for the caption. Add the heights of figures together. Divide this by 19.5 and you have the number of pages occupied by the figures. For the title of the paper, allow 0.17 ge.

INSTITUTIONAL LISTINGS

The IEEE Instrumentation and Measurement Society invites application for Institutional Listings from firms interested in the field of instrumentation and measurement.

An Institutional Listing recognizes contributions to support the publication of the IEEE TRANSACTIONS ON INSTRUMENTATION AND MEASUREMENT. Minimum rates are $100 for listing in one issue, or $300.00 for four issues. Larger contributions will be most welcome. No agency fee is granted for soliciting such contributions. Inquiries, or contributions made payable to the IEEE, plus instructions on how you wish your institutional listing to appear, should be sent to M. Bonaviso, The Institute of Electrical and Electronics Engineers, Inc., 345 East 47 Street, New York, N. Y. 10017.